Non-adiabatic effects in transition metal complexes

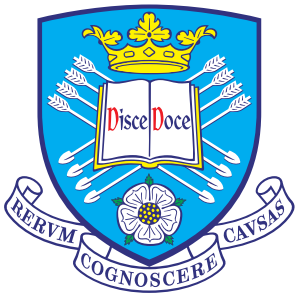

The University Of Sheffield.

Theo Keane

Project supervisors: Dr A. J. H. M. Meijer, Prof. J. A. Weinstein

A thesis submitted in partial fulfilment of the

requirements for the degree of Doctor of Philosophy

19th December 2016

Abstract

Electron transfer (ET) is a fundamental process that underpins a vast array of science and technology. Recent experiments (Delor *et al.*, *Science*, **2014**, 346, 1492 and Delor *et al.*, *Nature Chem.*, **2015**, 7, 689.) have demonstrated that excited state ET may be manipulated using selective vibrational excitation on an ultrafast (~fs) timescale. This work seeks to identify the underlying mechanisms behind the "vibrational control" phenomenon observed. This is achieved by means of quantum chemical calculations of the ground and excited state properties of these systems: a series of Pt(II) bis-acetylide complexes. Two mechanisms are identified that may contribute towards "vibrational control:" the presence of crossovers between the targeted electronically excited state within the energy range of vibrational excitation, resulting in selective inter-state coupling, and transient polarisation of the excited state along the vibrational coordinates which increases inter-state coupling. These proposed mechanisms could provide guidance in the design of future functional materials. Selected results from this thesis have been published in two articles (Delor *et al.*, *Nature Chem.*, **2015**, 7, 689; Archer *et al.*, *Inorg. Chem.*, **2016**, 55, 8251) and a further two manuscripts are forthcoming (Yang *et al.*, *Nature Comm.*, **2016**, accepted; Delor *et al.*, submitted).

Acknowledgements

The past three years have been an enjoyable journey, though not without trials. I would not have been able to do this alone and I owe many people many more thanks than I can include here. To my supervisors, Anthony J. H. M. Meijer and Julia A. Weinstein, I extend my infinite gratitude: you have been incredibly supportive throughout the course of my Ph.D. and have pushed me to develop myself intellectually and personally, sometimes in spite of my own best efforts. Thank you both so much.

My research has been built on the success of my colleagues in both the Weinstein and Meijer groups and it has been both a great privilege and a great pleasure to work with you all. In particular, my work would have been far less exciting had it not been for the incredible synthetic feats achieved by Paul Scattergood and Stuart Archer, as well as the masterful spectroscopic work of Milan Delor. Indeed, I owe Milan a special thanks for our many discussions about electron transfer, from which I learnt a great deal and without which I am not sure I would have been able to complete this thesis. On the theoretical side, the skills I have developed are entirely due to the guidance of Christopher M. Parks, Julong Jiang and Benjamin Irving. I learnt everything I know about computational chemistry from the three of you.

I feel lucky to count many of my colleagues as friends, as well as co-workers. I have enjoyed many a tea break over the past three years and equally many trips to the pub. Only some of these occasions have been scientifically fruitful, but all of them have been fun. I must also mention my friends Marcus Desai, Rory Summerley, Christy Salter, Alun Meredith, David Schofield and Declan Kolakowski. The past 16 years of "debates" have been instrumental in my growth as a person. May they long continue.

I am very grateful to my family for your unending love and support, and especially for believing in me even when I have failed. To my parents, Nial and Tanja, thank you for raising me to be the person I am today - this thesis is dedicated to you both, with love. Luke and Katja, my brilliant, hilarious, infuriating siblings: you both smell, but I love you anyway. Finally, to Maya Singer Hobbs: thank you for being part of my life.

Contents

List of Figures

List of Tables

Part I

Introduction

Chapter 1

Background

The potential of a civilization is defined by its capacity to do work. In an article speculating on the energetic requirements of inter-stellar information broadcasting, the Soviet astrophysicist Nikolai S. Kardashev developed a classification scheme to describe technological progress for hypothetical civilizations.[1] The scheme, later dubbed the Kardashev scale, was based on the quantity of energy at the disposal of a hypothetical civilization and was as follows:

Class I Approximately equal to total human output in the mid 1960s.
$\sim 4 \times 10^{19}\,\mathrm{erg\,s^{-1}}$.

Class II A civilization able to utilise the entire output of a star like the Sun.
$\sim 4 \times 10^{33}\,\mathrm{erg\,s^{-1}}$.

Class III A civilization able to utilise the entire output of a galaxy like the Milky Way.
$\sim 4 \times 10^{44}\,\mathrm{erg\,s^{-1}}$.

The Kardashev scale has had a broad influence both within the scientific community and without.[2] Whilst somewhat simplistic, the philosophy behind the Kardashev scale suggests that technological progress depends on greater access to energy. Indeed, the importance of the development of energy-related technologies is reflected in the degree to which it currently receives funding from the Engineering and Physical Sciences Research Council (EPSRC) of the UK: the "energy" research sector receives the greatest amount of grant funding from the EPSRC of any specific research sector, at 23.7% of total funding, and research within the

"energy" theme also receives the greatest amount of funding of any theme, at 15.1% of total funding.[3] This is amplified by the fact that the development of novel energy technologies is considered to be a critical component in reducing the impact of anthropogenic climate change.[4,5]

As alluded to by the Kardashev scale, one abundant energy source is solar radiation.[6] Incident solar energy may be captured using three major strategies: by using it to heat an object or a medium, conversion into electrical energy either directly by photo-absorption or indirectly, for example by means of turbines, and finally incident energy may be used to drive chemical reactions.[7] The later of these avenues is known as photosynthesis, although in general the term photosynthesis specifically refers to the energy conversion processes common in plants and bacteria. To distinguish "natural" photosynthesis from anthropogenic photosynthesis, the latter is known as artificial photosynthesis.[8–11] Broadly speaking, the target compounds in artificial photosynthetic processes are either chemical products[12–14] or fuels.[14–17] One of the major issues in artificial photosynthetic systems energy transport from the site of photon absorption to the reaction site.[8,13,18] Unless these two sites are the same, this energy transfer usually takes the form of Electron Transfer (ET).

Electron Transfer is the simplest chemical reaction and constitutes a fundamental process in physics, chemistry and biology, and underpins almost all modern technology.[19] Exerting influence over ET processes through the use of external perturbations, such as light, is a long standing aim in chemistry[20,21] and is one of the key challenges that must be overcome in the effort to achieve artificial photosynthesis.[9]

The induction of ET by photons requires the absorption of a photon by a molecule that matches the energy of an electronic transition in that molecule. Following photo-induced ET, a number of Excited State (ES) processes begin as the molecular wavepacket proceeds on the ES portion of the Potential Energy Surface (PES).[22] These processes; Internal Conversion (IC), Inter-System Crossing (ISC) and Vibrational Cooling (VC), are shown in the Jablonski diagram in Figure 1.1. A further process that occurs is Intramolecular Vibrational Redistribution (IVR), in which energy from an excited vibrational mode is redistributed amongst lower energy

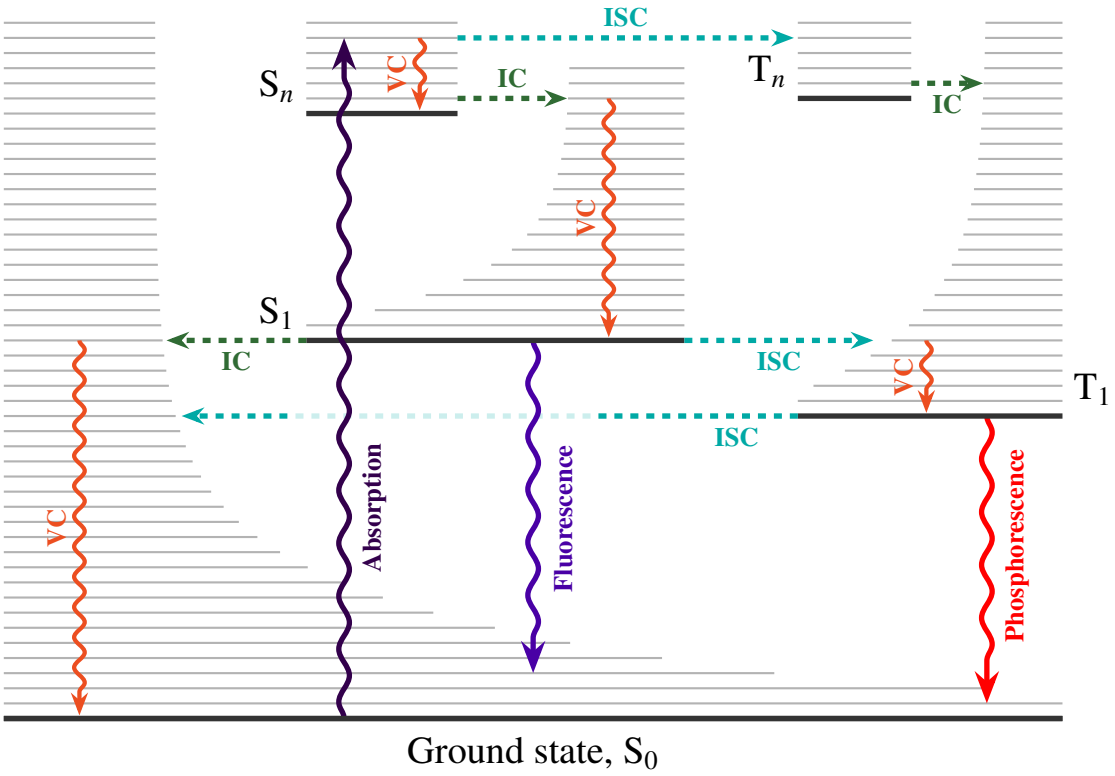

Figure 1.1: The Jablonski diagram, showing the processes that govern photochemistry. ISC = Inter-system crossing, IC = internal conversion, VC = vibrational cooling.[i]

vibrational modes which the excited mode is coupled to.[22–24]

The idea of exerting control over ET is part of the broader aim of achieving, in the words of the late Ahmed H. Zewail, "laser-selective chemistry".[20] Laser selectivity can take two forms: "coherent control", where the influence over a chemical reaction is achieved by means of preparing the wavepacket in a specific phase, or "non-coherent control", where it is the population of certain microstates of the target molecule selectively in time, space and energy such that the outcome of a reaction is altered. An overall control effect may be a combination of both of these types. There are a number of challenges that must be overcome when attempting to achieve laser selectivity. Maintaining a well-defined alignment or orientation of over the target molecules is of particular concern in coherent control experiments. This is especially problematic in the solution phase, where collision dynamics will rapidly remove any transient non-stochastic alignment. There are, however, experimental techniques that may be employed that may side-step these issues, though these introduce other problems.[25] Nevertheless, the first examples of coherent control were reported by Zewail and co-workers in the early 1990s.[26,27]

[i]Figure adapted from `http://www.texample.net/tikz/examples/the-perrin-jablonski-diagram/`

These involved manipulation of the wavepacket in I_2 in the gas phase. Later, coherent control over photoisomerisation in biological chromophores in solution was reported by R. J. Dwayne Miller and co-workers,[28,29] and by others;[30] however, recent work has called into question the veracity of these experiments.[31]

Opportunities for "non-coherent" control have also been thoroughly pursued and were first achieved in the context of ET, as will be described shortly; however, it is important to note that it was by this avenue that control over chemical reactivity was first achieved in the gas phase. In 2013, Roberts and co-workers showed through a set of elegant experiments that the branching dynamics of thioanisole could be altered by the careful preparation of selectively vibrationally excited excited state wavepackets.[32] Vibrational excitation altered passage through two conical intersections, thus changing the photodissociation dynamics in the system.

In the last decade, the question of controlling ET by external means has been investigated theoretically in multiple frameworks. The work of Skourtis and Beratan showed first how non-adiabatic coupling between an electron and a vibrational mode, known as vibronic coupling, in a Donor-Bridge-Acceptor (D-B-A) assembly could alter ET behaviour.[33] Their subsequent work suggested that it would be possible to entirely enable or disable ET pathways by excitation of specific bridge-centred vibrational modes using IR radiation.[34,35] In collaboration with experimentalists, they provided the first empirical evidence of such an effect through a "non-coherent" control scheme: a D-B-H$\cdots$B-A assembly in which the two segments are connected by hydrogen bonds that, under excitation of the H-bonds, showed reduced ET efficiency.[36] The expansion of the framework to explicitly include a vibrational mode driving field and computation of the resultant dynamics showed unequivocally that this was possible.[37] More recently, they have moved to establish more explicit requirements for scenarios in which ET control should be possible,[38] investigated symmetrical A-B-D-B-A systems,[38] and multi-electron transfer pathways.[39]

Other researchers have used non-adiabatic dynamic simulations combined with excited state normal mode analysis to demonstrate how specific vibrational modes of excited states could be directly responsible for ET events, which suggests that driving such modes with an external perturbation could influence ET.[40] Furthermore, it was shown that one of the signatures of

participation of a vibrational coordinate in ET would be signified by large shifts in the energy of such a mode, the magnitude of shifting being correlated with magnitude in participation.[41] Numerical simulations of the effect of vibrational excitation on the rate of charge transfer have been performed, which demonstrate that vibrational excitation can not only increase the rate of charge transfer, but also decrease it.[42,43] It has also been shown that ET can be perturbed by means of targeted excitation of core electrons using X-ray pulses to achieve similar effects to the "vibrational" control scenario.[44]

Following the pioneering work of Skourtis, Beratan and their experimental colleagues, demonstrating control of ET on the molecular scale, Bakulin et al. showed that similar opportunities were available in solid semiconductors.[45] Vibrational excitation was used to drive the localised excited states formed after regular photoexcitation toward more delocalised excited states, improving the efficacy of the semiconductor. This work was recently extended to another system, in which the effect was also seen.[46] Computational investigations identified phonon modes of high similarity to the electronic coupling vectors associated with the charge transfer transition promoted.[46,47] Theoretical methods to identify the molecular vibrational modes of maximal similarity with electronic coupling vectors have recently been developed Yang and Bittner.[48,49]

The preceding efforts led to the recent demonstration of the selective disabling of ET pathways in the excited state using bond-specific vibrational excitation, as predicted by Skourtis and Beratan,[34] in a Pt(II) *trans*-acetylide D-B-A system.[50,51] The molecule used in these experiments, **PTZ-CH_2-Pt-NAP**, is shown in Figure 4.1. Photoexcitation of **PTZ-CH_2-Pt-NAP** results in the rapid formation of a Charge-Transfer (CT) excited state. In the CT state, the molecule concurrently undergoes IVR, VC and ISC processes, and has a lifetime of approximately 14 ps. The CT state is able to decay via three channels, the first of which is to simply relax back down to the ground state (GS) through IC, which happens in 33% of cases. Alternatively, ET in the CT state may occur, leading to the formation of a Charge-Separated State (CSS) in 10% of cases, or, through charge recombination, a π-π^* intra-ligand triplet state, centred on the NAP moiety (^{3}NAP) in the remaining 57% of cases. The two lower-energy excited states may themselves decay down to the GS through either ISC or phosphorescence. The CSS has a lifetime of

approximately 1 ns and the ^{3}NAP state approximately 190 μs.

It is the second ET event, which occurs in the excited CT state, that can be controlled using vibrational excitation. If the asymmetric acetylide combination mode in the CT state is excited from $v_0 \rightarrow v_1$, the ultimate yield of states goes from 33%GS:10%CSS:57%^{3}NAP to 33%GS:0%CSS:67%^{3}NAP, *i.e.* the ET pathway from the CT to the CSS is completely disabled. It was hypothesised that the mechanism by which this occurs is that along the asymmetric acetylide vibrational coordinate, previously identified as the reaction coordinate for ET in related Pt(II) acetylides,[52] the PESs of the CSS and CT states cross-over and that a wavepacket in the v_1 vibrational state may proceed past the cross-over, and decay to the ^{3}NAP state. This was evidenced by Density-Functional Theory (DFT) and Time-Dependent DFT (TD-DFT) computations using a model system.

There are, however, some observations that are not explained by this hypothesis. Control experiments performed, in which the vibrational excitation came before electronic excitation, showed no change in excited state yield but did show an acceleration in excited state ET (See Supporting Information of Ref. [51]). As will be shown in Chapter 4, it is unclear from calculations why "pre-excitation" of the vibrational modes has no effect, nor the reason for the resultant accelerated excited state dynamics. Furthermore, the nature of the crossing between the CSS and ^{3}NAP PESs has not been established.

This work seeks to extend the previous investigations to a new set of compounds recently synthesised, similar in nature to **PTZ-CH$_2$-Pt-NAP**, that are predicted to show similar excited state characteristics and which have been investigated using ultrafast spectroscopic techniques.[53] These investigations will use improved theoretical methods to those with which these systems have already been treated to seek to deepen understanding of the ultrafast behaviour of these compounds, as well as to pave the way for future rigorous theoretical treatment of these systems.

Building on the preceding investigations, the possibility of increasing the number of controllable outcomes of ET by increasing the number of Donor and Bridge components in the assembly will also be explored. In Chapter 5, the vibrational and electronic structure of a D-B-A-B-D assembly will be investigated. The possibility of directional electron transfer along either

D-B component, made spectroscopically distinct by means of selective isotopic labelling,[54] and comparisons with experimental data will be drawn.[54,55] This chapter highlights the importance of including anharmonic corrections to harmonic vibrational frequency calculations, as well as the influence of relativistic effects on the excited state electronic structure of complexes of this kind.

In Chapter 6, computational investigations will be used to characterize the vibrational spectra of two recently synthesised, low-valent main group tri-azide complexes.[56] This chapter highlights the importance of careful consideration of conformational flexibility in molecules as well as the judicious selection of an appropriate basis set.

Before these results are presented, however, it is necessary to first consider the requisite theoretical apparatus to conduct computational investigations into quantum chemical systems. These are presented in Chapter 2.

Chapter 2

Theory

Modern computational chemistry has its origins in 1926, when Erwin Schrödinger published a series of six articles detailing a "non-relativistic and unperturbed" wave equation form of quantum mechanics, partitioned in a manner analogous to classical Hamiltonian mechanics.[57–62] These articles, originally in German and subsequently reviewed by Schrödinger in English in Ref. [63], describe the time-independent form of the wave equation (e.g. Eqn. 26, Ref. [63]), which is a special case of the more general time-dependent equation (e.g. Eqn. 31, Ref. [63]). Using these equations, one may can link the wavefunction, Ψ, of a system of particles with the energy, E, of that system. In the time-independent case, the equation takes the form:

$$\hat{H}\Psi = E\Psi. \tag{2.1}$$

The wavefunction, Ψ, fully describes the state of a system of particles. However, the wavefunction has no direct physical interpretation. One cannot measure directly the wavefunction of a system, instead one must infer from measurements of the system what the wavefunction of the system is. The most common interpretation of the wavefunction, the Born or Copenhagen interpretation, is that $|\Psi|^2$ is the probability density of finding a given particle at a given place, r_i, upon measurement, where $r_i = \{x_i, y_i, z_i\}$. Indeed, this was identified by Schrödinger in an addendum to the first paper on quantum wave mechanics.[57]

In the time-independent Schrödinger equation, Ψ and E are linked by the Hamiltonian operator, $\hat{H}$. For a well-behaved wavefunction, the Hamiltonian operator (also known as just the

Hamiltonian) has *eigenvectors*, ψ_i, that are the well-defined states of Ψ, and their associated *eigenvalues*, E_i, that are the energies of these well-defined states and form the 'spectrum,' $\{E_i\}$, for that Hamiltonian.[64]

The Hamiltonian can be separated into two component operators:

$$\hat{H} = \hat{T} + \hat{V}, \tag{2.2}$$

where $\hat{T}$ is the kinetic operator and $\hat{V}$ is the potential operator. The kinetic operator, $\hat{T}$, can be further separated to describe potential energy derived from translational motion in three dimensions:

$$\hat{T} = \frac{\hat{p}^2}{2m} = -\frac{\hbar^2}{2m}\left(\frac{\partial^2}{\partial x^2} + \frac{\partial^2}{\partial y^2} + \frac{\partial^2}{\partial z^2}\right) = -\frac{\hbar^2}{2m}\hat{\nabla}^2, \tag{2.3}$$

where $\hat{p}$ is the momentum operator, m is the mass of the particle in question, $\hbar$ is the reduced Planck's constant, also known as the Dirac constant, $\frac{h}{2\pi}$, and $\hat{\nabla}$ is the Laplacian or gradient operator, which is used to abbreviate an n-dimensional partial differentiation. Note that $\hat{p} = i\hbar\hat{\nabla}$.

The potential operator, $\hat{V}$, describes the potential resulting from the interactions between the charged subatomic particles of the system, as quantified by Coulomb's law. For a system consisting of a number of electrons $(a, b, c, \dots)$ and nuclei $(A, B, C, \dots)$, and by separating their contributions to $\hat{V}$, the Hamiltonian can thus be rewritten:

$$\hat{H} = \overbrace{\underbrace{-\frac{\hbar^2}{2}\sum_A \frac{1}{M_A}\hat{\nabla}_R^2}_{\text{nuclear}} \underbrace{-\frac{\hbar^2}{2m_e}\sum_a \hat{\nabla}_r^2}_{\text{electronic}}}^{\text{kinetic energy}} + \frac{e^2}{4\pi\varepsilon_0}\overbrace{\left(\underbrace{\sum_{A>B}\frac{Z_A Z_B}{R_{AB}}}_{\text{nuc.-nuc.}} \underbrace{-\sum_{A,a}\frac{Z_A}{r_{Aa}}}_{\text{nuc.-elec.}} + \underbrace{\sum_{a>b}\frac{1}{r_{ab}}}_{\text{elec.-elec.}}\right)}^{\text{potential energy}}, \tag{2.4}$$

where m_e is the mass of an electron, M_A is the mass of nucleus A, $\hat{\nabla}_R$ and $\hat{\nabla}_r$ are the gradient operators along nuclear and electronic coordinates, respectively, e is the elementary charge, ε_0 is the electrical permittivity of free space, Z_A is the charge of nucleus A, R_{AB} is the separation between nuclei A and B, r_{Aa} is the separation between nucleus A and electron a, and r_{ab} is the separation between electrons a and b.

Both electronic and nuclear kinetic terms are negative and thus favourable. The nuclear-

nuclear and electron-electron potential terms are both positive, as interactions between like charges are repulsive and the nuclear-electron potential term is negative, since interactions between opposite charges are attractive. The Hamiltonian can be simplified by employing Hartree atomic units, where $e \equiv 1$, $m_e \equiv 1$, $\hbar \equiv 1$ and $4\pi\varepsilon_0 = 1$, in which case the Hamiltonian becomes:

$$\hat{H} = -\frac{1}{2}\sum_{A}\frac{1}{M_A}\hat{\nabla}_R^2 - \frac{1}{2}\sum_{a}\hat{\nabla}_r^2 + \left(\sum_{A>B}\frac{Z_A Z_B}{R_{AB}} - \sum_{A,a}\frac{Z_A}{r_{Aa}} - \sum_{a>b}\frac{1}{r_{ab}}\right). \tag{2.5}$$

In this form, the Hamiltonian can be used to analytically solve the Schrödinger equation of a hydrogenic atom; that is, an atom which has only 1 electron. However, for any non-hydrogenic system, the Schrödinger equation becomes an N-body problem. Whilst N-body problems are, contrary to popular belief, analytically soluble by a power series,[65–68] the convergence of such series has been shown to be so poor as to be practically useless.[67,69] An alternative, practical route towards developing solutions to the Schrödinger equation is to separate the variables **r** and **R**. This approach is known as the adiabatic, or Born-Oppenheimer, approximation.

2.1 The Born-Oppenheimer approximation

The separation of the variables **r** and **R** pre-dates Schrödinger's "new" quantum mechanics.[70] Indeed, several articles from the mid-1920s contain illustrative graphs in which the energy of a molecule is plotted against nuclear configuration (See M. Born and J. Franck 1925,[71] J. Franck, 1926[72]). The second of these examples, due to Franck in 1926, is of particular note in the context of the present work, since it examines how changes in nuclear geometry might effect a change in the photochemistry of simple diatomic molecules. Later that year, Condon extended the ideas of Franck in an attempt to explain the effect now known as a vibrational progression in absorption and luminescence spectra.[22,73] Following the development of quantum wave mechanics, Condon further postulated that electronic and nuclear motion may be decoupled on the basis of the difference in mass between nuclei and electrons.[74] This allows the wavefunction to be factorised. However, this assertion was not proven by Condon. In their seminal 1927 paper, M. Born and R. Oppenheimer employ perturbation theory up to fourth order to rigorously separate the total

wavefunction into nuclear and electronic components (original paper: [75], translation: [76]). We can therefore rewrite the wavefunction as

$$\Psi(\mathbf{r}, \mathbf{R}) = \Phi(\mathbf{r}; \mathbf{R})X(\mathbf{R}), \tag{2.6}$$

where Φ is the electronic wavefunction, X is the nuclear wavefunction, $\mathbf{r}$ are the coordinates of the electrons and $\mathbf{R}$ are the coordinates of the nuclei.

It is commonly stated that a natural result of the Born-Oppenheimer approximation of Ref. [75] is that one could solve the Schrödinger equation iteratively by 1) solving the "clamped nucleus" electronic *eigenvalue* problem for a given set of nuclear coordinates, $\mathbf{R}$, with *eigenvectors* describing the adiabatic electronic states (*eigenstates*) of well-defined energy and their associated energy *eigenvalues*. 2) Repeating the process for many values of $\mathbf{R}$, allowing an energy profile to be constructed for each *eigenstate*, showing how the energy of the system varies as the nuclear geometry changes. These profiles are called Potential Energy Surfaces (PESs). The suggestion that this is a result of Ref. [75] is in fact false, since Born and Oppenheimer presuppose that the total electronic *eigenvalue* problem is in fact solved (See translation, Ref. [76], §2). That contribution merely shows that Condon's postulate is analytical within some boundaries. The idea of a PES clearly pre-dates 1927, as evidenced by the illustrations discussed above.[71,72]

The common justification for the separation of variables is also due to Condon.[77] This is that the mass of an electron, m_e is ~1836 times smaller than the mass of a proton, m_p, meaning that for even the lightest possible nucleus, a lone proton, the timescales upon which electrons and nuclei move are completely different. The adiabatic theorem can thus be applied,[78] and for the majority of the PES, one may employ an adiabatic approximation and separate nuclear and electronic wavefunctions.[79] To cast light on situations in which the *adiabatic* approximation breaks down, i.e. the conditions in which *non-adiabatic* effects are prominent, it is useful to reconsider Condon's justification. Since the mass of the nuclei is relatively large and the kinetic energy is inversely proportional to mass, the change in kinetic energy associated with exciting nuclear motion is far smaller than the change in potential energy between electronic *eigenstates*. If, however, in some region of the PES two electronic *eigenstates* become close in energy, this

may no longer be the case. This situation which will be explored in Section 2.6.

Let us now examine the impact of the separation of $\mathbf{r}$ and $\mathbf{R}$ on the Schrödinger equation and so derive the "Born-Oppenheimer" approximation. Recalling Eqn. 2.6, we may rewrite Eqn. 2.1 as

$$\hat{H}[\Phi(\mathbf{r};\mathbf{R})X(\mathbf{R})] = E[\Phi(\mathbf{r};\mathbf{R})X(\mathbf{R})]. \tag{2.7}$$

Now, using the expansion of the Hamiltonian from Eqn. 2.5 and noting that the potential operator is unaffected by the separation, we obtain

$$\begin{aligned}\hat{H}[\Phi(\mathbf{r};\mathbf{R})X(\mathbf{R})] = &-\frac{\hbar^2}{2}\sum_{A,a}\frac{1}{M_A}\hat{\nabla}_R^2[\Phi(\mathbf{r};\mathbf{R})\,X(\mathbf{R})] \\ &-\frac{\hbar^2}{2m_e}\sum_{a}\hat{\nabla}_r^2[\Phi(\mathbf{r};\mathbf{R})] \\ &+\hat{V}[\Phi(\mathbf{r};\mathbf{R})\,X(\mathbf{R})] \\ &= E[\Phi(\mathbf{r};\mathbf{R})X(\mathbf{R})]\end{aligned} \tag{2.8}$$

Note that since the nuclear wavefunction has no dependence on $\mathbf{r}$, $\hat{\nabla}_r X(\mathbf{R}) = 0$ and so components of the second term including the nuclear wavefunction are omitted. However, since the electronic wavefunction is dependent on $\mathbf{R}$, $\Phi(\mathbf{r};\mathbf{R})$ remains in the first term. Using the product rule, we may expand the first term:[80]

$$\begin{aligned}\hat{H}[\Phi(\mathbf{r};\mathbf{R})X(\mathbf{R})] = &-\frac{\hbar^2}{2}\sum_{a}\Phi_a(\mathbf{r};\mathbf{R})\sum_{A}\frac{1}{M_A}\hat{\nabla}_R^2 X(\mathbf{R}) \\ &-\frac{\hbar^2}{2}\sum_{A,a}\frac{1}{M_A}2\left(\hat{\nabla}_R\Phi(\mathbf{r};\mathbf{R})\,\hat{\nabla}_R X(\mathbf{R})\right) \\ &-\frac{\hbar^2}{2}\sum_{A}\frac{1}{M_A}X_A(\mathbf{R})\sum_{a}\hat{\nabla}_R^2\Phi_A(\mathbf{r};\mathbf{R}) \\ &-\frac{\hbar^2}{2m_e}\sum_{a}\hat{\nabla}_r^2[\Phi(\mathbf{r};\mathbf{R})] \\ &+\hat{V}[\Phi(\mathbf{r};\mathbf{R})\,X(\mathbf{R})] \\ &= E[\Phi(\mathbf{r};\mathbf{R})X(\mathbf{R})].\end{aligned} \tag{2.9}$$

The first term of Eqn. 2.9 equals the purely nuclear component of the kinetic energy multiplied

by the adiabatic electronic wavefunction(s). This term is exact with respect to the non-separated wavefunction representation. The fourth term is the adiabatic, purely electronic kinetic energy. This is not the same as the one obtained in the non-separated wavefunction, or "non-adiabatic," representation. The difference between the non-adiabatic and adiabatic electronic kinetic energies comes from the second and third terms, highlighted in red, which are represent the corrections to the adiabatic electronic kinetic energy due to nuclear motion. The second term is the so-called "first-derivative" momentum non-adiabatic correction term, since it is first-order in $\hat{\nabla}$, and the third term is the so-called "second-derivative" kinetic energy non-adiabatic correction term, since it is second-order in $\hat{\nabla}$.[81,82]

As previously mentioned, $M_A \gg m_a$. Therefore, the terms that are inversely proportional to M_A should be small. Thus, it should be reasonable to neglect the non-adiabatic contributions to the electronic kinetic energy in Eqn. 2.9. This *adiabatic* approximation is what is commonly called the Born-Oppenheimer approximation,

$$\begin{aligned}\hat{H}[\Phi(\mathbf{r};\mathbf{R})X(\mathbf{R})] = &-\frac{\hbar^2}{2}\sum_a \Phi_a(\mathbf{r};\mathbf{R})\sum_A \frac{1}{M_A}\hat{\nabla}_R^2 X(\mathbf{R}) \\ &-\frac{\hbar^2}{2m_e}\sum_a \hat{\nabla}_r^2[\Phi(\mathbf{r};\mathbf{R})] \\ &+\hat{V}[\Phi(\mathbf{r};\mathbf{R})X(\mathbf{R})] \\ =&E^{BO}[\Phi(\mathbf{r};\mathbf{R})X(\mathbf{R})],\end{aligned} \tag{2.10}$$

where E^{BO} is the total energy within the adiabatic (Born-Oppenheimer) approximation, which differs from the exact, non-relativistic total energy, E, by

$$E = E^{BO} + T^{nBO}, \tag{2.11}$$

where T^{nBO} is the non-adiabatic correction to the kinetic energy. For the sake of simplicity, the remainder of this chapter will omit the superscript in E^{BO}, unless otherwise noted.

Returning to the concept of a PES, computational chemists use reaction coordinates, $\mathbf{q} = \{\mathbf{q}_i\}$, to represent changes in nuclear geometry along a PES. These coordinates consist of interatomic separations, the angles made between three atoms and the dihedral or torsion angles

made by two atoms down the plane of a bond. The shape of the PESs of different *eigenstates* along these coordinates shows how a system may respond to an external perturbation. The two basic features of the PES are minima and the transition states that connect them. These are stationary points on the PES, which occur when

$$\frac{\partial E}{\partial \mathbf{q}_i} = 0 \quad \forall \ \mathbf{q}_i. \tag{2.12}$$

A minimum is a stationary point where an infinitesimal change in nuclear coordinates results in a less energetically favourable geometry. Minima define the resting states of the system. A PES may have many local minima, but only one global minimum, correspond to the most favourable nuclear geometry. These structures are connected by transition states. Transition states are saddle points on the potential energy surface. They are minima along all coordinates except one, for which they are a maximum.

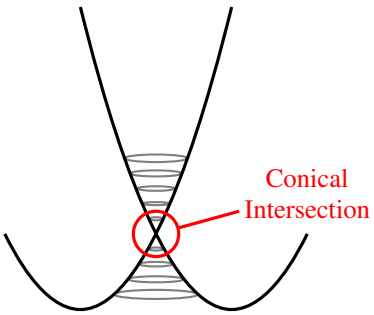

Figure 2.1: A conical intersection between two potential energy surfaces. This is an example of a Jahn-Teller conical intersection.

When the PESs of two *eigenstates* cross, there is a nuclear configuration for which these two states are isoenergetic. The crossover point may be at a geometry that is a stationary point for both of the *eigenstates*. Such points are known as Renner-Teller intersections.[83] Renner-Teller intersections are common in small polyatomic systems, such as NH_2.[84–87] Indeed, any triatomic molecule with at least one atom with $l \geq 1$ must display a Renner-Teller intersection. However, intersections may also occur at arbitrary, non-stationary points on the surfaces, in which case the crossover point is known as a (Jahn-Teller) Conical Intersection (CI), due to the double cone topology of the surface in the vicinity of the CI (See Figure 2.1).[88,89] Jahn-Teller CIs may occur at points where two states become symmetrically degenerate. Conical intersections are of great

importance to photochemistry, as they can be responsible for many interesting photochemical phenomena, including electron transfer and in particular processes that occur on ultrafast (~fs) timescales.[24,90] For example, the excited state photo-dissociation dynamics of NH_3 are strongly influenced by the presence of a Jahn-Teller conical intersection.[91,92]

To properly describe the behaviour of a wavepacket in the presence of a CI, some key features of the CI must be noted. In simplest terms, a CI is a $\mathbf{q}-2$ dimensional feature in a $\mathbf{q}$ dimensional PES and is constructed by two coordinates: the "tuning" mode, a symmetry conserving mode along which the two *eigenstates* become close in energy; and the "coupling" coordinate, a symmetry breaking coordinate along which a wavepacket may pass from one *eigenstate* to another.[93] Conical intersections have a number of further properties; however, investigation of these goes beyond the scope of this report.[90]

As previously mentioned, the Born-Oppenheimer approximation does not hold in all scenarios. The behaviour of a wavepacket in the vicinity of a CI is one such scenario. Far from the CI, changes in electronic state correspond to much greater changes in energy than changes in the vibrational state of the nuclei, as illustrated in Figure 1.1. However, as the two *eigenstates* become close in energy in the vicinity of a CI, the gap in energy between *eigenstates* becomes similar to the gap in energy between vibrational states, leading to the possibility of strong coupling between nuclear and electronic degrees of freedom. This invalidates the Born-Oppenheimer approximation.

The adiabatic approximation allows the Schrödinger equation to be simplified by separating nuclear and electronic components. Within the clamped nucleus approximation, it is then possible to solve the nuclear part. However, for non-hydrogenic systems the electronic wavefunction remains an N-body problem and thus practically insoluble.[69,94] To render the electronic structure problem soluble, we must reduce the complexity of the electronic wavefunction by invoking some approximations. In wavefunction theory, this is achieved by using a mean-field approximation.[64] The resultant model for electronic structure is known as Hartree Fock (HF) theory.

2.2 Hartree Fock theory

The first step in reducing the complexity of the electronic structure problem is to examine how we might simplify the representation of the electronic wavefunction.[95,96] Consider the components of the Hamiltonian within the adiabatic approximation

$$\hat{H} = \hat{T}_n + \hat{T}_e + \hat{V}_{nn} - \hat{V}_{ne} + \hat{V}_{ee}, \tag{2.13}$$

where $\hat{T}_n$ is the purely nuclear kinetic operator, $\hat{T}_e$ is the purely electronic kinetic operator, $\hat{V}_{nn}$ is the nuclear-nuclear potential operator, $\hat{V}_{ne}$ is the nuclear-electronic potential operator and $\hat{V}_{ee}$ is the electronic-electronic potential operator. If we neglect $\hat{V}_{ee}$, that is to say if the electrons are treated as independent particles, we may rewrite our N-particle electronic wavefunction as the product of N independent, orthogonal single electron functions

$$\Phi(r_1, r_2, \ldots, r_N) = \phi_1(r_1)\phi_2(r_2)\cdots\phi_N(r_N) = \prod_i^N \phi_i(r_i), \tag{2.14}$$

where ϕ_i is the single electron wavefunction of electron i with spatial coordinates $r_i = \{x_i, y_i, z_i\}$. This form of the electronic wavefunction is known as the Hartree Product (HP) form, Φ_{HP}. Neglecting $\hat{V}_{ee}$ is known as the independent particle, or orbital, approximation. Note that thus far, we have only employed spatial coordinates in the description of electronic degrees of freedom. However, electrons also have a spin coordinate σ_i which must be considered. Extending the coordinate system to $\tau_i = \{r_i, \sigma_i\} = \{x_i, y_i, z_i, \sigma_i\}$, we rewrite Eqn. 2.14 in terms of the N-particle space-spin wavefunction $\Theta(\tau) = \Phi(r)\Xi(\sigma)$ that is constructed from N single particle space-spin wavefunctions $\theta_i(\tau_i) = \phi_i(r_i)\xi_i(\sigma_i)$,

$$\Theta_{HP}(\tau_1, \tau_2, \ldots, \tau_N) = \theta_1(\tau_1)\theta_2(\tau_2)\cdots\theta_N(\tau_N) = \prod_i^N \theta_i(\tau_i). \tag{2.15}$$

It is at this point that the deficiencies in the HP form of the electronic wavefunction become apparent. Since electrons are indistinguishable fermions, they must obey the Pauli antisymmetry principle, which is to say that the electronic wavefunction must change sign when the coordinates of any two electrons are exchanged.[64,95] In the case of two electrons, it is easy to

demonstrate this property:

$$\begin{aligned} \Theta(\tau_1, \tau_2) &= -\Theta(\tau_2, \tau_1) \\ \theta_1(\tau_1)\theta_2(\tau_2) &= -\theta_1(\tau_2)\theta_2(\tau_1). \end{aligned} \tag{2.16}$$

In the HP electronic wavefunction this is not the case:

$$\begin{aligned} \Theta_{HP}(\tau_1, \tau_2) &= \Theta_{HP}(\tau_2, \tau_1) \\ \theta_1(\tau_1)\theta_2(\tau_2) &= \theta_1(\tau_2)\theta_2(\tau_1). \end{aligned} \tag{2.17}$$

To overcome this issue whilst retaining the advantages the independent particle approximation, we must find an alternative manner of representing the wavefunction. A convenient manner of doing this is to rewrite our wavefunction as a normalised determinant. In the two particle case

$$\begin{aligned} \Theta(\tau_1, \tau_2) &= \frac{1}{\sqrt{2!}} \begin{vmatrix} \theta_1(\tau_1) & \theta_2(\tau_1) \\ \theta_1(\tau_2) & \theta_2(\tau_2) \end{vmatrix} \\ &= \frac{1}{\sqrt{2!}} \Big[\theta_1(\tau_1)\theta_2(\tau_2) - \theta_1(\tau_2)\theta_2(\tau_1) \Big]. \end{aligned} \tag{2.18}$$

A wavefunction constructed as a normalised determinant, known as a Slater determinant, in this manner would be antisymmetric, since

$$\begin{aligned} \Theta(\tau_2, \tau_1) &= \frac{1}{\sqrt{2!}} \begin{vmatrix} \theta_1(\tau_2) & \theta_2(\tau_2) \\ \theta_1(\tau_1) & \theta_2(\tau_1) \end{vmatrix} \\ &= \frac{1}{\sqrt{2!}} \Big[\theta_1(\tau_2)\theta_2(\tau_1) - \theta_1(\tau_1)\theta_2(\tau_2) \Big] \\ \frac{1}{\sqrt{2!}} \Big[\theta_1(\tau_2)\theta_2(\tau_1) - \theta_1(\tau_1)\theta_2(\tau_2) \Big] &= -\left(\frac{1}{\sqrt{2!}} \Big[\theta_1(\tau_1)\theta_2(\tau_2) - \theta_1(\tau_2)\theta_2(\tau_1) \Big] \right). \end{aligned} \tag{2.19}$$

Extending to the more general case of an N-electron wavefunction, the Slater determinant takes the form

$$\Theta(\tau_1, \tau_2, \ldots, \tau_N) = \frac{1}{\sqrt{N!}} \begin{vmatrix} \theta_1(\tau_1) & \theta_2(\tau_1) & \cdots & \theta_N(\tau_1) \\ \theta_1(\tau_2) & \theta_2(\tau_2) & \cdots & \theta_N(\tau_2) \\ \vdots & \vdots & \ddots & \vdots \\ \theta_1(\tau_N) & \theta_2(\tau_N) & \cdots & \theta_N(\tau_N) \end{vmatrix}. \tag{2.20}$$

This provides us with a convenient way of representing the electronic wavefunction that ensures it is physically sound. An alternative and exactly equivalent way of enforcing antisymmetry is by employing the antisymmetrizing operator or antisymmetrizer, $\hat{\mathcal{A}}$, to enforce antisymmetry on a wavefunction[64,96]

$$\hat{\mathcal{A}} = \frac{1}{N!} \sum_{\hat{\pi} \in S_n} \epsilon_\pi \hat{\pi}, \tag{2.21}$$

where $\hat{\pi}$ is the permutation operator, which acts to exchange the coordinates of particles and is a member of the symmetry group, S_n, where N is the number of particles and ϵ_π is the sign change that accompanies the permutation π. It should be noted that $\hat{\mathcal{A}}$ is both Hermitian and idempotent. Using the antisymmetrizer we may write an expression for a wavefunction

$$\Theta(\tau_1, \tau_2, \ldots, \tau_N) = \sqrt{N!}\, \hat{\mathcal{A}}\, \theta_1(\tau_1)\theta_2(\tau_2)\cdots\theta_N(\tau_N), \tag{2.22}$$

which is equivalent to the Slater determinant wavefunction.

The antisymmetric wavefunction turns out to have many advantageous properties from a computational stand-point. These are revealed when we examine the effect of applying the Hamiltonian within the Born-Oppenheimer approximation. It is advantageous to first collect the terms of the Hamiltonian (Eqn. 2.13) by the number of electrons they take action upon:

$$\begin{aligned} \hat{H} &= \overbrace{-\frac{1}{2}\sum_a \hat{\nabla}_a^2 - \sum_{A,a} \frac{Z_A}{r_{Aa}}}^{\text{one electron terms}} + \overbrace{\sum_{a>b} \frac{1}{r_{ab}}}^{\text{two electron term}} + \overbrace{\hat{T}_n + \hat{V}_{nn}}^{\text{nuclear terms}} \\ &= \sum_a \hat{h}_a + \sum_{a>b} \hat{v}_{ab} + \hat{T}_n + \hat{V}_{nn}, \end{aligned} \tag{2.23}$$

where $\hat{h}_a$ is the one electron operator, acting on electron a, and $\hat{v}_{ab}$ is the two electron operator, acting on electrons a and b, where $a \neq b$. Concentrating on the electronic contributions and utilising Dirac bra-ket notation,[97] we may express the electronic energy, E_e, of the antisymmetrized wavefunction, Θ, with the equation

$$\begin{aligned} E_e &= \left\langle \Theta \middle| \hat{H}_e \middle| \Theta \right\rangle \\ &= \left\langle \Theta \middle| \left(\sum_a \hat{h}_a + \sum_{a>b} \hat{v}_{ab} \right) \middle| \Theta \right\rangle . \end{aligned} \tag{2.24}$$

First, we examine the one electron terms:

$$\left\langle \Theta \middle| \sum_a \hat{h}_a \middle| \Theta \right\rangle = \left\langle \Theta \middle| \hat{h}_1 \middle| \Theta \right\rangle + \ \ldots \tag{2.25}$$

and expanding Θ by means of the antisymmetrizer, $\hat{\mathcal{A}}$,

$$= N! \left(\left\langle \hat{\mathcal{A}} \theta_1 \theta_2 \cdots \middle| \hat{h}_1 \middle| \hat{\mathcal{A}} \theta_1 \theta_2 \cdots \right\rangle + \ \ldots \right) \tag{2.26}$$

and recalling that $\hat{\mathcal{A}}$ is both Hermitian and idempotent, we may rearrange to

$$= N! \left(\left\langle \hat{\mathcal{A}} \theta_1 \theta_2 \cdots \middle| \hat{h}_1 \middle| \theta_1 \theta_2 \cdots \right\rangle + \ \ldots \right). \tag{2.27}$$

Expanding the antisymmetrizer according to Eqn. 2.21 and applying the permutation operations, we obtain

$$= \frac{1}{N!} \left(\left\langle \theta_1 \theta_2 \cdots \middle| \hat{h}_1 \middle| \theta_1 \theta_2 \cdots \right\rangle + \left\langle \theta_2 \theta_1 \cdots \middle| \hat{h}_1 \middle| \theta_1 \theta_2 \cdots \right\rangle + \ \ldots \right). \tag{2.28}$$

This simplifies to

$$= \frac{1}{N!} \left(\left\langle \theta_1 \middle| \hat{h} \middle| \theta_1 \right\rangle + \left\langle \theta_2 \middle| \hat{h} \middle| \theta_2 \right\rangle + \ \ldots \right) \tag{2.29}$$

$$\left\langle \Theta \middle| \sum_a \hat{h}_a \middle| \Theta \right\rangle = \overbrace{\sum_a \left\langle \theta_a \middle| \hat{h} \middle| \theta_a \right\rangle}^{h_a}. \tag{2.30}$$

We may treat the two electron terms in a similar manner. By expanding Θ again by means of

the antisymmetrizer, we arrive at the expression

$$\left\langle \Theta \middle| \sum_{a>b} \hat{v}_{ab} \middle| \Theta \right\rangle = \frac{1}{2} \sum_{ab} \Big(\overbrace{\left\langle \theta_a \theta_b \middle| \hat{v}_{ab} \middle| \theta_a \theta_b \right\rangle}^{J_{ab}} - \overbrace{\left\langle \theta_a \theta_b \middle| \hat{v}_{ab} \middle| \theta_b \theta_a \right\rangle}^{K_{ab}} \Big), \tag{2.31}$$

where the first term, J, is the Coulomb integral and the second term, K, is the exchange integral. Combining Eqns. 2.30 and 2.31, we obtain the full expression for the electronic energy,

$$E = \langle \Theta | \hat{H}_e | \Theta \rangle = \overbrace{\sum_a \left\langle \theta_a \middle| \hat{h} \middle| \theta_a \right\rangle}^{h_a} + \frac{1}{2} \sum_{ab} \Big(\overbrace{\left\langle \theta_a \theta_b \middle| \hat{v}_{ab} \middle| \theta_a \theta_b \right\rangle}^{J_{ab}} - \overbrace{\left\langle \theta_a \theta_b \middle| \hat{v}_{ab} \middle| \theta_b \theta_a \right\rangle}^{K_{ab}} \Big) \tag{2.32}$$

The ways in which we have been able to separate one- and two-electron terms are called the Slater-Condon rules.[98–100] To obtain physically meaningful solutions to these equations, we must seek the set of one electron functions, $\Theta = \{\theta_1, \theta_2, \ldots, \theta_n\}$ that minimise the energy in a variational manner. This can be achieved by means of Lagrange multipliers and results in the equation[95,96]

$$\hat{F} = \hat{h} + \sum_a \left(\hat{J}_a - \hat{K}_a \right), \tag{2.33}$$

where $\hat{F}$ is the Fock operator, $\hat{h}$ is the one electron operator (See Eqn. 2.23), $\hat{J}_a$ is the Coulomb operator and $\hat{K}_a$ is the exchange operator. Up to this point our derivation remains in principle exact within the Born-Oppenheimer approximation. The electronic structure problem in this formulation remains computationally infeasible. To render it soluble, we must introduce approximations to the Coulomb and exchange integrals. In Hartree-Fock theory, the Coulomb and exchange operators are defined by their actions on the one electron space-spin function $\theta_b(\tau_1)$:

$$\hat{J}_a \theta_b(\tau_1) = \int \theta_a^*(\tau_2) \hat{v}_{12} \theta_a(\tau_2) \, \mathrm{d}\tau_2 \cdot \theta_b(\tau_1) \tag{2.34}$$

and

$$\hat{K}_a \theta_b(\tau_1) = \int \theta_a^*(\tau_2) \hat{v}_{12} \theta_b(\tau_2) \, \mathrm{d}\tau_2 \cdot \theta_a(\tau_1). \tag{2.35}$$

Inspecting Eqns. 2.34 and 2.35 reveal the "mean-field" characteristic of Hartree-Fock theory.[101–104] The Coulomb operator, $\hat{J}$, describes the average repulsion experienced by the one electron wavefunction θ_b by all of the other one electron functions. The exchange operator, $\hat{K}$ is similar to the Coulomb operator but differs by permutation. This is due to the Slater determinant wavefunction having to obey the Pauli antisymmetry principle (see Eqn. 2.21) and has no classical analogue.

If we apply the Fock operator to one of the one electron wavefunctions we obtain the energy *eigenvalue* associated with that one electron function,

$$\hat{F}\left|\theta_i\right\rangle = \varepsilon_i \left|\theta_i\right\rangle . \tag{2.36}$$

The physical interpretation of this, due to Koopman's theorem,[96] is that the one electron wavefunctions, $\left|\theta_i\right\rangle$, are in fact the electronic orbitals with *eigenvalues*, ε_i, that correspond to the instantaneous ionization energy in the case of an electron being removed from that orbital.

In principle, the Hartree-Fock equations may be solved exactly using numerical methods. However, not the most common approach for dealing with systems containing multiple electrons. Instead, the one electron orbitals, θ_i, are expanded in terms of basis functions

$$\theta_i = \sum_{\mu} c_{\mu i} \vartheta_{\mu} \tag{2.37}$$

where ϑ_{μ} is the basis function, μ, and $c_{\mu i}$ is the coefficient describing the weight of that basis function in orbital i. Applying this expansion to the Fock equation, 2.36, we obtain

$$\hat{F} \sum_{\mu} c_{\mu i} \left|\vartheta_{\mu}\right\rangle = \varepsilon_i \sum_{\mu} c_{\mu i} \left|\vartheta_{\mu}\right\rangle . \tag{2.38}$$

We may seek solutions to these equations by applying $\left\langle\vartheta_{\kappa}\right|$, yielding

$$\sum_{\mu} c_{\mu i} \left\langle\vartheta_{\kappa}\middle|\hat{F}\middle|\vartheta_{\mu}\right\rangle = \varepsilon_i \sum_{\mu} c_{\mu i} \left\langle\vartheta_{\kappa}\middle|\vartheta_{\mu}\right\rangle , \tag{2.39}$$

which is a matrix equation, where the matrix elements

$$S_{\kappa\mu} = \left\langle \vartheta_\kappa \middle| \vartheta_\mu \right\rangle \tag{2.40}$$

and

$$F_{\kappa\mu} = \left\langle \vartheta_\kappa \middle| \hat{F} \middle| \vartheta_\mu \right\rangle \tag{2.41}$$

are the overlap matrix element, $S_{\kappa\mu}$, and Fock matrix element, $F_{\kappa\mu}$, respectively. Reforming Eqn. 2.39 in terms of these matrices, we obtain the Hartree-Fock-Roothaan matrix equation:

$$\mathbf{Fc} = \boldsymbol{\varepsilon}\mathbf{Sc}, \tag{2.42}$$

where **F** is the Fock matrix, **c** is the matrix of coefficients, $\boldsymbol{\varepsilon}$ is the diagonal matrix of orbital energy *eigenvalues* and **S** is the overlap matrix. We can seek the lowest energy solution within a given basis by varying the coefficients matrix, **c**, iteratively until we reach a stable set of coefficients. This process is called the Self-Consistent Field (SCF) procedure and forms the basis for quantum chemical calculations.

Hartree-Fock theory provides a first approximation towards calculating the electronic energy of a wavefunction. It is, however, not exact for any system with more than one electron. This is a result of the fact that in the definition of the two electron operators (Eqns. 2.34 and 2.35), specific interactions between particles are neglected. Instead the particles are subject to the average interaction with all of the remaining particles. Furthermore, since only a single Slater determinant is used in Hartree-Fock theory, only one electronic configuration is considered. Some systems can only be described well by including more than one electron configuration, i.e. by employed a linear combination of Slater determinants. This absence of specific interactions is known as electron correlation. We may define the correlation energy, $E^{Corr.}$ as[105]

$$E^{Corr.} = E^{Exact} - E^{HF}, \tag{2.43}$$

where E^{Exact} is electronic energy calculated using some multi-determinant method that is ex-

act within the Born-Oppenheimer approximation. Following Ramos-Cordoba *et al.*,[106–109] we may separate $E^{Corr.}$ into two components, the dynamic correlation energy, $E^{dyn.}$, and the non-dynamic, or static, correlation energy, $E^{ndyn.}$, as illustrated in Figure 2.2.

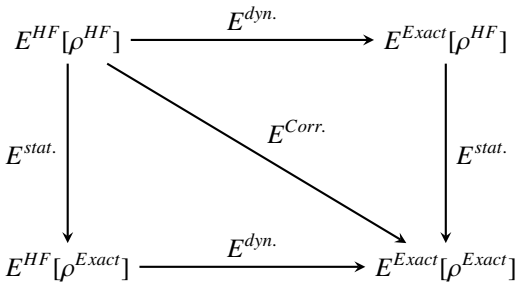

Figure 2.2: Decomposition of the correlation energy, $E^{Corr.}$ into the dynamic and static correlation energy, $E^{dyn.}$ and $E^{stat.}$, respectively. Note that $E^{HF}[\rho^{Exact}]$ denotes the Hartree-Fock energy calculated using a Slater determinant with density $\left|\Phi^{HF}\right|^2 = \rho^{HF}$ that is constrained to be equal to the exact density, ρ^{Exact}. Adapted from Ref. [109].

Within this *Ansatz*, static correlation can be thought of as the error induced by the use of only a single Slater determinant to describe the system. The origin of the dynamic correlation is due to the mean-field nature of Hartree-Fock theory and is illustrated in Fig. 2.3. Fig. 2.3(i)

(i) Exact method.

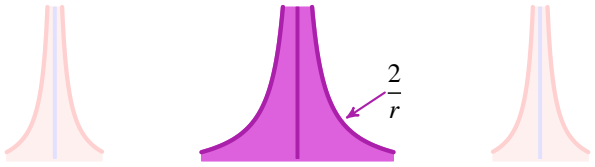

(ii) Mean-field method.

Figure 2.3: Representation of the difference in potential experienced by the third particle in a three body system in 2.3(i) an exact method and 2.3(ii) a mean-field method. The blue lines indicate the position of two of the particles and the shaded areas indicate regions of very high repulsion.

depicts an exact model with electrons located at the blue points. The red shaded areas represent areas that other electrons would be unlikely to occupy due to the high inter-electronic repulsion that would be experienced. In this case there are two clear domains in the vicinity of each

electron that would be unfavourable to occupy. In contrast, in a mean-field model, depicted in Fig. 2.3(ii), electrons are influenced by the average position of all other electrons. This is represented by the shaded purple area. As a result, electrons are likely to locate themselves in unphysically close proximity to each other, leading to additional inter-electronic repulsion when compared to the exact case. This additional repulsion in mean-field models is called the dynamic correlation energy. A common way of introducing correlation in electronic structure methods is to use the Slater determinantal wavefunction as a "reference" from which the specific interactions may be reintroduced. As a result of this, multi-determinantal approaches that seek to include static correlation are sometimes known as multi-reference methods.[109]

The aim of post-Hartree Fock wavefunction-based methods is to reintroduce correlation to the electronic wavefunction to as high degree of accuracy possible, using methods that are as computationally efficient as possible. There are a number of approaches that can be made to do this, the details of which are beyond the scope of this work. Instead, we will explore alternative representations of the electronic structure that avoid the electronic wavefunction.

2.3 Density functional theory

The wavefunctions hitherto described are of significant complexity. Whilst many electronic structure methods exist that seek to formulate accurate approximations of the electronic wavefunction,[95,110–112] an alternative approach is examined herein: Density Functional Theory (DFT). The approach of DFT is based on the intuitive statement that an electronic wavefunction must be related to an electron density, ρ_e. The electron density, unlike the electronic wavefunction, is a simple function of the spatial coordinates only and is itself in principle an observable.

The relationship between electron density and energy was formalised by Pierre Hohenberg and Walter Kohn in 1964, resulting in the two Hohenburg-Kohn (HK) theorems.[113] The first HK theorem is that any property of the ground state of a system is a functional of the ground state electron density, $\rho_0(\mathbf{r})$. For example, the ground state energy, E_0 of a molecule is:

$$E_0 = F[\rho_0] = E[\rho_0], \tag{2.44}$$

where F is the exact functional linking E_0 and ρ_0. It can then be suggested that for some approximate functional, F^a, a corresponding approximate ground state energy, E_0^a can be calculated. The second HK theorem is that for a trial electron density, $\tilde{\rho}$, the resultant energy from the application of the functional, $\tilde{E}$, is bounded from below by the energy for the true electronic density, ρ_0:

$$F^a[\tilde{\rho}] = \tilde{E}^a \geq E_0^a. \tag{2.45}$$

Thus, the trial electron density is variational and the variation principle can be applied to optimise it. It must be noted however, that this does not mean that $\tilde{E}^a$ must be higher in energy than the true ground state energy, E_0. This is only true if the functional used is the true functional that maps ρ with E. For some approximate functional, F^a, the lower bound for the energy may be higher or lower than the true ground state energy.

Though the two HK theorems show that some functional exists that provides the exact electronic energy from the exact electron density, they neither suggest the form of this functional nor suggest how the electron density should be constructed. The HK theorems also make no reference to the properties of molecules with which chemists are most familiar, such as orbitals. Moreover, the HK theorems are slightly incomplete, in that they are not guaranteed to be unique for a degenerate ground state nor do they guarantee that the wavefunction the density corresponds to is antisymmetric. These requirements are known as v-representability and were satisfied by later work from Levy and Lieb,[114,115] who showed that the v-representability problem could be relaxed to the n-representability problem, which had previously been shown to be satisfied by any arbitrary density.[116,117]

Whilst it is possible to derive the electron density from the results of high-level wavefunction theory calculations,[118] this slightly defeats the point of DFT. There are also some efforts that utilise so-called orbital free DFT, which abandons molecular orbitals and calculates the electron density directly; however, these methods are uncommon due to their complexity.[119] The most common approach to DFT, the Kohn-Sham (KS) approach,[120] which harnesses the mean-field techniques explored in Section 2.2 and the associated Self-Consistent Field method[95,111] and reintroduces orbitals.

Within the Born-Oppenheimer approximation, the HK theorems result in the following expression for the electronic energy

$$\begin{aligned} E[\rho_0] =& V_{ne}[\rho_0] + F_{HK}[\rho_0] \\ =& \left\langle \rho_0 \middle| \hat{V}_{ne} \middle| \rho_0 \right\rangle + \left\langle \rho_0 \middle| \hat{T}_e \middle| \rho_0 \right\rangle + \left\langle \rho_0 \middle| \hat{V}_{ee} \middle| \rho_0 \right\rangle \\ =& V_{ne}[\rho_0] + T_e[\rho_0] + V_{ee}[\rho_0], \end{aligned} \tag{2.46}$$

where $F_{HK}[\rho_0]$ is the result of evaluating the HK functional, $\hat{F}_{HK}$, on the ground state density, ρ_0. The HK functional has a kinetic and a potential component; however, the forms of these operators are not clear. The potential operator, $\hat{V}_{ee}$, must at least contain the Coulomb interaction and so we may write it as

$$\hat{V}_{ee} = \frac{1}{2}\hat{v}_{12} + \hat{V}_{nC}, \tag{2.47}$$

where the first term is the familiar Coulomb operator (See Eqn. 2.34) and the second term is the non-Coulomb potential operator, $\hat{V}_{nC}$. The key problem in DFT is to identify the forms of the kinetic operator, $\hat{T}_e$, and the non-Coulomb potential operator, $\hat{V}_{nC}$. Comparing Eqn. 2.47 with the results of Hartree-Fock theory (especially Eqn. 2.31), it is possible to suggest that $\hat{V}_{nC}$ should at least contain a term correcting for exchange. Indeed, it is the consideration of Hartree-Fock theory that yielded the most common approach to DFT.

The Kohn-Sham method of Walter Kohn and Lu Jeu Sham utilises a similar method to Hartree-Fock theory to obtain workable equations.[120] As with the derivation of the Hartree product wavefunction, the KS *Ansatz* begins by substituting the electron density, ρ, for a system of non-interacting particles with density, ϱ, such that

$$\varrho \equiv \rho. \tag{2.48}$$

Similar to the Hartree product wavefunction, this allows for the fictitious density to be written

as the sum of single particle densities

$$\varrho(\tau) = \sum_i |\varphi_i(\tau_i)|^2, \tag{2.49}$$

where φ_i is the single particle function of particle i. The electronic energy of such a system, $E[\varrho]$, is

$$\begin{aligned} E[\rho] \equiv E[\varrho] &= \left\langle \varrho \middle| \hat{T}_e \middle| \varrho \right\rangle - \left\langle \varrho \middle| \hat{V}_{ne} \middle| \varrho \right\rangle + \left\langle \varrho \middle| \frac{1}{2}\hat{v}_{12} \middle| \varrho \right\rangle + \left\langle \varrho \middle| \hat{f}_{xc} \middle| \varrho \right\rangle \\ &= -\frac{1}{2}\sum_i \left\langle \varphi_i \middle| \hat{\nabla}_r^2 \middle| \varphi_i \right\rangle - \sum_{A,i} \left\langle \varphi_i \middle| \frac{Z_A}{r_{Ai}} \middle| \varphi_i \right\rangle + \frac{1}{2}\sum_{i>j} \left\langle \varphi_i \middle| \hat{v}_{ij} \middle| \varphi_j \right\rangle + \left\langle \varrho \middle| \hat{f}_{xc} \middle| \varrho \right\rangle \\ &= T_e[\varrho] + V_{ne}[\varrho] + J[\varrho] + E_{xc}[\varrho], \end{aligned} \tag{2.50}$$

where $T[\varrho]$ is the kinetic energy of the non-interacting electrons, $V_{ne}[\varrho]$ is the Coulombic interaction between the nuclei and the non-interacting electron density, $J[\varrho]$ is the Coulombic interaction between the particles in ϱ and $E_{xc}[\varrho]$ is the exchange-correlation energy, which is defined as

$$E_{xc}[\varrho] \equiv (T[\rho] - T[\varrho]) + (E_{ee}[\rho] - J[\varrho]). \tag{2.51}$$

The KS exchange-correlation functional operator, $\hat{f}_{xc}$ is the major variable in KS-DFT calculations and, similar to the HK functional, has no clear form. As with Hartree-Fock theory, we wish to develop equations in terms of the single particle functions, φ_i. Since the form of $\hat{f}_{xc}$ is undefined, for the purposes of further derivation it is convenient to consider the effect of $\hat{f}_{xc}$ on φ_i,

$$\left\langle \varphi_i \middle| \hat{f}_{xc} \middle| \varphi_i \right\rangle = f_i^{xc}, \tag{2.52}$$

where f_i^{xc} is the exchange correlation energy of φ_i. Using this assumption, we may write an

expression for the *eigenvalue* of the single particle function, ε_i, as

$$\overbrace{\left(-\frac{1}{2}\hat{\nabla}_r^2 - \sum_A \frac{Z_A}{r_{Ai}} + \sum_{j\neq i}\left\langle\varphi_j\right|\hat{v}_{ij} + \hat{f}_{xc}\right)}^{\hat{F}^{KS}}\left|\varphi_i\right\rangle = \varepsilon_i\left|\varphi_i\right\rangle, \tag{2.53}$$

noting that the operator $\hat{F}^{KS}$ is directly analogous to the Fock operator (Eqn. 2.33), but including correlation and so is known as the Kohn-Sham-Fock operator. The *eigenvalue*, ε_i, is the energy of the single particle function, φ_i. This allows us to write the total energy of the fictitious density, $E[\varrho]$ as

$$E[\varrho] = \sum_i^{occ.} \varepsilon_i, \tag{2.54}$$

where $\sum_i^{occ.}$ denotes summation over the occupied functions. This leads to the conclusion that the single particle functions, $\{\varphi_i\}$, are in fact the orbitals of the electrons. However, it should be noted that the KS orbitals and orbital energies have a different interpretation to those of HF theory. If the *exact* KS functional is employed, the occupied KS orbitals energies correspond to the ionization energy for that electron, similar to the HF orbitals (since HF theory neglects correlation, the HF *eigenvalues* are unlikely to be exact).[118] The difference is more pronounced when comparing the HF and KS virtual orbitals. The KS virtual orbitals are *eigenfunctions* of an electron under the influence of the nuclei of the system and the remaining $N-1$ other electrons of the system, whilst the first HF virtual orbital is instead subject to the mean field of N occupied orbitals.[118] In KS theory, the gap between the highest occupied orbital and lowest virtual orbital is thus similar to the energy required to excite an electron from HOMO to LUMO; however, in HF theory the same gap is an approximation of the so called fundamental gap - the difference between the first ionization energy and first electron affinity.[118,121] Returning to the result of Eqn. 2.53, we can attempt to expand the single particle functions, φ_i, in terms of basis functions, in direct analogy to the Hartree-Fock-Roothaan equations of Section 2.2:[122]

$$\varphi_i = \sum_\mu c_{\mu i}\vartheta_\mu, \tag{2.55}$$

where ϑ_μ is the basis function, μ, and $c_{\mu i}$ is the coefficient of that basis function in function i. Combining Eqns. 2.53 and 2.55 we can develop an expression for the Kohn-Sham-Fock matrix element, similar to Eqn. 2.41

$$\begin{aligned} F_{\kappa\mu}^{KS} &= \left\langle \vartheta_\kappa \middle| \hat{F}^{KS} \middle| \vartheta_\mu \right\rangle \\ &= -\frac{1}{2}\left\langle \vartheta_\kappa \middle| \hat{\nabla}_r^{\,2} \middle| \vartheta_\mu \right\rangle - \left\langle \vartheta_\kappa \middle| \sum_A \frac{Z_A}{r_{Ai}} \middle| \vartheta_\mu \right\rangle + \sum_{j>i} \left\langle \vartheta_\kappa \middle| \frac{\left|\varphi_j\right|^2}{r_{ij}} \middle| \vartheta_\mu \right\rangle + \left\langle \vartheta_\kappa \middle| \hat{f}_{xc} \middle| \vartheta_\mu \right\rangle \end{aligned} \tag{2.56}$$

and noting that since

$$\varrho_j = \left|\varphi_j\right|^2 = \sum_{\lambda,\eta} c_{\lambda j} c_{\eta j} \vartheta_\lambda \vartheta_\eta, \tag{2.57}$$

the third term of Eqn. 2.56 involves summation over a total for four basis functions. As with Hartree-Fock theory, we can utilise Eqn. 2.56 to form a matrix equation equivalent to the Hartree-Fock-Roothaan matrix equation, 2.42,[122]

$$\mathbf{F^{KS}c} = \boldsymbol{\varepsilon}\mathbf{Sc}, \tag{2.58}$$

which we can solve using the same Self-Consistent Field methods developed originally for use within Hartree-Fock theory

The success of KS theory is in part due to its similarity with wavefunction methods. Tantalizingly, KS theory provides the exact electronic energy provided that $\varrho_0 \equiv \rho_0$ and the exact form of $\hat{f}_{xc}$ is known. This second requirement, however, is yet to be met, though many approximations to the exchange-correlation functional are available. Due to this approximate nature, contemporary electronic structure methods that utilise approximate exchange-correlation functionals are sometimes known collectively as Density Functional Approximations, DFAs, in contrast to the exact DFT.[123] The choice of $\hat{f}_{xc}$ when performing quantum chemical calculations is one of the main concerns to those that utilise DFT. Broadly speaking, functionals may be split into two categories: pure functionals, which only contain terms dependent on the density, and

hybrid functionals in which the exchange correlation energy functional, $E_{xc}[\varrho]$ is defined as

$$E_{xc}[\varrho] = c_{HF} \left\langle \varrho \middle| \hat{K} \middle| \varrho \right\rangle + (1 - c_{HF}) \left\langle \varrho \middle| \hat{f}_{xc} \middle| \varrho \right\rangle, \tag{2.59}$$

where $\hat{K}$ is the exchange operator from HF theory (See Eqn. 2.35) which provides "exact exchange," and c_{HF} is the fraction of HF exchange included in the functional. The coefficient c_{HF} may be constant for all values of r_{12}, in which case the DFA is called a "global" hybrid functional, or may be a function of r_{12}, in which case the DFA may be called a "range-separated" or "range-corrected" hybrid.

In this work, the only exchange-correlation functional used was the popular, perhaps outrageously so, B3LYP global hybrid functional, composed of the Becke three-parameter exchange functional, B3,[124] and the Lee-Yang-Parr correlation functional, LYP,[125] the combination of which was first employed in Frisch and co-workers in 1994.[126] Whilst this functional is much maligned,[127–129] it performs well in the calculation of vibrational frequencies in complexes of the type investigated herein,[130] and adequately in the calculation of electronic energies.[131–133] In the calculation of electronic transitions, the means by which will be shortly discussed, B3LYP also performs adequately, though few benchmarks currently exist that include significant numbers of transition metal compounds.[134–136]

When investigating the photochemistry of molecules, it is not only the properties of the ground state that are of concern: it is the excited states that are of main interest. To probe such states, the time-dependent behaviour of molecules must be understood.

2.4 Time-dependent density functional theory

The Hohenberg-Kohn (HK) theorems show that an analogue to the time-independent Schrödinger equation within the Born-Oppenheimer approximation may be constructed which is based on the electron density, $\rho(\tau)$, rather than the electronic wavefunction, $\Theta(\tau)$.[113] The stationary states of a time-independent Schrödinger equation are the states that can be accessed under equilibrium conditions. However, much of chemistry occurs away from equilibrium. If for example, we wish to simulate the response of a system over time to external perturbation,

i.e. from an electro-magnetic field in a spectroscopic experiment, we cannot employ a time-independent Schrödinger equation to do so (unless the perturbation does not vary over time). The extension of the HK theorems to the time-dependent regime was derived by Erich Runge and Eberhard K. U. Gross in 1984.[137] Whilst this had previously been achieved for an oscillating external potential[138–140] and in the perturbative, linear-response regime,[141,142] the RG theorems extended these to any arbitrary external potential. It should be noted that the veracity of original RG derivation of TD-DFT was fiercely debated within the literature.[143–152] The key issue is whether the time-dependent density is v-representable, an issue that remains unsolved outside of specific boundary conditions.[153,154] Fortunately within the formalism employed in the calculations presented herein, this has been resolved[155,156] and so a brief overview of the RG theorems will be given.

Consider a system of N-electrons in some time-dependent external field, defined by the time-dependent Schrödinger equation,

$$\hat{H}(\tau,t)\Theta(\tau,t) = i\frac{\partial}{\partial t}\Theta(\tau,t), \tag{2.60}$$

where $\hat{H}(\tau,t)$ is the time-dependent Hamiltonian,

$$\hat{H}(\tau,t) = \hat{T}(\tau) + \hat{V}(\tau) + \hat{U}(\tau,t), \tag{2.61}$$

where the kinetic and potential operators defined previously (Eqn. 2.5) and the time-dependent external potential operator, $\hat{U}(\tau,t)$ is

$$\hat{U}(\tau,t) = \sum_{i}^{N} \hat{u}(\tau_i,t). \tag{2.62}$$

If we consider a system in which the external potential is switched on at t_0, then a time-dependent parallel to the first HK theorem can be derived. The first RG theorem shows that the time dependent electron density, $\rho(\tau,t)$ determines the wavefunction plus a phase factor:

$$\Theta(\tau,t) = e^{-i\phi(t)}\Theta[\rho,\Theta_0](\tau,t), \tag{2.63}$$

where Θ_0 is the initial wavefunction, $\Theta(\tau_0, t_0)$. If the initial wavefunction is the ground state, then the first RG theorem may be combined with the first HK theorem, meaning that the time-dependent wavefunction is only dependent on the initial electron density, up to some phase factor. There are two conditions to the first RG theorem as originally derived, which are that the external field in question must not induce a current (i.e. it must be an electric field) and that the time-dependence of the field must be continuous around t_0.[137,157,158] Whilst these may not be true in many cases, for the cases of interest herein these approximations are valid.

The second HK theorem, which is that the energy functional is variational, may also be extended to the time domain. In the time-dependent case, this involves the time dependent action

$$A = \int_{t_0}^{t_1} \left\langle \Theta(\tau, t) \middle| i\frac{\partial}{\partial t} - \hat{H}(\tau, t) \middle| \Theta(\tau, t) \right\rangle \mathrm{d}t \,. \tag{2.64}$$

Since the time-dependent wavefunction, $\Theta(\tau, t)$, is uniquely defined by the time-dependent electron density, $\rho(\tau, t)$, *via* the first RG theorem, there is must be a density functional form of Eqn. 2.64:

$$A[\rho(\tau, t)] = \int_{t_0}^{t_1} \left\langle \Theta[\rho(\tau, t)] \middle| i\frac{\partial}{\partial t} - \hat{H}(\tau, t) \middle| \Theta[\rho(\tau, t)] \right\rangle \mathrm{d}t \,, \tag{2.65}$$

which must have a stationary point at the correct time-dependent density, due to the Dirac-Frenkel variational principle.[157,159] We can seek this density by taking the functional derivative

$$0 = \frac{\delta A[\rho(\tau, t)]}{\delta \rho(\tau, t)} = \int_{t_0}^{t_1} \left\langle \frac{\delta \Theta[\rho(\tau, t')]}{\delta \rho(\tau, t)} \middle| i\frac{\partial}{\partial t'} - \hat{H}(\tau, t') \middle| \Theta[\rho(\tau, t')] \right\rangle \mathrm{d}t' + c.c. \,. \tag{2.66}$$

Since the time-dependent densities at $t_1 \neq t_0$ differ only by some phase factor due to the first RG theorem, the action functional that satisfies this equation will have the form

$$A[\rho(\tau, t)] = \int_{t_0}^{t_1} \left\langle \Theta[\rho(\tau, t)] \middle| i\frac{\partial}{\partial t} - \hat{H}(\tau, t) \middle| \Theta[\rho(\tau, t)] \right\rangle \mathrm{d}t + \phi(t_1) - \phi(t_0), \tag{2.67}$$

and so will satisfy the variational condition up to some phase factor.[137,157,158] It is convenient

to rewrite the time-dependent action functional in terms of the time-dependent analogue of the HK functional:

$$A[\rho(\tau,t)] = F^{HK}[\rho(\tau,t)] - \int_{t_0}^{t_1} \int \hat{u}(\tau,t)\rho(\tau,t)\,\mathrm{d}\tau\,\mathrm{d}t\,, \tag{2.68}$$

where $F^{HK}[\rho(\tau,t)]$ is the expectation value of the time-dependent HK functional and the second term contains the time-dependent external potential operator, $\hat{u}(\tau,t)$. To maintain continuity with the treatment of ground state DFT, it is convenient to invoke the Kohn-Sham *Ansatz* (see Section 2.3) and develop the time-dependent KS equations. It should be noted that, similar to the ground state case, there is a question of whether the time-dependent density is v-representable.[158] As previously stated, this remains to be proven for the general case of an arbitrary time-dependent electron density; however, within the adiabatic linear-response regime, that will be employed throughout this work, v-representability has been proven.[154–156] Given this, we may seek to express the universal time-dependent HK functional, $F^{HK}[\rho(\tau,t)]$, within the KS *Ansatz*:

$$F^{HK}[\rho(\tau,t)] \equiv \; F^{KS}[\varrho(\tau,t)], \tag{2.69}$$

where $\varrho(\tau,t)$ is the time-dependent non-interacting particle density and

$$\begin{aligned} F^{KS}[\varrho(\tau,t)] = & \sum_j \int_{t_0}^{t_1} \zeta_j(t) \left\langle \varphi_j(\tau_j,t) \middle| i\frac{\partial}{\partial t'} - \frac{1}{2}\hat{\nabla}_r^2 \middle| \varphi_j(\tau_j,t) \right\rangle \mathrm{d}t \\ & - \frac{1}{2}\sum_{j>k} \int_{t_0}^{t_1} \zeta_j(t)\zeta_j(t) \left\langle \varphi_j(\tau_j,t) \middle| \hat{v}_{jk} \middle| \varphi_k(\tau_k,t) \right\rangle \mathrm{d}t \\ & - A_{xc}[\varrho(\tau,t)], \end{aligned} \tag{2.70}$$

where $\zeta_j(t)$ is the time-dependent occupation number of KS orbital φ_j and $A_{xc}[\varrho(\tau,t)]$ is the time-dependent exchange-correlation action density functional, which is analogous to the time-independent exchange correlation density functional. We may use this to develop the time-

dependent analogue to the KS single-particle function *eigenvalue* equation, Eqn. 2.53,

$$\overbrace{\left(-\frac{1}{2}\hat{\nabla}_r^2 - \sum_A \frac{Z_A}{r_{Ai}} + \sum_{k\neq j} \left\langle \varphi_k(\tau_k,t)\right| \hat{v}_{jk} + \hat{u}(\tau,t) + \hat{\alpha}_{xc}(\tau,t)\right)}^{\hat{A}(t)} \left|\varphi_j(\tau_j,t)\right\rangle = i\frac{\partial}{\partial t}\left|\varphi_j(\tau_j,t)\right\rangle, \quad (2.71)$$

where $\hat{A}(t)$ is the time-dependent action functional operator and $\hat{\alpha}_{xc}(\tau,t)$ is the time-dependent action exchange-correlation functional operator,

$$\hat{\alpha}_{xc}(\tau,t) = \frac{\delta A_{xc}[\varrho]}{\delta\varrho(\tau,t)}. \quad (2.72)$$

Much like its time-independent analogue, the form of the time-dependent action exchange-correlation functional operator is unknown. Indeed, remarkably few attempts to develop time-dependent action exchange-correlation functionals are documented in the literature.[152,160] This is, perhaps, not too surprising considering that the time-independent exchange-correlation is itself quite vexing. Instead, the approach taken almost exclusively in TD-DFT calculations is to use the time-independent exchange-correlation functional instead. This is known as the adiabatic approximation within TD-DFT and suggests that the exchange-correlation potential reacts instantaneously to the time evolution of ϱ. One of the consequences invoking the adiabatic approximation within TD-DFT is that double excitations cannot be described with conventional adiabatic TD-DFT.[152,161,162] Furthermore, adiabatic TD-DFT cannot correctly describe a conical intersection between the ground and first electronically excited state and the PES near this region is fraught with topological defects.[162] Despite these deficiencies, adiabatic TD-DFT has been found to be fairly successful in the description of many systems of chemical interest, though it is not without its issues.[127,134,154,162–173]

The adiabatic TD-DFT formalism can also be used to propagate equations of motion for a given system. Time-dependent simulations performed in this manner are known in the literature as Real Time TD-DFT (RT-TD-DFT) simulations and can be used to directly simulate laser excitation.[174–178] It can even be used to produce some quite pleasing visualisations of electronic excitation.[179] This is, however, not the most commonly found incarnation of adiabatic TD-DFT.

The most simple approximation to TD-DFT is Linear-Response adiabatic TD-DFT (LR-TD-

DFT). This were derived by considering the time-dependent extension of Hartree-Fock theory, Time-Dependent HF (TD-HF), also known as the Random Phase Approximation (RPA).[180] The approach was based on using at the polarizability of the ground state to give information on the singly excited electronic states. The "response" of the ground state wavefunction to external perturbation is simulated. When there is a peak in the response, a transition to an excited state has been located. Interestingly, in the original paper, the authors note that this is essentially a property of the ground state electron density.[180]

As previously mentioned, LR-TD-DFT predates the RG theorems[141,142] and features prominently in the founding papers of TD-DFT.[137,157] However, the most common implementation of LR-TD-DFT is due to Mark E. Casida and the associated equations are known as the Casida equations.[158,181] The derivation of these equations is tedious and goes beyond the scope of this work. The most salient features are elegantly described in the context of their difference with HF theory in the excellent review of Dreuw and Head-Gordon,[167] but for a thorough understanding one must refer to the original works, Refs. [158] and [181]. An alternative and complimentary derivation, from the perspective of variational excited state DFT, due to the late Tom Ziegler, is also instructive but perhaps more advanced.[182] The Casida equation poses the non-Hermitian *eigenvalue* problem

$$\begin{bmatrix} \mathbf{A} & \mathbf{B} \\ \mathbf{B}^* & \mathbf{A}^* \end{bmatrix} \begin{bmatrix} \mathbf{X} \\ \mathbf{Y} \end{bmatrix} = \vec{\omega} \begin{bmatrix} 1 & 0 \\ 0 & -1 \end{bmatrix} \begin{bmatrix} \mathbf{X} \\ \mathbf{Y} \end{bmatrix}, \tag{2.73}$$

where $\mathbf{A}$ and $\mathbf{B}$ are the orbital rotation Hessian matrices, $\mathbf{X}$ and $\mathbf{Y}$ are the coefficient matrices, containing the *eigenfunctions* of $\mathbf{A}$ and $\mathbf{B}$, and the vector $\vec{\omega}$ contains the excitation energies. The matrices $\mathbf{A}$ and $\mathbf{B}$ are defined by their matrix elements

$$\begin{aligned} A_{ia,jb} = {} & \delta_{ij}\delta_{ab}(\varepsilon_a - \varepsilon_i) \\ & + 2\left\langle \varphi_i\varphi_a \middle| \hat{v}_{12} \middle| \varphi_j\varphi_b \right\rangle - c_{HF}\left\langle \varphi_i\varphi_j \middle| \hat{v}_{12} \middle| \varphi_a\varphi_b \right\rangle + (1 - c_{HF})\left\langle \varphi_i\varphi_a \middle| \hat{f}_{xc} \middle| \varphi_j\varphi_b \right\rangle \end{aligned} \tag{2.74}$$

and

$$B_{ia,jb} = 2\left\langle \varphi_i\varphi_a \middle| \hat{v}_{12} \middle| \varphi_b\varphi_j \right\rangle - c_{HF}\left\langle \varphi_i\varphi_a \middle| \hat{v}_{12} \middle| \varphi_a\varphi_j \right\rangle + (1 - c_{HF})\left\langle \varphi_i\varphi_a \middle| \hat{f}_{xc} \middle| \varphi_b\varphi_j \right\rangle, \tag{2.75}$$

where the indices $i, j, \ldots$ denote occupied KS orbitals and $a, b, \ldots$ denote virtual KS orbitals, δ_{ij} is the Kronecker delta function, ε_i is the energy *eigenvalue* of KS orbital φ_i, c_{HF} is the coefficient of Hartree-Fock exact exchange employed and $\hat{f}_{xc}$ is the exchange-correlation functional operator. Note that the KS orbitals are taken from time-independent KS-DFT calculations. In conventional KS-DFT, the orbitals are real-valued and so $\mathbf{A}^* = \mathbf{A}$ and the Casida equations reduce to a Hermitian problem. This allows Eqn. 2.73 to be rewritten as

$$(\mathbf{A} - \mathbf{B})^{\frac{1}{2}}(\mathbf{A} + \mathbf{B})(\mathbf{A} - \mathbf{B})^{\frac{1}{2}}\mathbf{Z} = \vec{\omega}^2\mathbf{Z}, \tag{2.76}$$

where

$$\mathbf{Z} = (\mathbf{A} - \mathbf{B})^{-\frac{1}{2}}(\mathbf{X} + \mathbf{Y}). \tag{2.77}$$

Solving these equations involves diagonalising the matrices $(\mathbf{A}-\mathbf{B})$. Since $\vec{\omega}$ has dimensionality $N_{occ.}\dot{N}_{virt.}$, it is not always desirable or computationally feasible to attempt to solve the full Casida problem. Instead it is common to use an iterative *eigenvalue* solver,[183] such as the Davidson-Liu[184,185] algorithm or one of the modified Davidson-type algorithms.[186–191]

It is instructive to consider the form of the matrix elements $A_{ia,jb}$ and $B_{ia,jb}$ in more detail, since this provides insight into when LR-TD-DFT is and is not applicable. In the case of an *intermolecular* excitation, i.e. *charge transfer* from molecule A to molecule B, LR-TD-DFT is deficient. Let us suppose that the overlap of the occupied KS orbital of A, φ_i^A, with the virtual KS orbital of B, φ_a^B, is zero. This means that any term in Eqns. 2.74 and 2.75 that involves a product of these occupied and virtual KS orbitals is zero. In this case the matrix elements simplify to

$$A^{CT}_{ia,jb} = \delta^A_{ij}\delta^B_{ab}(\varepsilon^B_a - \varepsilon^A_i) - c_{HF}\left\langle \varphi^A_i\varphi^A_j\middle|\hat{v}_{12}\middle|\varphi^B_a\varphi^B_b\right\rangle, \tag{2.78}$$

and

$$B^{CT}_{ia,jb} = 0, \tag{2.79}$$

where superscript CT reminds us that this only in the case of *intermolecular* charge transfer case, and the superscript A or B indicates on which molecule the KS orbital is centred. Recalling the meaning of the KS virtual orbital *eigenvalues*, which is the energy of a particle under the influence of $N-1$ other particles (see Section 2.3 for further details), we can see that this is clearly not a physically accurate description of *intermolecular* charge transfer. This is error is most critical in pure functionals, where c_{HF} is zero. In the case of hybrid functionals this error is somewhat mitigated and some, so-called asymptotically correct, range-separated hybrids have been constructed to accurately deal with *intermolecular* charge transfer. In the case of *intramolecular* charge transfer, this error is somewhat less extreme, since orbital overlap will be non-zero by definition. Nevertheless, LR-TD-DFT tends to underestimate charge transfer excitations of any kind, though may still perform well through favourable cancellation of errors.[167–170,173]

The full Casida equations are the density-functional equivalent of the RPA problem within HF theory.[167] This form of TD-DFT, sometimes called Linear-Response RPA-TD-DFT (LR-RPA-TD-DFT), is the form most often referenced when the name TD-DFT is invoked. Outside of this chapter this work will refer to LR-RPA-TD-DFT as simply TD-DFT, in accordance to the regrettably erroneous convention of the majority of existing literature.

There are a number of approximations to Eqn. 2.76 that can be made. The matrix $\mathbf{B}$ may be neglected, reducing the problem from the equivalent to the RPA problem to the equivalent to Configuration Interaction with Single excitations (CIS), alternatively known as the Tamm-Dancoff Approximation (TDA),[190]

$$\mathbf{A}\mathbf{X}_{TDA} = \vec{\omega}_{TDA}\mathbf{X}_{TDA}, \tag{2.80}$$

where $\mathbf{X}_{TDA}$ is the LR-TDA-TD-DFT coefficients matrix and $\vec{\omega}_{TDA}$ is the vector containing the excitations energies within the TDA approximation to LR-TD-DFT.

Approximations to the Casida equations of both LR-TDA-TD-DFT and LR-RPA-TD-DFT have been developed by Stefan Grimme, named the simplified Tamm-Dancoff Approximation (sTDA) and simplified Time-Dependent DFT (sTD-DFT).[192–194] These simplified methods introduce a number drastic approximations, neglecting a number of terms and ruthlessly approx-

imating integrals. The first step in both LR-sTDA- and LR-sTD-DFT is to neglect the final term in the matrix element $A_{ia,jb}$, i.e. the term involving the exchange-correlation functional operator. This is a very extreme approximation, but reduces the computational cost of performing the calculation drastically since evaluation of this term requires numerical integration. The next simplification is to replace the four-index, two-electron integrals (the second and third terms of Eqn. 2.74) with a parametrised, damped Coulombic repulsion called the Mataga-Nishimoto-Ohno-Klopman operators,[195–197], γ_{AB}, which have the forms

$$\gamma_{AB}^{J} = \left(\frac{1}{(R_{AB})^{\beta} + (c_{HF}\eta)^{-\beta}} \right)^{\frac{1}{\beta}} \tag{2.81}$$

for the Coulomb-type interaction, where q_{ia}^{A} is the change in charge densities from resulting from the KS orbital transition from φ_i^A to φ_a^A on atom A, derived from Löwdin population analysis of the basis functions,[198] β is a parameter and η is the mean chemical hardness of the atoms A and B, taken from Ref. [199], and

$$\gamma_{AB}^{K} = \left(\frac{1}{(R_{AB})^{\alpha} + (\eta)^{-\alpha}} \right)^{\frac{1}{\alpha}}, \tag{2.82}$$

for the exchange-type interaction, where α is another parameter. This results in new forms for the simplified matrix elements, denoted by the superscript s,

$$A_{ia,jb}^{s} = \delta_{ij}\delta_{ab}(\varepsilon_a - \varepsilon_i) + \sum_{AB}(2q_{ia}^{A}\gamma_{AB}^{K}q_{jb}^{B} - q_{ij}^{A}\gamma_{AB}^{J}q_{ab}^{B}) \tag{2.83}$$

and

$$B_{ia,jb}^{s} = \sum_{AB}(2q_{ia}^{A}\gamma_{AB}^{K}q_{bj}^{B} - c_{HF}q_{ib}^{A}\gamma_{AB}^{K}q_{aj}^{B}), \tag{2.84}$$

where $\sum_{AB}$ denotes summation over the atoms $\{A, B, \dots\}$. The parameters α and β are fitted based on a small training set of calculations and are dependent on the exchange-correlation functional employed in the calculation. The authors of the papers describing the simplified methods argue that since the parameters are dependent on the functional, they somehow act to compensate for

the neglected $\left\langle \varphi_i \varphi_a \middle| \hat{f}_{xc} \middle| \varphi_j \varphi_b \right\rangle$ term of the full matrix element $A_{ia,jb}$ (Eqn. 2.74).[192,193] The final simplification involved in these methods is the truncation of the excitation space on the basis of the difference in the KS orbital energy *eigenvalues*, meaning that elements of the coefficient matrices $\mathbf{X}^s$ and $\mathbf{Y}^s$ are neglected if $\varepsilon_a - \varepsilon_i$ is greater than a certain threshold.

The combination of these drastic approximations results in dramatic reductions in calculation time when LR-sTD(A)-DFT is employed, in comparison with calculations using full LR-TD-DFT. Since the simplified methods are so approximate and reliant on parametrisation, it is of paramount importance that, if used, they are compared against full LR-RPA-TD-DFT calculations to ensure that the approximations do not break down.

It should be noted that since excited states calculated using LR-TD-DFT are derived from ground state DFT calculations performed within the Born-Oppenheimer approximation, these states are adiabatic in nature. Methods to calculate non-adiabatic couplings between the ground and excited states,[200,201] and between excited states,[202] within the framework of TD-DFT, have recently been made available.

The methods hitherto discussed provide the means to solve electronic structure problems in both time-independent and time-dependent regimes, and provides the toolset required to begin simulating non-adiabatic dynamics involving both nuclei and electrons.

2.5 Relativistic quantum mechanics

The theories of relativity were initially proposed by Albert Einstein in 1905 and were enhanced by Einstein and others over the first few decades of the 20$^{\text{th}}$ Century.[203] Indeed, by the time of the development of Schrödinger's quantum wave mechanics, the potential significance of relativistic effects on molecular quantum mechanics had already been recognised.[57,63] The effects of relativistic corrections to molecular systems are widely documented[204] and can even have an effect on aromaticity.[205] An interested reader is referred to the work of Pekka Pyykkö, who has highlighted some prominent examples, such as the fact that silver is essentially non-relativistic gold.[206,207] There are two key components to the theories of relativity that have major impacts on attempts to reformulate quantum wave mechanics in relativistic terms. The first of these is

the relativistic mass, $\mathcal{M}$, which is related to the non-relativistic mass, m_0, by the equation

$$\mathcal{M} = \gamma m_0, \tag{2.85}$$

where γ is the Lorentz factor, which is defined by the equation

$$\gamma = \frac{1}{\sqrt{1 - \left(\frac{v}{c}\right)^2}}, \tag{2.86}$$

where v is the velocity of a particle and c is the speed of light. In essence, Lorentz factor describes the deviation from non-relativity based on how close the speed of an object is to the speed limit of the universe, the speed of light. When the speed of an object is zero, i.e. it is at rest, $\gamma = 1$ and therefore $\mathcal{M} = m_0$ and so m_0 is often called the *rest mass* of an object. Evaluating the Lorentz factor for a particle is a convenient way of estimating the magnitude of relativistic effects for that particle. In Fig. 2.4, the Lorentz factor for the 1s electron of elements Z = 1-118 are given to illustrate how the Lorentz factor changes with Z.

The second component is the effect of relativity on the energy of a free particle. The non-relativistic energy of a free particle, E_{NR} is simply its kinetic energy:

$$E_{NR} = \frac{p^2}{2m}, \tag{2.87}$$

where p is the momentum and m the non-relativistic mass. In the non-relativistic case, the momentum is defined as $p = mv$, where v is the velocity. This is altered in the relativistic case, since the relativistic mass is related to the non-relativistic mass by γ:

$$p = \gamma m_0 v = \mathcal{M} v. \tag{2.88}$$

The relativistic energy of a free particle, E_R has a more complicated expression. The complete form of Einstein's famous expression is

$$E_R^2 = (pc)^2 + (m_0 c^2)^2. \tag{2.89}$$

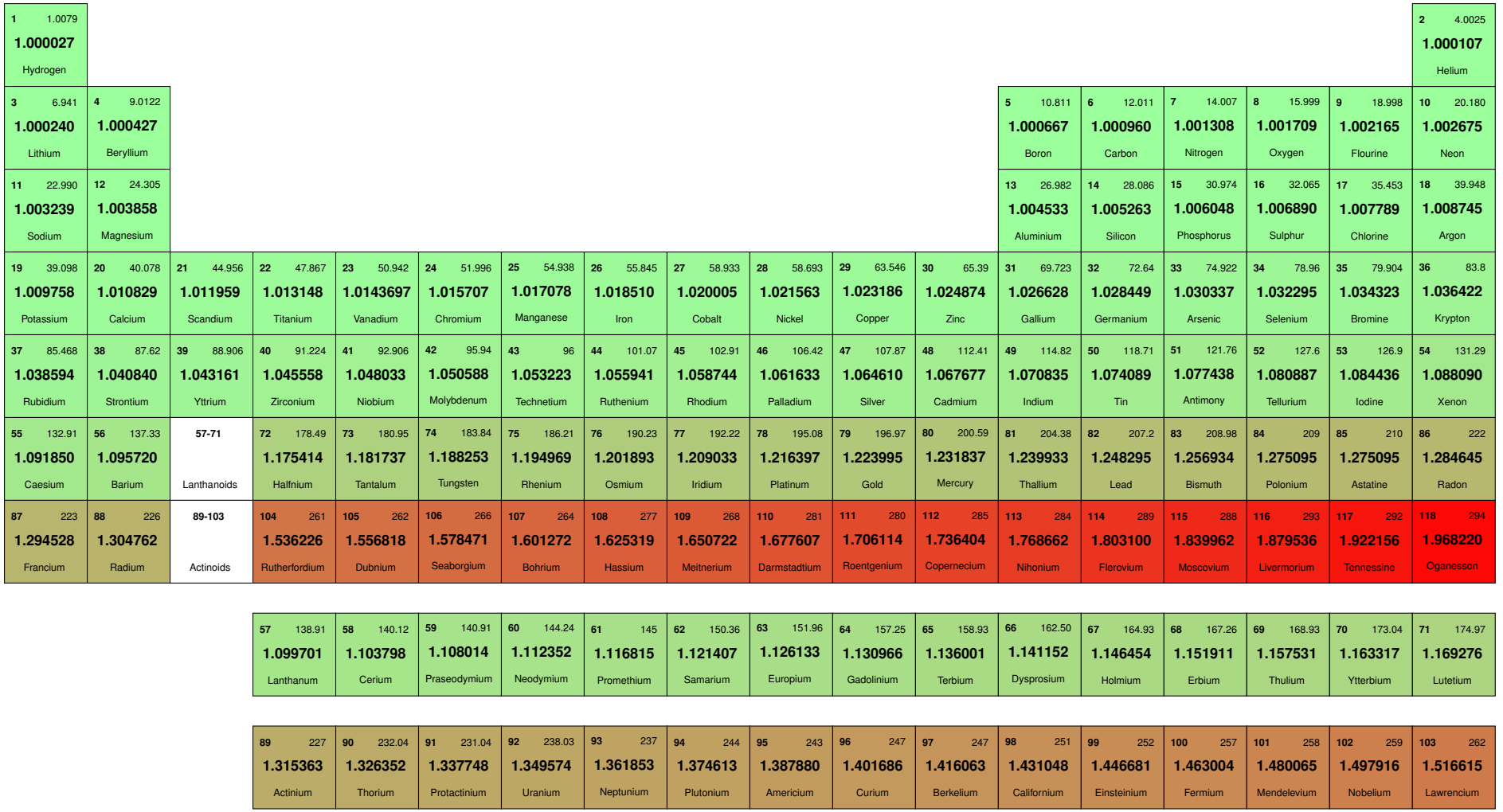

Figure 2.4: Lorentz factor, γ for the 1s electron for elements, Z = 1-118. The Lorentz factor is defined by the equation $\gamma = \left(\sqrt{1 - \left(\frac{v_e}{c} \right)^2} \right)^{-1}$, where v_e is the velocity of the electron and c is the speed of light. For the 1s electron, we may calculate v_e approximately as $v_e = \frac{Z}{137}$. Figure adapted from `http://www.texample.net/tikz/examples/periodic-table-of-chemical-elements/`

To obtain E_R, we must take the square root of Eqn. 2.89; however, to do so we must also chose a sign for the solution. We can also see spectrum of solutions to this relation would not be continuous through 0, rather, they would be separated by $2m_0c^2$.

The relativistic analogue to the Schrödinger wave equation (Eqn. 2.1) is the Dirac equation, which was developed by Paul A. M. Dirac in the late 1920s.[208–211] Somewhat entertainingly, Dirac noted in the introduction to Ref. [210] that relativistic effects are "of no importance in the consideration of atomic and molecular structure and ordinary chemical reactions". Nevertheless, the remainder of this section will be concerned with the Dirac equation in the context of molecular systems. For one electron in an external field, the Dirac equation for the relativistic energy, ε_R, in atomic units appears deceptively simple and is written as[204,212]

$$\hat{h}_D\vec{\boldsymbol{\psi}}(\mathbf{r}) = \left(c\vec{\boldsymbol{\alpha}}\cdot\vec{p} + \boldsymbol{\beta}m_ec^2 + V(\mathbf{r})\right)\vec{\boldsymbol{\psi}}(\mathbf{r}) = \varepsilon_R\vec{\boldsymbol{\psi}}(\mathbf{r}), \tag{2.90}$$

where $\hat{h}_D$ is the one-electron Dirac Hamiltonian, $\vec{\boldsymbol{\psi}}(\mathbf{r})$ is the Four-Component (4C) spinor, the relativistic equivalent to the wavefunction, $\vec{\boldsymbol{\alpha}}$ is a vector the containing Dirac $\boldsymbol{\alpha}_i$ matrices, $i = \{x, y, z\}$, $\vec{p}$ is a vector containing the momentum operators, $\hat{p}_i$, $\boldsymbol{\beta}$ is another Dirac matrix, $V(\mathbf{r})$ is the external field potential and noting that for an electron, $m_0 = m_e$. These components will be dealt with in turn, beginning with the 4C spinor, $\vec{\boldsymbol{\psi}}(\mathbf{r})$, which is the vector

$$\vec{\boldsymbol{\psi}}(\mathbf{r}) = \begin{pmatrix} \boldsymbol{\psi}^+(\mathbf{r}) \\ \bar{\boldsymbol{\psi}}^+(\mathbf{r}) \\ \boldsymbol{\psi}^-(\mathbf{r}) \\ \bar{\boldsymbol{\psi}}^-(\mathbf{r}) \end{pmatrix} = \begin{pmatrix} \vec{\boldsymbol{\psi}}^+(\mathbf{r}) \\ \vec{\boldsymbol{\psi}}^-(\mathbf{r}) \end{pmatrix}, \tag{2.91}$$

which has four elements which correspond to the "up" and "down" spinors, denoted respectively by the absence and presence of an over-bar, for the positive and negative energy solutions to the equation, denoted respectively by a superscript + or −. The 4C spinor may be separated into the two, Two-Component (2C) spinors containing the pairs of positive and negative energy spinors, $\vec{\boldsymbol{\psi}}^+(\mathbf{r})$ and $\vec{\boldsymbol{\psi}}^-(\mathbf{r})$. It should be noted that the positive and negative 2C spinors are also commonly known as the "large" and "small" components, respectively.

The next component of Eqn. 2.90, $\vec{\alpha}$ is also a vector,

$$\vec{\alpha} = \left(\alpha_x, \alpha_y, \alpha_z\right), \tag{2.92}$$

with elements α_i are 4×4 matrices

$$\alpha_i = \begin{bmatrix} \mathbf{0}_2 & \sigma_i \\ \sigma_i & \mathbf{0}_2 \end{bmatrix}, \tag{2.93}$$

where $\mathbf{0}_2$ is the 2×2 null matrix and σ_i are the Pauli matrices

$$\sigma_x = \begin{bmatrix} 0 & 1 \\ 1 & 0 \end{bmatrix}, \qquad \sigma_y = \begin{bmatrix} 0 & -i \\ i & 0 \end{bmatrix}, \qquad \sigma_z = \begin{bmatrix} 1 & 0 \\ 0 & -1 \end{bmatrix}, \tag{2.94}$$

and thus the Dirac α matrices are

$$\alpha_x = \begin{bmatrix} 0 & 0 & 0 & 1 \\ 0 & 0 & 1 & 0 \\ 0 & 1 & 0 & 0 \\ 1 & 0 & 0 & 0 \end{bmatrix}, \quad \alpha_y = \begin{bmatrix} 0 & 0 & 0 & -i \\ 0 & 0 & i & 0 \\ 0 & -i & 0 & 0 \\ i & 0 & 0 & 0 \end{bmatrix}, \quad \alpha_z = \begin{bmatrix} 0 & 0 & 1 & 0 \\ 0 & 0 & 0 & -1 \\ 1 & 0 & 0 & 0 \\ 0 & -1 & 0 & 0 \end{bmatrix}. \tag{2.95}$$

The momentum vector, $\vec{p}$, is

$$\vec{p} = \begin{pmatrix} \hat{p}_x \\ \hat{p}_y \\ \hat{p}_z \end{pmatrix}, \tag{2.96}$$

with elements

$$\hat{p}_i = -i \cdot \hat{\nabla}_i, \tag{2.97}$$

noting for the sake of clarity that the first term in Eqn. 2.97 is the imaginary number. Finally

the Dirac $\boldsymbol{\beta}$ is the 4×4 matrix,

$$\boldsymbol{\beta} = \begin{bmatrix} \mathbf{I}_2 & \mathbf{0}_2 \\ \mathbf{0}_2 & -\mathbf{I}_2 \end{bmatrix}, \tag{2.98}$$

where $\mathbf{I}_2$ is the 2×2 identity matrix.

The representation of the Dirac equation in Eqn. 2.90 is quite cumbersome. It is therefore convenient to re-write the Dirac one-electron Hamiltonian operator in the form of a 4×4 matrix:

$$\hat{h}_D = \begin{bmatrix} m_e c^2 + V(\mathbf{r}) & 0 & -c\hat{p}_z & -c\left(\hat{p}_x - i\hat{p}_y\right) \\ 0 & m_e c^2 + V(\mathbf{r}) & -c\left(\hat{p}_x + i\hat{p}_y\right) & c\hat{p}_z \\ -c\hat{p}_z & -c\left(\hat{p}_x - i\hat{p}_y\right) & -m_e c^2 + V(\mathbf{r}) & 0 \\ -c\left(\hat{p}_x + i\hat{p}_y\right) & c\hat{p}_z & 0 & -m_e c^2 + V(\mathbf{r}) \end{bmatrix}, \tag{2.99}$$

which may again be re-written in a slightly more compact fashion

$$\hat{h}_D = \begin{bmatrix} m_e c^2 + V(\mathbf{r}) & c\vec{\boldsymbol{\sigma}} \cdot \vec{p} \\ c\vec{\boldsymbol{\sigma}} \cdot \vec{p} & -m_e c^2 + V(\mathbf{r}) \end{bmatrix}, \tag{2.100}$$

where $\vec{\boldsymbol{\sigma}}$ is a vector with elements

$$\vec{\boldsymbol{\sigma}} = \left(\boldsymbol{\sigma}_x, \boldsymbol{\sigma}_y, \boldsymbol{\sigma}_z\right). \tag{2.101}$$

By combining Eqn. 2.100 with Eqn. 2.91, we may re-write the Dirac equation for a single electron in an external field (Eqn. 2.90) in matrix form as

$$\hat{h}_D \vec{\boldsymbol{\psi}}(\mathbf{r}) = \begin{bmatrix} m_e c^2 + V(\mathbf{r}) & c\vec{\boldsymbol{\sigma}} \cdot \vec{p} \\ c\vec{\boldsymbol{\sigma}} \cdot \vec{p} & -m_e c^2 + V(\mathbf{r}) \end{bmatrix} \begin{pmatrix} \vec{\boldsymbol{\psi}}^{+}(\mathbf{r}) \\ \vec{\boldsymbol{\psi}}^{-}(\mathbf{r}) \end{pmatrix} = \varepsilon_R \vec{\boldsymbol{\psi}}(\mathbf{r}). \tag{2.102}$$

Thus far, the nature of the external field has remained unspecified. For the purposes of further simplifying the Dirac Hamiltonian such that it can be separated into "scalar" and "spin-orbit" components, it is convenient to take the external potential to be spherically symmetrical. We

may recast therefore recast the equations into a radial form. First it is instructive to examine the non-relativistic, Schrödinger equation for such a scenario:

$$\hat{h}_S \Theta = \left(-\frac{1}{2}\hat{\nabla}^2 + V(r) \right) \Theta = \varepsilon_{NR} \Theta, \tag{2.103}$$

recalling that Θ is the electronic wavefunction and $\hat{h}_S$ is the Schrödinger Hamiltonian. For a spherically symmetrical potential we re-write this expression in terms of polar coordinates,[204] such that

$$\Theta_{n,l,m_l}(r) = R_{n,l}(r) Y_{l,m_l}(\theta, \varphi), \tag{2.104}$$

where n, l, m_l are the principle, angular momentum and projected angular momentum quantum numbers, $R_{n,l}$ is the radial wavefunction and Y_{l,m_l} is the angular wavefunction, which takes the form of spherical harmonics. The Schrödinger equation in SI units therefore simplifies to

$$\left(-\frac{\hbar^2}{2m_e} \frac{1}{r^2} \frac{\mathrm{d}}{\mathrm{d}r} \left(r^2 \frac{\mathrm{d}}{\mathrm{d}r} \right) + \frac{\hbar^2}{2m_e} \frac{l(l+1)}{r^2} + V(r) \right) R(r) = \varepsilon_{NR} R(r). \tag{2.105}$$

Returning to the Dirac equation within a spherically symmetrical potential, to perform a similar manipulation we must first reform the 2C spinor, $\vec{\boldsymbol{\psi}}(\mathbf{r})$, in a similar manner as Eqn. 2.104:

$$\vec{\boldsymbol{\psi}}_{n\kappa m_j}(\mathbf{r}) = \begin{pmatrix} \vec{\boldsymbol{\psi}}^{+}_{n\kappa m_j}(\mathbf{r}) \\ \vec{\boldsymbol{\psi}}^{-}_{n\kappa m_j}(\mathbf{r}) \end{pmatrix} = \begin{pmatrix} F_{n,\kappa}(r) \chi_{\kappa, m_j}(\theta, \varphi) \\ iG_{n,\kappa}(r) \chi_{-\kappa, m_j}(\theta, \varphi) \end{pmatrix}, \tag{2.106}$$

where $F_{n,\kappa}(r)$ and $G_{n,\kappa}(r)$ are the radial components of the spinors, with principal quantum number, n, and the relativistic angular momentum quantum number κ, which is related to the total angular momentum, angular momentum and spin-projection quantum numbers, j, l and m_s by

$$\kappa = -2m_s \left(j + \frac{1}{2} \right) = -2m_s \left(l + m_s + \frac{1}{2} \right), \tag{2.107}$$

and $\chi_{\kappa, n_j}(\theta, \varphi)$ and $\chi_{-\kappa, n_j}(\theta, \varphi)$ are the spherical Pauli spinors with quantum numbers $\pm\kappa$ and n_j, the latter of which is the secondary total angular momentum quantum number. To form

expressions for the radial components, it is convenient to define the adjusted energy, ε'_R, such that

$$\varepsilon'_R = \varepsilon_R \pm m_e c^2, \tag{2.108}$$

where the sign is appropriate so as to remove the $m_e c^2$ gap to 0, and to define the radially varying mass, $\mathcal{M}_e(r)$

$$\mathcal{M}_e(r) = m_e + \frac{\varepsilon'_R - V(r)}{2c^2}. \tag{2.109}$$

We may utilise these to develop an expression for a relativistic electron in a spherically symmetrical potential. Focusing on the case of $F_{n,\kappa}(r)$, for simplicity, we may derive the expression[204]

$$\begin{aligned}\varepsilon'_R F_{n,\kappa}(r) = &\overbrace{\left(-\frac{\hbar^2}{2\mathcal{M}_e(r)}\frac{1}{r^2}\frac{\mathrm{d}}{\mathrm{d}r}\left(r^2\frac{\mathrm{d}}{\mathrm{d}r}\right) + \frac{\hbar^2}{2\mathcal{M}_e(r)}\frac{l(l+1)}{r^2} + V(r)\right)}^{\text{Mass-velocity corrections}} F_{n,\kappa}(r) - \overbrace{\frac{\hbar^2}{(2\mathcal{M}_e(r)c)^2}\frac{\mathrm{d}V(r)}{\mathrm{d}r}\frac{\mathrm{d}F_{n,\kappa}(r)}{\mathrm{d}r}}^{\text{Darwin term}} \\ &\underbrace{-\frac{\hbar^2}{(2\mathcal{M}_e(r)c)^2}\frac{\mathrm{d}V(r)}{\mathrm{d}r}\frac{(1+\kappa)}{r}}_{\text{Spin-orbit coupling term}} F_{n,\kappa}(r).\end{aligned} \tag{2.110}$$

Comparing the relativistic and non-relativistic (Eqn. 2.105) radial equations, we can see that the first term of the relativistic equation is almost identical to the non-relativistic counterpart, apart from the inclusion of the mass-velocity correction, *via* $\mathcal{M}_e(r)$. The second term is the Darwin term, which has no non-relativistic analogue and can be interpreted as an increase in kinetic energy as a result of transient interactions between the $\boldsymbol{\psi}^+$ and $\boldsymbol{\psi}^-$ spinors.[204,213] The third term is called the spin-orbit coupling term, due to the presence of the relativistic angular momentum quantum number, κ. The mass-velocity and Darwin corrections are known as *scalar* relativistic effects.

All of the Hamiltonians discussed so far have been for a single electron in an external potential and are of significant complexity. The construction of relativistic many-body Hamiltonians is lengthy and beyond the scope of this work. Instead, an interested reader is referred to Ref.s

[204], [212], [213], [214] and [215]. Instead we will note that there exist a number of approximate ways of dealing with relativistic effects within quantum chemistry. This can be achieved by using an approximate Hamiltonian, or by changing the representation of the wavefunction (spinor).

Focusing first on the representation of the wavefunction: a fully relativistic treatment requires the use of a Four-Component (4C) spinor, a highly complicated object (see Eqn. 2.91). One way of reducing complexity is the Foldy-Wouthuysen transformation, in which the negative-energy solutions are projected out.[214,216,217] This leaves only a Two-Component (2C) spinor. This transformation can be performed exactly, in which case it is called the Exact Two-Component (X2C) method.[204,213,217,218] An even greater approximation is to abandon spinors all-together and use a non-relativistic wavefunction instead.[213] This is an appealing approach, since much mathematical machinery has been developed to deal with non-relativistic wavefunctions.

The Hamiltonian may also be approximated to improve computational feasibility. The Hamiltonians are based on various approximations to the Dirac-Coulomb and Dirac-Coulomb-Briet Hamiltonians[204,213] and include perturbative approaches, such as the CPD Hamiltonian.[219,220] Others include the Zero Order Regular Approximation (ZORA) Hamiltonian[94,221–228] and its higher extensions,[229] and the Douglas-Kroll-Hess (DKH) Hamiltonian.[230,231] It should be noted that many approximate Hamiltonians may be used in the context of 4C and 2C spinors or even using a normal wavefunction. It should also be noted that many approximate Hamiltonians, such as the DKH Hamiltonian, exclude spin-orbit coupling terms. This is because for atoms with low total angular momentum, spin-orbit coupling terms are small. Spin-orbit coupling can be reintroduced perturbatively.[94,227]

One need not remain within the realms of wavefunction theory. Relativistic extensions to DFT have also been developed,[232] including for Kohn-Sham DFT.[233,234] Relativistic KS-DFT employs spinors and may be of the 4C or 2C variety. Relativistic approaches to TD-KS-DFT are of particular relevance to the present work.[94,227]

Finally, it should be noted that the preceding discussion focuses purely on relativistic effects on electronic structure alone. Relativity does have an influence on the nuclear wavefunction

also;[204] however, these are routinely neglected in quantum chemical calculations.

2.6 Beyond the adiabatic approximation

The preceding sections demonstrated methods to solve electronic structure problems. As mentioned in section 2.1, the coupling between electronic and nuclear wavefunctions must be taken into account to properly describe the dynamic (*i.e.* time-dependent) behaviour of photoexcited systems.[24] Achieving this without approximation fundamentally requires that the overall wavefunction must be exactly factorizable by the electronic and nuclear wavefunctions in some form. Recall that the work of Born and Oppenheimer showed that factorization of the wavefunction is exact up to fourth order perturbation and for only small vibrational motions.[75,76] That this factorization is unconditionally exact was first shown by Hunter in 1975 and the consequences subsequently explored.[235–237]

The extension of the Born-Oppenheimer approximation to a time-dependent form followed,[238–240] and recently these have been combined and an exact factorization of the time-dependent wavefunction[241–243] and electron density[244] has been achieved. These methods provide the framework in which the dynamics of the total nuclear and electronic system can be modelled.[172]

There are two main approaches to modelling the progression of a nuclear system under the influence of electrons. The first approach is to treat the nuclei in a classical manner, that is, to put define the position of the nuclei on the electronic PESs, define their momentum, and then to propagate the nuclear wavefunction classically and follow its trajectory as it moves like a marble along the surfaces. The movement of the nuclear wavefunction between the surfaces corresponding to different electronic *eigenstates* must be considered. An early implementation of this approach, by Preston and Tully, is the basis for most modern, so called surface-hopping, methods.[245–247] Since each trajectory is essentially classical in nature, a large number of trajectories must be investigated and their properties averaged to recover the statistical nature of the real, quantum mechanical system.

Alternatively, the nuclear wavefunction can be treated quantum mechanically. Just as the position of the electrons are described with basis functions rather than points, so are the nuc-

lei. For molecular systems of reasonable size, the most popular method by which this can be computed is the Multi Configurational Time Dependent Hartree (MCTDH) method.[248–250] In the MCTDH approach, the nuclei are described using Gaussian basis functions and propagated along the potential energy surface, which is represented on a grid. Since the resultant nuclear wavepackets are intrinsically quantum objects, unlike the classical trajectories described above, they may behave in a more physical manner, for example, by splitting into more than one wavepacket on more than one PES when passing through a conical intersection. Other approaches toward quantum wavepacket simulations do exist; however, these tend to be limited to smaller systems due to unfavourable scaling.[251,252] An interested reader is referred to Ref.s [253] and [254] for further details.

The use of electronic structure methods in combination with the methods described above to simulate nuclei allows quantum chemists to simulate the experiments that laboratorial chemists perform every day. This work utilises only some of the methods discussed above; however, it is hoped that in future work more of the techniques can be utilised to deepen the understanding of the physical and chemical phenomena described herein.

Chapter 3

Computational methods

The majority of calculations were performed using the Gaussian 09 suite of programs.[255] DFT[113,120] and TD-DFT[137] calculations were performed using the B3LYP exchange-correlation functional.[124,125] In all calculations, unless otherwise specified, the Integral Equation Formalism of the Polarizable Continuum Model (IEFPCM) was used to simulate the solvent.[256,257] In Chapter 4, the following basis sets were used in the calculations: the SDD basis set, as implemented in Gaussian, for all atoms,[258,259] which is denoted SDD in the text; the SDD basis set[258] for Pt and the 6-31G(d) basis set for all other atoms,[260,261] which is denoted SDD+6-31G(d) in the text; and the cc-pVTZ-PP and cc-pVTZ basis sets for Pt and all other atoms respectively,[262–264] denoted cc-pVTZ in the text. In Chapter 5, some calculations employed the SDD basis set for Pt and the 6-311G(d,p) basis set for all other atoms.[265,266] In time-dependent calculations performed within Gaussian 09, the *eigenvalue* problem is solved iteratively using a modified form of the Davidson-Liu algorithm.[184,186,187,189]

In Chapter 4, the ground state geometries of **PTZ-CH_2-Pt-NAP**, **PTZ-Pt-NAP** and **OMePTZ-Pt-NAP** were optimised at the B3LYP/cc-pVTZ level, and **PTZ-Pt-NAP** and **PTZ-Pt^H-NAP** were further optimised at the B3LYP/SDD and B3LYP/SDD+6-31G(d) levels of theory and confirmed as minima by the absence of imaginary frequencies in their vibrational spectra within the harmonic approximation.[i] The geometries of some of the electronically excited states of **PTZ-Pt^H-NAP** were optimised at the B3LYP/SDD+6-31G(d) level of theory and confirmed as minima by the absence of imaginary frequencies in their vibrational spectra,

which were calculated numerically.

The vibrational frequencies reported are scaled empirically to account for anharmonicity and inadequacies in the method to obtain good agreement with experimental results, in accordance with widely known methods.[267–270] It also well known that different regions of the vibrational spectrum may require different scaling factors, in part due to their differing anharmonicities.[268,271] This methodology has been successfully applied to similar compounds containing acetylides in the past.[271,272] Accordingly, the following scaling factors have been applied to the reported vibrational frequencies: at the B3LYP/SDD+6-31G(d) level, 0.955 for the acetylide modes, 0.964 for all other modes; at the B3LYP/cc-pVTZ level, 0.969 for the acetylide modes, 0.986 for all other modes.

A number of slices of the potential energy surfaces (PESs) of **PTZ-CH_2-Pt-NAP**, **PTZ-Pt-NAP**, **PTZ-Pt^H-NAP** and **OMePTZ-Pt-NAP** were calculated and are referred to as Franck-Condon (FC) surfaces if the optimised ground state geometry is used as a starting point, or non-Franck-Condon (non-FC) surfaces if the excited state geometries are also used as starting points. The surfaces were calculated as follows:

- "Unrelaxed" surfaces, in which the length of NAP side C≡C is lengthened and shortened without re-optimising the geometry.
- "Relaxed" surfaces, in which the length of NAP side C≡C is lengthened and shortened and the geometry is re-optimised with the constraint that the C≡C bond length remains fixed.
- "Frozen framework" surfaces, in which all other atoms apart from the NAP side C≡C remain frozen and that bond is lengthened and shortened.
- "Unrelaxed antisymmetrical" surfaces, in which the PTZ side C≡C and NAP side C≡C are set to opposite lengths along the scale investigated, i.e. on a scale ranging from −1 to 1, the pairs of distances would be −1 and 1, 0 and 0, and 1 and −1, without re-optimising the geometry.
- "Relaxed antisymmetrical" surfaces, in which the PTZ side C≡C and NAP side C≡C are

[i] See Figure 4.1 for structure diagrams.

set to opposite lengths along the scale investigated and the geometry is re-optimised with the constraint that the two C≡C bond lengths remain fixed.

- "Vibrational" surfaces, in which the asymmetrical C≡C combination mode (ν_a(C≡C)) is followed.

For all surfaces apart from the "vibrational" surfaces, points were taken in intervals of 0.02 Å from 1.06 Å to 1.40 Å, plus one point for the equilibrium geometry, resulting in a total of 19 points. For the vibrational surfaces, points were taken by following the mass-weighted Cartesian displacement coordinates for the vibrations in question,[273,274] with the change in length of C≡C on the order of 0.014 Å from ∼1.04 Å to ∼1.40 Å, resulting in a total of 27 points.

A number of slices of the PESs of various isotopomers of [Pt(bipyCOOEt)(C≡C-Ph-CH_2-PTZ)$_2$] were obtained in a similar manner to that described above. In these cases the "vibrational" protocol described above was employed.

Calculations using Slater Type Orbitals (STOs) were performed using Amsterdam Density Functional, 2016 (ADF 2016).[275–278] In some of these calculations, the Zero-Order Regular Approximation (ZORA) Hamiltonian was used, incorporating scalar relativistic effects.[221–225] If the ZORA Hamiltonian was used, the appropriately fitted basis set of a given ζ quality was used. It should be noted that no ZORA fitted basis set of DZP quality exists for Pt and so in calculations using the DZP basis set for the remaining atoms, the TZP basis set was used for Pt. Time-Dependent (TD) and Simplified Time-Dependent (sTD) DFT calculations were performed in which Spin-Orbit Coupling (SOC) was included perturbatively.[279,280] In some calculations, core orbitals were frozen according to the scheme described in Ref. [278], a total of 212 electrons in the case of [Pt(bipyCOOEt)(C≡C-Ph-CH_2-PTZ)$_2$] (Chapter 5). Solvent was included implicitly by means of the Conductor-like Screening Model (COSMO)[281] as implemented in ADF.[282] Density fitting was employed in the calculations in the assessment of the Coulbomb potential.[283] A "good" Becke fuzzy cell integration scheme was used in all calculations, as defined by ADF.[284,285] In time-dependent calculations, the *eigenvalue* problem is solved iteratively using the Davidson-Liu algorithm.[184,187,191]

The calculations reported in Chapter 6 were performed using Gaussian 09, revision D.01.[255]

The B3LYP exchange-correlation functional was used in all calculations.[124,125] Tetrahydrofuran (THF) solvent was included implicitly using the PCM.[256,257] The Dunning-type correlation consistent basis sets of triple-ζ quality were used in all calculations.[262] In the case of Ge, the majority of calculations used a small-core relativistic pseudopotential and the appropriate valence basis set, denoted cc-pVTZ-PP.[286] However, in some cases the all-electron basis set suitable for use with a Douglas-Kroll-Hess Hamiltonian was instead used, denoted cc-pVTZ-DK.[287] All calculations featuring Sn utilised the cc-pVTZ-PP pseudopotential and valence basis set.[288] Nuclear Magnetic Resonance (NMR) chemical shifts were computed using the Gauge Independent Atomic Orbital method,[289–291] as implemented in Gaussian.[292,293] Basis Set Superposition Error (BSSE) was estimated in some cases using gas phase, counterpoise corrected calculations.[294,295]

Part II

Controlling electron transfer

Chapter 4

Electron transfer in Pt *trans*-acetylides

Recent advances have demonstrated that it is possible to influence electron transfer (ET) in the excited state.[36,51] Of particular interest are the investigations described in References [50] and [51]. In these works, a Donor-Bridge-Acceptor (D-B-A) assembly, **PTZ-CH_2-Pt-NAP** of Fig. 4.1, is described that exhibits controllable ET dynamics. By exciting the asymmetric acetylide combination vibrational mode, ν_a(C≡C), of the Charge Transfer (CT) state of this molecule, a change in yield of two other excited states can be induced. This work seeks to extend these investigations by manipulating the elements of **PTZ-CH_2-Pt-NAP**, with the intention of deepening the understanding of the effect observed in the family of compounds shown in Figure 4.1.

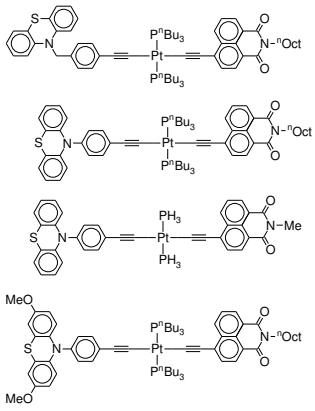

PTZ-CH_2-Pt-NAP

PTZ-Pt-NAP

PTZ-Pt^H-NAP

OMePTZ-Pt-NAP

Figure 4.1: Compounds investigated (left), and their labels in the text (right). **PTZ-Pt^H-NAP** (69 atoms, 390 electrons) is a simplified model version of **PTZ-Pt-NAP** (162 atoms, 638 electrons) and is used in some excited state calculations.

Three of the compounds; **PTZ-CH_2-Pt-NAP**, **PTZ-Pt-NAP** and **OMePTZ-Pt-NAP**,

have been studied experimentally using ultrafast techniques, whilst the fourth compound, **PTZ-Pt^{H}-NAP**, is used in some calculations as a representative model of reduced complexity.[53] The ground and excited state properties of these compounds have been computed, as specified in Chapter 3, using Density Functional Theory (DFT) and Time-Dependent DFT (TD-DFT). Scans along specific coordinates of the Potential Energy Surfaces (PESs) of the compounds were performed as described in Chapter 3 to further elucidate the excited state behaviour of the compounds.

4.1 Ground and excited state properties

The optimised ground state singlet geometries of **PTZ-CH$_2$-Pt-NAP**, **PTZ-Pt-NAP** and **OMePTZ-Pt-NAP** are shown in Figures 4.2, 4.3 and 4.4 respectively. For all three compounds, the NAP (acceptor) and Ph (bridge) moieties are co-planar, with the donor moiety orthogonal to the Ph due to steric repulsion. This configuration provides a great degree of conjugation between the bridge and NAP regions of the molecule, as demonstrated by the significant delocalization shown in many of the ground state singlet frontier molecular orbitals of **PTZ-Pt-NAP** illustrated in Figure 4.5. The bulky P^{n}Bu$_3$ ligands are completely orthogonal to the NAP and Ph moieties, due to strong steric repulsion.

Due to the strong steric repulsion between the alkyl chains of the phosphine ligands and the aromatic systems of the other ligands, it would be expected that the framework of the molecules would be quite rigid and resistant to major conformational changes. This is in line with experimental observations of rapid Inter-System Crossing (ISC) in these compounds as well as rapid Intramolecular Vibrational Redistribution (IVR) in the excited state, since both of these processes are partially dependent on geometry.[23] This suggests that there should be minimal geometrical change between the ground state and the initial excited state, the CT state.

Examining the frontier molecular orbitals of **PTZ-Pt-NAP**, shown in Figure 4.5, which are representative of the orbitals of **PTZ-CH$_2$-Pt-NAP** and **OMePTZ-Pt-NAP**, it can be seen that the HOMO of these compounds lies on the donor and the LUMO on the acceptor, as may be expected. H$-$1, H$-$2 and H$-$3 are dπ anti-bonding orbitals, involving the d_{xy}, d_{xz} and d_{yz} orbitals of the Pt respectively and one of the degenerate acetylide π orbitals. Since the π orbitals

involved in H−1 and H−3 are parallel with those of the Ph and NAP moieties, H−1 and H−3 are delocalised across the bridge and acceptor. The π orbitals involved in H−2, however, are orthogonal to those of the Ph and NAP and thus H−2 is localised on the Pt acetylide portion of the bridge, with a small contribution from adjacent σ(C–C) bonds. Importantly, in the occupied orbitals there is very limited delocalization between the donor and the bridge: the donor is essentially electronically isolated from the rest of the system.

The LUMO in these compounds is localised on the acceptor, though there is some contribution from a parallel non-/anti-bonding acetylide π orbital. It is therefore expected that transitions from HOMO→LUMO, which would form a CSS, should be completely disallowed due to lack of overlap. The CT transitions from H−1 →LUMO or H−3 →LUMO should be allowed due to good overlap; however, the H−2 →LUMO transition, also of CT character, should not be allowed due to poor overlap. The LUMO of **PTZ-Pt-NAP** is well separated from the rest of the unoccupied orbitals, with $\Delta\varepsilon_{L\rightarrow L+1} = 1.48$ eV. For **OMePTZ-Pt-NAP**, this value is $\Delta\varepsilon_{L\rightarrow L+1} = 1.50$ eV and for **PTZ-CH$_2$-Pt-NAP**, $\Delta\varepsilon_{L\rightarrow L+1} = 1.55$ eV.

Comparing the singlet orbitals with the unrestricted triplet orbitals, shown in Figure 4.6, there are relatively few differences. The two singly occupied molecular orbitals, denoted H−1$_\alpha$ and HOMO$_\alpha$ resemble the singlet HOMO and LUMO respectively, thus there is an additional

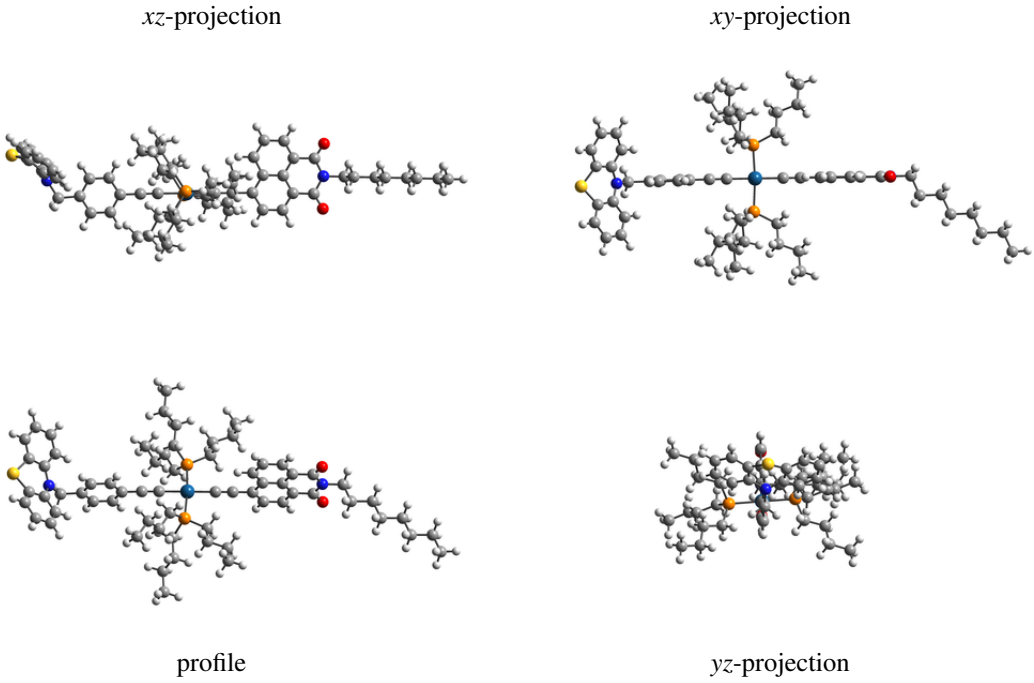

Figure 4.2: B3LYP/cc-pVTZ optimised singlet geometry of **PTZ-CH$_2$-Pt-NAP**

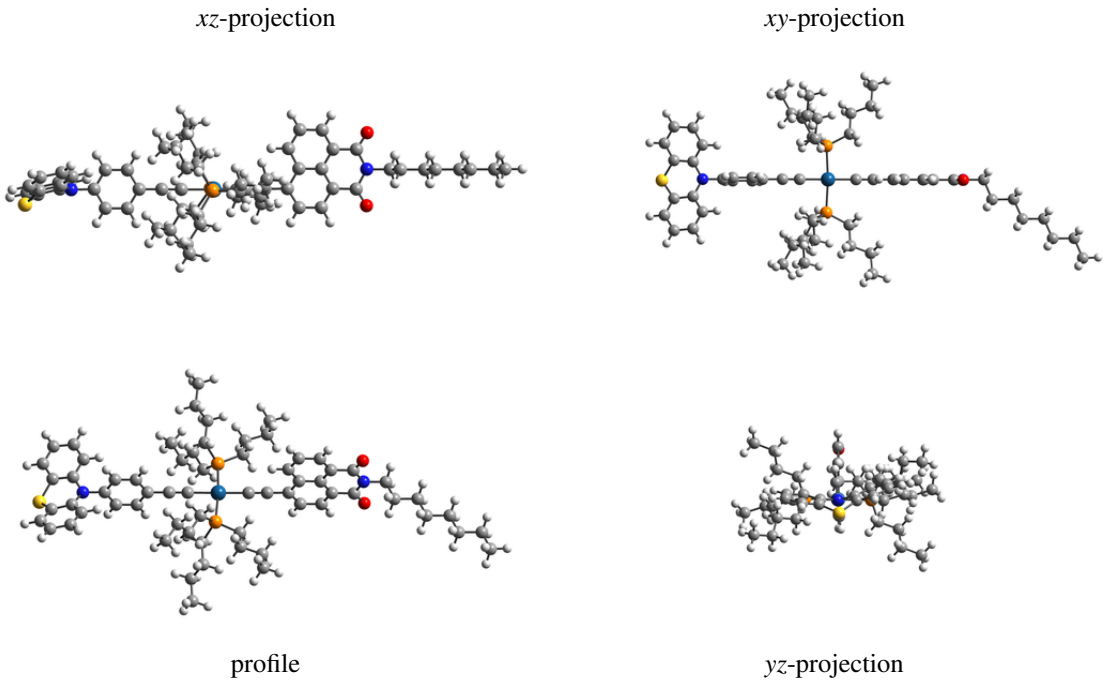

Figure 4.3: B3LYP/cc-pVTZ optimised singlet geometry of **PTZ-Pt-NAP**

α electron on the NAP and so the lowest triplet state is denoted ^{3}NAP. The energetically lowest unoccupied orbital, LUMO$_\beta$, is very close in energy to HOMO$_\beta$ and may be expected to resemble the singlet HOMO but instead LUMO$_\beta$ is a bridge/NAP delocalised dπ orbital similar in character to the singlet H$-$1. Correspondingly, HOMO$_\beta$ resembles the singlet HOMO, from which an electron should have been removed. This is likely the result of reorganization of the

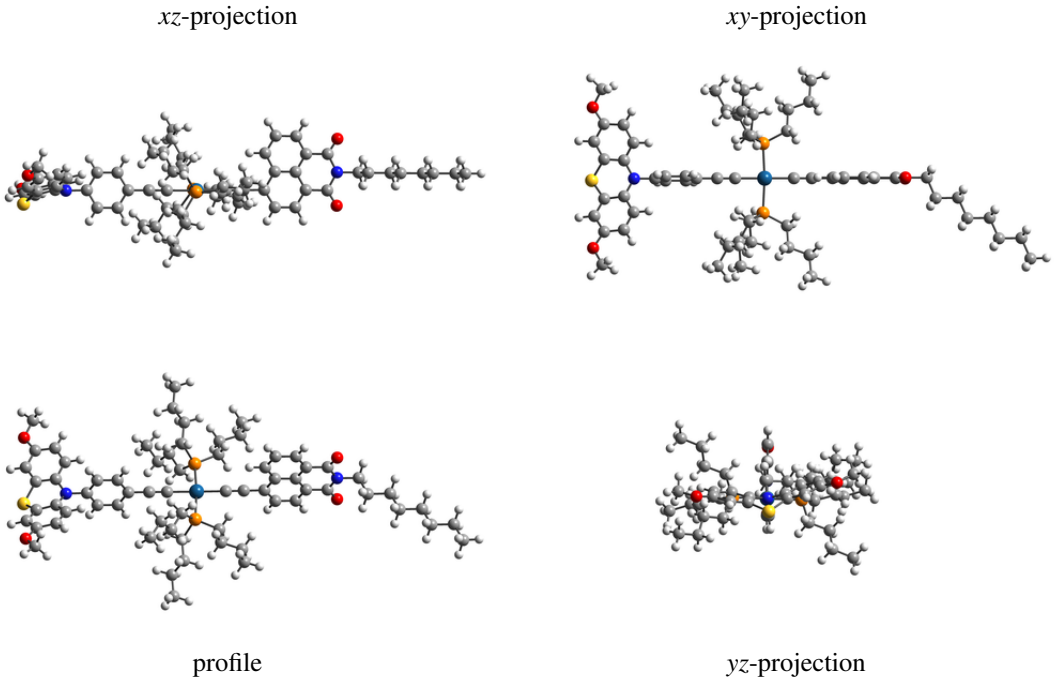

Figure 4.4: B3LYP/cc-pVTZ optimised singlet geometry of **OMePTZ-Pt-NAP**

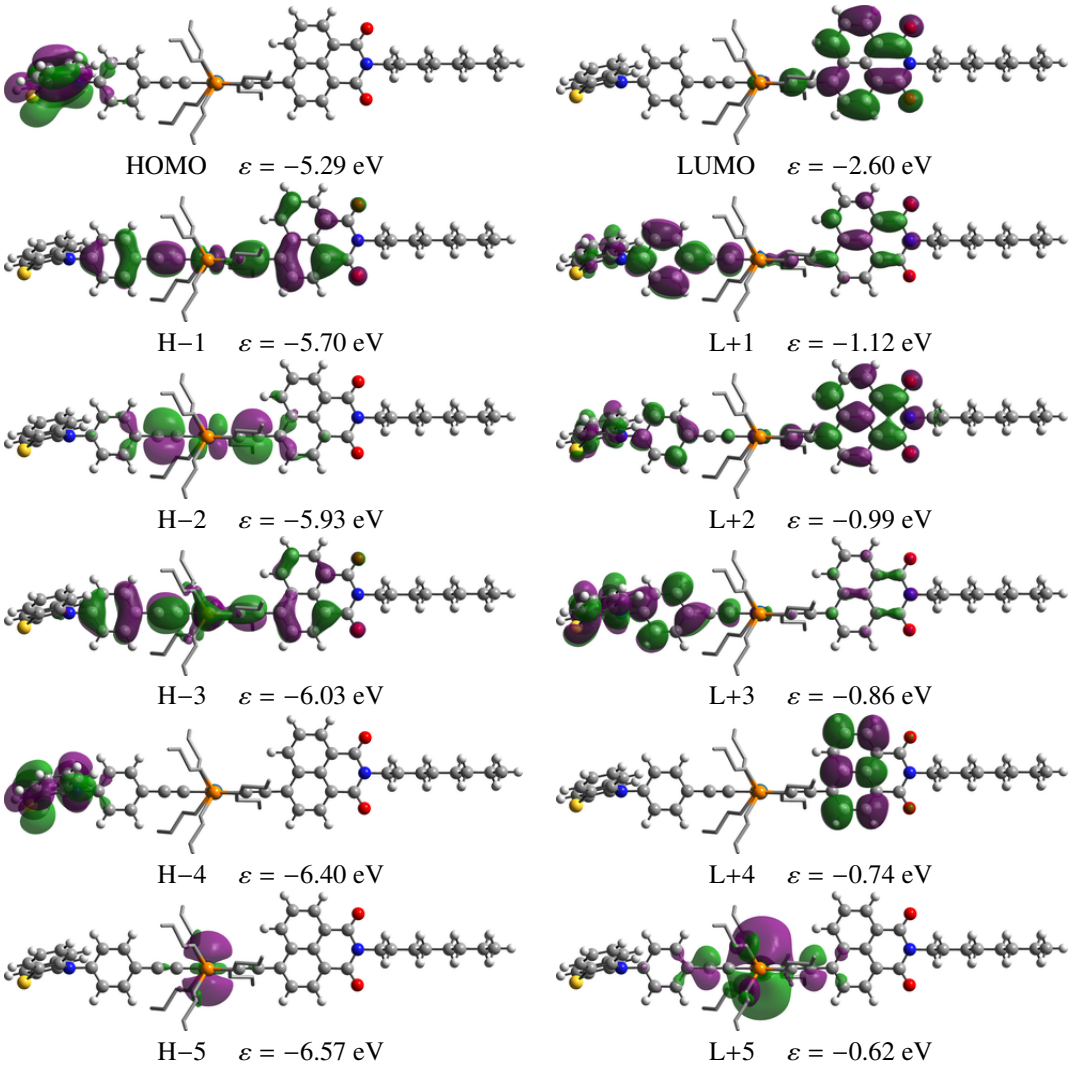

Figure 4.5: Singlet frontier molecular orbitals of **PTZ-Pt-NAP** at the B3LYP/cc-pVTZ level (Some atoms hidden for clarity).

β manifold. The low energy transition from $HOMO_\beta$ $\rightarrow$$LUMO_\beta$ would result in relocation of electron density from the donor to the acceptor, corresponding to a CSS, whilst the transitions from the dπ bridge orbitals $H-1_\beta$ and $H-2_\beta$ into $LUMO_\beta$ would correspond to the formation of CT states, similar to the case of the singlet.

To establish that the ground and excited state properties of these molecules have been well described by the methods employed in this investigation, it is instructive to compare the calculated vibrational and electronic spectra with those measured experimetally. These comparisons are made in Figure 4.7 using **PTZ-Pt-NAP** as a representative case; the remaining results are tabulated and assigned in Appendix A.1. Panels (*c*) and (*d*) of Figure 4.7 compare computations at the B3LYP/cc-pVTZ level using the full **PTZ-Pt-NAP** structure. The vibrational spectrum, shown in panel (*c*) is in very good agreement with experiment; the important acetylide vibra-

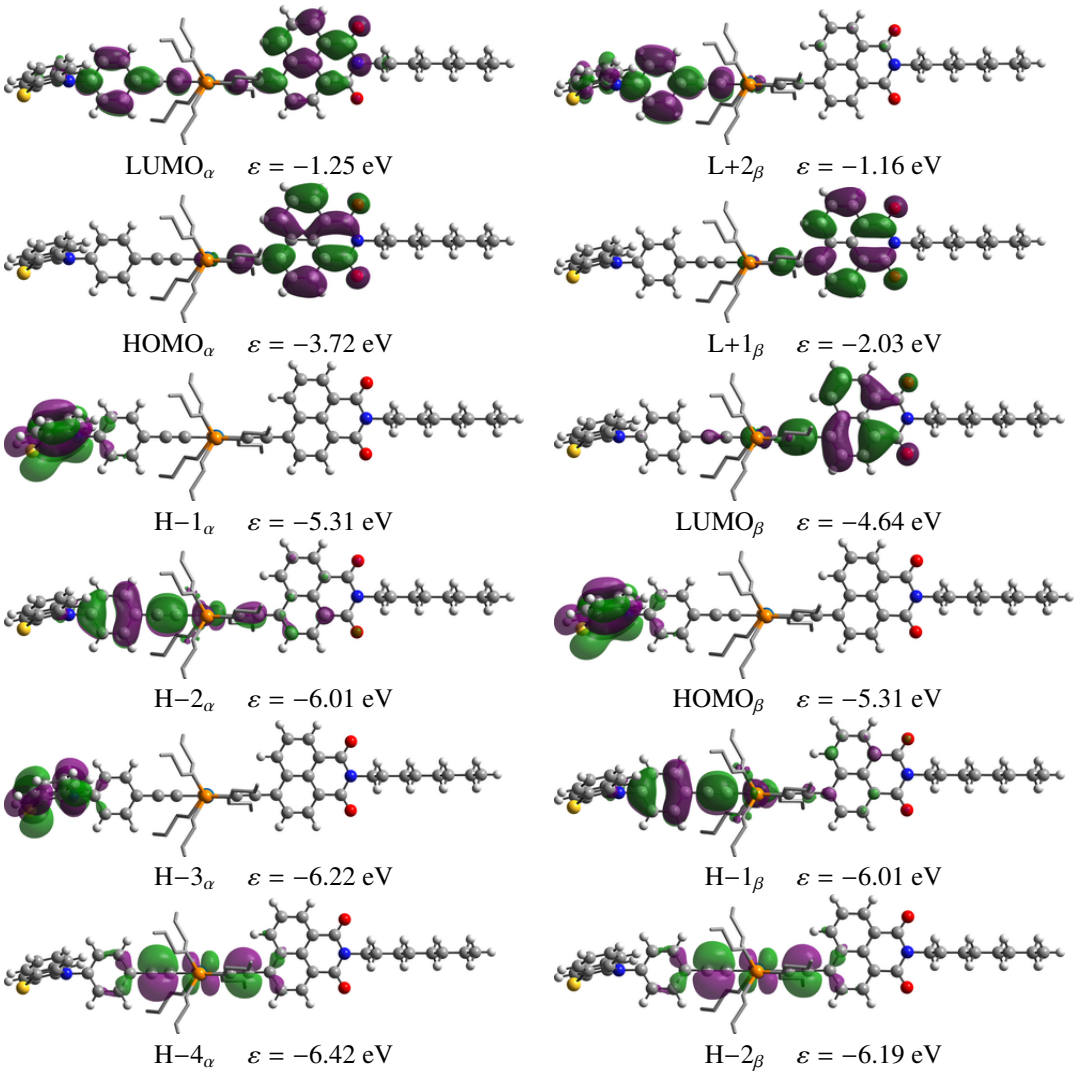

Figure 4.6: Franck-Condon triplet frontier molecular orbitals of **PTZ-Pt-NAP** at the B3LYP/cc-pVTZ level (Some atoms hidden for clarity).

tional modes in the 2100 cm^{-1} region are well positioned, and the donor and acceptor localised modes from 1500 to 1750 cm^{-1} are in excellent agreement in both position and intensity.

The electronic spectrum, shown in Figure 4.7(*c*) has slightly poorer agreement. The broad band from 360 to 500 nm in the experimental spectrum has three humps, the most important of which are the features at approximately 400 and 425 nm, which likely correspond to two CT states involving transitions from the bridge centred H−1 and H−2 to the acceptor centred LUMO. These CT states are well separated from the remainder of the excited state manifold, lending confidence that the calculated excited states are representative of those of the real compounds. Since the CSS state cannot be directly accessed, there is no peak in the experimental spectrum with which to verify the calculated energy. This is problematic, since TD-DFT has well documented problems with under-estimating the energies of transitions featuring a large

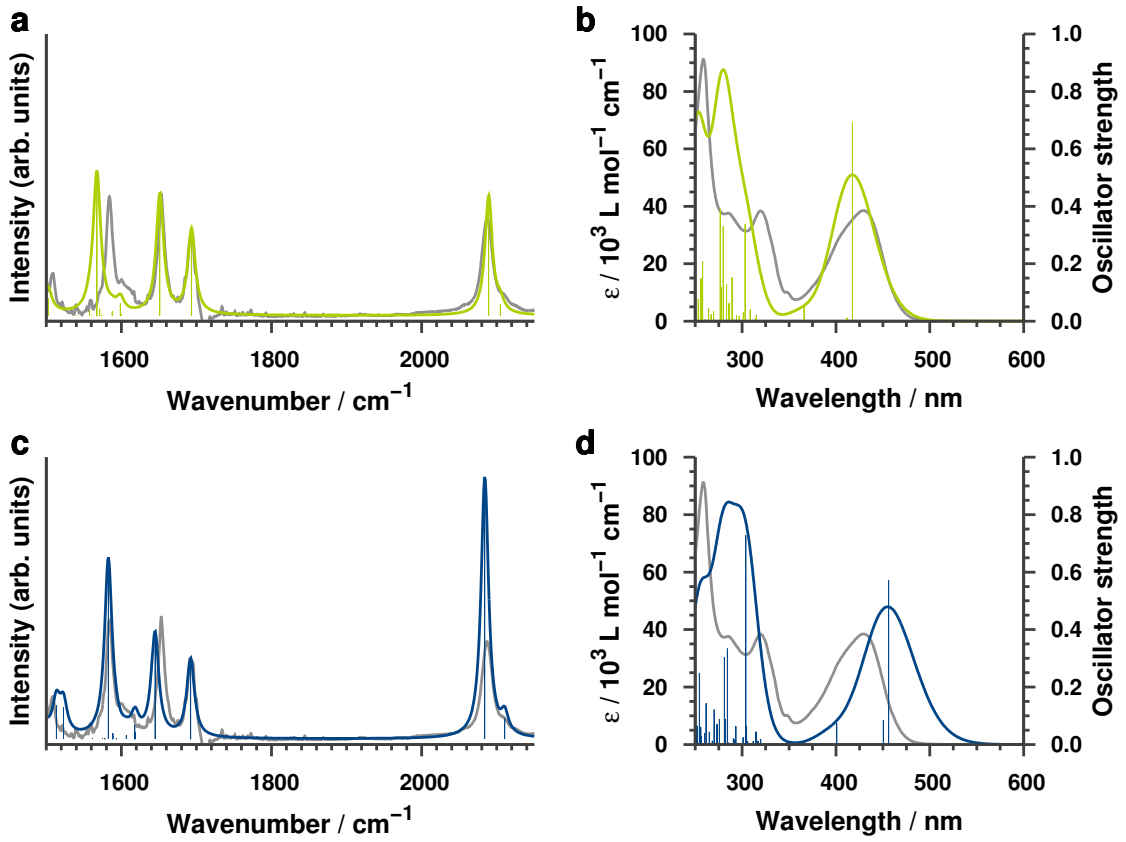

Figure 4.7: Comparison of calculated (coloured lines) and experimental (grey lines) (*a*), (*c*) vibrational, and (*b*), (*d*) electronic spectra of ground state **PTZ-Pt-NAP**; (*a*), (*b*) at the B3LYP/SDD+6-31G(d) level with singlet **PTZ-Pt^{H}-NAP** as a model, and (*c*), (*d*) at the B3LYP/cc-pVTZ level with singlet **PTZ-Pt-NAP** as a model.

degree of charge transfer character, as is the case for both the two CT transitions and the transition into the CSS.[134] Comparing the peaks at 400 and 425 nm with the corresponding calculated CT transitions suggests that their energies are underestimated by approximately 0.1 eV, a small margin. It is therefore reasonable to conclude that the CSS and CT states are qualitatively well described by TD-DFT. The large size of these systems makes it difficult to substantiate this, for example by means of high level wavefunction theory calculations, though this could be an avenue for further investigation.

As shown in the figures above, **PTZ-CH$_2$-Pt-NAP** and its derivatives are of significant size and complexity; the smallest, **PTZ-Pt-NAP**, consists of 162 atoms and 638 electrons. In their current implementation, the second derivative of energy with respect to nuclear position for excited states in TD-DFT must be calculated by numerical methods. To retain computational tractability, it is therefore necessary to use "pruned" model complexes when exploring the chemistry of the excited state molecules of this size. The "pruned" model used in this case

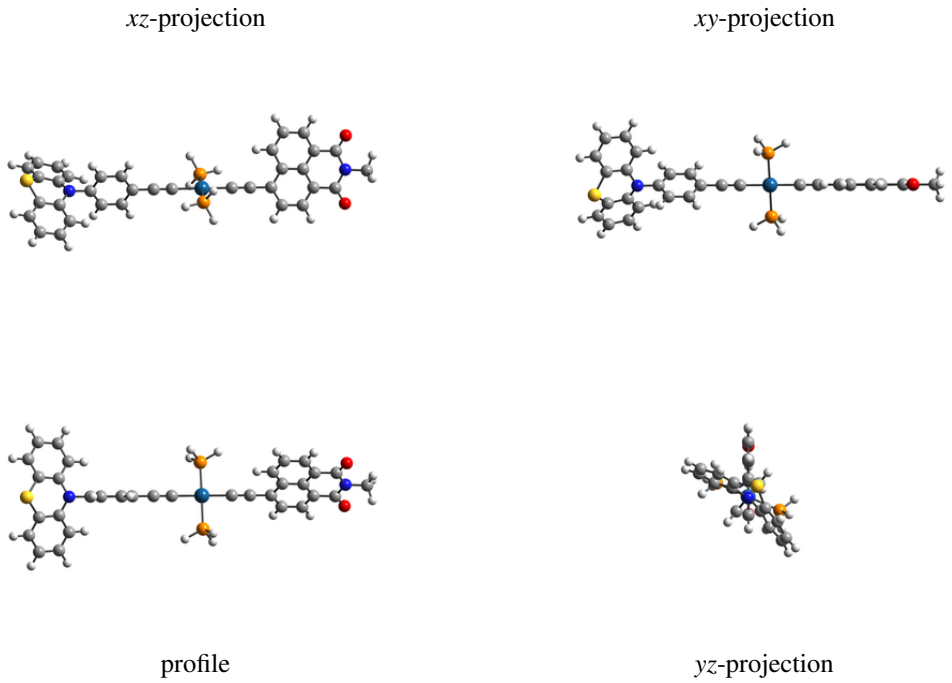

Figure 4.8: B3LYP/SDD+6-31G(d) optimised singlet geometry of **PTZ-Pt^{H}-NAP**

is **PTZ-Pt^{H}-NAP**, the optimised ground state geometry of which is shown in Figure 4.8. There are a number of key differences between this geometry and that of the equivalent "unpruned" complex, **PTZ-Pt-NAP**, the geometry of which is discussed above.

In **PTZ-Pt^{H}-NAP**, the large *n*-butyl groups of the phosphines found in **PTZ-Pt-NAP** have been replaced with hydrogens. The implications of this are that there is much reduced steric congestion in the bridge region: unlike **PTZ-Pt-NAP**, the Ph and NAP moieties of **PTZ-Pt^{H}-NAP** are not coplanar, though the donor and Ph moieties are orthogonal in **PTZ-Pt^{H}-NAP**, as expected. Furthermore the phosphines themselves are no longer orthogonal, but instead offset from plane perpendicular to NAP by approximately 25°. The non-planar relationships between the various sections of the donor, bridge and acceptor have consequences for both the MOs and for excited state geometries. Before considering the B3LYP/SDD+6-31G(d) orbitals of **PTZ-Pt^{H}-NAP** presented in Figure 4.9, it should first be established that the small basis set employed in those calculations have not had a deleterious effect. As such, the B3LYP/cc-pVTZ frontier orbitals of **PTZ-Pt^{H}-NAP** are shown in Figure A.1. Comparing these figures reveals that there is some reorganization of orbitals but no substantial changes. The occupied manifold is similar at both levels of theory, with only H−5 changing character from a d_{z^2} orbital at the B3LYP/cc-pVTZ level to a bridge/donor delocalised π orbital at the B3LYP/SDD+6-31G(d)

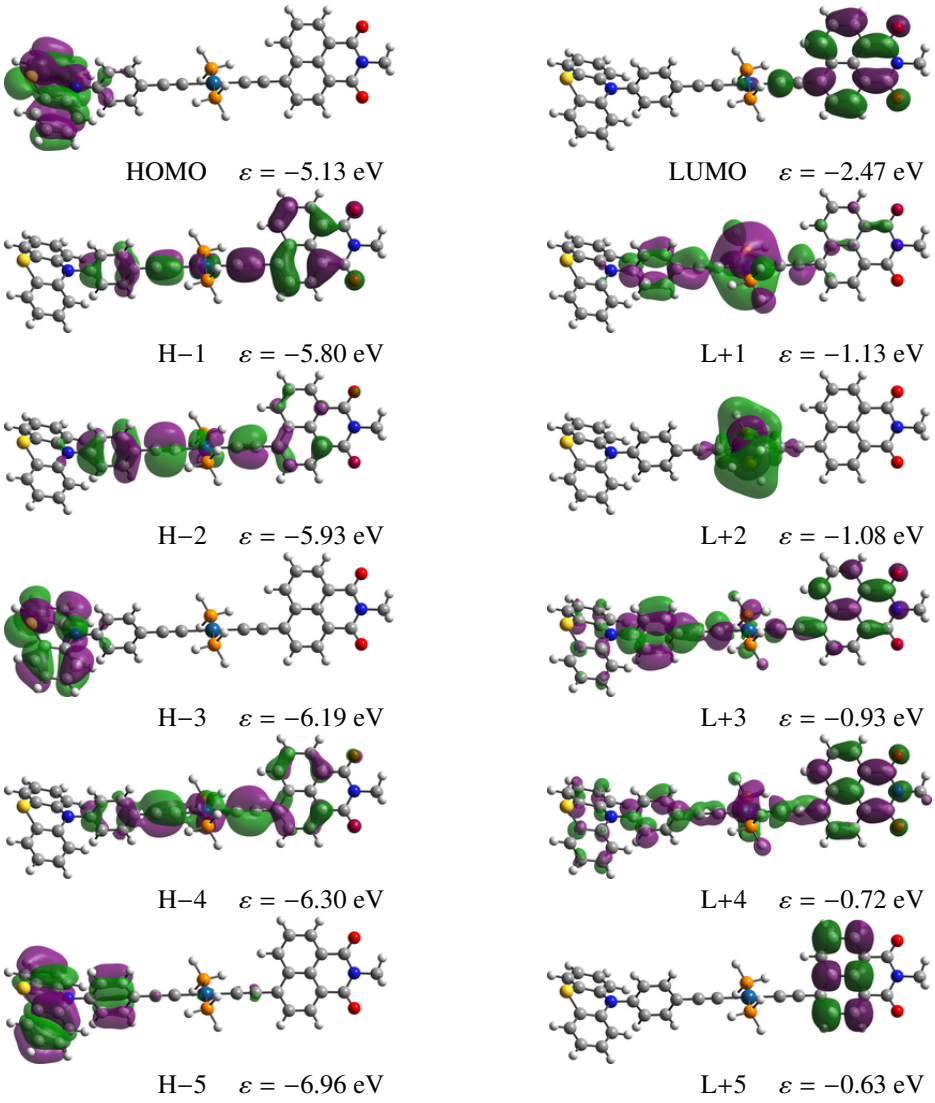

Figure 4.9: Singlet frontier molecular orbitals of **PTZ-Pt^{H}-NAP** at the B3LYP/SDD+6-31G(d) level.

level. The HOMO→LUMO gap is marginally smaller (0.05 eV) at the lower level of theory; however, the LUMO remains well separated from the rest of the occupied manifold at both high and low levels of theory. The unoccupied L+1 to L+5 orbitals are re-ordered between the B3LYP/SDD+6-31G(d) and B3LYP/cc-pVTZ level but remain essentially the same in character. Thus it can be concluded that the effect of reducing the quality of the basis set is minimal for **PTZ-Pt^{H}-NAP**.

The effect of "pruning" can then be established by comparing the B3LYP/SDD+6-31G(d) orbitals of **PTZ-Pt-NAP**, shown in Figure 4.5, with those of **PTZ-Pt^{H}-NAP** at the B3LYP/cc-pVTZ level, shown in Figure 4.9. Broadly, the orbitals retain the same character but undergo some slight reordering between the two levels of theory, with the less planar geometry

of **PTZ-Pt^{H}-NAP** resulting in marginally less extensively conjugated orbitals that are not as strictly orthogonal as in **PTZ-Pt-NAP**. Importantly, the identities of the HOMO, H−1 and H−2 orbitals are the same in both models and have quite similar energies. H−3 and H−4 are reordered between the two cases and H−5 changes character, similar to the effect of only changing the basis set. This suggests that the description of the Pt orbitals provided by the SDD basis set is slightly lacking when compared to the higher quality cc-pVTZ-PP basis set used for Pt in the higher level calculations, though this should have minimal influence for the most important transitions. The LUMO shown in Figure 4.9 is NAP centred, in accordance with the higher level calculations and is well separated from the remainder of the unoccupied manifold ($\Delta\varepsilon_{L\rightarrow L+1}$ = 1.34 eV.) L+1 through to L+5 reorganise between the two levels of theory, with the exception of L+2 of **PTZ-Pt^{H}-NAP**, which does not appear in the frontier orbitals of **PTZ-Pt-NAP**. Fortunately L+2 is not involved in any of the low lying transitions of **PTZ-Pt^{H}-NAP**, shown in Table A.7, so this should have marginal effects on the electronic spectrum.

The computed vibrational and electronic spectra of **PTZ-Pt^{H}-NAP**at the B3LYP/SDD+6-31G(d) level are shown in Figure 4.7(*a*) and (*b*) respectively, and compared with the experimentally measured spectra of **PTZ-Pt-NAP**. The computed vibrational spectrum is in very good agreement with the experimental one; both the acetylide mode positions and relative intensities are in very good agreement, and the carbonyl modes at 1650 and 1700 cm^{-1} are well described, though the remainder of the fingerprint region is in less good agreement. The computed electronic spectrum, shown in Figure 4.7(*b*), shows very good agreement with experiment; however, since the higher level calculations shown in panel (*d*) are in less good agreement, the remarkably good agreement at the B3LYP/SDD+6-31G(d) level is likely due to fortuitous cancellation of errors. The good agreement of both vibrational and electronic spectra suggests that **PTZ-Pt^{H}-NAP** is indeed a good model of **PTZ-Pt-NAP** for quantum chemical purposes.

The good agreement of the B3LYP/SDD+6-31G(d) calculations using **PTZ-Pt^{H}-NAP** in the ground state with experimental data lends confidence that it may also be a suitable model for the excited state chemistry of **PTZ-Pt-NAP**. As such, excited state geometry optimization and frequency calculations were performed for the lowest three excited states of **PTZ-Pt^{H}-NAP** in

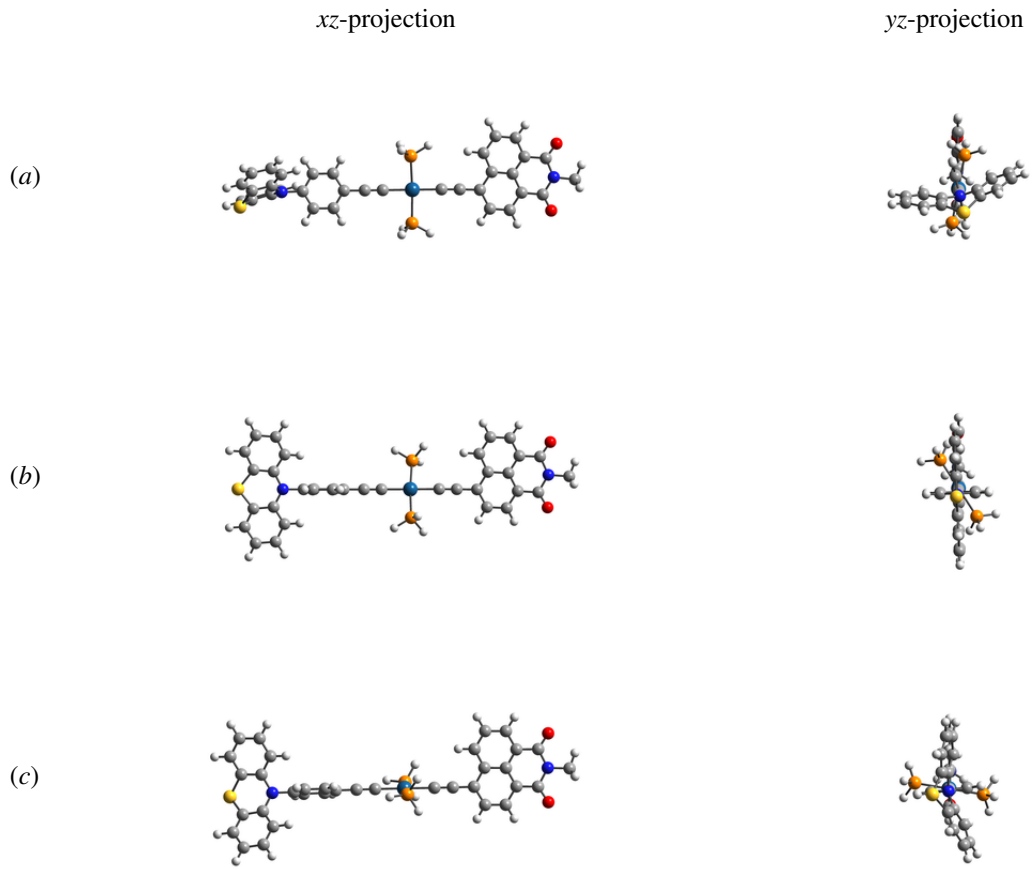

Figure 4.10: Optimised excited state geometries of **PTZ-Pt^{H}-NAP** of the (*a*) ^{3}NAPstate, (*b*) singlet CSS and (*c*) triplet CT state, all at the B3LYP/SDD+6-31G(d) level.

both the singlet and triplet manifolds. Selected optimised excited state geometries are shown in Figure 4.10. The lowest excited state on the triplet manifold, ^{3}NAP, is shown in Figure 4.10(*a*) and displays some geometrical reorganization when compared to the ground state geometry of **PTZ-Pt^{H}-NAP**. The Ph and NAP moieties have become almost coplanar, though most interesting is the fact that the phosphines have also become almost coplanar. It is very unlikely that the far more bulky P^{n}Bu$_3$ ligands found in the "unpruned" complexes would undergo such a rearrangement due to the massive steric repulsion that would be involved. This exposes one of the major limitations of model chemistry in which large amounts of complexity are removed; however, the previously mentioned limitations imposed by the nature of excited state frequency calculations leave few alternatives.

The geometry of the singlet CSS is shown in Figure 4.10(*b*). The CSS displays significant geometrical changes when compared to the ground state. The donor, which formally has lost an electron, has become completely planar as is clearly shown in the *yz* projection and is now

coplanar with the acceptor moiety, leaving the Ph orthogonal. This poses questions about what would happen were the model PH_3 ligands replaced with the correct P^nBu_3 ligands. For the donor and acceptor to be coplanar, the Ph must be orthogonal to the NAP. The bulky phosphines would then have to be either orthogonal to the NAP or to the Ph, but not both, or in some intermediate geometry. Since the Ph is less bulky than the NAP, it is likely that in the "unpruned" complexes, the P^nBu_3 ligands would remain orthogonal to the NAP and the Ph would rotate to become coplanar with the phosphine ligands. This unfavourable rearrangement, likely with a not insignificant associated barrier to rotation, may go some way to explaining the low yield of the CSS in experiments, even in the absence of the IR pump that closes this pathway (See page 7.) Attempts were made to optimise the triplet equivalent, which would be more representative of the likely experimentally observed species; however, these were unsuccessful.

The geometry of the triplet CT state is shown in Figure 4.10(*c*) and resembles that of the CSS in part. Unlike the CSS, the donor in the CT is not planar, though the Ph moiety has become orthogonal to the acceptor in the CT state as in the CSS. In the CT state, the phosphine ligands are now coplanar with the Ph moiety. It is unlikely that the rearrangement observed in the model **PTZ-Pt^H-NAP** is reflected in the behaviour of the real **PTZ-Pt-NAP**, since this represents a large geometric rearrangement between the ground and CT states, which is inconsistent with the rapid relaxation of the CT state in experiments. Other than this potentially artefactual donor side rearrangement, the CT state resembles the ground state quite strongly. This is reflected by the strong absorption shown in both the experimental and computed electronic spectra shown in Figure 4.7.

The calculated ground and excited state vibrational frequencies of **PTZ-Pt^H-NAP** are tabulated in Table 4.1 compared to experimental Time-Resolved Infra-Red (TRIR) experiments per-

State	Type	ν_a(C≡C) / cm^{-1}	ν_s(C≡C) / cm^{-1}
S_0	GS	2089	2104
S_1	CSS	2055	2095
S_2	CT	1951	2038
T_1	^{3}NAP	1936	2091
T_2	CSS	-	-
T_3	CT	1921	2040

Table 4.1: Calculated ground and excited state acetylide centred vibrational frequencies of **PTZ-Pt^H-NAP** at the B3LYP/SDD+6-31G(d) level. T_2 could not be optimised. Frequencies scaled by 0.955

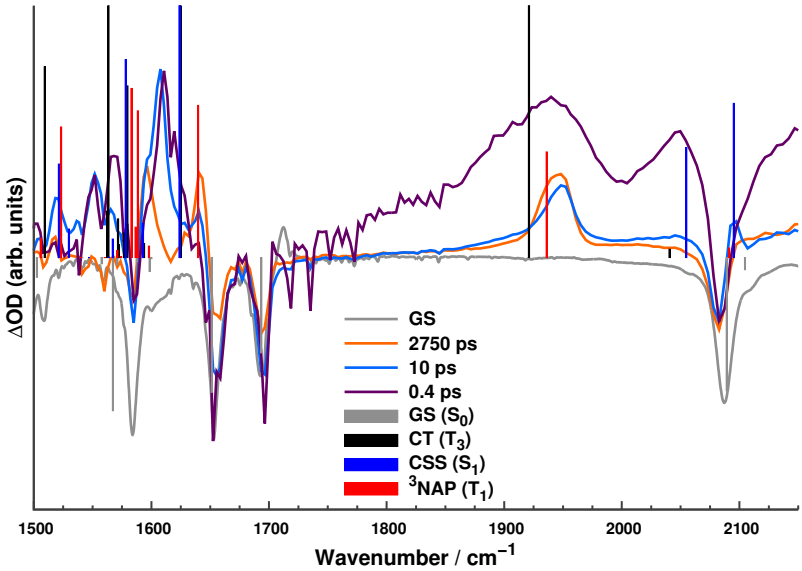

Figure 4.11: Comparison of calculated excited state frequencies and select TRIR traces of **PTZ-Pt-NAP**. The purple trace corresponds to 0.4 ps after electronic excitation and is representative of the CT state, the blue trace corresponds to 10 ps after electronic excitation and is representative of the CSS and ^{3}NAP states, and the orange trace corresponds to 2750 ps after electronic excitation and is representative of the ^{3}NAP state only. The black sticks correspond to the triplet CT state, the blue sticks correspond to the singlet CSS, and the red sticks correspond to the ^{3}NAP state, all at the B3LYP/SDD+6-31G(d) level.

formed on **PTZ-Pt-NAP** in Figure 4.11. The experimental data at three different time delays following electronic excitation are shown, which are representative of differing majority excited state population regimes, as well as the ground state IR spectrum, which is plotted for convenience. Concentrating on the acetylide region of the spectrum, the shortest time delay, at t =0.4 ps, is representative of the CT dominant regime and shows a very broad band from 1750 to 2000 cm^{-1}, peaking at 1940 cm^{-1} and another at 2050 cm^{-1}. There is also a broad baseline offset that extends beyond 2100 cm^{-1}. The broadness of these exceedingly short timescale peaks is potentially suggestive of transitions with significant vibronic character.[41,296–298] Excited state frequency calculations shown in Table 4.1 suggest that the low energy band corresponds to the asymmetric acetylide vibrational mode and the high energy band the symmetric vibrational mode.

The intermediate delay shown, at t =10 ps, is representative of a ^{3}NAP dominant regime, but with some CSS population. There is a peak at approximately 1950 cm^{-1}, perhaps a slight shoulder in the region of 2050 cm^{-1} and a peak at 2095 cm^{-1}. Since the CT state has a lifetime of only 2 ps, it is unlikely that it makes any significant contribution to these states. Comparing

the frequencies shown in Table 4.1 with these peaks, it is likely that the band at 1950 cm^{-1} corresponds to the ^{3}NAP state and the shoulder at 2050 cm^{-1} and peak at 2095 cm^{-1} correspond to the CSS.

The long timescale delay shown, which is at the limit of the experimental set-up, t =2750 ps, has only one band in the acetylide region, around 1950 cm^{-1}. The lack of a high energy band in the region may be explained by the closeness in energy of the calculated ground state ν_a(C≡C) and ^{3}NAP ν_s(C≡C) modes, shown in Table 4.1. Overall, the agreement between the excited state vibrational modes calculated and those recording in ultrafast TRIR experiments is good. This is despite the fact that the model used, **PTZ-Pt$^{\mathbf{H}}$-NAP**, is of significantly reduced complexity than the true compound, **PTZ-Pt-NAP**, and that a moderately small basis set was employed in these calculations. This lends confidence that computed ground and excited states are of a sufficient standard to build a qualitative model of the dynamics of the excited state.

4.2 Potential energy surfaces

Due to the good agreement of calculated ground and excited state properties with experiment, investigations were performed with the intention of elucidating the mechanism by which excitation of specific vibrational coordinates in the excited states of the compounds shown in Figure 4.1 effects the dynamics of the systems. It is prohibitively expensive to explore the entirety of the PESs for these systems. It is therefore necessary to choose specific regions of the PESs to investigate. Since the vibrational mode that causes the effect is the asymmetric acetylide vibrational mode, aspects of the ground and excited PESs were investigated.

There are two key questions that must be answered when constructing the coordinates along which the PESs are to be investigated:

1. Which geometry will be used to represent each state?

2. How will the asymmetric acetylide vibration be described in each state?

Firstly, due to the nature of the experiments performed, it is difficult to determine to what extent geometrical relaxation has occurred at a given point in time, not only of the excited molecules but also of the surrounding solvent. It is therefore very difficult to be confident of

the exactly correct geometry to use to represent each state and so some approximations must be made. As previously discussed, it is reasonable to assume that the CT state, which is the state targeted by the IR pump, is reasonably similar in geometry to the ground state. Thus it is reasonable to approximate the geometry of the CT state with the geometry of the ground state. For **PTZ-Pt^{H}-NAP**, the geometry of the CT state was successfully optimised. It is therefore be possible to follow the ν_a(C≡C) coordinate in the CT state of **PTZ-Pt^{H}-NAP**, a method that should be quite representative of the actual dynamics of **PTZ-Pt-NAP**; however, as will be shown below, there are some questions as to whether the **PTZ-Pt^{H}-NAP** is sufficient to properly describe the excited states.

The second question is more difficult to answer and is slightly dependent on the methodology adopted to answer the first. Since it was not possible to optimise all of states of **PTZ-Pt^{H}-NAP** at the B3LYP/SDD+6-31G(d) level, it is not possible to simply take the calculated equilibrium geometries of all of the states and scan along their associated vibrational coordinates. In any case, there is some question to the value in this approach, since the nature of nuclear changes induced by this vibrational mode in each state is partly dependent on the equilibrium nuclear geometry (selected displacements are tabulated in Appendix A.3.) As discussed above, there is some question as to the validity of the equilibrium geometries of the excited states of **PTZ-Pt^{H}-NAP** that have been calculated, due to the simplifications made to the phosphine ligands. As a result of this, a number of different coordinates were investigated and will be discussed below. The specifications for these coordinates are given in Chapter 3.

It should be noted at this point that the prior work performed on **PTZ-CH$_2$-Pt-NAP** in Ref. [51] used a "pruned" equivalent of **PTZ-CH$_2$-Pt-NAP**, the most important component of which was the substitution of the P^{n}Bu$_3$ ligands with PMe$_3$ ligands, and utilised a basis set consisting of SDD for Pt and 6-311G(d,p) for all other atoms, and investigated the "unrelaxed" coordinate. The successful application of this methodology should be kept in mind when discussing the results of the B3LYP/SDD+6-31G(d) calculations on **PTZ-Pt^{H}-NAP**, which will be discussed below.

Initial investigations utilising **PTZ-Pt^{H}-NAP** are presented in Figures 4.12, 4.13, 4.14, 4.15, and 4.16. All of these surfaces used the optimised ground state geometry as a starting point. The

"unrelaxed", "relaxed" and "frozen framework" surfaces, shown in Figures 4.12, 4.13 and 4.14 respectively, take the most simple approach to describing the vibrational mode, representing fully decoupled acetylide vibrations. The "unrelaxed" and "relaxed" surfaces are constructed by lengthening or shortening the acceptor side C≡C bond (NAP-CC) and moving the acceptor and donor moieties further apart or closer together; the "unrelaxed" coordinate has no further reorganization whilst for the "relaxed" coordinate, the NAP-CC is fixed and the remaining degrees of freedom are optimised for the ground state. The "frozen framework" surface on the other hand keeps the distance between donor and acceptor fixed, and changes the length of the NAP-CC. These three approaches represent marginally different interpretations of molecular vibration. Comparing the two most similar of these surfaces, "unrelaxed" of Figure 4.12 and the "relaxed" of Figure 4.13, there are very slight differences. Both show slight asymmetry, due to increased nuclear repulsion as the NAP-CC becomes short, but importantly show no crossover between CSS and CT states at any point investigated. The "frozen framework" surface of Figure 4.14 is broadly the same, though does show crossover between the triplet CSS and triplet CT states at the very extreme of Figure 4.14(ii). For a crossover point to be accessible by vibrational excitation, it should be close to the minimum point of the CT curve, both energetically and geometrically. The "unrelaxed", "relaxed" and "frozen framework" surfaces are therefore inconsistent with the hypothesis that it is presence of a crossover between CT and CSS surfaces that leads to the observed effect in these complexes.

As previously discussed, there is some question as to the way in which the vibrational coordinate is to be represented. With this in mind, the "unrelaxed antisymmetrical" and "relaxed antisymmetrical" surfaces were constructed, and are shown in Figures 4.15 and 4.16 respect-

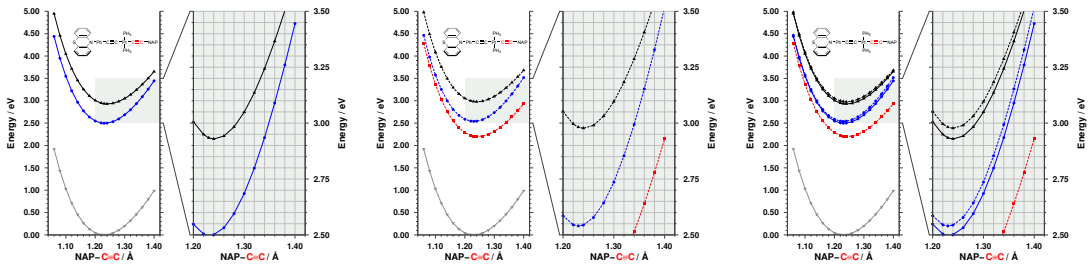

(i) Singlet manifold **(ii)** Triplet manifold **(iii)** Both manifolds

Figure 4.12: Calculated energies for the ground (▼), CT (▲), CSS (●) and ^{3}NAP (■) along the "unrelaxed" FC coordinate of **PTZ-Pt^H-NAP** at the B3LYP/SDD+6-31G(d) level.

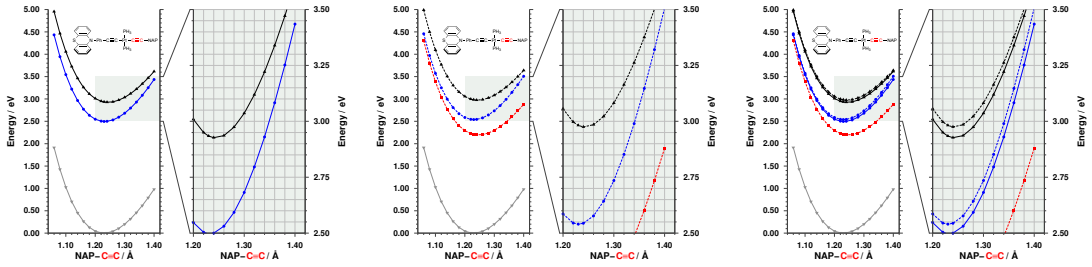

(i) Singlet manifold **(ii)** Triplet manifold **(iii)** Both manifolds

Figure 4.13: Calculated energies for the ground (▼), CT (▲), CSS (●) and ^{3}NAP (■) along the "relaxed" FC coordinate of **PTZ-Pt^{H}-NAP** at the B3LYP/SDD+6-31G(d) level.

ively. The "unrelaxed antisymmetrical" and "relaxed antisymmetrical" surfaces were constructed in a similar fashion to the "unrelaxed" and "relaxed" surfaces but the donor side C≡C (PTZ-CC) bond length was also manipulated in the opposite manner to the NAP-CC, i.e. the NAP-CC length was increased and the PTZ-CC reduced and vice versa. This description is closest to fully coupled acetylide vibrational modes.

As with the simpler coordinates, there is remarkably little difference between the "unrelaxed antisymmetrical" and "relaxed antisymmetrical" curves. The "antisymmetrical" curves are slightly more parabolic in nature and extend up to higher energies due to the more extreme nuclear distortion involved in these coordinates. It might be expected that the "antisymmetrical" curves would display crossover points at lower energies than the simpler coordinates due to the greater disruption of equilibrium geometry; however, this is not the case and neither of the two "antisymmetrical" coordinates show any crossover in energetically accessible regions of the potential energy surfaces.

The lack of a crossover in a vibrationally accessible region between the CSS and CT states along any of the coordinates representative of the ν_a(C≡C) suggests that there may be some

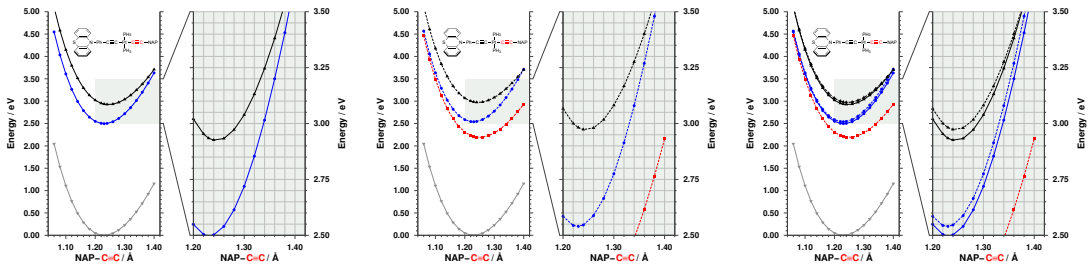

(i) Singlet manifold **(ii)** Triplet manifold **(iii)** Both manifolds

Figure 4.14: Calculated energies for the ground (▼), CT (▲), CSS (●) and ^{3}NAP (■) along the "frozen framework" FC coordinate of **PTZ-Pt^{H}-NAP** at the B3LYP/SDD+6-31G(d) level.

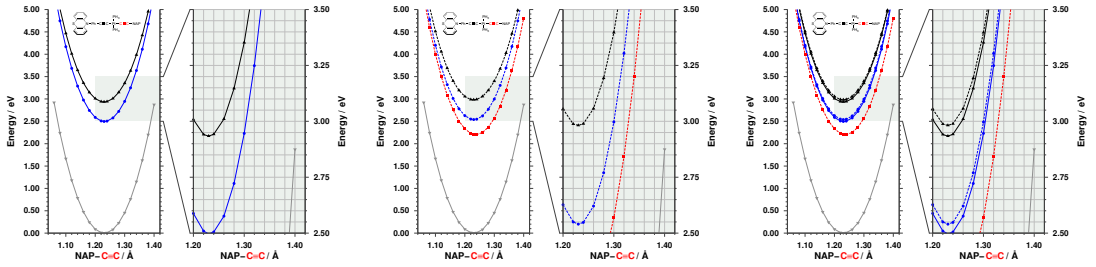

(i) Singlet manifold **(ii)** Triplet manifold **(iii)** Both manifolds

Figure 4.15: Calculated energies for the ground (▼), CT (▲), CSS (●) and ^{3}NAP (■) along the "unrelaxed antisymmetrical" FC coordinate of **PTZ-Pt^H-NAP** at the B3LYP/SDD+6-31G(d) level.

insufficiencies in the model employed in the **PTZ-Pt^H-NAP** calculations. There are a number of potential explanations for this. Despite the good agreement of the ground state vibrational, TRIR and ground state electronic spectra with the B3LYP/SDD+6-31G(d) computed properties of **PTZ-Pt^H-NAP**, this level of theory may simply be inadequate for describing the excited states. In particular, any deficiency of this method in describing the CSS would be hard to detect from electronic spectra, since the transition from the ground state to the CSS is forbidden due to exceedingly poor overlap. It may also be the case that the "pruning" utilised in the choice of the model **PTZ-Pt^H-NAP** complex was too severe, particularly in the use of the PH_3 ligands to represent the phosphines. It may also be the case that the representations of the vibrational coordinates chosen were not adequate. This, however, seems less likely given the success of the original investigations on **PTZ-CH$_2$-Pt-NAP** when using the simple "unrelaxed" coordinate.[51]

To overcome the deficiencies displayed by the **PTZ-Pt^H-NAP** model, it was deemed that more robust theoretical methods were needed. As such, each of the full size complexes **PTZ-CH$_2$-Pt-NAP**, **PTZ-Pt-NAP** and **OMePTZ-Pt-NAP** were modelled using a higher qual-

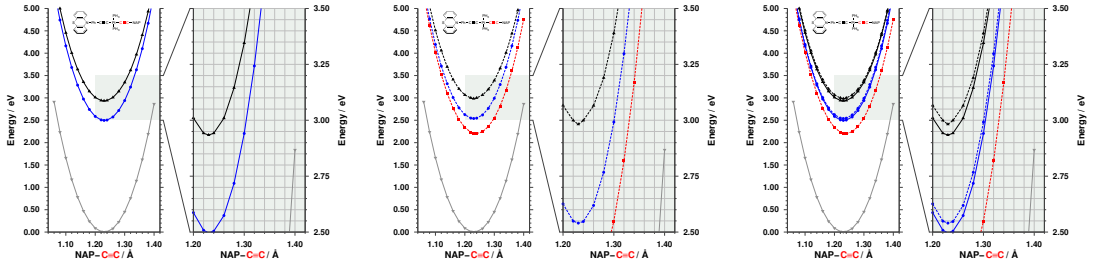

(i) Singlet manifold **(ii)** Triplet manifold **(iii)** Both manifolds

Figure 4.16: Calculated energies for the ground (▼), CT (▲), CSS (●) and ^{3}NAP (■) along the "relaxed antisymmetrical" FC coordinate of **PTZ-Pt^H-NAP** at the B3LYP/SDD+6-31G(d) level.

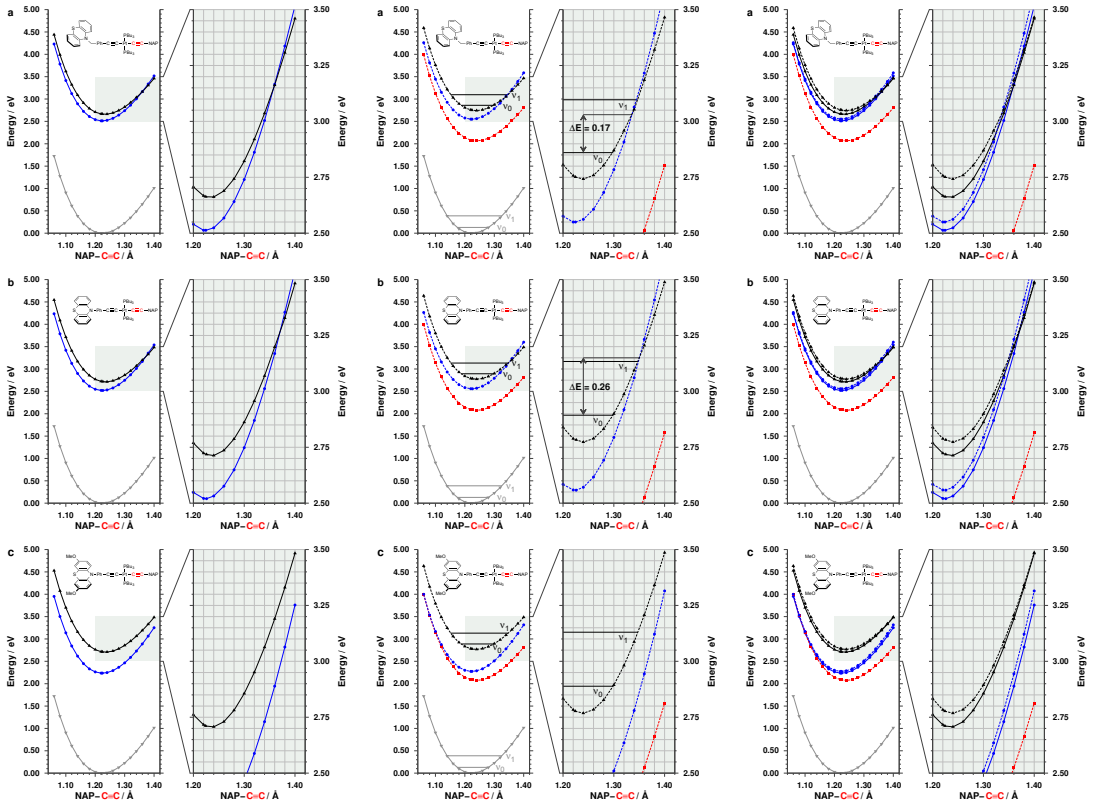

(i) Singlet manifold **(ii)** Triplet manifold **(iii)** Both manifolds

Figure 4.17: Calculated energies for the ground (▼), CT (▲), CSS (●) and ^{3}NAP (■) along the "unrelaxed" FC coordinate of a) **PTZ-CH$_2$-Pt-NAP** b) **PTZ-Pt-NAP** and c) **OMePTZ-Pt-NAP** at the B3LYP/cc-pVTZ level. The experimentally determined first and second vibrational energy levels of ν_a(C≡C) are shown for the ground and CT states, and the energy gap from ν_0 to the intersection between the CT and CSS are shown, where appropriate, in (ii).

ity basis set. For these calculations, presented in Figures 4.17 and 4.18, utilised the "unrelaxed" coordinate, previously described, as well as a "vibrational" coordinate, that was constructed by following the ground state ν_a(C≡C) vibrational mode. This provided an intermediate between the completely decoupled "unrelaxed" representation and the completely coupled "antisymmetric" representation previously utilised. The "unrelaxed" surfaces, shown in Figure 4.17 are in good agreement with the hypothesis that a low lying crossover between the CSS and CT is critical to the behaviour observed in these compounds. As is clearly shown in Figure 4.17(ii), **PTZ-CH$_2$-Pt-NAP** and **PTZ-Pt-NAP** both have a crossover between the triplet CSS and triplet CT states quite close to the minimum energy point on the triplet CT surface, whilst **OMePTZ-Pt-NAP** shows no such crossing in the region investigated. The vibrational levels of the ν_a(C≡C) for the ground and CT states are plotted using the experimentally determined

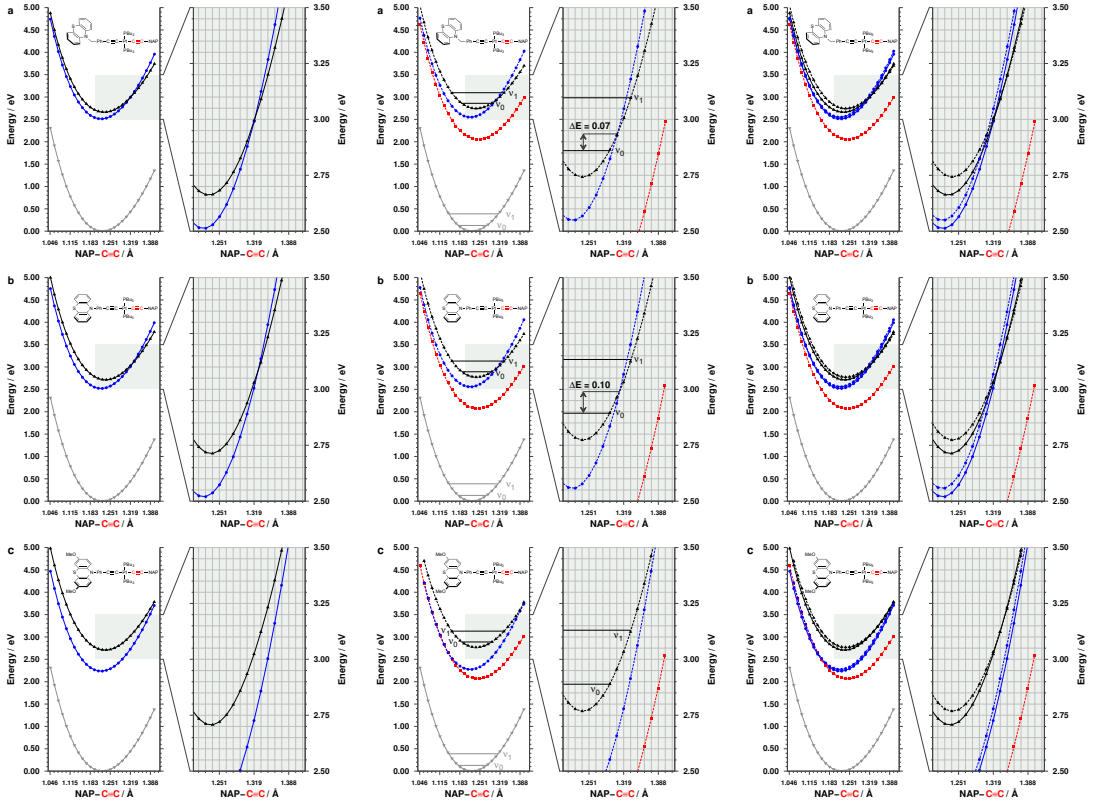

(i) Singlet manifold **(ii)** Triplet manifold **(iii)** Both manifolds

Figure 4.18: Calculated energies for the ground (▼), CT (▲), CSS (●) and ^{3}NAP (■) along the "vibrational" FC coordinate of a) **PTZ-CH$_2$-Pt-NAP** b) **PTZ-Pt-NAP** and c) **OMePTZ-Pt-NAP** at the B3LYP/cc-pVTZ level. The experimentally determined first and second vibrational energy levels of ν_a(C≡C) are shown for the ground and CT states, and the energy gap from ν_0 to the intersection between the CT and CSS are shown, where appropriate, in (ii).

vibrational frequencies to provide a comparator to the height of the barrier to the crossover point relative to the zero-point energy in these coordinates and the vibrational excitation energy. This provides exceedingly good agreement with experiment: **PTZ-CH$_2$-Pt-NAP** has the lower calculated barrier, significantly below the ν_1 level and experimentally shows that each photon absorbed by the CT state results in the formation of a CSS;[51] **PTZ-Pt-NAP** has a slightly higher calculated barrier height, marginally above the ν_1 level and experimentally shows a much reduced effect; and **OMePTZ-Pt-NAP** has no crossover point and experimentally shows no effect. The remarkable agreement between the calculated barrier heights relative to vibrational energies and observed effect is likely at least in part fortuitous, as there are some deficiencies with the methods employed in these calculations to represent the vibrational coordinate.

The surfaces shown in Figure 4.18 used the "vibrational" coordinate, constructed by follow-

ing the ground state ν_a(C≡C) vibrational mode. As with the "unrelaxed" surfaces, there are crossovers between the triplet CT and triplet CSS surfaces of **PTZ-CH_2-Pt-NAP** and **PTZ-Pt-NAP**, shown in Figure 4.18(ii), but not **OMePTZ-Pt-NAP**, consistent with the hypothesis proposed above. The "vibrational" surface crossovers are lower in energy than those of the "unrelaxed" surfaces, indeed, far lower than the experimentally determined vibrational energy levels, which are displayed. Drawing conclusions in a similar manner to the "unrelaxed" surfaces would lead to the erroneous prediction that both **PTZ-CH_2-Pt-NAP** and **PTZ-Pt-NAP** would show the same degree of effect, were the "vibrational" surfaces used. A possible explanation for this is that the ν_a(C≡C) vibrational mode of the ground state is a poor representation of equivalent modes in the excited states, as suggested by the excited state frequency calculations presented in Section 4.1.

In conclusion, the "unrelaxed" and "vibrational" potential energy curves shown in Figures 4.17 and 4.18 are in reasonable agreement with the experimentally observed ultrafast dynamics of **PTZ-CH_2-Pt-NAP**, **PTZ-Pt-NAP** and **OMePTZ-Pt-NAP**. These calculations suggest that the presence of a crossover between the CSS and CT states in the vicinity of the minimum energy point for the CT state is required for the effect to be observed. Calculations of this type could therefore serve as a predictive diagnostic to guide future experimental investigations toward potentially interesting target compounds. However, these calculations shed no further light on the mechanism behind the rapid population change from CT to ^{3}NAP when vibrational excitation occurs in the excited state. This rate acceleration effect is especially puzzling for the case of **OMePTZ-Pt-NAP**, for which these calculations predict there should be no effect whatsoever. To answer the remaining questions, future investigations should include a more expansive exploration of the excited state PESs of these complexes. Furthermore, non-adiabatic effects in these complexes are neglected in the methods employed to conduct the above investigations. It would therefore be potentially fruitful to include non-adiabatic effects in future investigations, particularly with regards to the rate acceleration effect discussed above. Lastly, the combination of high quality PESs with non-adiabatic couplings would provide fertile ground for quantum dynamics investigations, which could be used to establish a more quantitative description of the ultrafast dynamics of this family of compounds.

Chapter 5

Electron transfer in Pt *cis*-acetylides

The existing examples of controllable electron transfer on the molecular scale have all been based on quasi-linear systems. The early theoretical work of Skourtis, Beratan and co-workers,[33,34,37] which established that manipulating electron transfer through vibrational excitation was indeed possible, focused on linear Donor-Acceptor (D-A) arrangements in which two parallel pathways could be taken from donor to acceptor. The realisation of these ideas came in the form of Donor-Bridge-Acceptor (D-B-A) systems that, whilst not necessarily maintaining a spatially linear arrangement, had only one of each component.[36,51,53,299] A logical extension of this work is to increase the number of components in the system, increasing either the number of acceptors or donors. This would provide the possibility of introducing directionality into the manipulation of electron transfer. Both of these scenarios have been suggested and explored theoretically by Skourtis, Beratan and co-workers.[38,39] The approach taken in this chapter, in which a D-B-A-B-D architecture is constructed based on the building blocks of a D-B-A system, is illustrated in Figure 5.1.

5.1 Designing directionality

Within the scope of platinum chemistry, the implementation of the proposed D-B-A-B-D architecture could take a number of forms. One way to achieve this would be to retain the *trans*-acetylide geometry employed in Chapter 4, using two donor 'arms' on either side a the platinum centre, with a cyclic acceptor ligand attached to the platinum, yielding a linear, rotaxane-like

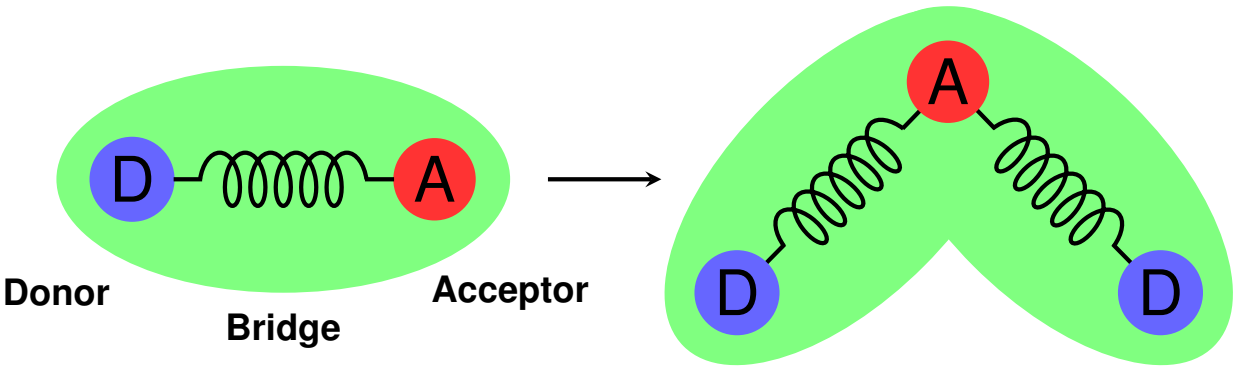

Figure 5.1: Creating directionally controllable electron transfer using linear systems as a template.

geometry. This would be challenging, however, since it would necessitate the use of Pt(IV) in place of Pt(II) and likely result in a large change in the photochemistry of the system,[300] and it is desirable to change as little as possible whilst increasing complexity.

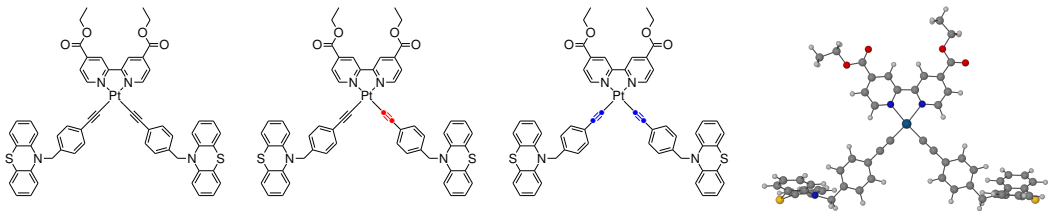

12-12 **13-12** **13-13**

Figure 5.2: Chemical structures of the three isotopologues of [Pt(bipyCOOEt)(C≡C-Ph-CH_2-PTZ)$_2$]: **12-12**, **13-12** and **13-13**. ^{13}C is represented by •. The B3LYP/SDD[Pt]6-311G(d,p)[H,C,N,O,S]/IEFPCM(CH_2Cl_2) optimised geometry is shown on the right-hand side.

Alternatively, a non-linear D-B-A-B-D architecture could be realised with a Pt(II) *cis*-acetylide complex. This would allow the D-B fragments previously investigated to be utilised to construct a new D-B-A-B-D pentad. Given that experimentally the vibrational control experiments are monitored by infra-red absorption spectroscopy, a candidate complex must also contain 'IR reporter' groups, such as carbonyls or nitriles. Fortunately, the synthesis of just such a complex, [Pt(bipyCOOEt)(C≡C-Ph-CH_2-PTZ)$_2$] (**12-12**), was reported by McGarrah and Eisenberg in 2003.[301] The chemical structure is illustrated in Figure 5.2. The electron transfer properties of this complex are well documented: a number of Metal to Ligand Charge Transfer (MLCT) and Charge Separated States (CSSs) may be observed following the absorp-

tion of a photon of visible light.[301,302] The presence of two, spatially separated phenothiazine donors means that any CSSs come in degenerate pairs, formally localized either on the 'left-' or 'right-' side of the molecule. The electronic structure of the complex will be discussed in detail in Section 5.3.

For the purposes of directional control over electron transfer, however, there is one major issue with **12-12**: the presence of two planes of symmetry. This means that the two acetylide vibrations cannot be distinguished spectroscopically in a conventional, solution-phase experiment. Gas phase molecular beam experiments could potentially provide access to directionally aligned molecules;[303,304] however, it is likely population transfer would still occur between the two degenerate acetylide vibrational modes.[305] It is also of note that **12-12** is not stable in the gas phase. There is therefore no way of specifically exciting one of the two acetylides in **12-12**. However, the spectroscopic equivalence between the two vibrational modes could be lifted by selective isotopic labelling of one acetylide, as illustrated in Figure 5.2. Within the Born-Oppenheimer approximation, the electronic structure of the system will be unaffected by isotopic substitution; however, the addition of two atomic mass units to one of the acetylides should result in two spectroscopically distinct acetylide vibrational modes, separated by $\sim$80 cm^{-1} due to the change in reduced mass. This would lead to a scenario analogous to that described in Ref. [37], which explores the effect of coupling of only one of two pathways from donor to acceptor with vibrational excitation on the rate of electron transfer. It was shown in that reference that vibrational excitation could have either a strong, positive or weak, negative effect on the rate of electron transfer.

It should be noted that asymmetric isotopic labelling of Pt(II) diimine *cis*-acetylides presents a significant synthetic challenge, since there is no known synthetic procedure that results in the mono-ligation of Pt(II) diimine dichloride, the most commonly used starting material for this family of compounds, by an acetylide.[306,307] A statistical mixture of the unlabelled form of [Pt(bipyCOOEt)(C≡C-Ph-CH_2-PTZ)$_2$], **12-12**, the partially isotopically labelled isotopomer, **13-12** and the doubly labelled isotopomer, **13-13**, could be achieved by mixing labelled and unlabelled forms of the acetylide ligand and performing the transmetallation reaction. The isotopomers are illustrated in Figure 5.2 It would, however, be quite time consuming to separate

the isotopomers on the basis of mass, since **12-12** has a molecular weight of ~1120 atomic mass units and thus the incremental difference in mass between isotopomers is on the order of 0.2%. Chemical separation is impossible since **12-12** and **13-12** have identical reactivity.

An alternate route to **13-12** is *via* a *bis*-acetylide intermediate, in which one C≡C-Ph-CH_2-PTZ 'arm' is installed alongside an isotopically labelled $^{13}C\equiv{}^{13}C$-TMS. The remaining Ph-CH_2-PTZ can then be attached to the isotopically labelled acetylide by Sonogashira coupling. This technique was used by S. Archer in the synthesis of **13-12** and is described in detail in Ref. [54]. One advantage of this method is that it reduces the possibility of cross-contamination of **12-12**, **13-12** and **13-13**, since all of the products formed in the reaction can be separated before the final Ph-CH_2-PTZ is attached.

5.2 Vibrational structure of [Pt(bipyCOOEt)(C≡C-Ph-CH_2-PTZ)$_2$]

Since the purpose of **13-12** is to be used in vibrational control experiments, it is vital that the vibrational structure is well understood. As the only difference between **12-12** and **13-12** is the addition of two neutrons, one would expect little difference in their IR absorption spectra. This, however, is not the case. Figure 5.3 depicts the 1450 cm^{-1} to 2200 cm^{-1} portion of the ground state FTIR spectra of the three isotopomers, **12-12**, **13-12** and **13-13**, in CH_2Cl_2. As expected, outside of the acetylide region (~2000 cm^{-1} to ~2200 cm^{-1}) there is very little difference between the isotopomers. **13-12** and **13-13** both display a small shoulder on the carbonyl peak at ~1710 cm^{-1} that is slightly more intense for **13-13**. In the region of 1600 cm^{-1}, **13-13** displays slightly increased absorption when compared to the other two isotopologues investigated.

The most marked differences are observed in the acetylide region. The most significant features from this region are enumerated in Table 5.1. As expected, the unlabelled **12-12** has two peaks in the acetylide region, at 2127 cm^{-1} and 2117 cm^{-1}, corresponding to the symmetric and asymmetric acetylide combination modes, respectively. One would therefore expect the partially labelled isotopomer, **13-12**, to have one peak with energy approximately midway between these two peaks at 2122 cm^{-1}, corresponding to the $\nu(^{12}C\equiv{}^{12}C)$ stretch and another ap-

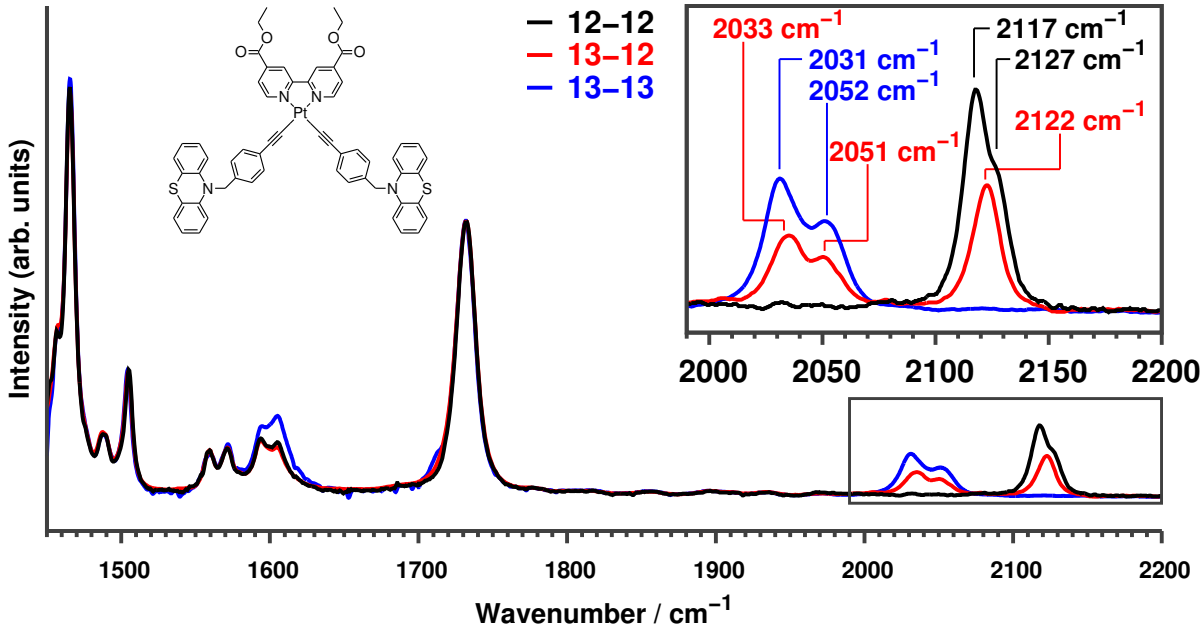

Figure 5.3: Experimental ground state FTIR spectra of the three isotopologues of [Pt(bipyCOOEt)(C≡C-Ph-CH_2-PTZ)$_2$]. The unlabelled isotopomer, **12-12**, is depicted in black. The partially labelled isotopomer, **13-12**, is depicted in red. The doubly labelled isotopomer, **13-13**, is depicted in blue. The 1450 cm^{-1} to 1800 cm^{-1} region is almost identical for all three isotopologues. The 2000 cm^{-1} to 2150 cm^{-1} region is magnified in the inset.[54]

proximately 80 cm^{-1} below this at approximately 2142 cm^{-1}, corresponding to the $\nu(^{13}C\equiv^{13}C)$ stretch. Finally, the doubly isotopically labelled species, **13-13**, would be expected to have two peaks at approximately 2047 cm^{-1} and 2037 cm^{-1}. Indeed, vibrational frequencies of these isotopomers within the harmonic approximation in the conformation shown in Figure 5.2, calculated using B3LYP/SDD[Pt]6-311G(d,p)[H,C,N,O,S]/IEFPCM(CH_2Cl_2) and scaled with an appropriate scaling factor[54,271,272,308,309] yield frequencies in very good agreement with these predictions.

Unfortunately, the experimentally observed vibrational frequencies do not agree well with these predictions. Instead of the expected two band structure, **13-12** displays three peaks, at 2122 cm^{-1}, 2051 cm^{-1} and 2033 cm^{-1}. **13-13** displays two peaks, as expected, at 2052 cm^{-1} and 2031 cm^{-1}. These peaks are, however, unexpectedly broad and not in the expected position. Deconvolution suggests up to four peaks contribute to the two bands of **13-13**.[54] The possibility that the additional peaks are due to interactions with the solvent can be ruled out, since spectra recorded in toluene and in the solid state using Attenuated Total Reflectance (ATR) retain

the unexpected peaks.[54] Furthermore, Two-Dimensional IR (2DIR) experiments performed on **13-12** show that the lifetime of the high and low energy vibrations are significantly different: the band at 2122 cm^{-1} has a lifetime of 5.6 ± 0.4 ps whereas the band at 2051 cm^{-1} has a lifetime of 2.5 ± 0.2 ps.[55]

To investigate the origin of the unexpected bands in the vibrational spectrum of **13-12**, it was determined that anharmonic corrections should be included in the calculations. There are a number of ways that anharmonicity can be accounted for, in analogy to the hierarchy of approaches to include electron correlation.[310] Unfortunately, as with correlated electronic structure methods, methods for including anharmonicity scale poorly with system size. For a large system such as [Pt(bipyCOOEt)(C≡C-Ph-CH_2-PTZ)$_2$], containing 562 electrons and consisting of 113 atoms and therefore 333 vibrational degrees of freedom, only anharmonic corrections of modest computational cost are tractable. Fortunately, Generalized Vibrational Perturbation Theory to second order (GVPT2)[311–316] has been shown to perform exceedingly well in the description of transition metal complexes such as those at hand.[130,317,318] In particular, the combination of a hybrid functional, such as B3LYP, with GVPT2 has been shown to perform well in the description of ligand-centred vibrations in organometallic transition metal complexes.[130] Furthermore, unlike conventional VPT2, GVPT2 is capable of correctly describing resonances by de-perturbation followed by reduced dimensionality variational treatment of the resonant

Substituent	Isotopes of acetylides	Experiment / cm^{-1}	Harmonic frequency[(a)] / cm^{-1}	Anharmonic frequency[(b)] / cm^{-1}
p-CH_2-PTZ	^{12}C both sides	2127, 2117	2130, 2117	2129, 2124
	^{13}C and ^{12}C	2122, 2051, 2033	2125, 2041	2123, 2048, 2035
	^{13}C both sides	2052, 2031	2048, 2036	2045, 2043
p-CH_3[(c)]	^{13}C and ^{12}C	2121, 2050, 2030, 2027	2123, 2040	2121, 2044, 2029, 2028, 2009, 2005

Table 5.1: Comparison between experimental FTIR and calculated vibrational frequencies in the acetylide region for various isotopomers of [Pt(bipyCOOEt)(C≡C-Ph-R)$_2$] (R = *p*-CH_2-PTZ, *p*-CH_3) in CH_2Cl_2. Calculations performed using B3LYP/SDD[Pt]6-311G(d,p)[H,C,N,O,S]/IEFPCM(CH_2Cl_2). (a) Harmonic frequencies are empirically scaled by ×0.966, in accordance with previous work.[271,272,308,309] (b) Anharmonic corrections included using Generalized Vibrational Perturbation Theory to 2nd order (GVPT2) in which normal modes below 100 cm^{-1} were excluded from the perturbative treatment, frequencies are empirically shifted by −46 cm^{-1} and −40 cm^{-1} when R = *p*-CH_2-PTZ and *p*-CH_3, respectively. (c) Calculations with R = *p*-CH_3 employed a truncated geometry, in which the esters are removed from the bipy-type ligand.

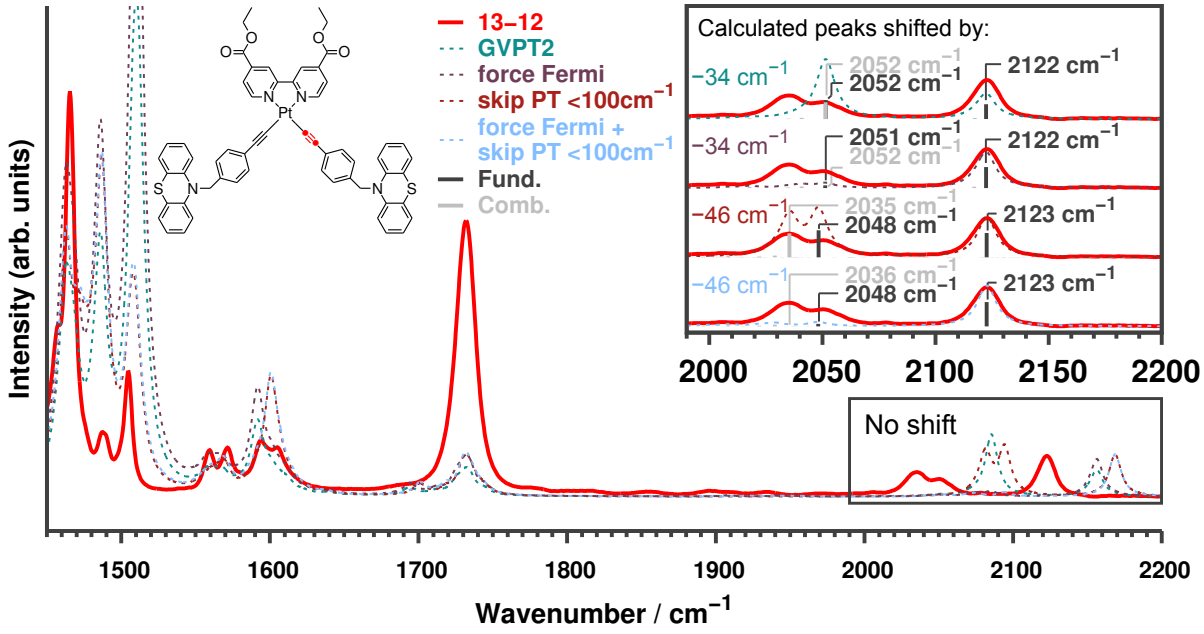

Figure 5.4: Comparison of experimental ground state FTIR spectra of **13-12** (thick, red line) to calculated vibrational spectra with anharmonic corrections. Calculations were performed using B3LYP/SDD[Pt]6-311G(d,p)[H,C,N,O,S]/IEFPCM(CH_2Cl_2), with anharmonic corrections included using Generalized Vibrational Perturbation Theory to 2nd order (GVPT2) and calculated spectra, convoluted with Lorentzian functions with FWHM = 10 cm^{-1}, are shown as dashed lines. The anharmonic corrections were included in 4 ways: GVPT2 was applied to all normal modes of the systems with no further corrections ("GVPT2", turquoise), GVPT2 was applied to all normal modes and a Fermi resonance was specifically included between $^{13}\nu_{288}$ and $^{13}\nu_{234} + {}^{13}\nu_{130}$ ("force Fermi", purple), normal modes below 100 cm^{-1} were excluded from the perturbative treatment ("skip PT", scarlet), and normal modes below 100 cm^{-1} were excluded from the perturbative treatment and a Fermi resonance was specifically included between $^{13}\nu_{288}$ and $^{13}\nu_{234} + {}^{13}\nu_{130}$ ("force Fermi + skip PT", blue). The 2000 cm^{-1} to 2150 cm^{-1} region is magnified in the inset. Within the inset all calculated peaks are empirically shifted by as indicated to guide the eye. The contributions from fundamental and combination bands are shown as darker and lighter sticks, respectively, in the inset.

modes.[314,319,320] This is of particular concern in the cases of **13-12** and **13-13**, since isotopic substitution has been known to result in accidental first-order "Fermi" resonances[321] and higher-order "Darling-Dennison" resonances.[322,323] These can have large effects on fundamental modes and vibrational dynamics.[324,325]

Therefore, vibrational frequency calculations of [Pt(bipyCOOEt)(C≡C-Ph-CH_2-PTZ)$_2$] were performed using the B3LYP functional[124,125] and a moderately large basis set consisting of SDD for platinum[258] and 6-311G(d,p) for all other atoms[265,266] in CH_2Cl_2 solvent as described by the Integral Equation Formalism of the Polarizable Continuum Model (IEFPCM),[256,257]

and including anharmonic corrections using GVPT2[311–316] as implemented in Gaussian 09, revision D.01.[255] The calculation yielded 333 anharmonically corrected fundamental modes, 333 overtone modes and $\frac{333\times332}{2}$ = 55278 combination modes. It is therefore impractical to tabulate all calculated modes in this work. Instead, the calculated frequencies of select modes are provided in Table 5.1. The experimental spectrum of **13-12** is compared to calculated vibrational spectra that have been anharmonically corrected in a number of ways in Figure 5.4. Initial calculations were performed in which all 333 normal modes of the molecule were included in the perturbative treatment, shown in turquoise. Comparing the raw calculated spectrum with experiment, there is reasonable agreement in the 1450 cm^{-1} to 1800 cm^{-1} region, although calculated intensities are slightly over-estimated at ~1500 cm^{-1} and significantly underestimated at ~1730 cm^{-1}, the carbonyl region. One possible explanation for the discrepancy in calculated intensity in the carbonyl region is that anharmonic corrections were calculated for only one conformer of the molecule, illustrated in Figure 5.2, due to the computational cost. Other conformers, related by rotation of the ester groups, could have higher transition dipole moments associated with their carbonyl stretches and thus more intense peaks in this region. It should be noted that this conformer was specifically chosen to reduce the pseudo-symmetry of the molecule and therefore simplify excited state assignment (See Section 5.3).

For the majority of the spectrum it is unnecessary to include any empirical adjustment to the calculated spectrum for good agreement with experimental measurements to be obtained; however, in the acetylide region there remains a deviation between calculations and observations, both in peak position and peak shape. When all 333 normal modes are included in the perturbative treatment there appear to be only two peaks in the acetylide region, blue shifted from the experimentally observed peaks. Examining the region in detail, it is observed that a combination band appears in the calculations to be almost iso-energetic with the $\nu(^{13}C\equiv^{13}C)$ stretch, mode $^{13}\nu_{288}$. The combination band consists of two fundamental bands, $^{13}\nu_{234}$ and $^{13}\nu_{130}$. Displacement vectors for the normal modes are presented in Figures 5.5 and 5.6. Since one of the conditions of a Fermi resonance is that the one and two quanta modes must be almost energetically degenerate, it would be expected that the fundamental ν_{288} should be resonant with the combination $\nu_{234} + \nu_{130}$; however, GVPT2 does not predict that the two modes are reson-

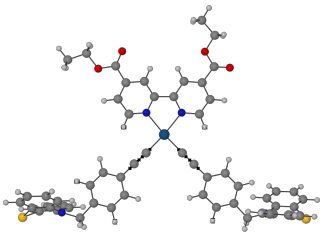

(i) 12-12 $^{12}\nu_{289}$: the symmetric acetylide combination.
$\nu_{\text{Anh.}} = 2175\,\text{cm}^{-1}$

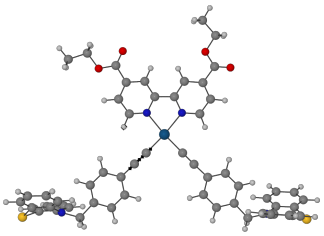

(ii) 13-12 $^{13}\nu_{289}$: $^{12}\text{C}\equiv^{12}\text{C}$ stretch.
$\nu_{\text{Anh.}} = 2169\,\text{cm}^{-1}$

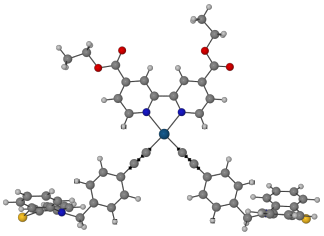

(iii) 12-12 $^{12}\nu_{288}$: the asymmetric acetylide combination.
$\nu_{\text{Anh.}} = 2170\,\text{cm}^{-1}$

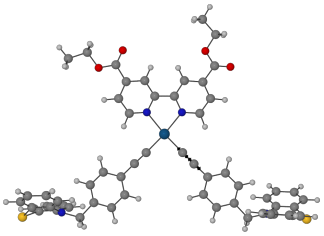

(iv) 13-12 $^{13}\nu_{288}$: $^{13}\text{C}\equiv^{13}\text{C}$ stretch.
$\nu_{\text{Anh.}} = 2094\,\text{cm}^{-1}$

Figure 5.5: Displacement vectors of acetylide-centred vibrational modes of two isotopomers of [Pt(bipyCOOEt)(C≡C-Ph-CH_2-PTZ)$_2$], **12-12** and **13-12**. Calculated anharmonically corrected vibrational energies are displayed below each vibrational mode. Calculations were performed using B3LYP/SDD[Pt]6-311G(d,p)[H,C,N,O,S]/IEFPCM(CH_2Cl_2), with anharmonic corrections included using Generalized Vibrational Perturbation Theory to 2$^{\text{nd}}$ order (GVPT2) in which normal modes below 100 cm^{-1} were excluded from the perturbative treatment.[54]

ant. Indeed, if the calculation is specifically instructed to treat $^{13}\nu_{288}$ and $^{13}\nu_{234} + ^{13}\nu_{130}$ to be resonant, "force Fermi" in Figure 5.4, further discrepancies arise in the calculated spectrum. The intensities of the now resonant modes drop to near 0, though peak positions are almost unaffected. Curiously, there are also marked changes in absorption intensity in the 1450 cm^{-1} to 1800 cm^{-1} region, despite the fact that these modes should ostensibly be unaffected by the additional resonance.

Careful inspection of the GVPT2 and force Fermi calculations reveal one possible source of the inconsistent behaviour: low energy vibrational modes vary in energy and intensity wildly following the perturbative treatment. Since the potential energy surface is shallow in the regions that these modes span, numerical errors in the 3$^{\text{rd}}$ and 4$^{\text{th}}$ order derivatives, combined with potentially significant rotational character may lead to breakdown of the perturbative treatment.[326] Accordingly, it is advisable to exclude the high-order couplings from these modes from the

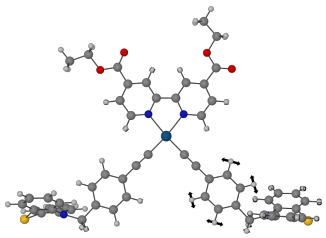

(i) 12-12 $^{12}\nu_{234}$: right-hand side wave.
$\nu_{\text{Anh.}} = 1304\,\text{cm}^{-1}$

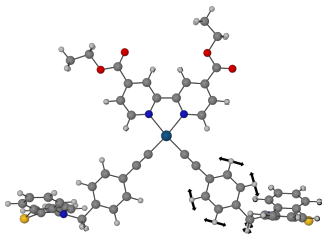

(ii) 13-12 $^{13}\nu_{234}$: ^{13}C side wave.
$\nu_{\text{Anh.}} = 1304\,\text{cm}^{-1}$

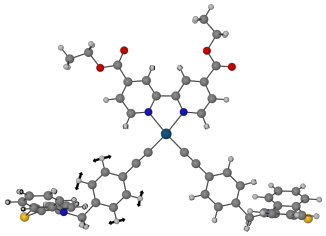

(iii) 12-12 $^{12}\nu_{233}$: left-hand side wave.
$\nu_{\text{Anh.}} = 1309\,\text{cm}^{-1}$

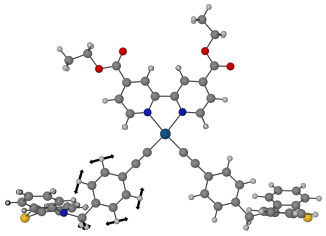

(iv) 13-12 $^{13}\nu_{233}$: ^{12}C side wave.
$\nu_{\text{Anh.}} = 1308\,\text{cm}^{-1}$

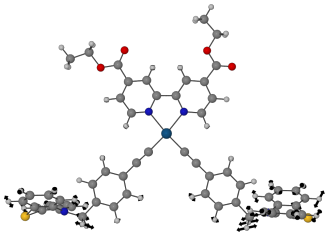

(v) 12-12 $^{12}\nu_{131}$: the symmetric breathing combination.
$\nu_{\text{Anh.}} = 781\,\text{cm}^{-1}$

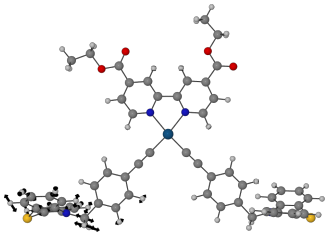

(vi) 13-12 $^{13}\nu_{131}$: ^{12}C side breathing mode.
$\nu_{\text{Anh.}} = 781\,\text{cm}^{-1}$

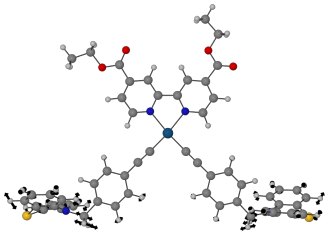

(vii) 12-12 $^{12}\nu_{130}$: the asymmetric breathing combination.
$\nu_{\text{Anh.}} = 779\,\text{cm}^{-1}$

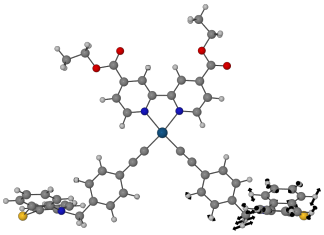

(viii) 13-12 $^{13}\nu_{130}$: ^{13}C side breathing mode.
$\nu_{\text{Anh.}} = 778\,\text{cm}^{-1}$

Figure 5.6: Displacement vectors of the component fundamental modes of significant combination modes of two isotopomers of [Pt(bipyCOOEt)(C≡C-Ph-CH_2-PTZ)$_2$], **12-12** and **13-12**. Calculated anharmonically corrected vibrational energies are displayed below each vibrational mode. Calculations were performed using B3LYP/SDD[Pt]6-311G(d,p)[H,C,N,O,S]/IEFPCM(CH_2Cl_2), with anharmonic corrections included using Generalized Vibrational Perturbation Theory to 2$^{\text{nd}}$ order (GVPT2) in which normal modes below 100 cm^{-1} were excluded from the perturbative treatment. Note that modes are numbered with descending harmonic vibrational energy.[54]

perturbation.[327] As a result of this, the calculations were repeated such that all normal modes with harmonic frequencies <100 cm^{-1} (a total of 27 modes in the case of **13-12**) were excluded from the perturbative treatment. The resultant spectrum is denoted "skip PT" in Figure 5.4. Exclusion of the low energy modes results in significant changes in the spectrum overall. In the 1450 cm^{-1} to 1600 cm^{-1} region absorption intensity as calculated by "skip PT" decreases compared to "GVPT2". The majority of peaks in this region move little, apart from the peak at ~1590 cm^{-1} which undergoes a blue-shift of approximately 10 cm^{-1} under the "skip PT" approach. It is in the acetylide region, however, that the largest differences between "skip PT" and "GVPT2" are observed in Fig. 5.4. The acetylide centred fundamental bands are also blue-shifted by an average of approximately 10 cm^{-1} in "skip PT" compared to "GVPT2". The previously near-degenerate combination mode, $^{13}\nu_{234} + ^{13}\nu_{130}$, is red-shifted by approximately 5 cm^{-1}. The combination of these shifts results in a three-band pattern in the acetylide region, similar to that observed experimentally. However, the calculated vibrational energies are blue-shifted compared to experiments. If a constant red-shift of $-46\,cm^{-1}$ is applied to the acetylide region, excellent agreement between the calculated and experimental spectra can be achieved. When scaling harmonic vibrational frequencies obtained *via* B3LYP, it is observed that a different scaling factor is required to correct the acetylide region compared to the fingerprint region.[51,271,272] There are a number of possible explanations for this: 1) acetylide-centred vibrations are more anharmonic than other vibrations, 2) B3LYP does not correctly describe the 2^{nd} derivatives associated with acetylide-centred vibrations correctly, 3) some combination of these factors. It should also be noted that it has been observed that calculated anharmonicities are relatively conserved, even between DFT- and WFT-based methods, which has lead to the adoption of so called "hybrid" approaches, in which anharmonic corrections obtained through a method with favourable scaling are combined with harmonic frequencies from higher level methods.[130,328–331] It may be inferred from the success of these techniques that for methods that do not correctly describe the second derivatives associated with a vibration correctly, i.e. the corresponding peak is incorrectly placed, the *shape* of the PES as described by the higher-order derivatives and thus the inter-mode anharmonic coupling is still adequately described by such a method. It is therefore reasonable to assume that the unexpected third band in the acetylide

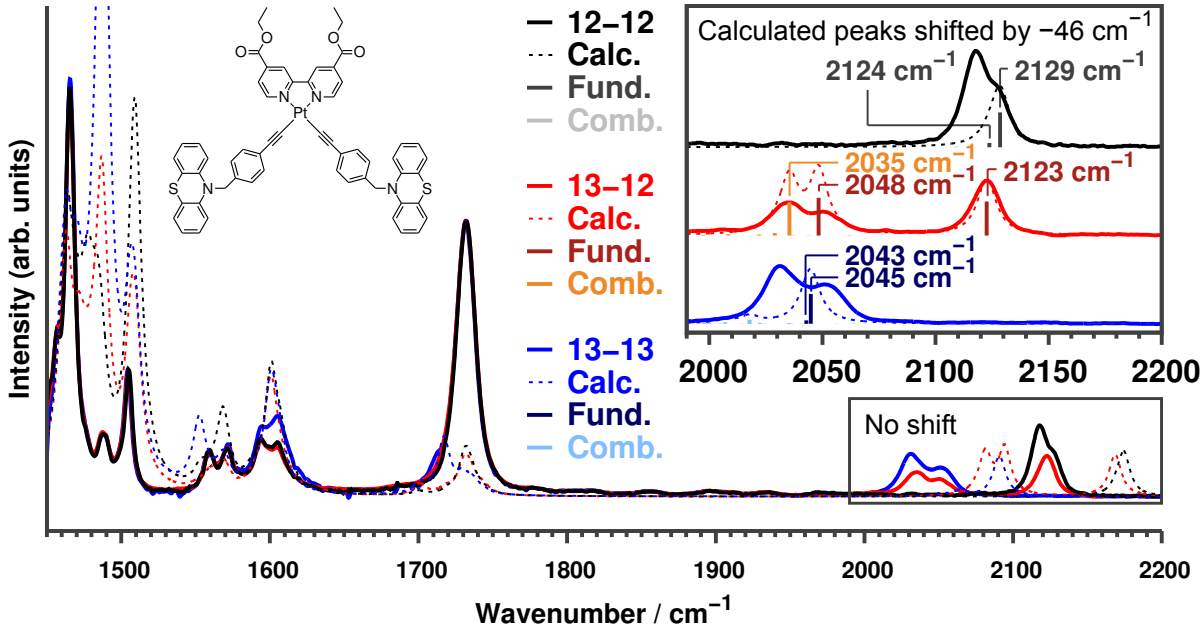

Figure 5.7: Comparison of experimental ground state FTIR spectra of the three isotopologues of [Pt(bipyCOOEt)(C≡C-Ph-CH_2-PTZ)$_2$] to calculated vibrational spectra with anharmonic corrections. The experimental spectra (thick lines) of **12-12** (black), **13-12** (red) and **13-13** (blue) are shown alongside calculated spectra (dashed lines), convoluted with Lorentzian functions with FWHM = 10 cm^{-1}. The 2000 cm^{-1} to 2150 cm^{-1} region is magnified in the inset. Within the inset all calculated peaks are empirically shifted by −46 cm^{-1} to guide the eye. The contributions from fundamental and combination bands are shown as darker and lighter sticks, respectively, in the inset. Calculations were performed using B3LYP/SDD[Pt]6-311G(d,p)[H,C,N,O,S]/IEFPCM(CH_2Cl_2), with anharmonic corrections included using Generalized Vibrational Perturbation Theory to 2nd order (GVPT2). Normal modes below 100 cm^{-1} were excluded from the perturbative treatment.[54]

region observed in the experimental FTIR spectrum of **13-12** can indeed be assigned to the combination band $^{13}\nu_{234} + ^{13}\nu_{130}$ on the basis of calculations involving correcting B3LYP/SDD[Pt]6-311G(d,p)[H,C,N,O,S]/IEFPCM(CH_2Cl_2) harmonic frequencies with anharmonic corrections obtained by GVPT2 in which low energy modes are removed from the perturbative treatment.

Calculations for all three of the isotopomers of [Pt(bipyCOOEt)(C≡C-Ph-CH_2-PTZ)$_2$] studied are presented in Figure 5.7. In the 1450 cm^{-1} to 1580 cm^{-1} region, calculations predict a more marked difference between the isotopomers than is observed experimentally, particularly in terms of band intensity. In contrast, the peak at ~1600 cm^{-1} is calculated to be of almost equal intensity for all three isotopomers, unlike experimental observations. For **13-13**, the inclusion of anharmonic corrections suggest a red-shifted shoulder should be present in the carbonyl region, in good agreement with experimental observations. In the acetylide region, calculations

of **12-12** predict that the two acetylide fundamentals should be separated by 5 cm^{-1}, approximately half of the observed splitting. Furthermore the intensity of the lower energy, asymmetric combination normal mode is underestimated by calculations. Importantly, the calculations do not predict that the combination bands on either 'side' of the molecule that are equivalent to those found in **13-12** should be of significant intensity, in agreement with experiment. The displacement vectors of these modes are illustrated in Figures 5.5 and 5.6.

As previously discussed, the calculated spectrum of **13-12** is in good agreement with experiments in acetylide region. For the doubly labelled isotopomer, **13-13**, calculations predict that the two acetylide-centred vibrational modes should be close in energy to each other, similar to the case of **12-12**. This is in disagreement with experimental observations. For **13-13**, calculations also do not suggest that the combination bands equivalent to those found in **13-12** should have appreciable intensity. One possible explanation for this is that since the two $^{13}C{\equiv}^{13}C$ acetylides of **13-13** are equivalent, the resulting coupled acetylide normal modes are delocalised across both 'arms' of the molecule, disrupting anharmonic coupling with the phenyl- and PTZ-centred modes that constitute the combination bands seen in **13-12**.

In addition to [Pt(bipyCOOEt)(C≡C-Ph-CH_2-PTZ)$_2$], another Pt complex was synthesised by the route discussed above, in which the phenothiazine moieties are replaced with hydrogens.[54] The chemical structure of this compound, **ptol-s**, and its FTIR absorption spectrum are presented in Figure 5.8. The spectrum of **ptol-s** is much less congested in the 1450 cm^{-1} to 1650 cm^{-1} region than in the larger molecules previously discussed, with a total of six easily distinguishable peaks in this region. A prominent carbonyl band is observed at ~1730 cm^{-1} with a small shoulder on the red side of the peak, followed by a complex pattern of at least 5 peaks in the acetylide region, despite the presence of only two acetylide bonds in **ptol-s**. The vibrational spectrum of **ptol-s** was therefore calculated using B3LYP/SDD[Pt]6-311G(d,p)[H,C,N]/IEFPCM(CH_2Cl_2), including the previously described GVPT2 to introduce anharmonic corrections in which normal modes with harmonic frequencies below 100 cm^{-1} were excluded from the perturbative treatment, a total of 13 modes in the case of **ptol-s**. It is important to note that in calculations of **ptol-s** a truncated geometry was used in which the esters are removed, reducing the size of the system from 358 electrons and 71

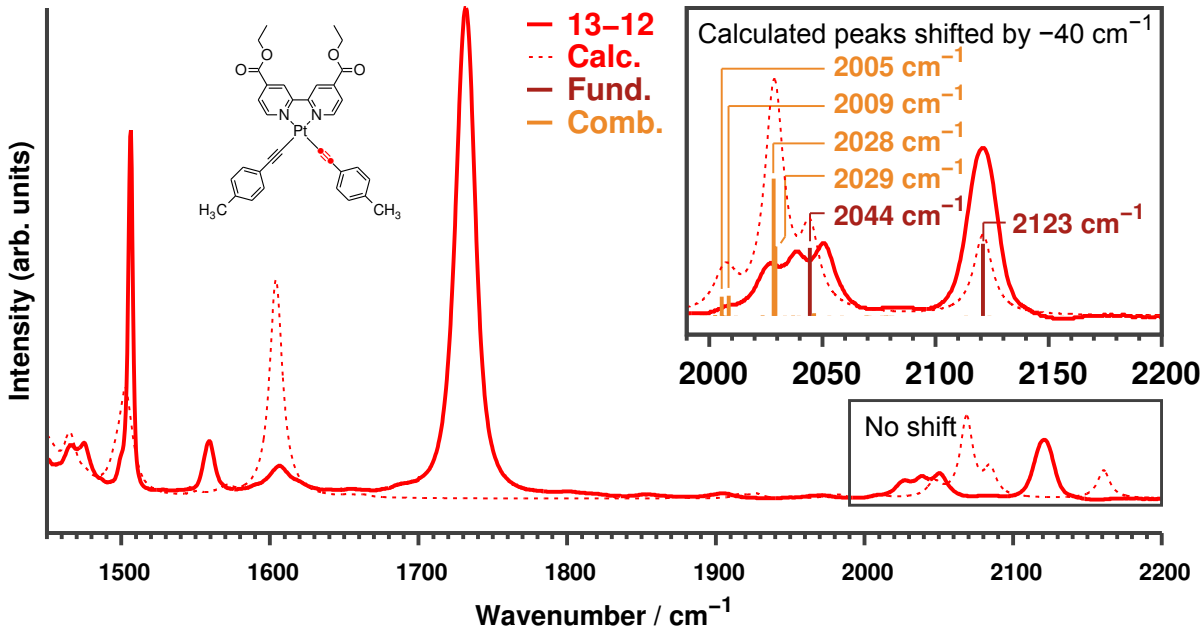

Figure 5.8: Comparison of experimental ground state FTIR spectra of **ptol-s** to the calculated vibrational spectra with anharmonic corrections. The experimental spectra (thick line) are shown alongside calculated spectra (dashed lines), convoluted with Lorentzian functions with FWHM = 10 cm^{-1}. The 2000 cm^{-1} to 2150 cm^{-1} region is magnified in the inset. Within the inset all calculated peaks are empirically shifted by −40 cm^{-1} to guide the eye. The contributions from fundamental and combination bands are shown as darker and lighter sticks, respectively, in the inset. Calculations were performed using B3LYP/SDD[Pt]6-311G(d,p)[H,C,N]/IEFPCM(CH_2Cl_2), with anharmonic corrections included using Generalized Vibrational Perturbation Theory to 2nd order (GVPT2) and were performed with a truncated geometry, in which the ester groups are absent. Normal modes below 100 cm^{-1} were excluded from the perturbative treatment.[54]

atoms to 282 electrons and 53 atoms, and therefore 153 vibrational degrees of freedom. The calculated spectrum of **ptol-s**, also presented in Figure 5.8, is in very good agreement with the experimentally observed FTIR spectrum. In the 1450 cm^{-1} to 1650 cm^{-1} region all peaks apart from an absent peak at ~1560 cm^{-1} are found in the calculated spectrum to be close in energy to the experimental observations. The slight disagreement between the calculations and experiment in this region may be due to the truncated geometry employed in the calculation, which also explains the absence of peaks in the ester region.

In the acetylide region of **ptol-s**, a number of peaks are calculated. The two acetylide-centred fundamentals, illustrated in Figure 5.9, are separated by ~80 cm^{-1}, in accordance with the difference in reduced mass between the two acetylides. The acetylide modes are joined by four prominent combination bands, constructed of low energy fundamentals located mainly

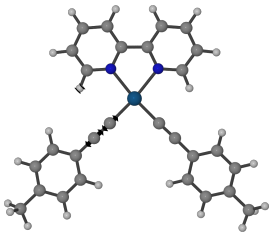

(i) ptol-s ν_{131}: $^{12}C{\equiv}^{12}C$ stretch.
$\nu_{Anh.} = 2161\,cm^{-1}$

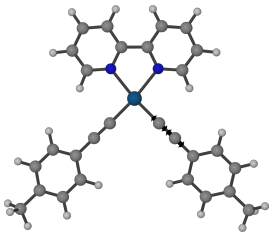

(ii) ptol-s ν_{130}: $^{13}C{\equiv}^{13}C$ stretch.
$\nu_{Anh.} = 2084\,cm^{-1}$

Figure 5.9: Displacement vectors of acetylide-centred vibrational modes of **ptol-s**. Calculated anharmonically corrected vibrational energies are displayed below each vibrational mode. Calculations were performed using B3LYP/SDD[Pt]6-311G(d,p)[H,C,N]/IEFPCM(CH_2Cl_2), with anharmonic corrections included using Generalized Vibrational Perturbation Theory to 2nd order (GVPT2) in which normal modes below $100\,cm^{-1}$ were excluded from the perturbative treatment.[54]

on the *p*-tolyl fragments and illustrated in Figure 5.6. Of particular note are ν_{98} and ν_{97} of **ptol-s**, which are equivalent to modes ν_{234} and ν_{233} in **13-12**, the former of which is one of the components of the combination band $\nu_{234} + \nu_{130}$ that is responsible for the additional peak observed in **13-12**. These two modes are both involved in combinations with a second pair of phenyl-centred modes, ν_{63} and ν_{62}, resulting in the two combination bands $\nu_{98} + \nu_{62}$ and $\nu_{97} + \nu_{63}$ that, when empirically shifted by $-40\,cm^{-1}$, are co-incident with an experimentally observed peak at $\sim 2005\,cm^{-1}$. At slightly higher energy another pair of near degenerate combination modes consisting of phenyl-centred modes on either side of the molecule, ν_{123} and ν_{122}, both combined with the in-plane bend of the $^{12}C{\equiv}^{12}C$ acetylide, mode ν_{41}. The near-degeneracy of these modes may suggest they could engage in a second-order, "Darling-Dennison", resonance; however, this type of four-quanta resonance is not included in GVPT2.[313] The resultant splitting of this peak could lead the calculated spectrum to reproduce the experimental spectrum to good accuracy.

In summary, the unexpectedly complex vibrational spectra of three isotopomers of [Pt(bipyCOOEt)(C≡C-Ph-CH_2-PTZ)$_2$]; **12-12**, **13-12** and **13-13**, as well as one isotopomer of [Pt(bipyCOOEt)(C≡C-Ph-CH_2-Me)$_2$]; **ptol-s**, were successfully described using the B3LYP/SDD[Pt]6-311G(d,p)[H,C,N,O,S]/IEFPCM(CH_2Cl_2) method including anharmonic corrections with GVPT2 in which normal modes below $100\,cm^{-1}$ were excluded from the perturbative treatment. The additional peaks in the experimental spectra of the partially

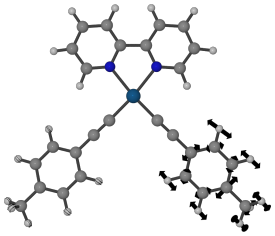

(i) ptol-s ν_{123}: ^{13}C side phenyl in plane twist.
$\nu_{\text{Anh.}} = 1551\,\text{cm}^{-1}$

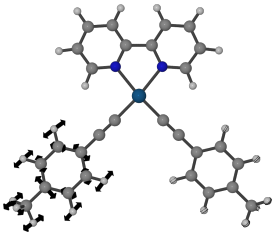

(ii) ptol-s ν_{122}: ^{12}C side phenyl in plane twist.
$\nu_{\text{Anh.}} = 1551\,\text{cm}^{-1}$

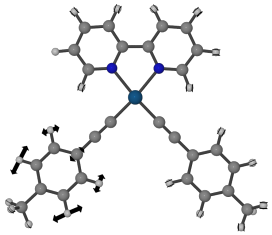

(iii) ptol-s ν_{98}: ^{12}C side wave.
$\nu_{\text{Anh.}} = 1220\,\text{cm}^{-1}$

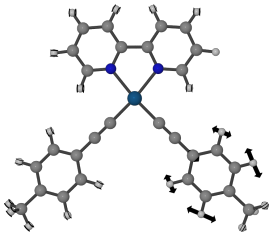

(iv) ptol-s ν_{97}: ^{13}C side wave.
$\nu_{\text{Anh.}} = 1216\,\text{cm}^{-1}$

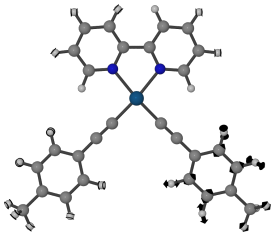

(v) ptol-s ν_{63}: ^{13}C side phenyl out of plane twist.
$\nu_{\text{Anh.}} = 836\,\text{cm}^{-1}$

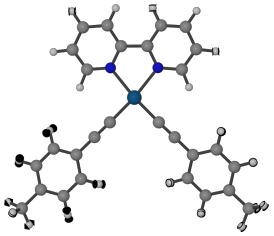

(vi) ptol-s ν_{62}: ^{12}C side phenyl out of plane twist.
$\nu_{\text{Anh.}} = 832\,\text{cm}^{-1}$

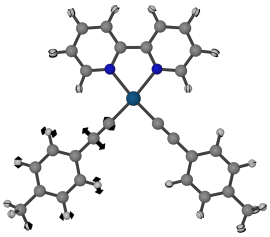

(vii) ptol-s ν_{41}: ^{12}C acetylide in plane bend.
$\nu_{\text{Anh.}} = 519\,\text{cm}^{-1}$

Figure 5.10: Displacement vectors of the component fundamental modes of significant combination modes of **ptol-s**. Calculated anharmonically corrected vibrational energies are displayed below each vibrational mode. Calculations were performed using B3LYP/SDD[Pt]6-311G(d,p)[H,C,N]/IEFPCM(CH_2Cl_2), with anharmonic corrections included using Generalized Vibrational Perturbation Theory to 2$^{\text{nd}}$ order (GVPT2) in which normal modes below 100 cm^{-1} were excluded from the perturbative treatment. Note that modes are numbered with descending harmonic vibrational energy.[54]

isotopically labelled **13-12** and **ptol-s** were found to be due to the presence of relatively strongly allowed combination modes, consisting mainly of phenyl-acetylide-centred vibrations. A selection of the most important calculated vibrational frequencies are provided in Table 5.2. The normal modes that are strongly coupled to the acetylide vibrations of **13-12** are of particular interest, since they could be expected to play a significant role in the dynamics of vibrational excitation in the molecule. The successful description of the vibrational structure of **13-12** enabled the investigation of its potential in "vibrational control" experiments, to which we will next turn our attention.

Species	Mode	Frequency / cm^{-1}	Intensity / km mol^{-1}
13-12	$^{13}\nu_{289}$	2168.636	501.06
	$^{13}\nu_{288}$	2094.321	555.67
	$^{13}\nu_{234} + ^{13}\nu_{130}$	2081.426	491.77
ptol-s	ν_{131}	2160.962	54.48
	ν_{130}	2084.443	51.43
	$\nu_{123} + \nu_{41}$	2068.451	103.72
	$\nu_{122} + \nu_{41}$	2069.240	53.39
	$\nu_{98} + \nu_{62}$	2048.592	15.27
	$\nu_{97} + \nu_{63}$	2045.463	14.48

Table 5.2: Selected calculated vibrational frequencies of **13-12** and **ptol-s**. Calculations performed using B3LYP/SDD[Pt]6-311G(d,p)[H,C,N,O,S]/IEFPCM(CH_2Cl_2) including anharmonic corrections included using Generalized Vibrational Perturbation Theory to 2nd order (GVPT2) in which normal modes below 100 cm^{-1} were excluded from the perturbative treatment. Displacement vectors of the vibrational modes are given in Figures 5.5, 5.6, 5.9 and 5.10. Calculations of **ptol-s** employed a truncated geometry, in which the esters are removed from the bipy-type ligand.

5.2.1 Ultrafast spectroscopy of [Pt(bipyCOOEt)(C≡C-Ph-CH_2-PTZ)$_2$]

As discussed in Section 5.1, the motivation for the synthesis and characterization of **13-12** was to enable investigations into the use of **13-12** in ultrafast (~fs) spectroscopic experiments in which the evolution of the electronically excited state is directly manipulated by means of targeted vibrational excitation of the selected molecular modes. Before exploring the results of these investigations, a brief overview of the electronic structure is presented to aid in the interpretation of the results. A more extensive investigation of the electronic structure is be presented in Section 5.3, including validation of the methods discussed below.

To retain consistency with the methods used in Section 5.2 to explore the vibrational structure of [Pt(bipyCOOEt)(C≡C-Ph-CH_2-PTZ)$_2$], calculations were initially performed using ground state and time-dependent B3LYP/SDD[Pt]6-311G(d,p)[H,C,N,O,S]/IEFPCM(CH_2Cl_2). As well as providing a good description of the vibrational structure in organometallic complexes, these methods have been shown to perform relatively well in general in the calculation of excited state properties,[170] and specifically well in the calculation of ground-to-excited state energy gaps for a series of Pt complexes.[332]

Select frontier molecular orbitals are shown in Figure 5.11. As expected, the LUMO lies on the bipyCOOEt fragment of the molecule: the acceptor in the D-B-A-B-D structure. The LUMO also has very minor Pt $5d_{yz}$ and acetylide π^* character. The next lowest unoccupied orbital (not shown) is ~0.75 eV higher in energy than the LUMO and also localised on the acceptor. The occupied orbitals are localised on either of the two donors, or on the bridge. The HOMO and H−1 are almost degenerate in energy and are centred on the two PTZ fragments. Since the conformation used in the calculations is asymmetrical, the orbital on the right-hand side is slightly less favoured than the left-hand side, though the effect is small (<0.01 eV). As a result of this small difference in energy it is expected that in the equilibrium geometry the right-hand side localised CSS (**12-12**: ^{RHS}CSS, **13-12**: ^{13}CSS) should be marginally lower in energy than the left-hand side localised equivalent (**12-12**: ^{LHS}CSS, **13-12**: ^{12}CSS).

Below these orbitals, there are three occupied orbitals constructed from different combinations of Pt d-orbitals and acetylide in- and out-of-plane π-orbitals. The highest of these, H−2, is a combination of the Pt $5d_{xz}$ with two out-of-plane π-orbitals of opposite phase that are con-

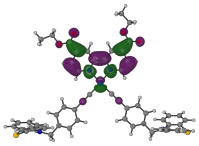

(i) LUMO: $\varepsilon = -3.18\,\text{eV}$

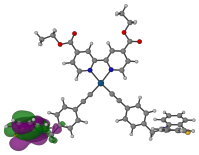

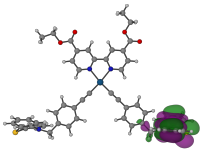

(ii) H−1: $\varepsilon = -5.31\,\text{eV}$ **(iii)** HOMO: $\varepsilon = -5.30\,\text{eV}$

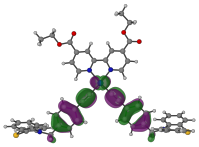

(iv) H−2: $\varepsilon = -5.66\,\text{eV}$

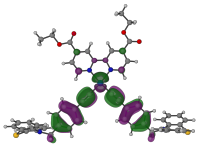

(v) H−3: $\varepsilon = -5.86\,\text{eV}$

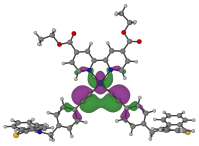

(vi) H−4: $\varepsilon = -6.38\,\text{eV}$

Figure 5.11: Selected singlet frontier molecular orbitals of [Pt(bipyCOOEt)(C≡C-Ph-CH_2-PTZ)$_2$] calculated using Restricted B3LYP/SDD[Pt]6-311G(d,p)[H,C,N,O,S]/IEFPCM(CH_2Cl_2). Isovalue = 0.02 $\sqrt{e^{-}\text{bohr}^{-3}}$.

jugated to the phenyl π system. The H−3 orbital is close in energy to H−2 and consists of the same out-of-plane, bridge centred orbitals, this time in phase, combined with the Pt $5d_{yz}$ orbital. Unlike H−2, H−3 also has a very small amount of character coming from p-orbitals of the bipy fragment. The H−4 orbital is slightly different to the previous two orbitals. In H−4 the Pt $5d_{x^2-y^2}$ combines with two acetylide in-plane π-orbitals that are of the same phase. There is also a very small contribution from σ-orbitals from both of the bridge phenyl groups as well as the bipy fragment.

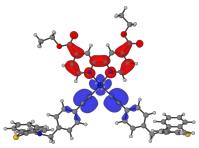

(i) $d_{x^2-y^2}$CT.

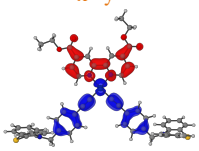

(ii) d_{yz}CT.

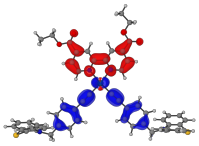

(iii) d_{xz}CT.

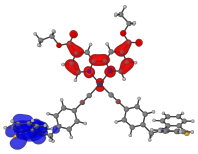

(iv) 12-12: ^{LHS}CSS, **13-12**: ^{12}CSS.

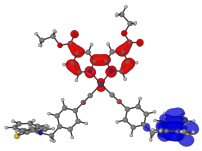

(v) 12-12: ^{RHS}CSS, **13-12**: ^{13}CSS.

Figure 5.12: Electron density difference diagrams for selected electronically excited singlet states of [Pt(bipyCOOEt)(C≡C-Ph-CH_2-PTZ)$_2$] calculated using Restricted B3LYP/SDD[Pt]6-311G(d,p)[H,C,N,O,S]/IEFPCM(CH_2Cl_2). Blue regions define a volume within which electron density is lost and red regions a volume within which electron density is gained with respect to the ground state. Isovalue = 0.004 e^-bohr^{-3}.

Transitions between the occupied and unoccupied orbitals discussed result in a number of electronically excited states. For the sake of simplicity, only states of singlet character are detailed in this section. A more thorough examination of the electronic structure is presented in Section 5.3. Maps of the difference in electron density between the ground and five lowest singlet excited states are shown in Figure 5.12. These diagrams are constructed by calculating the electron density as a function of space for a given excited state and subtracting the electron density of the singlet ground state, revealing volumes within which the electron density is higher or lower in that excited state than in the ground state. The calculations reveal two types of excited state: MLCTs and CSSs. The three MLCT states correspond to transitions from H−2, H−3 and H−4 to LUMO, yielding d_{xz}CT, d_{yz}CT and $d_{x^2-y^2}$CT, respectively. In all three MLCT

states, electron density is lost from the Pt and bridge regions and gained on the bipyCOOEt fragment. In particular, the two MLCT states with out-of-plane π-character, d_{xz}CT and d_{yz}CT, differ only by the density difference around the metal centre. It would therefore be expected that it should be very difficult to distinguish between the three MLCT states spectroscopically, particularly in the acetylide region. There are two CSSs, localised on either side of the complex, corresponding to transitions from HOMO and H−1 to LUMO. These can be categorised based on isotopomer. The right-hand side localised CSS is denoted ^{RHS}CSS for the unlabelled **12-12** and ^{13}CSS for the partially labelled **13-12**. The corresponding left-hand side localised CSSs are ^{LHS}CSS and ^{12}CSS, respectively. Unlike the MLCTs, the CSSs exhibit very small increases in electron density on the Pt and the distal carbons of the acetylides. It should also be noted that when an electron is lost from PTZ, the fragment becomes planar, as illustrated in the optimised singlet CSS geometry of **PTZ-Pt^{H}-NAP** shown in Figure 4.10. The combination of these factors should lead to two spectroscopically identifiable CSSs in the case of **13-12**, in contrast with the unlabelled **12-12**, in which the CSSs are not spectroscopically distinguishable.[272] It should be noted that whilst the charge distributions derived from these calculations appear to be in disagreement to those found in Ref. [302], which are fitted to experimental data, the diagrams in Figure 5.12 are relative to the ground state which shows strong polarisation of the Pt-C bonds and is calculated to have a dipole moment μ=16.5 D, in good agreement with the experimentally measured value of μ=10.3 D for a similar complex, in which the bipy esters are replaced with ^{t}Bu groups.

In summary, the low-lying excited states of [Pt(bipyCOOEt)(C≡C-Ph-CH_2-PTZ)$_2$] are as follows: two CSSs, involving transfer from one of two phenothiazine-centred orbitals to a bipyCOOEt π^* orbital; and three MLCT states of similar character, involving transfer from Pt 5d and acetylide π orbitals of various types to the same bipyCOOEt π^* orbital.

With this in mind, the results of ultrafast UV pump-IR pump-IR probe investigations into the controllability of electron transfer in **13-12** are presented in Figure 5.13. The experiment is initiated by a UV-pump pulse at 400 nm. The results of this pump are probed by a broad-band IR pulse at varying time delays. There is also an optional additional narrowband IR pump pulse that is used to investigate the possibility of vibrational control of electron trans-

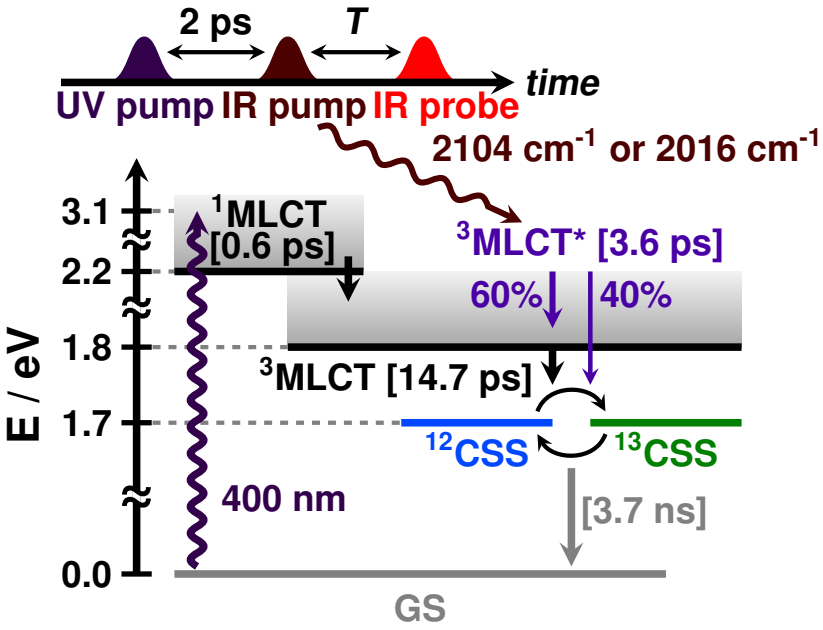

Figure 5.13: Summary of experimental ultrafast spectroscopic investigations into the dynamics of the electronically excited states of **13-12** from kinetic analysis. The experiment consists of a 400 nm UV pump followed broadband IR probe pulse at time delay *T*, with an optional IR pump pulse 2 ps after the actinic UV pulse. Electron transfer is initiated by the actinic pulse, leading to the formation of a singlet Metal to Ligand Charge Transfer (^{1}MLCT, black) state. The ^{1}MLCT state decays into a manifold of triplet MLCT states (^{3}MLCT, black) with a lifetime of 0.6 ps. Within this manifold, the signature an unrelaxed ^{3}MLCT (^{3}MLCT*, purple) can be extracted. The ^{3}MLCT state decays equally to the two Charge Separated States, localized on either the ^{12}C labelled side (^{12}CSS, blue) or ^{13}C labelled side (^{13}CSS, green) with a lifetime of 14.7 ps. If the population distribution of the CSSs is disturbed they re-equilibrate with a lifetime of 13.3 ps. The CSSs decay back to the ground state with a lifetime of 3.7 ns. The electron transfer pathways in **13-12** can be manipulated by IR excitation of the transient ^{3}MLCT* state with pulses at 2104 cm^{-1} or 2016 cm^{-1}, corresponding to the ^{12}C≡^{12}C and ^{13}C≡^{13}C stretches respectively. *Kinetic data courtesy M. Delor.*[55]

fer. The actinic (UV) pulse results in the formation of a high energy singlet state, which is assigned MLCT character based on Transient UV Absorption (TA) and ultrafast Time-Resolved IR (TRIR) data.[55,272,301,302] This state, denoted ^{1}MLCT in the diagram, has a lifetime of 0.6 ps. This state undergoes relaxation processes, one of which is Intersystem Crossing (ISC) to the triplet manifold. The calculations previously discussed describe a number of possible MLCT states of differing character. However, within the resolution of the experiment, it is not possible to distinguish between them. Therefore, within the kinetic model it assumed that ^{1}MLCT represents a manifold of singlet MLCT states of differing character. Decay of ^{1}MLCT *via* ISC results in the concomitant formation of two states, also of MLCT character, that are denoted ^{3}MLCT and ^{3}MLCT*. ^{3}MLCT is a triplet MLCT state with a lifetime of 14.7 ps. Like ^{1}MLCT,

^{3}MLCT represents part of a manifold of triplet MLCT states. One of these states is ^{3}MLCT*. Within the resolution of the experiments it is not possible to tell whether ^{3}MLCT* corresponds to a vibrationally "hot" form of ^{3}MLCT or whether it is a separate electronically excited state. ^{3}MLCT* decays with a lifetime of 3.6 ps and is clearly distinguishable from ^{3}MLCT in the TA and TRIR data, though the differences are small. (See supplementary information of Ref. [55]) The two triplet MLCT states decay to form two further excited states, denoted ^{12}CSS and ^{13}CSS. Since the two CSSs are electronically equivalent, they cannot be distinguished between in the TA experiment. However, the asymmetric isotopic labelling of the acetylides in **13-12** leads to different spectra observed in the TRIR experiment for ^{12}CSS and ^{13}CSS. A key observation from the results of TA experiments is that the CSSs are populated on two timescales: one with a lifetime of 3.6 ps that correlates with to population transfer from ^{3}MLCT* to the CSS pair and another with a lifetime of 14.7 ps that correlates with decay from ^{3}MLCT. The pair of CSSs are relatively long lived, with a lifetime of 3.7 ns. If the population distribution between the two CSSs is perturbed they re-equilibrate with a lifetime of 13.3 ps.[55]

To achieve the stated aim of asserting directional control in **13-12**, the system must be manipulable such that either ^{13}CSS or ^{12}CSS may be preferentially formed. Surveying the states identified in the kinetic scheme shown in Figure 5.13, ^{3}MLCT* provides an ideal target for manipulation since 1) it has two distinct acetylide peaks, at 2104 cm^{-1} and 2016 cm^{-1}, and 2) it decays rapidly to the pair of CSSs. By including the optional IR pump pulse at the given frequencies in the ultrafast TRIR experiments and comparing the resultant spectra to those recorded in the absence of an IR pump pulse, the possibility of a response as a result of vibrational perturbation can be investigated. The results of these experiments are shown in Figure 5.14.

Figure 5.14 plots the difference between the absorption due to a CSS recorded when the additional IR pump pulse is present and when the additional IR pump pulse is absent. If the IR pump pulse had no effect on the population of the CSSs then the result would be zero. This is not the case. Pumping either acetylide vibrational mode increases the observed absorption and thus the population of CSS in the first few ps following IR perturbation; however, the effect is not permanent as there is no difference in recorded spectra after ~40 ps have elapsed. This is similar to the acceleration observed in other systems,[36,299] although some of the previously studied Pt

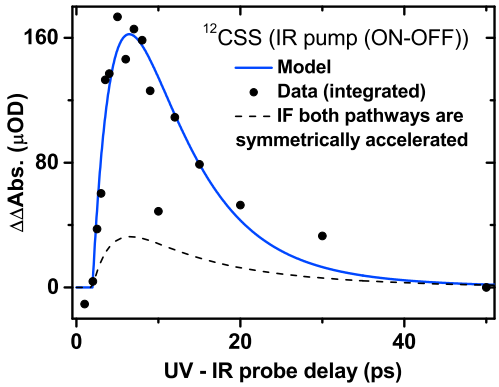

(i) Change in absorption due to ^{12}CSS following excitation of $\nu(^{13}C{\equiv}^{13}C)$ stretch of the ^{3}MLCT* state.

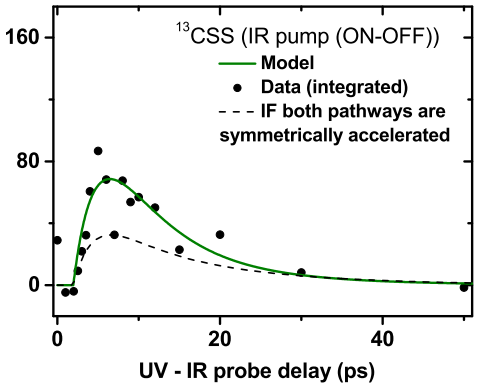

(ii) Change in absorption due to ^{13}CSS following excitation of $\nu(^{12}C{\equiv}^{12}C)$ stretch of the ^{3}MLCT* state.

Figure 5.14: Evidence of differential response after pumping the $\nu(^{13}C{\equiv}^{13}C)$ and $\nu(^{12}C{\equiv}^{12}C)$ stretches of **13-12**. See Figure 5.13 for a summary of experiments. Figures 5.14(i) and 5.14(ii) depict the change in absorption due to the increase in population of the ^{12}CSS (blue) and ^{13}CSS (green), respectively, as a result of pumping of the $\nu(^{13}C{\equiv}^{13}C)$ and $\nu(^{12}C{\equiv}^{12}C)$ stretches, respectively, of the ^{3}MLCT* state. The black dots denote individual data points. The dashed line simulates the population of the CSSs if IR excitation resulted in symmetrical acceleration of both pathways. Note that since excited state spectra are recorded as a difference with respect to the ground state, the *y* axis is a double difference. *Kinetic data courtesy M. Delor.*[55]

complexes displayed permanent changes in population as a result of perturbation (See Chapter 4). Importantly, the response from the CSSs is asymmetrical: perturbation on one side of the molecule preferentially accelerates formation of CSS on the other side of the molecule, e.g. exciting $\nu(^{13}C{\equiv}^{13}C)$ accelerates formation of ^{12}CSS. Moreover, there is a differential magnitude in the observed acceleration: exciting $\nu(^{13}C{\equiv}^{13}C)$ causes a greater rate acceleration than exciting $\nu(^{12}C{\equiv}^{12}C)$.

Simulated changes in the population dynamics as a result of these perturbations are shown in Figure 5.15. The unperturbed formation of CSS occurs at a rate of 0.0552 ps^{-1}. The effect of IR excitation on this rate constant is as follows: exciting $\nu(^{13}C{\equiv}^{13}C)$ (Figure 5.15(i)) increases

Vibration pumped	Rate of formation $k_{^{13}CSS}$	$k_{^{12}CSS}$
none	0.0552 ps^{-1}	
$\nu(^{13}C{\equiv}^{13}C)$	0.0328 ps^{-1} (−41 ± 10%)	0.0935 ps^{-1} (+69 ± 10%)
$\nu(^{12}C{\equiv}^{12}C)$	0.0714 ps^{-1} (+29 ± 8%)	0.0546 ps^{-1} (−1 ± 8%)

Table 5.3: Change in rate of CSS formation as a result of IR perturbation of the ^{3}MLCT* state of **13-12**

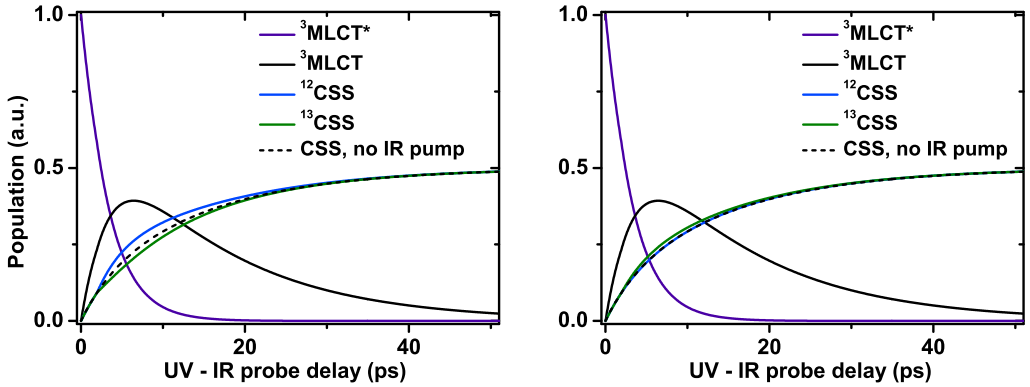

(i) Population dynamics following excitation of $\nu(^{13}C{\equiv}^{13}C)$ stretch of the ^{3}MLCT* state.

(ii) Population dynamics following excitation of $\nu(^{12}C{\equiv}^{12}C)$ stretch of the ^{3}MLCT* state.

Figure 5.15: Result of kinetic modelling of ultrafast IR control experiments of **13-12**. See Figure 5.13 for a summary of experiments. Figures 5.15(i) and 5.15(ii) depict the effect of excitation of the $\nu(^{13}C{\equiv}^{13}C)$ and $\nu(^{12}C{\equiv}^{12}C)$ stretches of the ^{3}MLCT* state, respectively, on the population of ^{3}MLCT* (purple), ^{3}MLCT (black), ^{12}CSS (blue) and ^{13}CSS (green) within the kinetic model. The dashed line illustrates the average population of both CSSs if no IR excitation had occurred. *Kinetic data courtesy M. Delor.*[55]

the rate of formation of ^{12}CSS to 0.0935 ps^{-1}, a 69 ± 10% acceleration, whilst the formation of ^{13}CSS is decreased to 0.0328 ps^{-1}, a 41 ± 10% deceleration; exciting $\nu(^{12}C{\equiv}^{12}C)$ (Figure 5.15(ii)) increases the rate of formation of ^{13}CSS to 0.0714 ps^{-1}, a 29 ± 8% acceleration, whilst the formation of ^{12}CSS is decreased to 0.0546 ps^{-1}, a statistically negligible 1 ± 8% deceleration.

There have been a number of theoretical models proposed to explain changes in rate of ET, k_{ET}, as a result of vibrational excitation.[37,38,42] It has been shown that vibrational perturbation can have both positive or negative effects on k_{ET}; though positive effects tend to be of a higher magnitude than negative ones.[37,42] A critical observation drawn in these models is that the influence of vibrational perturbation is greater if the lifetime of the vibrations are similar to that of ET. Indeed, in models that include vibrational relaxation lifetime as a parameter, it has been shown that reducing the vibrational relaxation lifetime (increasing the rate of vibrational re-

	Lifetime, τ / ps	
State	$\nu(^{13}C{\equiv}^{13}C)$	$\nu(^{12}C{\equiv}^{12}C)$
Ground State	2.5 ± 0.4 ps	5.6 ± 0.2 ps
CSSs	1.4 ± 0.3 ps	4.0 ± 0.2 ps
^{3}MLCT*	1.0 ± 0.4 ps	3.6 ± 0.4 ps

Table 5.4: Relaxation lifetimes of the acetylide-centred vibrational modes of **13-12** in the ground state, CSSs and ^{3}MLCT* state from (T-)2DIR experiments.[55]

laxation) reduces the effect of vibrational perturbation.[38,42,43] When comparing the vibrational lifetime of the two acetylide modes of **13-12** in various excited states (Table 5.4), however, it is clear that in the case of **13-12** such a reduction is not observed. The lower frequency $\nu(^{13}C\equiv^{13}C)$ mode consistently has a shorter lifetime than $\nu(^{12}C\equiv^{12}C)$, ~46% shorter in the ^{3}MLCT* state, yet the maximum observed change in rate of CSS formation is ~2.4× greater in magnitude for $\nu(^{13}C\equiv^{13}C)$ than $\nu(^{12}C\equiv^{12}C)$. One possible explanation for this observation is that Intramolecular Vibrational Redistribution (IVR) results in selective population of low energy vibrational modes due to strong coupling from $\nu(^{13}C\equiv^{13}C)$ to the components of the nearby combination mode (see Section 5.2) that may also influence the directionality of ET. Indeed, numerical simulations have shown that low energy modes can have large effects on ET dynamics.[38]

In summary, experiments have shown that electron transfer in **13-12** can be manipulated in a directional manner. However, to explain the observed effects, two questions must be answered:

1. What is the mechanism of directional influence over ET in **13-12**?

2. Why does exciting $\nu(^{13}C\equiv^{13}C)$ have a greater effect on ET than exciting $\nu(^{12}C\equiv^{12}C)$?

To answer these questions, calculations were performed to investigate the electronic structure of **13-12** and how it changes in response to vibrational perturbation.

5.3 Electronic structure of [Pt(bipyCOOEt)(C≡C-Ph-CH_2-PTZ)$_2$]

As briefly discussed in Section 5.2.1, the low lying excited states of **13-12** are as follows: two Charge Separated States (CSSs) located either on the ^{13}C labelled arm (^{13}CSS) or on the ^{12}C labelled arm (^{12}CSS) and three Metal-to-Ligand Charge Transfer (MLCT) states that differ chiefly by which Pt d-orbital is involved in the transition (d_{xz}CT, d_{yz}CT and $d_{x^2-y^2}$CT). The frontier molecular orbitals involved in these transitions at the TD-B3LYP/SDD[Pt]6-311G(d,p)[H,C,N,O,S]/IEFPCM(CH_2Cl_2 level of theory are displayed in Figure 5.11 and electron density difference diagrams showing the locations of the electron-hole pair for these states at the same level of theory are shown in Figure 5.12(v). The states shown in these figures are consistently found to be the lowest five states using the methods discussed below and so in the interest of brevity similar diagrams for each method tested are omitted.

There are a number of approaches that can be taken when simulating electronically excited molecules.[167,333] As with ground state methods, with great accuracy comes great cost, or rather, poor scaling. Due to the size of **13-12** (113 atoms, 562 electrons) the scope of tractable methods is limited to those with low-order scaling. As such, only single reference methods were utilised in these investigations. It should also be noted that **13-12** contains Pt, which has atomic number $Z = 78$. The Lorentz factor for the Pt 1s electron is therefore on the order $\gamma = 1.22$. The core electrons of Pt should thus behave in a distinctly relativistic manner. To take account of this, scalar relativistic effects and spin-orbit coupling are considered in some of the calculations discussed.

Due to the scale of **13-12** it is not possible to compute high accuracy wavefunctions to compare calculations against. Therefore to judge the accuracy of the methods utilised, calculated electronic excitation spectra are compared against those measured in experiments. In all of the calculations discussed below, the geometry of [Pt(bipyCOOEt)(C≡C-Ph-CH_2-PTZ)$_2$] optimised using B3LYP/SDD[Pt]6-311G(d,p)[H,C,N,O,S]/IEFPCM(CH_2Cl_2), shown in Figure 5.2, is used throughout. This method has been shown to deduce accurate geometries for organometallic complexes and the additional error introduced by using a geometry optimised

within a different method to that used to calculate the excitation energies has been shown to be small.[130,135,170,334–337]

5.3.1 Validation of methods

The first choice that must be made when simulating electronically excited states is the description of the ground state. The two main approaches that can be taken are *ab initio* based or DFT based methods. The excitations from the given ground state can then be obtained by seeking poles in its frequency dependent response to perturbation by an external field. If the Hartree-Fock wavefunction is taken as the *ab initio* reference and the ground state density as calculated using B3LYP is taken as the DFT reference, then the simplest, response-based approximations to the excitation energies are given by Configuration Interaction with Single substitutions (CIS), also known as the Tamm-Dancoff Approximation (TDA) to the Random-Phase Approximation (RPA).[95,190,338] In wavefunction based methods, this approach is known simply as CIS, whereas in DFT based methods it is known as TDA, even though the approaches involve the same way of perturbing the wavefunction or the density. The next level of approximation is to use the full RPA. For a HF reference, this is known as TD-HF whereas for a DFT reference this is known as RPA-TD-DFT or more commonly TD-DFT. In CIS/TDA, the response of the system to a photon is related to the polarizability tensor. The response can be decomposed into a weighted sum of single particle transitions from occupied to virtual orbitals. In RPA, this is augmented by allowing the system to relax to accommodate the change in density by including "de-excitations" from virtual to occupied orbitals.[167] For full details, see Section 2.4.

The results of CIS, TD-HF, TDA-TD-B3LYP and RPA-TD-B3LYP calculations of [Pt(bipyCOOEt)(C≡C-Ph-CH_2-PTZ)$_2$] are shown in Figure 5.16 and are compared against the experimentally measured UV-vis absorption spectrum. Spectra are displayed along with transitions that are convoluted by plotting a Gaussian curve with FWHM = 3000 cm^{-1} centred at each transition that is scaled appropriately based on the oscillator strength of the transition.[339] It is important to note that the calculated spectra are empirically shifted such that the relative transition energies and intensities can be more easily compared to experimental values. This is important since as UV/vis spectra are plotted with wavelength on the x axis, a constant blue

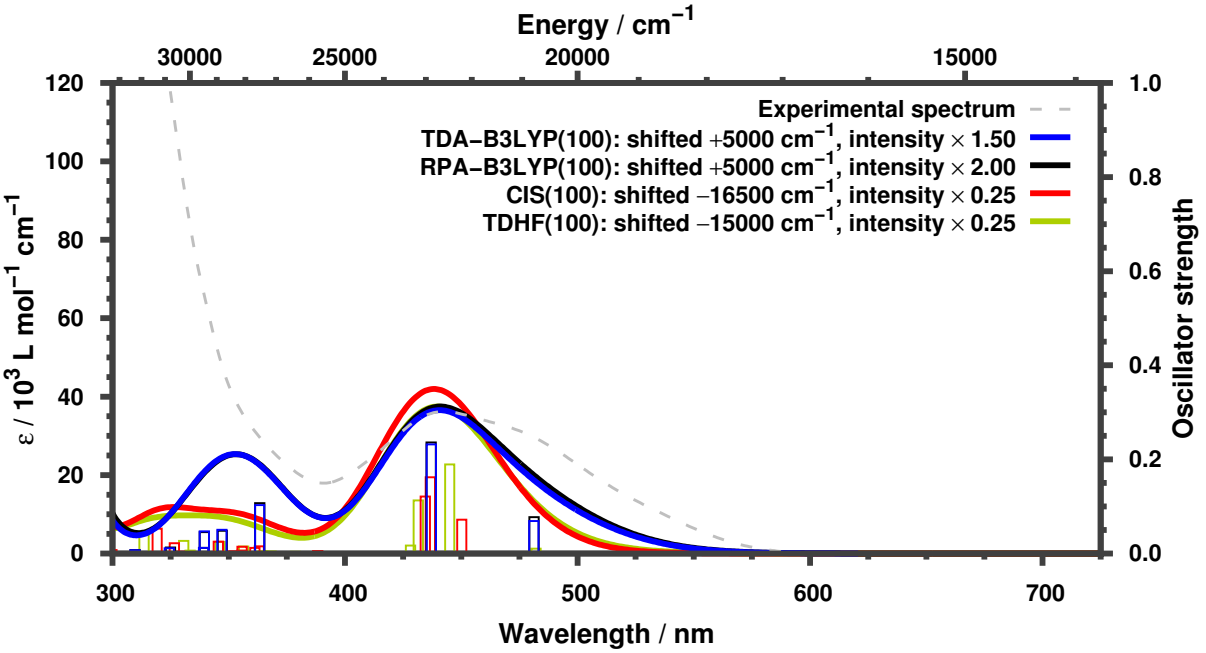

Figure 5.16: Comparison of experimental UV-vis absorption spectra (dashed, light grey) of [Pt(bipyCOOEt)(C≡C-Ph-CH_2-PTZ)$_2$] to convoluted calculated Configuration Interaction with Single substitutions (CIS, red), Time-Dependent Hartree Fock Theory (TD-HF, green), Tamm-Dancoff Approximation Time Dependent B3LYP (TDA-B3LYP, blue) and Random Phase Approximation Time Dependent B3LYP (RPA-B3LYP, black) spectra. Note that RPA Time Dependent Density Functional Theory is commonly called TD-DFT. Calculations were performed at the optimised B3LYP/SDD[Pt]6-311G(d,p)[H,C,N,O,S]/IEFPCM(CH_2Cl_2) geometry and this basis set was used in all four calculations. All calculations included 100 excitations and solvent (CH_2Cl_2) was included using IEF-PCM. The overall calculated spectra are convoluted using Gaussian functions with FWHM = 3000 cm^{-1}. The calculated transitions are shown as empty bars. The calculated spectra are empirically shifted to match the experimental peak at 443 nm and the intensity is scaled to guide the eye.

or red shift in calculated transitions would not be easily identified since the transformation from wavelength to wavenumber is non-linear. With this in mind, it is clear that CIS drastically overestimates excitation energies and transition probabilities: a −16500 cm^{-1} shift is required for agreement in excitation energy and intensities must be reduced by 75%. TD-HF also overestimates excitation energies: a slightly smaller −15000 cm^{-1} shift is required for good agreement to be reached. TD-HF requires the same scaling of transition probabilities as CIS. On the other hand, TDA/RPA-TD-B3LYP underestimates transition energies by 5000 cm^{-1}. The red shift of excitation energies calculated with TD-DFT should be expected as a result of the well known tendency of TD-DFT to underestimate the energy of transitions with significant Charge Transfer (CT) character.[127,170] TDA- and RPA-TD-B3LYP yield similar transition

energies; however, oscillator strengths calculated through TDA-TD-B3LYP are significantly higher than those calculated through RPA-TD-B3LYP.

Since the experimental ultrafast dynamics investigated are initiated by 400 nm pulse, it is critical that the excited states below this threshold are well described by the theoretical methods used. Comparing the experimental and shifted, convoluted spectra in the 400 nm to 600 nm region, there is reasonable agreement between theory and experiment, particularly when TD-DFT is used. The experimental spectrum in this region contains at least three identifiable peaks, centred at λ = 530 nm, 490 nm and 443 nm. (See Appendix A.4 for details) The two TD-DFT methods find two peaks in this region, consistent with the higher energy peaks. In the CIS calculation three peaks are found, although these are too tightly spaced to agree well with the fitted experimental peaks. The TD-HF calculation also has problems with peak spacing to a slightly lesser degree than the CIS calculation. Due to the poor performance of the wavefunction-based method, further investigations were not performed.

The effect of the size of basis set on performance of TD-DFT is investigated in Figure 5.17. RPA-TD-B3LYP calculations were performed using two basis sets: the SDD Effective Core Potential (ECP) and accompanying valence basis set for Pt,[258] and 6-311G(d,p) for all other atoms,[265,266] totalling 2621 primitive Gaussian functions; and the ECP60MDF ECP and cc-pVTZ-PP valence basis set for Pt,[264] and cc-pVTZ for all other atoms,[262,263] totalling 4587 primitive Gaussian functions. Increasing the quality of the basis set has a significant and non-uniform effect on excitation energy. The SDD ECP and valence basis are of lower quality than the cc-pVTZ-PP equivalent and thus excitations involving orbitals with significant Pt character

		SDD[Pt]6-311G(d,p)[H,C,N,O,S]			cc-pVTZ		
Excitation	Transition	Contribution	Energy / eV	f	Contribution	Energy / eV	f
1	HOMO→LUMO	99.88%	1.8826	0.0000	99.86%	1.8813	0.0000
2	H-1→LUMO	99.87%	1.8917	0.0000	99.83%	1.8911	0.0001
3	H-2→LUMO	98.60%	1.9560	0.0772	98.49%	1.9333	0.0806
4	H-3→LUMO	97.44%	2.2168	0.2360	97.31%	2.1955	0.2448
5	H-4→LUMO	99.20%	2.5162	0.0010	99.30%	2.4212	0.0015

Table 5.5: Effect of basis set on the five lowest singlet-to-singlet excitations of [Pt(bipyCOOEt)(C≡C-Ph-CH_2-PTZ)$_2$] within RPA-TD-DFT. Representative orbitals are displayed in Figure 5.11. f denotes oscillator strength. Calculations were performed at the optimised B3LYP/SDD[Pt]6-311G(d,p)[H,C,N,O,S]/IEFPCM(CH_2Cl_2) geometry. In both cases CH_2Cl_2 solvent was included implicitly with the IEFPCM.

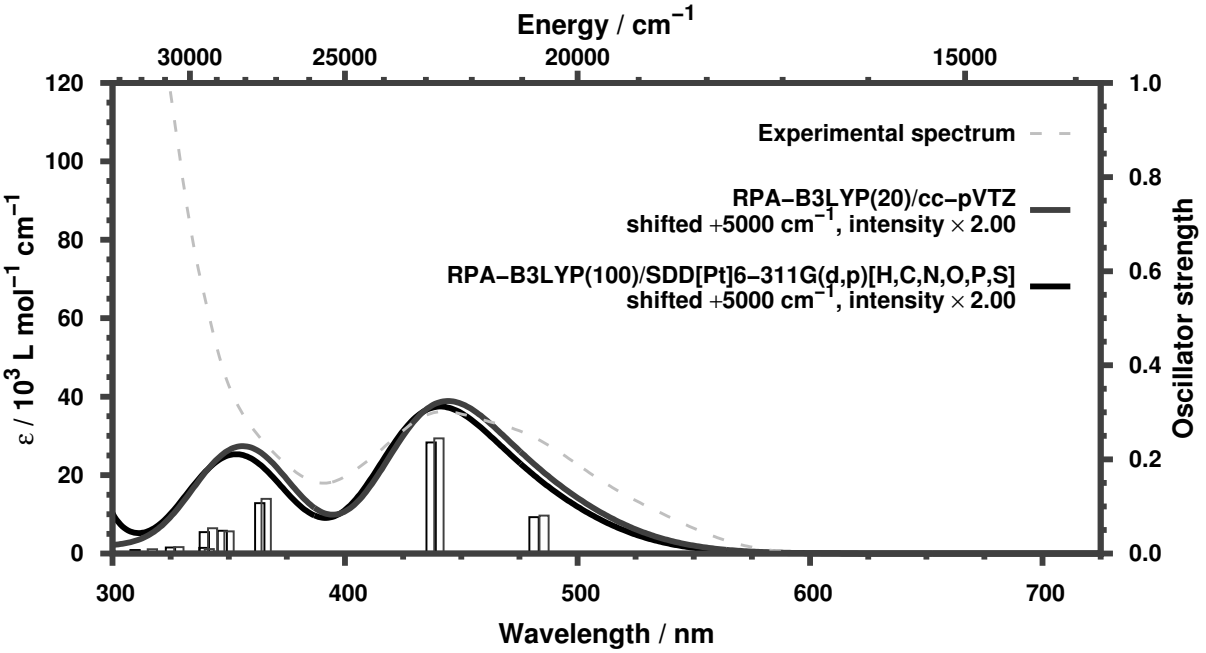

Figure 5.17: Comparison of experimental UV-vis absorption spectra (dashed, light grey) of [Pt(bipyCOOEt)(C≡C-Ph-CH_2-PTZ)$_2$] to convoluted calculated Random Phase Approximation Time Dependent B3LYP (RPA-B3LYP) spectra with the SDD[Pt]6-311G(d,p)[H,C,N,O,S] (black), for which the lowest 100 excitations were found and cc-pVTZ basis sets (dark grey), for which the lowest 20 excitations were found. Note that RPA Time Dependent Density Functional Theory is commonly called TD-DFT. Calculations were performed at the optimised B3LYP/SDD[Pt]6-311G(d,p)[H,C,N,O,S]/IEFPCM(CH_2Cl_2) geometry. The overall calculated spectra are convoluted using Gaussian functions with FWHM = 3000 cm^{-1}. The calculated spectra are empirically shifted to match the experimental peak at 443 nm and the intensity is scaled to guide the eye.

display a red shift when the larger basis set is employed. The two lowest energy excitations, which correspond to the formation of CSSs, are relatively unnaffected by increasing the size of the basis set, as shown in Table 5.5. The three MLCT states, however, are red-shifted by an average of 0.046 eV when the larger basis set is used. This could have an effect on the topology of the excited state Potential Energy Surfaces (PESs) of [Pt(bipyCOOEt)(C≡C-Ph-CH_2-PTZ)$_2$], particularly in the context of crossovers between states of CSS and MLCT character. There is, however, significant computational cost associated with increasing the basis set size. It should be noted that the size of the excitation space sought was significantly smaller in the cc-pVTZ calculation. This is due to the use of the iterative modified Davidson algorithm to find the *eigenvectors* and *eigenvalues* of the Casida equations.[189] There is a small degree of error introduced as a result of the use of this iterative approach; however, this error is smaller for

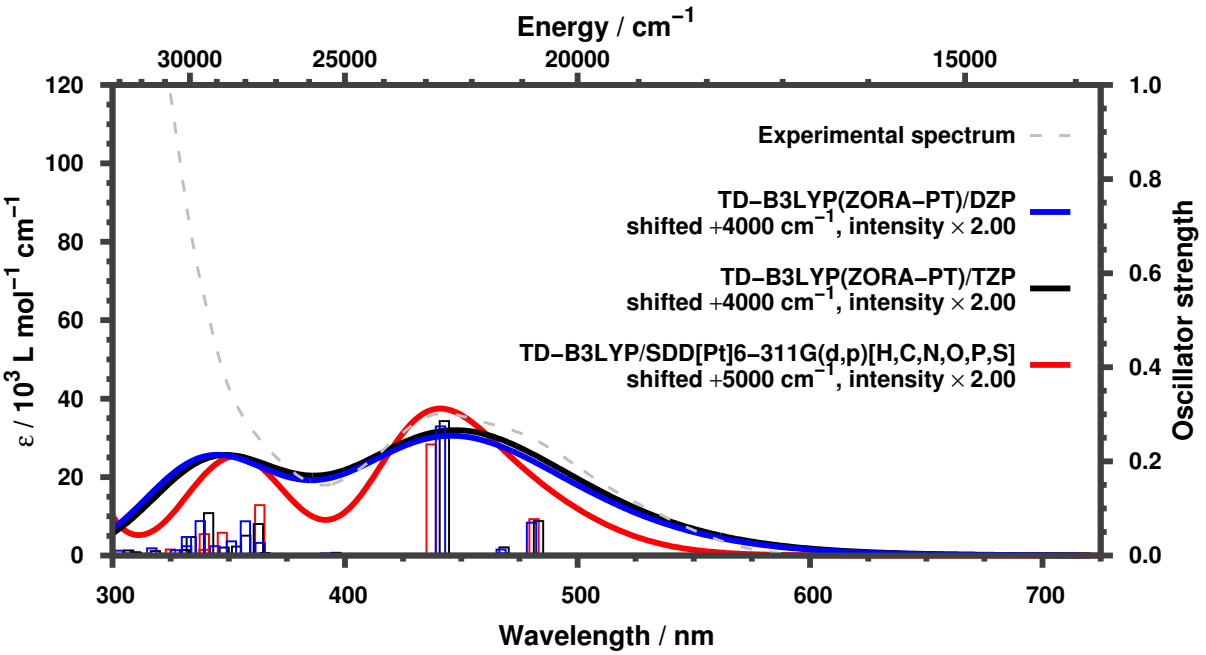

Figure 5.18: Comparison of experimental UV-vis absorption spectra (dashed, light grey) of [Pt(bipyCOOEt)(C≡C-Ph-CH_2-PTZ)$_2$] to convoluted calculated Time Dependent B3LYP (TD-B3LYP) spectra with the SDD[Pt]6-311G(d,p)[H,C,N,O,S] (red), for which the lowest 100 excitations were found and TD-B3LYP including Spin-Orbit Coupling (SOC) perturbatively in the TD procedure using the Zero-Order Regular Approximation (ZORA-PT) with the DZP (blue) and TZP (black) basis sets, for both of which the lowest 20 spin-pure excitations were found, resulting in a total of 80 spin-free excitations in both cases. Solvent (CH_2Cl_2) was included implicitly using IEF-PCM for the non-SOC calculation and using COSMO for the SOC calculations. The SOC calculations included a 'large' set of frozen core electrons, as defined by ADF. Calculations were performed at the optimised B3LYP/SDD[Pt]6-311G(d,p)[H,C,N,O,S]/IEFPCM(CH_2Cl_2) geometry. The overall calculated spectra are convoluted using Gaussian functions with FWHM = 3000 cm^{-1}. The calculated spectra are empirically shifted to match the experimental peak at 443 nm and the intensity is scaled to guide the eye.

eigenstates further from the end of the excitation space sought and thus the two approaches should be comparable.

As previously noted, [Pt(bipyCOOEt)(C≡C-Ph-CH_2-PTZ)$_2$] would be expected to display strong relativistic behaviour due to the high atomic number of Pt. Indeed, numerous recent studies have sought to examine the effects of both scalar and spin-orbit relativistic effects on the electronic structure of molecules that contain Pt.[227,340–344] Relativistic quantum mechanics is significantly more complex than non-relativistic quantum mechanics (See Section 2.5). One of the main reasons for this is that whereas the non-relativistic one electron operator is scalar, the fully relativistic Dirac Hamiltonian is a 4 × 4 matrix operator. Furthermore, electronic orbit-

als now have four components since they explicitly consider spin as well as the anti-particle of the electron, the positron.[204,213] Therefore, the first choice that must be made when computing relativistic wave- or density-functions is the representation of the electrons. There are three common approaches: the Scalar Relativistic (SR) approach, in which spin-orbit effects are ignored and electronic states remain of well-defined spin,[345–347] the Two-Component (2C) or quasi-relativistic approach in which the positronic solutions to the Dirac Hamiltonian are "projected out" and ignored,[214,216,217] or the fully relativistic, Four-Component (4C) approach, in which no approximations are made. If a SR approach is taken, SOC terms can be re-introduced by coupling the resultant spin-pure states perturbatively.[280]

There is a significant computational cost associated with the inclusion of relativistic effects, particularly when 2C or 4C Hamiltonians are used. Once again, the large size of [Pt(bipyCOOEt)(C≡C-Ph-CH_2-PTZ)$_2$] limits the extent of tractable methods. Fortunately, since the ground electronic state is well separated from the other electronic states, SOC-induced mixing between the ground state and the low-lying excited states should be small and so treating the ground state using the SR approximation should be sufficient. It is clear, however, that SOC will have a strong effect on the electronically excited states.[227,340,341] Therefore, SOC was included as a perturbative correction by mixing together a basis of SR-corrected spin-pure singlet and triplet excited states from TD-DFT to yield spin-free states.[280] The error introduced by the use this perturbative description of SOC compared to a 2C approach was estimated in Ref. [280] for $[Pt(CN)_4]^{2-}$, $[PtCl_4]^{2-}$ and $[PtCl_6]^{2-}$, for which the mean unsigned average error was 0.06 eV across 47 excited states with two functionals.

Relativistic effects on the electronic absorption spectrum of [Pt(bipyCOOEt)(C≡C-Ph-CH_2-PTZ)$_2$] are investigated in Figure 5.18 and are compared against the non-relativistic (NR) calculations previously discussed. The inclusion of SOC has a significant impact on the absorption spectrum, the most notable of which is the vast increase in the number of states that must be considered, since the states of majority triplet character are no-longer triply degenerate. Furthermore, SOC induces mixing between the singlet and triplet manifolds and so previously forbidden transitions are no longer so. The combination of these two phenomena results in an increase of allowed transitions and an overall broadening of the absorption spectrum. As

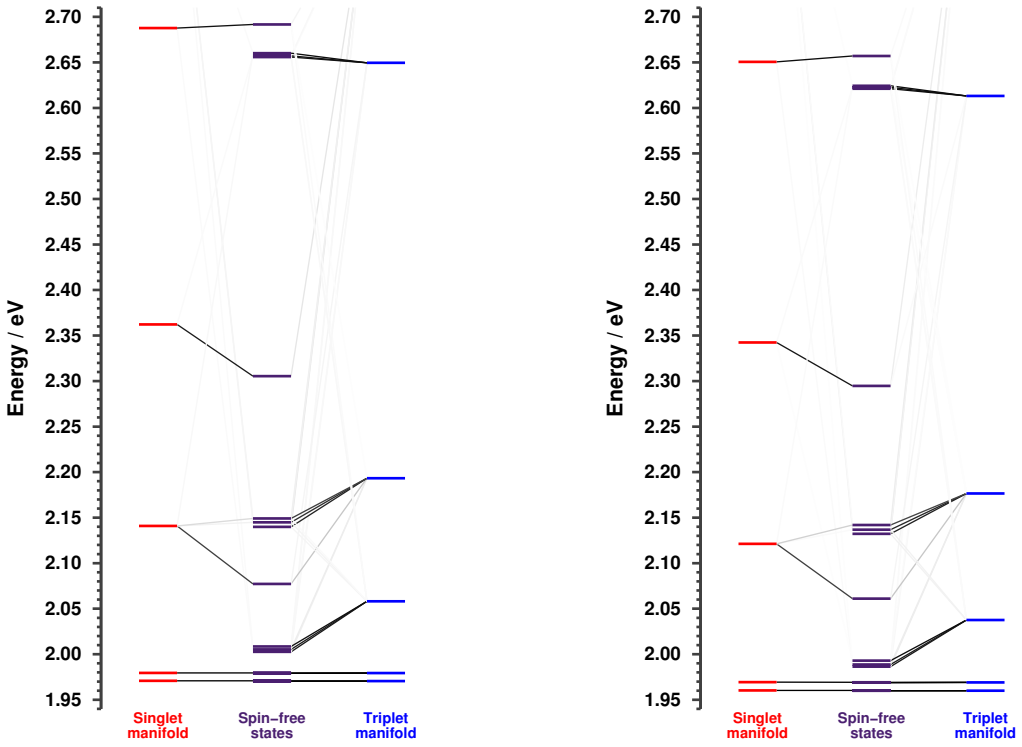

(i) TD-B3LYP(ZORA-PT)/DZP/COSMO **(ii)** TD-B3LYP(ZORA-PT)/TZP/COSMO

Figure 5.19: Construction of the lowest 20 spin-orbit coupled (spin-free) excited states of [Pt(bipyCOOEt)(C≡C-Ph-CH_2-PTZ)$_2$] from a basis of spin-pure, TD-B3LYP states within the perturbative approach using the Zero Order Regular Approximation (ZORA) Hamiltonian. The contribution from spin-pure state is colour coded from 0% (white) to 100% (black). The DZP and TZP basis sets were used in Figures 5.19(i) and 5.19(ii), respectively. A "large" frozen core, as defined by ADF, was employed in the calculations. Calculations were performed at the optimised B3LYP/SDD[Pt]6-311G(d,p)[H,C,N,O,S]/IEFPCM(CH_2Cl_2) geometry.

noted previously, the quality of the basis set can have an impact on the absorption spectrum. This is also considered in Figure 5.18, where double- and triple-ζ basis sets are compared, which contain 1137 and 1453 Core-orthogonalized Symmetrized Fragment Orbitals (CSFOs), respectively.[278] The convoluted spectra are very similar; however, careful inspection of the excitation energies reveals a red-shift, particularly for the metal-centred states, when the size of the basis set is increased. The effect is less marked than observed in Figure 5.17. This is due to the fact that no double-ζ quality, ZORA compatible basis set exists for Pt and so a triple-ζ Pt basis is used in its place.

The effect of SOC is explored in greater depth in Figure 5.19. The eight lowest energy spin-free states are CSSs localised on either side of the complex and are almost unnaffected by the inclusion of SOC when both DZP and TZP basis sets are used. Mixing between spin-

pure singlet and triplet states of these characters is vanishingly weak and the spin-free states are of ≥ 99.9% singlet or triplet character. Each set of four spin-free CSSs are also energetically degenerate to within 10^{-3} eV. The MLCT are more greatly effected by the inclusion of SOC than the CSSs. In particular the gap between the lowest MLCT, d_{xz}CT, and the CSSs is drastically reduced as strong SOC lowers the energy of the spin-free d_{xz}CT states of majority triplet character substantially. These majority triplet spin-free d_{xz}CT states are split by 0.006 eV and 0.007 eV in the DZP and TZP bases, respectively, and contain a ∼10% contribution each from higher spin-pure MLCT states in both bases. The d_{xz}CT spin-free state of majority singlet character contains a significant (∼20%) contribution from the d_{yz}CT spin-pure triplet. The spin-free d_{yz}CT states of majority triplet character also show strong splitting, 0.01 eV in both bases. These states contain between 7% and 15% spin-pure singlet or triplet d_{xz}CT, with further contributions from higher states. The contributions from higher states can be significant, up to 10% in total, highlighting the requirement of a large basis of spin-pure states when constructing spin-free states perturbatively. The strong mixing between d_{xz}CT and d_{yz}CT states could have an impact on the relaxation dynamics of the system. The spin-free d_{yz}CT state of majority singlet character is strongly effected by SOC; however, it remains well separated energetically from the lower energy states and so is not strongly mixed with the d_{xz}CT states. The highest energy spin-free states in this region, of $d_{x^2-y^2}$CT in character, are weakly blue-shifted with respect to their spin-pure counterparts by ∼0.01 eV. The $d_{x^2-y^2}$CT states are weakly mixed with other states, with a maximum 7% contribution from spin-pure states of non-$d_{x^2-y^2}$CT character.

These results highlight the importance of including SOC in the treatment of the electronic excited states of Pt complexes. It should also be noted that in these calculations, the core electrons of the complex have been frozen. This could result in additional errors; however, the inclusion of core electrons renders the calculation intractable. This is due to a balance between a large increase in the complexity of the SCF procedure, since 212 core electrons are frozen and increased difficulty in the convergence of the TD-DFT *eigenstates*. Since the stated intention of this work is to investigate the PES of [Pt(bipyCOOEt)(C≡C-Ph-CH_2-PTZ)$_2$], efforts were made to find lower cost approaches to the problem. The computational "bottleneck" is the *eigenvalue* problem presented by TD-DFT and constitutes between 97% and 99% of the total wall-clock

time of the calculations. One approach that could be taken is the use of the Tamm-Dancoff Approximation (TDA) previously discussed. This could reduce the time taken to solve the TD-DFT problem by approximately 30%. This, however, would still leave a more thorough investigation computationally intractable. Recently, the group of Stefan Grimme have developed approximations to the full TDA- and RPA-TD-DFT problem, dubbed simplified TDA and TD (sTDA and sTD).[192–194] These methods use three major simplifications: 1) the two-electron integrals that form part of the **A** matrix in the Casida equations are approximated by short range, damped Coulomb interactions from monopoles given by a Löwdin population analysis of the transition charge density 2) the global exchange portion of the two-electron integrals in **A** are ignored and 3) parts of the configuration space for the occupied-virtual pairs that contribute to each transition are ignored on the basis of energy and the CI space is truncated to about 1% of its original size. Whilst these approximations are, in the words of their developers, drastic, they reduce computation time of the (s)TD-DFT problem by two to three orders of magnitude.[193] Further theoretical details concerning these methods are provided in Section 2.4. These approximate methods have been implemented in ADF recently and thus provide an appealing approach to reduce computational time.

It is important to establish the accuracy of the sTD method. With this in mind, the calculated electronic absorption spectra using TD-B3LYP and sTD-B3LYP are compared in Figure 5.20. It should be noted that even though the sTD-DFT calculation sought an excitation space 5× larger than the TD-DFT calculation, the sTD-DFT calculation took 2.3% of the time to compute the excitations. If the same size excitation space was sought, the sTD-DFT calculation took 0.6% as long as the full TD-DFT calculation. There are, however, discrepancies between the calculated excitations using the two methods. The approximate sTD-B3LYP excitations require a larger empirical shift for good agreement with experiments to be achieved. Furthermore, the difference between sTD-B3LYP and TD-B3LYP is not linear as some peaks underestimated by sTD-B3LYP whereas others are overestimated. This is observed in the 400 nm to 600 nm region, where the energy of the majority singlet $d_{x^2-y^2}$CT state is overestimated by sTD-B3LYP, whereas the majority singlet d_{xz}CT state is underestimated. Furthermore, the low energy CSSs are strongly effected by the use of sTD-B3LYP, as highlighted in the inset. The gap between the

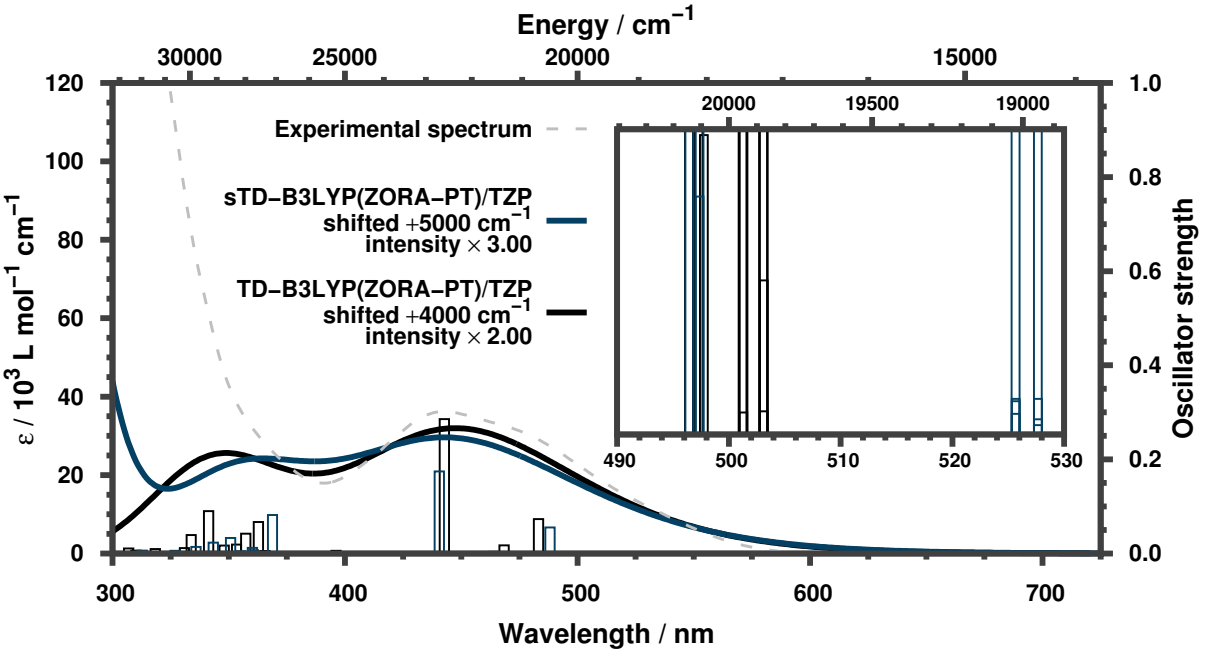

Figure 5.20: Comparison of experimental UV-vis absorption spectra (dashed, light grey) of [Pt(bipyCOOEt)(C≡C-Ph-CH_2-PTZ)$_2$] to convoluted calculated Time Dependent B3LYP (TD-B3LYP, black) and simplified TD-B3LYP (sTD-B3LYP, dark blue) spectra including Spin-Orbit Coupling (SOC) perturbatively in the (s)TD procedures using the Zero-Order Regular Approximation (ZORA-PT). The lowest 20 (TD) and 100 (sTD) spin-pure excitations were found, resulting in a total of 80 (TD) and 400 (sTD) spin-free excitations. The TZP basis set, including a 'large' set of frozen core electrons as defined by ADF, was used for both calculations. Solvent (CH_2Cl_2) was included implicitly using COSMO. Calculations were performed at the optimised B3LYP/SDD[Pt]6-311G(d,p)[H,C,N,O,S]/IEFPCM(CH_2Cl_2) geometry. The overall calculated spectra are convoluted using Gaussian functions with FWHM = 3000 cm^{-1}. The calculated spectra are empirically shifted to match the experimental peak at 443 nm and the intensity is scaled to guide the eye. The 490 nm to 530 nm region is magnified in the inset, highlighting low energy, weakly allowed transitions.

majority triplet d_{xz}CT states and the CSSs in TD-B3LYP is ~0.03 eV, whereas in sTD-B3LYP this gap is ~0.13 eV. Whilst the overestimation of the separation between the d_{xz}CTs and the CSSs will have an effect on the topology of the PES, the CSSs and CT states are not strongly mixed (See Figure 5.19) and so this effect should be limited to separation between and not the overall shapes of the surfaces. The spin-free states in sTD-B3LYP are also less strongly mixed than those from TD-B3LYP, as demonstrated by the fact that one of the TD-B3LYP majority triplet d_{yz}CT spin-free states can be seen in Figure 5.20 in the 470 nm region but is absent in the sTD-B3LYP spectrum. It should be noted that the oscillator strengths calculated using sTD-B3LYP are significantly lower than those derived from full TD-B3LYP.

Since sTD-DFT drastically reduces the time taken to calculate electronic excitations, the

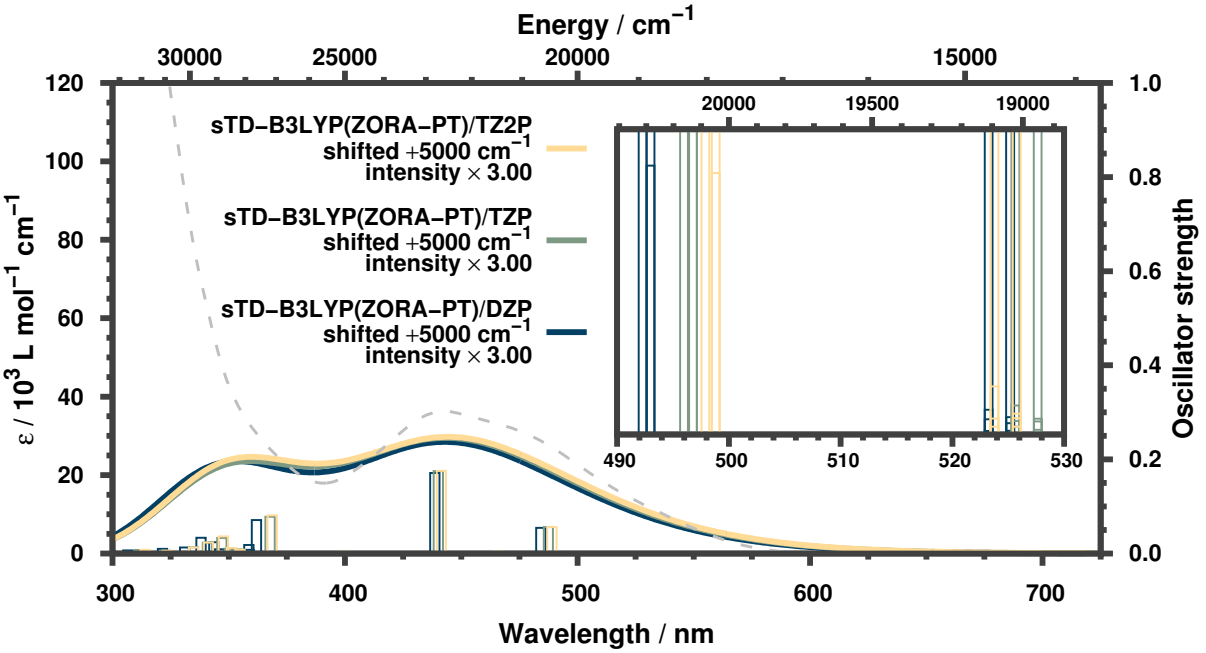

Figure 5.21: Comparison of experimental UV-vis absorption spectra (dashed, light grey) of [Pt(bipyCOOEt)(C≡C-Ph-CH_2-PTZ)$_2$] to convoluted calculated simplified Time Dependent B3LYP (sTD-B3LYP) spectra including Spin-Orbit Coupling (SOC) perturbatively in the sTD procedures using the Zero-Order Regular Approximation (ZORA-PT). The lowest 20 spin-pure excitations were found, resulting in a total of 80 spin-free excitations. The DZP (dark blue), TZP (grey-blue) and TZ2P (peach) were used, including a 'large' set of frozen core electrons as defined by ADF in all cases. Solvent (CH_2Cl_2) was included implicitly using COSMO. Calculations were performed at the optimised B3LYP/SDD[Pt]6-311G(d,p)[H,C,N,O,S]/IEFPCM(CH_2Cl_2) geometry. The overall calculated spectra are convoluted using Gaussian functions with FWHM = 3000 cm^{-1}. The calculated spectra are empirically shifted to match the experimental peak at 443 nm and the intensity is scaled to guide the eye. The 490 nm to 530 nm region is magnified in the inset, highlighting low energy, weakly allowed transitions.

quality of basis set can be expanded. Figure 5.21 compares the results of sTD-B3LYP calculations with the DZP, TZP and TZ2P basis sets. The TZ2P basis set contains addition polarisation functions, giving a total of 2156 CSFOs, significantly larger than the TZP basis. It should be noted that an even larger basis set is available (QZ4P) and attempts were made to perform sTD-B3LYP calculations using this basis set; however, a bug in the ADF program prevented the calculation from proceeding. (See "r52330" on the ADF bugfix change-log website.[348]) For the majority of excitations, increasing the size of the basis set results in a small red-shift in energy. As expected, the greatest effect is observed when DZP is expanded to TZP. The addition of further polarisation functions in TZ2P does influence excitation energies, but only slightly. The change in energy is not uniform, however. The lowest energy, CSSs are inconsistently ef-

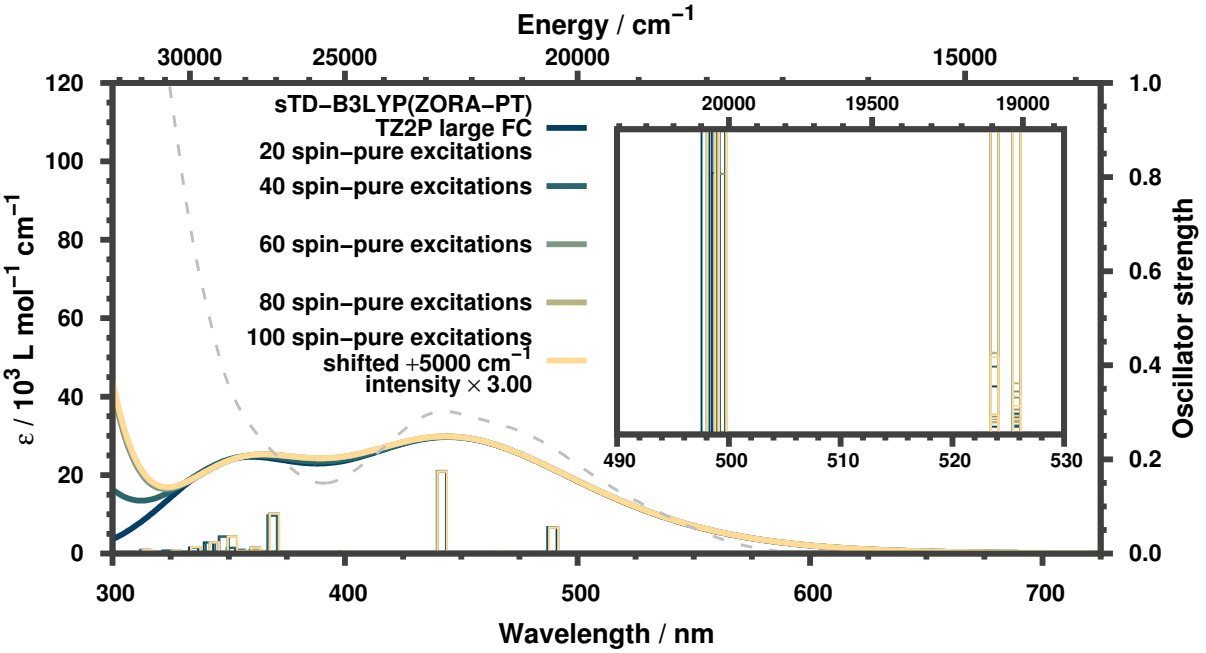

Figure 5.22: Comparison of experimental UV-vis absorption spectra (dashed, light grey) of [Pt(bipyCOOEt)(C≡C-Ph-CH_2-PTZ)$_2$] to convoluted calculated simplified Time Dependent B3LYP (sTD-B3LYP) spectra including Spin-Orbit Coupling (SOC) perturbatively in the sTD procedures using the Zero-Order Regular Approximation (ZORA-PT). The lowest 20, 40, 60, 80 and 100 spin-pure excitations were found, resulting in a total of 80, 160, 240, 320 and 400 spin-free excitations and are colour coded in order of increasing size of excitation space from dark blue to peach. The TZ2P basis set was used in all cases including a 'large' set of frozen core electrons as defined by ADF. Solvent (CH_2Cl_2) was included implicitly using COSMO. Calculations were performed at the optimised B3LYP/SDD[Pt]6-311G(d,p)[H,C,N,O,S]/IEFPCM(CH_2Cl_2) geometry. The overall calculated spectra are convoluted using Gaussian functions with FWHM = 3000 cm^{-1}. The calculated spectra are empirically shifted to match the experimental peak at 443 nm and the intensity is scaled to guide the eye. The 490 nm to 530 nm region is magnified in the inset, highlighting low energy, weakly allowed transitions.

fected by increasing the size of the basis set. Increasing from DZP to TZP lowers the energies by approximately 150 cm^{-1}. However, the addition of further polarisation functions in TZ2P raises the energy back by approximately 100 cm^{-1}, resulting in an overall very small reduction in energy of the CSSs when comparing DZP and TZ2P. The low energy spin-free d_{xz}CT states are consistently reduced by the expansion of the basis set and thus the anomalously large gap in sTD-B3LYP between the lowest d_{xz}CTs and CSSs is slightly reduced in TZ2P compared to DZP and TZP, although the effect is small. Oscillator strength is relatively unaffected by the increase in size of basis set.

Like the full TD-DFT method, the electronic excitation problem within sTD-DFT is solved

iteratively by a modified Davidson algorithm.[349] The additional errors introduced from this should have a very small effect on energies of the resultant spin-pure excitations; however, the spin-free excitations can have contributions from many spin-pure states, including ones much higher in energy than the dominant spin-pure states for a given spin-free state. In Figure 5.22 the convergence of the spin-free excitations with respect to the size of the spin-pure basis is examined. In the 400 nm to 600 nm region, the effect of expanding the excitation space is very limited. The biggest change, observed when expanding the space from 20 to 40 excitations, results in a difference below 50 cm^{-1} for all excitations in this region. Increasing the excitation space does change the degree of mixing between singlet and triplet spin-pure in the construction of spin-free states, as highlighted by the changes in oscillator strength of the CSS peaks at ~19000 cm^{-1}. The effects of the degree of mixing of the CSSs is very small and the corresponding oscillator strengths vary by $\sim 5\times10^{-7}$.

As previously mentioned, the high cost of full TD-DFT calculations meant that performing fully relaxed SCF calculations, *i.e.* without a frozen core of electrons, computationally intractable. The use of sTD-DFT, however, shifts the computational "bottleneck" to the solution of the SCF equations. This provides the opportunity to explore the effect of a fully relaxed SCF procedure on the electronic absorption spectrum of [Pt(bipyCOOEt)(C≡C-Ph-CH_2-PTZ)$_2$]. Figure 5.23 compares the results of sTD-B3LYP calculations with and without a frozen core of electrons in the TZ2P basis when a large excitation space of 100 spin-pure states is sought. The relaxation of the core orbitals has a relatively small effect but non-uniform on the electronic excitations in the 400 nm to 600 nm region. The high energy $d_{x^2-y^2}$CT states are slightly red-shifted, the medium energy d_{yz}CT states almost unaffected and the low energy d_{xz}CT states slightly blue-shifted as a result of core orbital relaxation. The lowest energy CSSs are also blue-shifted as a result of core orbital relaxation. This combination of shifts means that the gap between d_{xz}CT states and CSSs is slightly smaller in the relaxed core calculation than the frozen core calculation. The small effect of relaxing the core orbitals when sTD-DFT is used is expected, since the approximations employed in the sTD-DFT method include neglecting terms associated with orbital transitions that contribute weakly to transitions, thus the major effect will be due to subtle alterations in the valence orbitals as a result of changes in core orbital

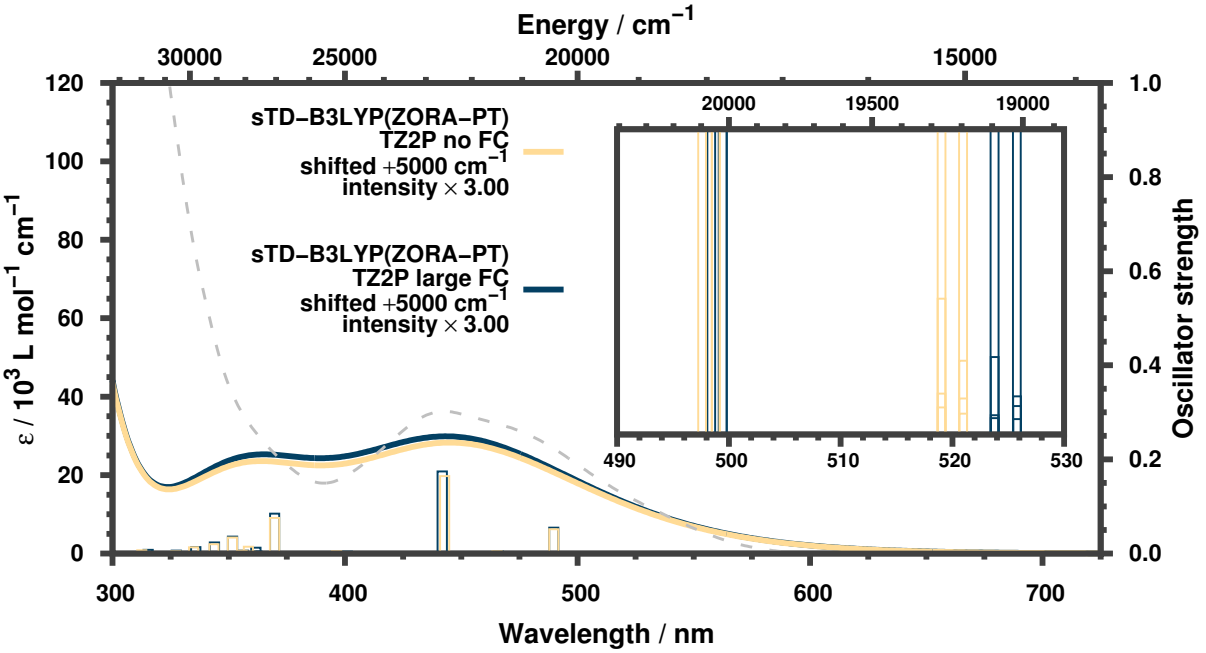

Figure 5.23: Comparison of experimental UV-vis absorption spectra (dashed, light grey) of [Pt(bipyCOOEt)(C≡C-Ph-CH_2-PTZ)$_2$] to convoluted calculated simplified Time Dependent B3LYP (sTD-B3LYP) spectra including Spin-Orbit Coupling (SOC) perturbatively in the sTD procedures using the Zero-Order Regular Approximation (ZORA-PT). The lowest 100 spin-pure excitations were found, resulting in a total of 400 spin-free excitations. The TZ2P basis set was used in both cases including a 'large' set of frozen core electrons as defined by ADF (peach) or no frozen core electrons (blue). Solvent (CH_2Cl_2) was included implicitly using COSMO. Calculations were performed at the optimised B3LYP/SDD[Pt]6-311G(d,p)[H,C,N,O,S]/IEFPCM(CH_2Cl_2) geometry. The overall calculated spectra are convoluted using Gaussian functions with FWHM = 3000 cm^{-1}. The calculated spectra are empirically shifted to match the experimental peak at 443 nm and the intensity is scaled to guide the eye. The 490 nm to 530 nm region is magnified in the inset, highlighting low energy, weakly allowed transitions.

shielding.

The construction of the spin-free states from a basis of spin-pure states within TD-B3LYP and sTD-B3LYP is compared in Figure 5.24. There are a number of differences observed between the results of full and simplified TD-DFT calculations. The overall gap between the highest and lowest spin-free state is 0.05 eV smaller in the full TD-DFT calculation. This is the result of a combination of a relative blue- and red-shift of the $d_{x^2-y^2}$CT and CSSs, respectively. (See Figure 5.20) The gap between the low energy CSSs and the spin-free states of d_{xz}CT character is ~0.07 eV larger in the sTD-B3LYP calculations than the TD-B3LYP calculations. This is due to a relative blue-shift of 0.07 eV and 0.10 eV on average of the spin-pure singlet and triplet CT states, respectively, in the simplified compared to the full TD-B3LYP approach.

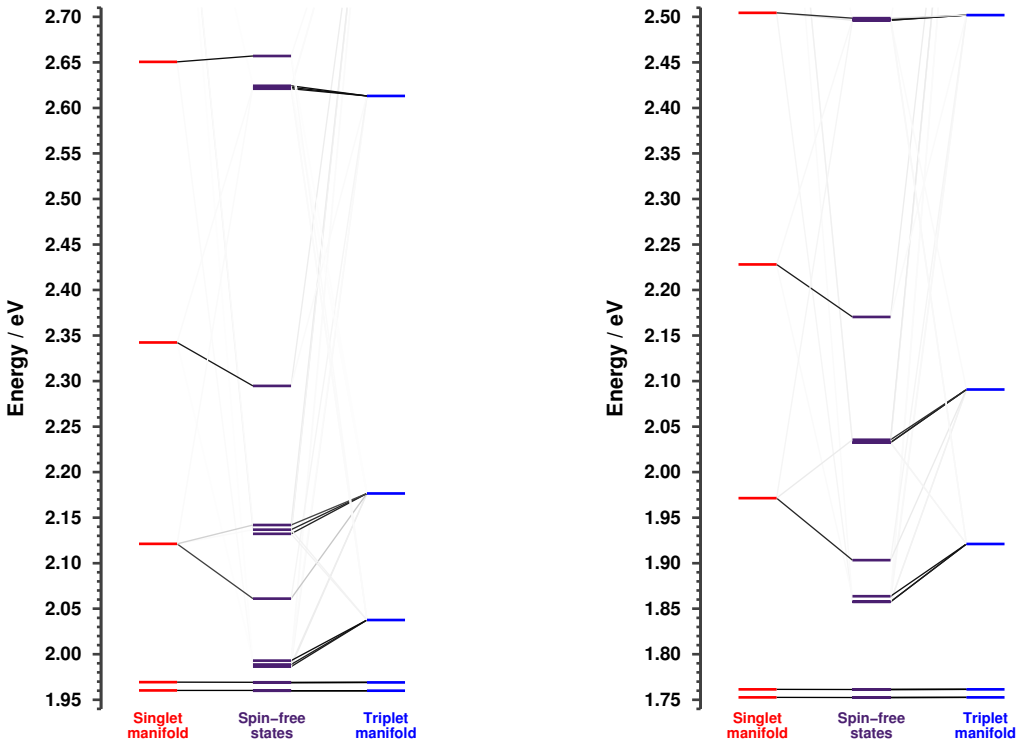

(i) TD-B3LYP(ZORA-PT)/TZP/COSMO **(ii)** sTD-B3LYP(ZORA-PT)/T2ZP/COSMO

Figure 5.24: Construction of the lowest 20 spin-orbit coupled (spin-free) excited states of [Pt(bipyCOOEt)(C≡C-Ph-CH_2-PTZ)$_2$] from a basis of spin-pure, (s)TD-B3LYP states within the perturbative approach using the Zero Order Regular Approximation (ZORA) Hamiltonian. The contribution from spin-pure state is colour coded from 0% (white) to 100% (black). The lowest 20 spin-pure excitations were found using full TD-B3LYP method along with the TZP basis which used a "large" frozen core, as defined by ADF, in Figure 5.24(i). The lowest 1000 spin-pure excitations were found using the sTD-B3LYP method and the TZ2P basis with no frozen core electrons in Figure 5.24(ii). In both cases solvent was included implicitly using COSMO. Calculations were performed at the optimised B3LYP/SDD[Pt]6-311G(d,p)[H,C,N,O,S]/IEFPCM(CH_2Cl_2) geometry. Note the difference in the y axis scale between the two figures.

The degree of mixing between spin-pure singlet and triplet basis states in the construction of spin-free states of CT character is similar in both simplified and full TD-DFT, with an average largest contribution from a spin-pure state of 87.2% and 88.7%, respectively. The splitting of the spin-pure states of majority triplet character of the same type is markedly smaller when simplified TD-DFT is used; however, it is difficult to explain why this is the case since the method by which the spin-pure basis is perturbatively combined to produce spin-free states is identical in both simplified and full TD-DFT. It should be noted that the energies of the spin-pure MLCT excitations calculated within sTD-B3LYP(ZORA-PT)/TZ2P/COSMO are remarkably similar to those calculated using non-relativistic TD-B3LYP/SDD[Pt]6-311G(d,p)[H,C,N,O,S]/IEFPCM.

(See Table 5.5) This is as a result of a cancellation of errors. Indeed, within TD-B3LYP(ZORA-PT)/TZP/COSMO it is the spin-free states that resemble the results derived from the non-relativistic calculations.

In summary, excellent agreement between calculated electronic absorption and experimental UV/visible spectra was achieved by use of Time-Dependent and simplified Time-Dependent Density Functional Theory calculations. Of particular note is the fact that the sTD-B3LYP approach combined with the scalar relativistic Zero Order Regular Approximation (ZORA) Hamiltonian with perturbative inclusion of Spin Orbit Coupling provided a cost-effective yet accurate means of extending calculations of the electronic absorption spectra of large molecules into the relativistic domain.

In combination with the results of Section 5.2, which showed that the unusually complex vibrational structure of isotopically labelled [Pt(bipyCOOEt)(C≡C-Ph-CH_2-PTZ)$_2$] could be well described by B3LYP/SDD[Pt]6-311G(d,p)[H,C,N,O,S]/IEFPCM(CH_2Cl_2) calculations, anharmonically corrected by means of Generalized Vibrational Perturbation Theory to second order (GVPT2), these results show that both the electronic and vibrational structure of [Pt(bipyCOOEt)(C≡C-Ph-CH_2-PTZ)$_2$] could be accurately investigated with these methods. The following section will seek to explore the Potential Energy Surface of [Pt(bipyCOOEt)(C≡C-Ph-CH_2-PTZ)$_2$] in an attempt to explain the ultrafast electron transfer dynamics observed experimentally and explained in Section 5.2.1.

5.4 Exploring the Potential Energy Surface along the vibrational coordinates of [Pt(bipyCOOEt)(C≡C-Ph-CH_2-PTZ)$_2$]

The time-dependent behaviour observed in a system are a result of the forces that act upon the system. In molecular systems, the forces that act upon a molecule depend upon the topology of the Potential Energy Surface (PES). To understand the dynamics that occur as a result of photoexcitation of [Pt(bipyCOOEt)(C≡C-Ph-CH_2-PTZ)$_2$], it is helpful to explore the PES of the molecule in its electronically excited states. Ideally, all 333 vibrational degrees of freedom of the system should be examined; however, this is computationally intractable. Instead, only a select few vibrational modes can be explored. Since the only vibrational modes whose excitation result in perturbation of the excited state population of **13-12** are the acetylide vibrations, these modes must be included in the investigations. Furthermore, the components of the combination band must also be included, since the combination band is strongly coupled to the $^{13}C\equiv{}^{13}C$ acetylide stretch and so these modes are very likely to become populated through Intramolecular Vibrational Relaxation (IVR) processes. The corresponding vibrational modes of **12-12** are also explored to act as a "control" experiment, since no directionality was observed in the dynamics of **12-12**. Therefore any features that are common in both **12-12** and **13-12** cannot be responsible for the directional control. Unlike in the case of the systems explored in Chapter 4, the prominent excited states involve atoms across the entire molecule. It is therefore not possible to truncate the geometry of [Pt(bipyCOOEt)(C≡C-Ph-CH_2-PTZ)$_2$] in a sensible manner. As a result of this, optimisation of the excited states of the system is not computationally feasible. Fortunately, the geometry of the MLCT states is very unlikely to be significantly different to that of the ground state, apart from changes in the Pt-C≡C regions, since these are the regions of greatest change in electron density (See Figure 5.12). As acetylide-centred vibrational modes will explore changes in these coordinates, it is convenient to restrict the investigations of the PES to the ground state normal modes of the types discussed above. It should be noted that within B3LYP/SDD[Pt]6-311G(d,p)[H,C,N,O,S]/IEFPCM(CH_2Cl_2), two optimised minimum energy geometries were found in the triplet manifold. These correspond to the two CSSs, con-

sistent with the experimental evidence.

The regions of the PES defined by the acetylide centred vibrational modes of **12-12** and **13-12** at the non-relativistic B3LYP/SDD[Pt]6-311G(d,p)[H,C,N,O,S]/IEFPCM(CH_2Cl_2) level of theory are shown in Figure 5.25. It should be noted that the surfaces are constructed by displacing the geometry of [Pt(bipyCOOEt)(C≡C-Ph-CH_2-PTZ)$_2$] along the dimensionless vibrational normal modes *eigenvectors*, *Q*, as defined by Gaussian.[274] To facilitate easier comparison between vibrational modes, an acetylide bond length is also shown. It is useful to recall that, as illustrated in Figure 5.2, the $^{13}C\equiv{}^{13}C$ acetylide is on the right-hand side of the molecule whereas the $^{12}C\equiv{}^{12}C$ acetylide is on the left-hand side of the molecule. Diagrams of the differences in electron density that occur as a result of the excitations are also provided in Figure 5.12. The *eigenvectors* and numbering of the vibrational modes are shown in Figure 5.5. It should be noted that due to the presence of Pt in the system and the long lifetime of excited states observed, it is assumed that the system undergoes rapid Intersystem Crossing (ISC) from the singlet to triplet manifold. However, due to the unusual shape of some of the PESs, it is necessary to include both of manifolds in the diagrams.

In general, the **12-12** and **13-12** PESs appear very similar to each other. The major difference is that the **12-12** surfaces appear to be a linear combination of the **13-12** surfaces. This is not surprising, as the **12-12** acetylide vibrations are coupled, linear combinations of uncoupled **13-12** modes. (See Appendix A.5) The unusual topological features in the PESs take the form of perceived discontinuities in the gradient that can be observed for some states when the singlet and triplet manifolds come close in energy. A clear example of this can be observed in the d_{yz}CT states along the **13-12** vibrations. A near-degeneracy between $^1d_{yz}$CT and $^3d_{yz}$CT occurs at R(C≡C)≈1.25 Å. Since $^3d_{yz}$CT has a minimum at R(C≡C)≈1.22 Å, as R(C≡C) increases it appears that $^3d_{yz}$CT should become higher in energy than $^1d_{yz}$CT. However, no crossover occurs and it appears that $^3d_{yz}$CT continues the shape of $^1d_{yz}$CT and vice versa. The apparent discontinuity is absent along the **12-12** coordinates. The presence of this discontinuity is confusing, since the calculations in each spin manifold are performed as linear excitations into the space of excitations of only that multiplicity from the electronic ground state at that multiplicity. With this in mind, one possible explanation is that in the region of R(C≡C)≈1.25 Å the ground state

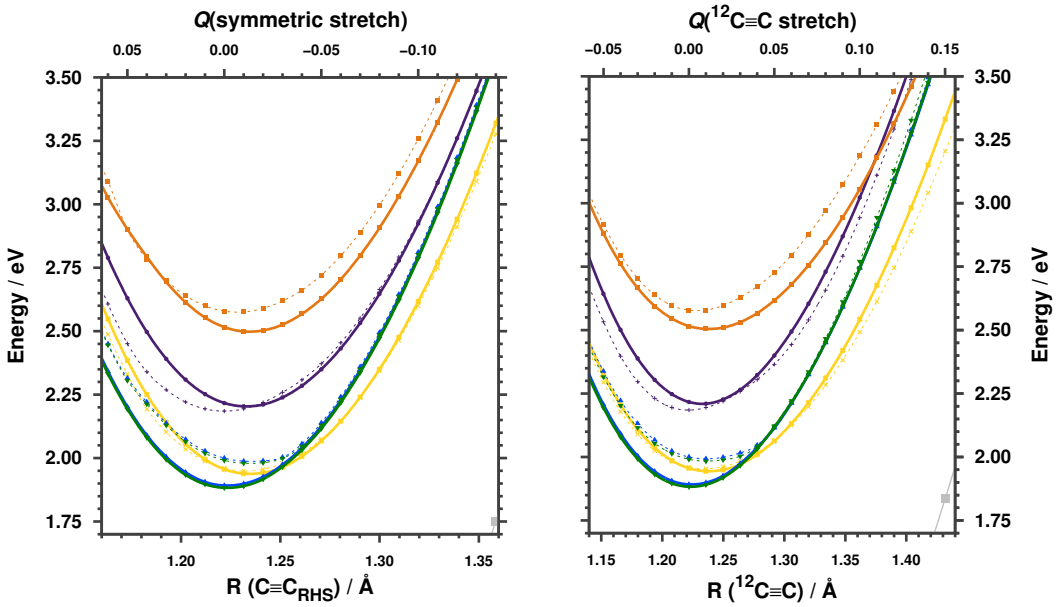

(i) 12-12: symmetric acetylide combination. $^{12}\nu_{289}$

(ii) 13-12: $^{12}C\equiv{}^{12}C$ stretch. $^{13}\nu_{289}$

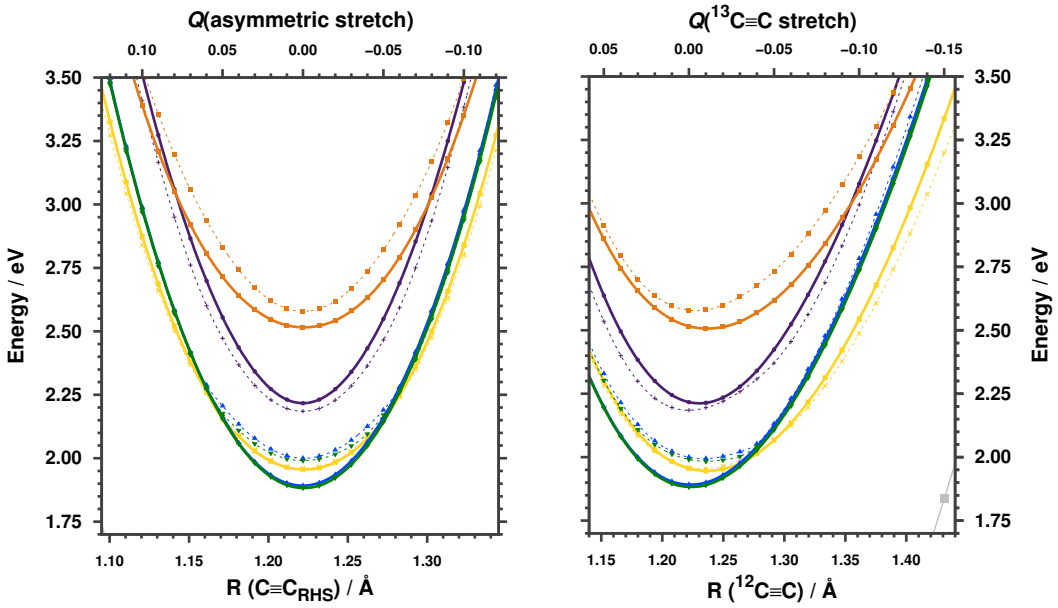

(iii) 12-12: asymmetric acetylide combination. $^{12}\nu_{288}$

(iv) 13-12: $^{13}C\equiv{}^{13}C$ stretch. $^{13}\nu_{288}$

Figure 5.25: Potential energy curves along the acetylide-centred vibrational modes of [Pt(bipyCOOEt)(C≡C-Ph-CH_2-PTZ)$_2$] calculated using ground state and time-dependent B3LYP/SDD[Pt]6-311G(d,p)[H,C,N,O,S]/IEFPCM(CH_2Cl_2). Displacement vectors for the vibrations are illustrated in Figure 5.5. Singlet states, calculated within the restricted formalism, are connected by thick lines, whereas triplet states, calculated within the unrestricted formalism, are connected by dashed thin lines. The states are colour coded as follows: ground state (grey), ^{RHS}CSS/^{13}CSS (green), ^{LHS}CSS/^{12}CSS (blue), d_{xz}CT (yellow), d_{yz}CT (purple) and $d_{x^2-y^2}$CT (orange). The changes in electron density associated with these states at the S_0 geometry are illustrated in Figure 5.12.

of the triplet manifold is of mixed character, since the d_{xz}CT and ^{13}CSS states become very close in energy and this mixed character leads to a breakdown in the approximations employed in linear response TD-DFT. This, however, would not explain why the singlet multiplicity calculations also show a derivative discontinuity, as the singlet ground state is well separated from the first singlet excited state. Another example of the perceived discontinuity can be found in the shape of the CSSs of triplet multiplicity. In the Franck-Condon region, the singlet CSSs are approximately 0.1 eV lower in energy than the triplet CSSs. However, as the stretching modes extend, the singlet and triplet CSSs become almost degenerate in energy. This results in a clear change in gradient of the triplet CSSs, though no perceptible change is observed in the singlets. One possible explanation for this is the well known deficiency of TD-DFT in the description of a Conical Intersection (CoIn) between the ground and first excited state of a spin manifold and the accompanying defective topology of the PES in this region.[162] Since in this region the triplet ground state, $^3d_{xz}$CT, and the triplet CSS become close in energy, this could possibly explain the perceived discontinuity if there was a CoIn in this region. However, it is not possible to directly optimise a CoIn using regular TD-DFT and so this cannot be confirmed. Furthermore, defects due to the presence of a CoIn between a ground and excited state would not explain the observed behaviour of the d_{yz}CT states. It is therefore difficult to explain the presence of the derivative discontinuities. It should also be noted that each single-point calculation performed in the construction of these PESs was independent: the SCF at each point was performed without an initial guess supplied from other calculations and the *eigenvectors* generated in the TD-DFT procedure from the results of the SCF were generated using the default settings in Gaussian 09.

Both the singlet and triplet CSSs remain almost energetically degenerate along all four acetylide stretching coordinates. This is to be expected since the acetylide-centred vibrational modes contain no motion on either of the phenothiazine groups and so an energetic preference for a CSS localised on either side is unlikely to develop from this perturbation. This effect is, however, very slightly asymmetrical: extension of the C≡C bond destabilizes the CSS located on the opposite side more than on that side, *i.e.* extending the ^{13}C≡^{13}C bond will destabilize ^{12}CSS more than ^{13}CSS. Since the ground state geometry employed in the calculations is asymmetrical, with a small 0.009 eV bias towards ^{13}CSS/^{RHS}CSS, this is most easily observed in the

vibrations of **13-12**, particularly $^{13}\nu_{288}$, where the separation between the triplet CSSs increases from 0.009 eV to 0.059 eV when R(^{13}C≡^{13}C)≈1.40 Å. This energetic preference is far too small to explain the observed vibrational control phenomena alone, although it does act in a manner consistent with the observations. If the gap in energy between CSSs becomes greater along similar vibrational coordinates in other regions of the PES, for example in the optimised geometries of the states of Charge Transfer (CT) character, this could have a significant effect on the dynamics; however, since optimisation of these states is not computationally feasible it is not possible to explore this.

The three sets of states of CT character are well separated from each other, approximately 0.25 eV apart in the equilibrium geometry. The lowest energy of these, the states of d_{xz}CT character, are close in energy to the CSSs. At the equilibrium geometry in the singlet manifold, the d_{xz}CT state is S_3 whereas in the triplet manifold it is T_1, the ground state of the triplet manifold. As the vibrations expand, $^1d_{xz}$CT intersects with the CSSs and becomes the lowest energy singlet excited state. Indeed, the lowest vibrational energy level of $^1d_{xz}$CT would sample this portion of the surface for each of the acetylide vibrational modes apart from $^{12}\nu_{288}$. In the triplet manifold, $^3d_{xz}$CT remains T_1 for along all coordinates apart from the contraction part of the totally symmetrical $^{12}\nu_{289}$ mode. For the two **12-12** modes, $^1d_{xz}$CT and $^3d_{xz}$CT are close in energy along the coordinates, whereas they separate slightly along the **13-12** coordinates, particularly as the bonds extend. The effect of the two **13-12** modes on the topology of the states of d_{xz}CT character is almost identical and no clear energetic origin for the observed vibrational control phenomenon can be identified if the ^{3}MLCT* state which is manipulated is of $^3d_{xz}$CT character.

The intermediate energy CT states, of d_{yz}CT character, are well separated from the higher and lower energy states for the majority of the regions of the PES defined by the vibrational modes, particularly in the triplet manifold. In the singlet manifold, $^1d_{yz}$CT intersects with the higher energy $^1d_{x^2-y^2}$CT state along all of the vibrational coordinates apart from $^{12}\nu_{289}$. In the triplet manifold, $^3d_{yz}$CT becomes relatively close in energy to the destabilised CSS along the extension of the two **13-12** coordinates and to both CSSs along $^{12}\nu_{289}$. This is most easily identified along $^{13}\nu_{289}$, where the energy gap between $^3d_{yz}$CT and ^{13}CSS becomes as low as

0.15 eV at when R(^{12}C≡^{12}C)≈1.40 Å. Due to the only weakly selective destabilization of the CSSs along the vibrational coordinates, this energy preference is not pronounced enough to lead to the directionality of the observed vibrational control.

The highest energy CT states are of $d_{x^2-y^2}$CT character and are well separated from the lower d_{yz}CT states in the Franck-Condon region, especially in the triplet manifold. In the triplet manifold, there are no crossings observed between the $^3d_{x^2-y^2}$CT state and other states along any of the coordinates investigated. Along the $^{12}\nu_{289}$ coordinate, however, an intersection between the $^1d_{x^2-y^2}$CT and $^3d_{x^2-y^2}$CT occurs at R(C≡C_{RHS})≈1.18 , resulting in a perceived gradient discontinuity in both spin manifolds. The $^1d_{x^2-y^2}$CT does undergo a number of crossings with the $^1d_{yz}$CT states in all of the modes apart from $^{12}\nu_{289}$. These crossovers take $^1d_{x^2-y^2}$CT relatively close in energy to the singlet CSSs, in particular along the **13-12** modes, leading to a gap as small as 0.15 eV between $^1d_{x^2-y^2}$CT and ^{12}CSS along $^{13}\nu_{288}$, similar to $^3d_{yz}$CT. However, like $^3d_{yz}$CT, the energetic preference is only weak and the excited state dynamics are likely to occur within the triplet manifold in this complex, so it is unlikely that this could be used to explain the experimental observations.

The sections of the PES defined by the components of the combination bands in **13-12** and the equivalent modes in **12-12** were also explored. The higher energy, phenyl-acetylide-centred fundamental "waving" modes are explored in Figure 5.26. It should be noted that these modes are almost identical in both isotopomers. (See *eigenvectors* in Figure 5.6). Comparison of the four modes yields little insight. Displacement along the dimensionless normal coordinate in either the positive or negative direction to $Q = \pm 0.25$ in the ν_{233} modes of either **12-12** or **13-12** results in an almost uniform increase in energy across the ten states plotted, an average of 0.272 eV. The two ν_{234} modes are slightly asymmetrical: an average increase of 0.272 eV at $Q = -0.25$, increasing to an average of 0.282 eV at $Q = +0.25$. The subtle difference between the ν_{234} and the ν_{233} modes could be due to the low numerical accuracy used in Gaussian in the expression of the normalized Cartesian displacement coordinates.[274] These are only expressed in the output to two decimal places and the normalization requires that the sum of squared coefficients is unity. This means that for delocalised vibrations with many small components, rounding errors may occur. Regardless, the almost uniform and symmetrical nature of the PESs

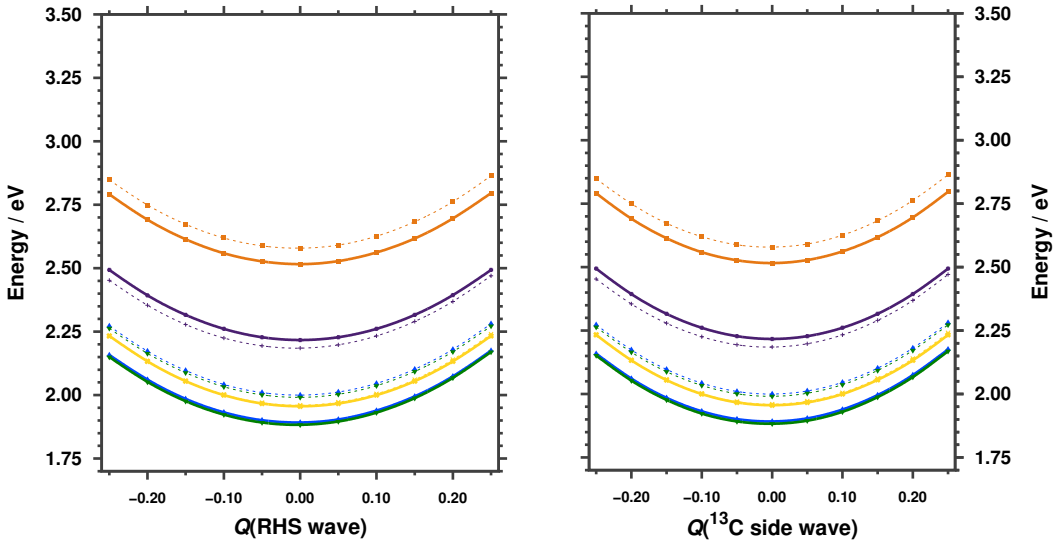

(i) 12-12: right-hand side wave. $^{12}\nu_{234}$

(ii) 13-12: ^{13}C side wave. $^{13}\nu_{234}$

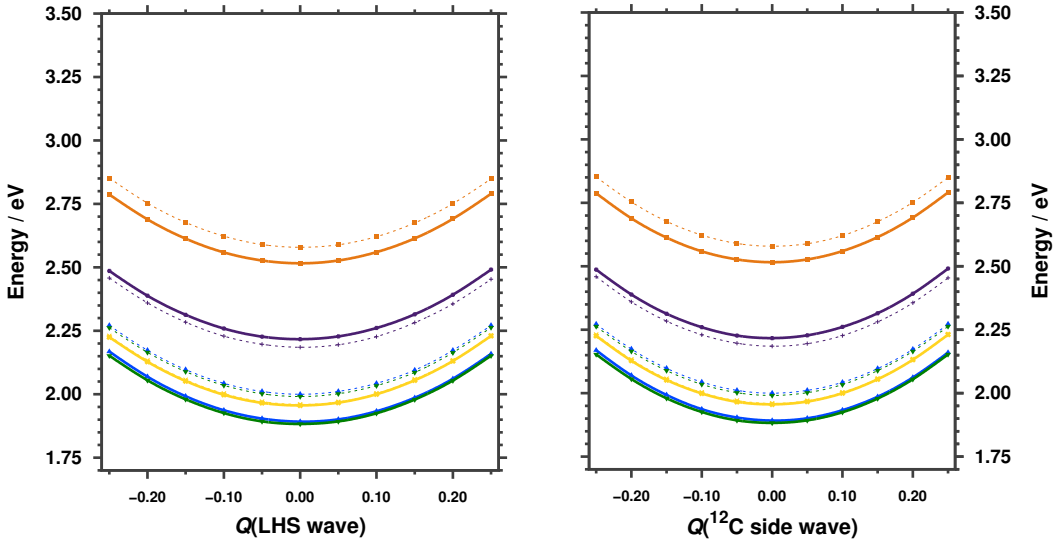

(iii) 12-12: left-hand side wave. $^{12}\nu_{233}$

(iv) 13-12: ^{12}C side wave. $^{13}\nu_{233}$

Figure 5.26: Potential energy curves along the bridge-centred vibrational modes of [Pt(bipyCOOEt)(C≡C-Ph-CH_2-PTZ)$_2$] calculated using ground state and time-dependent B3LYP/SDD[Pt]6-311G(d,p)[H,C,N,O,S]/IEFPCM(CH_2Cl_2). Displacement vectors for the vibrations are illustrated in Figure 5.6. Singlet states, calculated within the restricted formalism, are connected by thick lines, whereas triplet states, calculated within the unrestricted formalism, are connected by dashed thin lines. The states are colour coded as follows: ^{RHS}CSS/^{13}CSS (green), ^{LHS}CSS/^{12}CSS (blue), d_{xz}CT (yellow), d_{yz}CT (purple) and $d_{x^2-y^2}$CT (orange). The changes in electron density associated with these states at the S_0 geometry are illustrated in Figure 5.12.

along these coordinates suggests this mode alone would be very unlikely to a prominent effect on relaxation dynamics on the basis of purely energetic arguments.

The phenothiazine-centred fundamental bands that contribute to the combination bands are less symmetrical than the phenyl-acetylide ones and the corresponding PESs are shown in Figure 5.27. As is shown in Figure 5.6, the phenothiazine-centred modes cause significant distortions on the donor fragments of the complex. In **13-12**, these modes are localised on either donor whereas in **12-12** the two modes are delocalised across both donors, though the components are unevenly distributed. As a result of this, similar to the acetylide-centred vibrations, the PESs defined by the phenothiazine-centred in **12-12** resemble linear combinations of the **13-12** surfaces.

The CSSs are, as expected, strongly effected by changes in the geometry of the donors. In particular, the CSSs of singlet multiplicity are very strongly effected. The triplet multiplicity CSSs are effected but to a lesser extent. This is most easily identifiable along the **13-12** surfaces. It should be noted that this need not be a destabilization, since the loss on an electron on the phenothiazine group is accompanied by geometrical changes upon relaxation in which the group becomes planar (See Figure 4.10 for an illustration in a similar molecule). As the phenothiazine-centred mode *eigenvectors* have components that make the group more planar, the CSSs can be stabilised along these coordinates. Curiously whereas $^{13}\nu_{131}$ alternatively stabilises and destabilises the two singlet CSSs, $^{13}\nu_{130}$ only stabilises ^{12}CSS and destabilises ^{13}CSS. This may be an artefact of the geometry employed in the calculations, which favours ^{13}CSS slightly over ^{12}CSS. To verify that this is effect was not due to a computational problem in Gaussian 09 related to isotopic labelling, single point calculations at $Q = \pm 10$ along the equivalent vibrational coordinates of **13-13** were performed, yielding results almost identical to those along the **12-12** coordinates. In some regions of all of the coordinates, the most destabilised CSS becomes degenerate in energy with ^{1}d$_{xz}$CT. In the two **13-12** modes, this could lead to directionally selective increased transition probability from ^{1}d$_{xz}$CT to one of the singlet CSSs. Indeed, these regions would be accessible if the first vibrationally excited level was populated along these coordinates (~0.15 eV above the minimum of ^{1}d$_{xz}$CT). However, it is important to recall that the dynamics in these systems are more likely proceed in the triplet manifold. In the

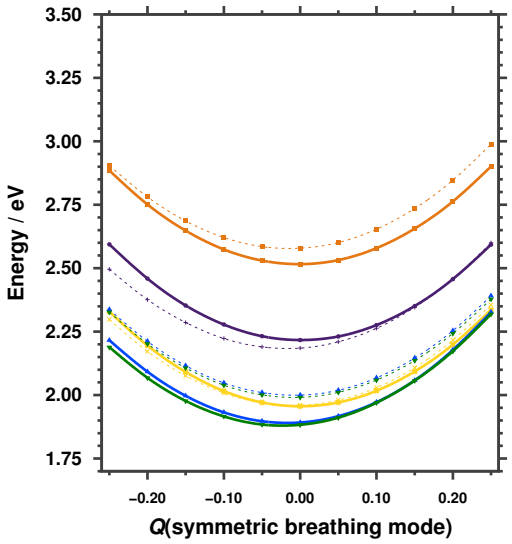

(i) 12-12: symmetric breathing combination mode. $^{13}\nu_{131}$

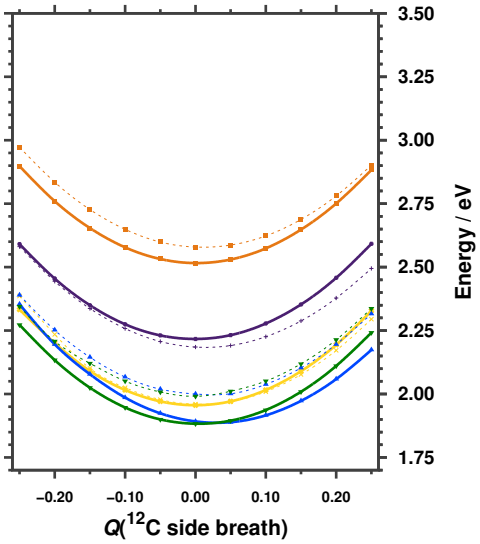

(ii) 13-12: ^{12}C side breathing mode. $^{13}\nu_{131}$

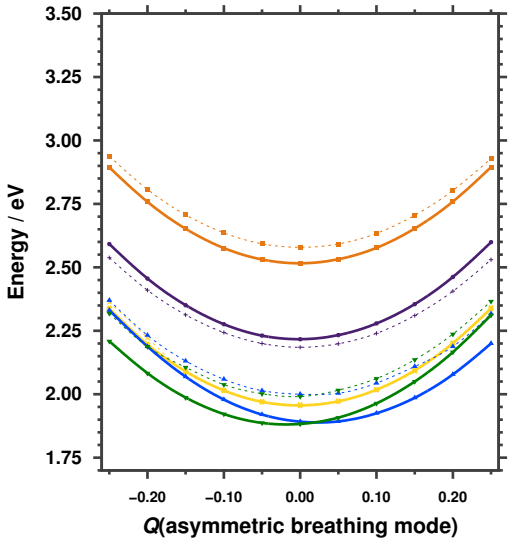

(iii) 12-12: asymmetric breathing combination mode. $^{12}\nu_{130}$

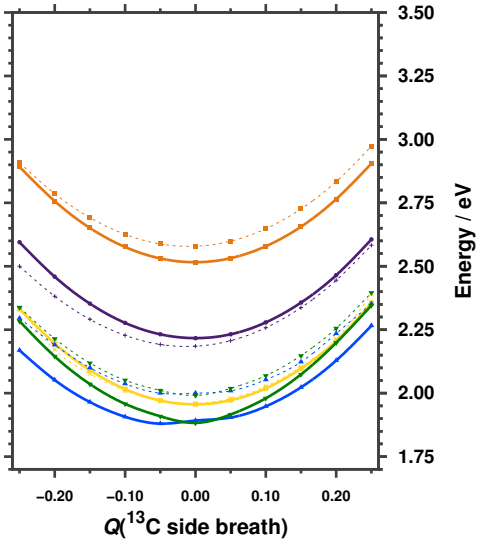

(iv) 13-12: ^{13}C side breathing mode. $^{13}\nu_{130}$

Figure 5.27: Potential energy curves along the PTZ-centred vibrational modes of [Pt(bipyCOOEt)(C≡C-Ph-CH_2-PTZ)$_2$] calculated using ground state and time-dependent B3LYP/SDD[Pt]6-311G(d,p)[H,C,N,O,S]/IEFPCM(CH_2Cl_2). Displacement vectors for the vibrations are illustrated in Figure 5.6. Singlet states, calculated within the restricted formalism, are connected by thick lines, whereas triplet states, calculated within the unrestricted formalism, are connected by dashed thin lines. The states are colour coded as follows: ^{RHS}CSS/^{13}CSS (green), ^{LHS}CSS/^{12}CSS (blue), d_{xz}CT (yellow), d_{yz}CT (purple) and $d_{x^2-y^2}$CT (orange). The changes in electron density associated with these states at the S_0 geometry are illustrated in Figure 5.12.

triplet manifold, the effect of the vibrational modes is much less pronounced.

The MLCT states of all three characters are less strongly effected than the CSS states. The MLCT states of singlet character are destabilised in a symmetrical fashion along the coordinates. In the triplet manifold the distortion does not have a symmetrical effect, though the asymmetry is not very pronounced, for example in Figure 5.27(iv), $^{3}d_{yz}$CT is 0.1 eV more stable along $^{13}\nu_{130}$ when $Q = -0.25$ than when $Q = +0.25$. There is no clear evidence that directional vibrational control along the phenothiazine-centred vibrational modes would be expected if $^{13}\nu_{131}$ or $^{13}\nu_{130}$ where selectively excited. Whilst very weak directionality from $^{3}d_{xz}$CT might be expected, this would be unlikely to occur since the energetic bias towards either CSS is weak. However, it should be noted that in the vibrational control experiments, only $^{13}\nu_{130}$ should be excited, as a result of the strong coupling between $\nu(^{13}C{\equiv}^{13}C)$ and the combination band. There may thus be a small contribution from this mode in the differential effect observed between exciting $\nu(^{13}C{\equiv}^{13}C)$ and $\nu(^{12}C{\equiv}^{12}C)$.

In summary, calculations at the B3LYP/SDD[Pt]6-311G(d,p)[H,C,N,O,S]/IEFPCM(CH_2Cl_2) level of theory provide little evidence that would suggest directional controllable electron transfer would be observed in **13-12** on the basis of changes in energy along the vibrational coordinates targeted in the experiments. Although slight differential energy changes are observed between ^{13}CSS and ^{12}CSS along the coordinates investigated, these effects are small. Perceived derivative discontinuities along some of the acetylide-centred vibrational modes are observed. The origin of these discontinuities is unclear.

To extend these investigations by including scalar relativistic effects and Spin-Orbit Coupling (SOC), further calculations were formed using the ADF 2016 program.[275] Due to the high cost of these calculations, only two coordinates could be investigated. Since the acetylide-centred modes were found to induce directional vibrational control in these molecules, $^{13}\nu_{288}$ was investigated and the equivalent **12-12** mode, $^{12}\nu_{288}$, was also investigated as a control. The spin-pure and spin-free PESs along these coordinates are shown in Figure 5.28.

The Scalar Relativistic (SR) spin-pure PESs calculated using sTD-B3LYP(ZORA-PT)/TZ2P/COSMO(CH_2Cl_2) bear strong resemblances to the Non-Relativistic (NR) equivalents calculated within TD-B3LYP/SDD[Pt]6-311G(d,p)[H,C,N,O,S]/IEFPCM(CH_2Cl_2). (See

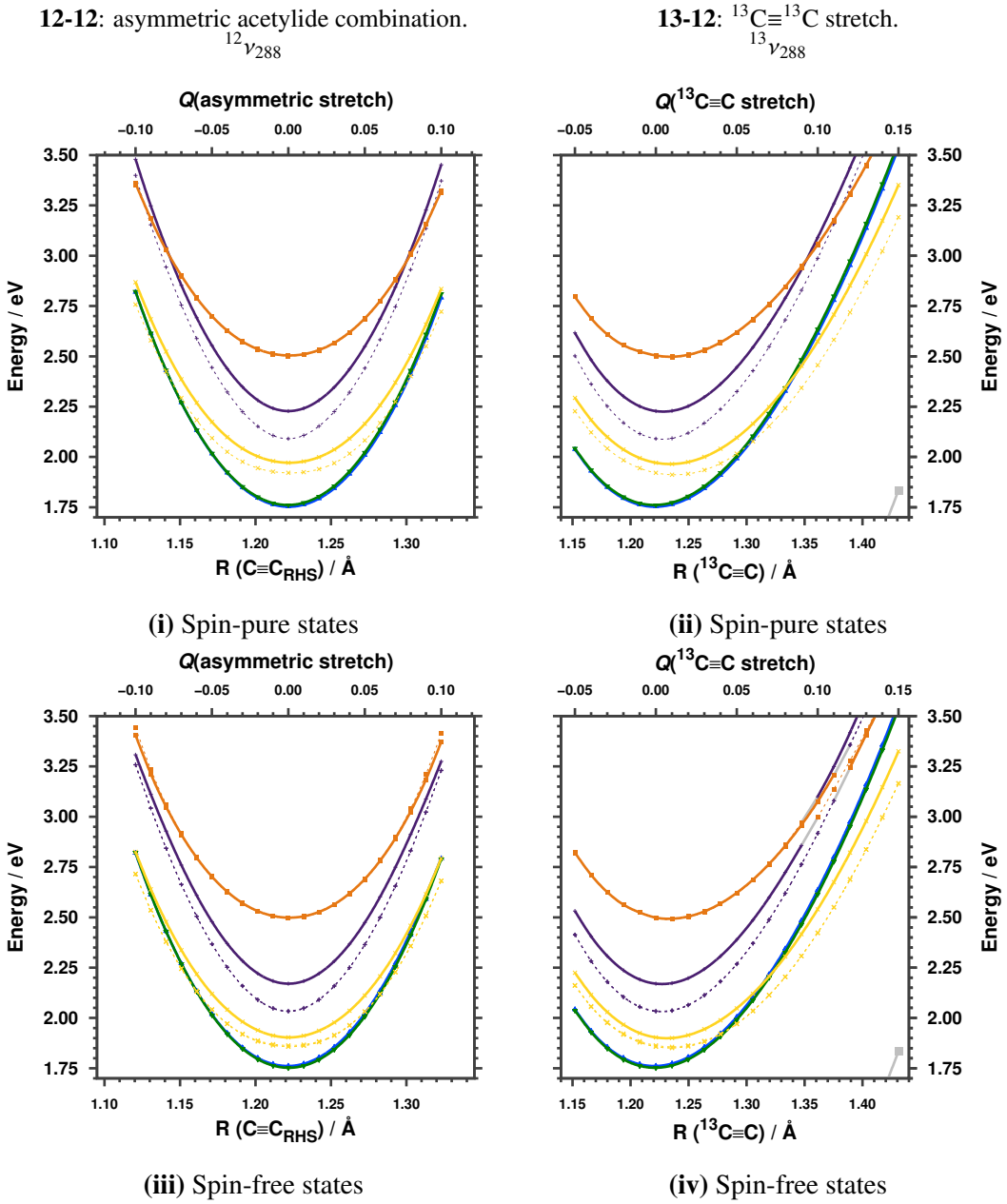

Figure 5.28: Potential energy curves along the acetylide-centred vibrational modes of [Pt(bipyCOOEt)(C≡C-Ph-CH_2-PTZ)$_2$] calculated using ground state and simplified Time-Dependent B3LYP(ZORA-PT)/TZ2P/COSMO(CH_2Cl_2), including scalar relativistic effects using the Zero-Order Regular Approximation (5.28(i), 5.28(ii)) and including Spin-Orbit Coupling (SOC) perturbatively in addition (5.28(iii), 5.28(iv)). Displacement vectors for the vibrations are illustrated in Figure 5.5. In the calculations none of the core electrons were frozen. 100 spin-pure excitations were found, resulting in a total of 400 spin-free excitations at each increment. Spin-pure singlet states are connected by thick lines and spin-pure triplet states are connected by dashed lines. Spin-free states are connected by lines according to which spin manifold provides the majority contribution. The states are colour coded as follows: ground state (grey), ^{RHS}CSS/^{13}CSS (green), ^{LHS}CSS/^{12}CSS (blue), d_{xz}CT (yellow), d_{yz}CT (purple) and $d_{x^2-y^2}$CT (orange). Note that in Figure 5.28(iv) a series of avoided crossings are observed in the region of Q = +0.10. The states involved in the crossings are connected with grey lines, to guide the eye.

Figure 5.25). However, the perceived derivative discontinuities present in the NR PESs are absent in the SR surfaces. It is difficult to rationalise why this is the case since the calculations differ in multiple ways. One of the major differences between the NR and SR calculations is that in the NR calculations, the singlet and triplet states of a given character go from regions in which they are energetically separated to regions of near energetic degeneracy, after which the gradients change. A clear example of this are the d_{yz}CT states along $^{13}\nu_{288}$, shown in Figure 5.25(iv), which cross in the region of $Q = +0.02$. This is not the case in the SR calculations, where singlet and triplet manifolds remain either degenerate (CSSs, $d_{x^2\text{-}y^2}$CT) or separated (d_{xz}CT, d_{yz}CT) in all regions of the coordinates. Since the SR calculations were performed using a simplified TD-DFT procedure, it is not possible to verify that the perceived derivative discontinuities would not also be present in full TD-DFT calculations performed within ADF. It should be noted that there is a subtle difference between the definition of the B3LYP function in Gaussian 09 and ADF: by default in Gaussian 09, the "type III" Vosko-Wilk-Nusair (VWN) correlation functional[350] is used within B3LYP (See Ref. [126]), whereas in ADF the VWN type V correlation functional is employed. However, forcing the use of VWN-V in Gaussian 09 leads to changes in excitation energy below 10^{-3} eV at the equilibrium geometry. It is therefore unlikely that this is the cause of the discrepancy. In the NR calculations, a relativistic Effective Core Potential (ECP) was used to describe the core electrons of Pt, since these would be incorrectly described with an NR Hamiltonian. In the SR calculations all electrons are included in the SCF procedure. It is unlikely that the use of an ECP would have a strong effect on the low-lying excited states, since these consist of valence orbitals only and so the influence of core electrons is limited to screening. The SR calculations utilised a slightly higher quality basis set than the NR calculations. Direct comparison of the basis sets is not possible since the SR calculations utilised Slater-Type Orbitals (STOs), whereas the NR calculations utilised Gaussian-Type Orbitals (GTOs). However, previous investigations comparing PESs calculated with GTO basis sets of increasing quality yielded qualitatively similar results. (See Chapter 4) It should also be noted that the iterative diagonalization procedure used to solve the (s)TD-DFT *eigenvalue* problem is subtly different in ADF to that used in Gaussian: in ADF the Davidson-Liu algorithm is used,[184,187,191] whereas in Gaussian 09 a modified form of this

algorithm is employed.[186,189] It is very unlikely that the use of different algorithms could be responsible for the difference in topology of the PESs calculated using Gaussian and ADF; to verify this would require exhaustive investigations that are beyond the scope of this work.

Apart from the absence of the perceived derivative discontinuities in the SR calculations, the PESs derived from SR calculations are very similar to those derived from NR calculations. Since in the SR calculations, the CSSs are found to be relatively more stable than in the NR calculations, the CSSs cross with the states of d_{xz}CT character further along the vibrational coordinate and thus at higher energy in the SR calculations than the NR calculations. One consequence of this is that for a wavepacket to reach these crossover regions would require greater vibrational excitation in the SR surfaces than the NR surfaces. This is particularly prominent on the $^{12}\nu_{288}$ coordinate, where the crossover regions are accessible in the vibrational ground state, v_0, of d_{xz}CT on the NR surfaces but would require significant vibrational excitation on the SR surfaces. The crossover between states of d_{yz}CT and $d_{x^2-y^2}$CT character is also altered in the SR calculations. For the singlet manifold, this crossover occurs at almost the same energy in both SR and NR surfaces along both vibrational modes. In SR calculations, $^3d_{yz}$CT and $^3d_{x^2-y^2}$CT are stabilised significantly compared to the NR calculations and thus a crossover between these states is observed in the SR calculations that was not observed in the NR calculations in the region of the PES explored.

As previously described, the spin-pure excited states obtained from SR calculations can be used as a basis in the construction of Spin-Free (SF) excited states by including SOC in a perturbative manner.[280] The results of these calculations are shown in Figures 5.28(iii) and 5.28(iv). It should be noted that in regions of the PES where spin-pure states of different character are well separated, such as the Franck-Condon region, the resultant spin-free states are not strongly mixed. (Figure 5.24(ii) shows the construction of the spin-free states in the equilibrium geometry) This does not hold in regions of the PES where states become close in energy. Furthermore, when spin-pure states of different manifolds become close in energy, the resultant spin-free states can be strongly mixed and no longer of near-integer spin. It should therefore be noted that in Figure 5.28, the SF states are colour coded according to the character that contributes the greatest amount to that state and likewise connected by thick or dashed lines according

to which spin-manifold contributes the greatest amount to that state. This is particularly significant in regions where states intersect. The assignment of character to the SF states was achieved by considering 1) the percentage contribution from singlet and triplet spin-pure states and 2) the change in electron density distribution with respect to the ground state *via* the changes in KS orbitals as a result of transitions in the spin-pure states that contribute to a given spin-free state. The extraction of this data from ADF calculations is trivial, but tedious. The raw data are provided in a supplemental electronic spreadsheet, `spin-free_state_analysis.ods`.

The SF surfaces, like the SR surfaces, do not exhibit the perceived derivative discontinuities observed in the NR calculations. The addition of spin-orbit coupling has little effect on the CSSs and so energetically the SR and SF states of CSS character are very similar. However, the states of d_{xz}CT character are stabilized by SOC, resulting in crossovers between the SF states of CSS and d_{xz}CT character at lower energy than the corresponding SR states. At the point closest to crossover, some SF states are of mixed character, containing both CSS and d_{xz}CT character. However the adjacent points return to being entirely CSS or d_{xz}CT. The strong mixing between states combined with the small energy gaps in this region suggests that conversion between SF states of differing character would be facile in this region. The regions of the SF PESs which correspond to crossovers between d_{yz}CT and $d_{x^2-y^2}$CT states in the SR PESs, $Q(^{13}\nu_{288}) \approx 0.9$ and $Q(^{12}\nu_{288}) \approx \pm 0.08$, exhibit mixing to an even greater extent. These regions are characterised by very strong mixing between states of d_{yz}CT and $d_{x^2-y^2}$CT character, as well as far from integer spin for many SF states. It is clear that smooth intersections between states in this region does not occur, rather, these regions are best described as avoided crossings between the manifolds of d_{yz}CT and $d_{x^2-y^2}$CT states. This suggests that a wavepacket on one of the higher energy SF states of $d_{x^2-y^2}$CT character could relax quite rapidly to the SF states of d_{yz}CT character if it sampled this portion of the surface. Indeed, these region would be expected to be easily accessible under the experimental conditions of a 400 nm (3.10 eV) UV-pump pulse.

Like the NR and SR surfaces previously discussed, the SF surfaces show little evidence for an energy based origin of the directional vibrational control phenomenon observed experimentally. Apart from the low energy intersections with states of d_{xz}CT character, the states of either ^{13}CSS or ^{12}CSS character remain energetically well separated from the MLCT states.

Moreover, there is no evidence that significant energetic differences between states of ^{13}CSS or ^{12}CSS character develop along either of the coordinates investigated. It is therefore not possible to explain the observations on the basis of changes in the topology of the PES of **13-12** along the coordinates investigated, unlike similar Pt complexes previously investigated. (See Chapter 4) However, one conclusions can be drawn, in particular from the results of calculations at the sTD-B3LYP(ZORA-PT)/TZ2P/COSMO(CH_2Cl_2) level of theory: whilst photoexcitation is most likely to populate states of $d_{x^2-y^2}$CT character, population transfer to states of d_{yz}CT character should be facile due to energetically accessible regions of strong coupling between states of these characters. It is therefore likely that the ^{3}MLCT* component identified in the kinetic scheme (See Figure 5.13) is either of d_{yz}CT- or vibrationally excited d_{xz}CT-character. Identifying a mechanism in which these states may couple preferentially to ^{13}CSS or ^{12}CSS along the acetylide-centred vibrational coordinates of **13-12** is therefore of paramount importance.

5.4.1 Excited state polarisation

As previously mentioned, it is possible to estimate the change in electron density distribution in the excited states with respect to the ground state in calculations performed in ADF by considering the KS orbital transitions involved in a given excitation. Since the atomic orbitals that contribute to each KS orbital are also provided in the output of an ADF calculation, it is trivial to estimate the change in electron density that occurs as a result of each spin-pure transition. When spin-orbit coupling is included perturbatively, the spin-free states are constructed from a basis of spin-pure states. Given the weighting of each spin-pure state to a spin-free state, it is trivial to estimate the electron density distribution in a spin-free state using a weighted sum of the electron density distributions of the contributing spin-pure states. By repeating this at each point and for each spin-free state along the vibrational coordinates, a graph of the change in electron density distribution of the spin-free excited states can be constructed. This information can be used to gain insight between the coupling between states at points along the vibrational coordinate. For example, in a charge-transfer reaction, such as the ones considered herein, we may employ the two-state Generalized Mulliken-Hush (GMH) model.[351–353] In the GMH

model, the coupling between two diabatic states, A and B, is defined as

$$V_{\mathrm{AB}} = \frac{\vec{\mu}_{12}\Delta E_{12}}{(\vec{\mu}_{\mathrm{A}} - \vec{\mu}_{\mathrm{B}})} = \frac{\vec{\mu}_{12}\Delta E_{12}}{\left[(\vec{\mu}_1 - \vec{\mu}_2)^2 + 4\,(\vec{\mu}_{12})^2\right]^{\frac{1}{2}}}, \tag{5.1}$$

where 1 and 2 are two adiabatic states, $\vec{\mu}_{12}$ is the transition dipole moment between 1 and 2, ΔE_{12} is the energy gap between 1 and 2, $\vec{\mu}_{\mathrm{A}}$ and $\vec{\mu}_{\mathrm{B}}$ are the dipole moments of A and B, and $\vec{\mu}_1$ and $\vec{\mu}_2$ are the dipole moments of 1 and 2. It is clear from this expression if the electron density distribution and therefore the dipole moments of two adiabatic states are similar, the coupling between the diabatic states that construct them would be high. V_{AB} is also proportional to the energy gap between adiabatic states. Thus, coupling between the two diabatic states is maximised when the energy gap is large and the states are electronically similar. It should be noted that since inter-excited state transition dipole moments are not available in ADF, diabatic coupling within the GMH model cannot be directly computed.

The changes in electron density distribution of the lowest spin-free MLCT states of majority triplet character in **13-12** as calculated at the sTD-B3LYP(ZORA-PT)/TZ2P/COSMO(CH_2Cl_2) level of theory along the $^{13}\nu_{288}$ and $^{12}\nu_{288}$ coordinates are plotted in Figures 5.29 and 5.30, respectively. Numerical values for the 40 lowest spin-free states at each increment are provided in the supplemental electronic spreadsheet, `spin-free_state_analysis.ods`. It is clear that along both coordinates, the excited states tend to "polarise," with the hole becoming localised onto one of the two phenyl-acetylides. Furthermore, the MLCT states can be separated into two categories: states of d_{xz}CT and $d_{x^2\text{-}y^2}$CT character, which polarise along the phenyl-acetylide whose acetylide bond has been stretched, i.e. onto the $^{13}C{\equiv}^{13}C$ side when $Q(^{13}\nu_{288}) > 0$, and states of d_{yz}CT character, which polarise in the opposite manner, along the phenyl-acetylide whose acetylide bond has been contracted, i.e. onto the $^{12}C{\equiv}^{12}C$ side when $Q(^{12}\nu_{288}) > 0$. It should be noted that the CSSs are almost completely invariant along these coordinates, apart from at points of near-degeneracy with other states, where some mixing does occur, for example, at $Q(^{12}\nu_{288}) = \pm 0.6$. Mixing also occurs between states of d_{yz}CT and $d_{x^2\text{-}y^2}$CT character in the regions of near degeneracy, for example, at $Q(^{12}\nu_{288}) = \pm 0.0$, and in the region of the avoided crossing at $Q(^{13}\nu_{288}) \approx +0.12$. The states of d_{xz}CT and d_{yz}CT character polarise more

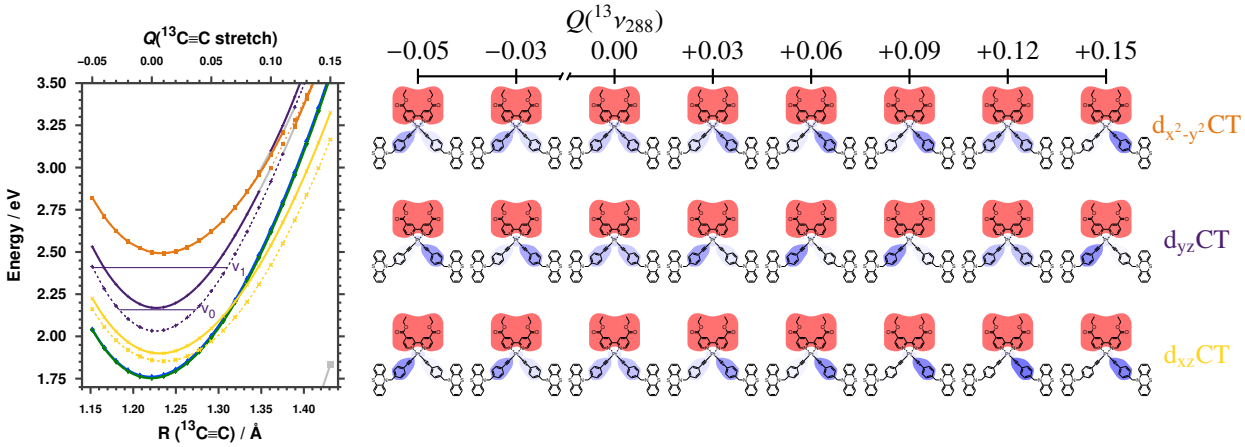

Figure 5.29: Potential energy curves along the ^{13}C≡C stretch mode, $^{13}\nu_{288}$, of [Pt(bipyCOOEt)(C≡C-Ph-CH_2-PTZ)$_2$], alongside representative electron density distributions for the three MLCT states, calculated using ground state and simplified Time-Dependent B3LYP(ZORA-PT)/TZ2P/COSMO(CH_2Cl_2). Scalar relativistic effects were included using the Zero-Order Regular Approximation (ZORA) Hamiltonian and spin-orbit coupling was included in the sTD procedure perturbatively. Displacement vectors for the vibrations are illustrated in Figure 5.5. In the calculations none of the core electrons were frozen. 100 spin-pure excitations were found, resulting in a total of 400 spin-free excitations at each increment. Spin-free states of majority singlet character are connected by thick lines, whereas spin-free states of majority triplet character are connected by thin, dashed lines. The states are colour coded as follows: ground state (grey), ^{13}CSS (green), ^{12}CSS (blue), d_{xz}CT (yellow), d_{yz}CT (purple) and $d_{x^2-y^2}$CT (orange). The electron density distributions shown are for the lowest energy spin-free states of majority triplet character. Blue regions denote an area of relative loss of electron density and red relative gain of electron density, with respect to the ground state at that geometry. Note that a series of avoided crossings are observed in the region of Q= +0.10. The states involved in the crossings are connected with grey lines, to guide the eye. The zeroth and first vibrational energy levels, v_0 and v_1, of the d_{yz}CT spin-free states of majority triplet character, based on experimental values, are indicated as thin purple lines.

strongly than the states of $d_{x^2-y^2}$CT character. Polarisation of the MLCT excited states along the vibrational modes will increase coupling with the CSS state in the direction of polarisation in comparison with the equilibrium structure, since this will cause the dipole moment to align with the CSS localised on that side. Moreover, the coupling of the polarised MLCT state with the CSS on the opposite side to the direction of polarisation will decrease. This provides a possible mechanism for the directionality observed in the vibrational control experiments.

As discussed in Section 5.2.1, it was observed experimentally that exciting the two acetylide coordinates of an intermediate excited state of **13-12**, ^{3}MLCT*, increased the rate of formation of the CSSs. Specifically, exciting the ^{13}C≡^{13}C stretch increased the rate of formation of ^{12}CSS more than that of ^{13}CSS and vice versa. Considering the polarisation of the excited states shown in Figure 5.29, this phenomenon could be explained if ^{3}MLCT* was one of the d_{yz}CT states of

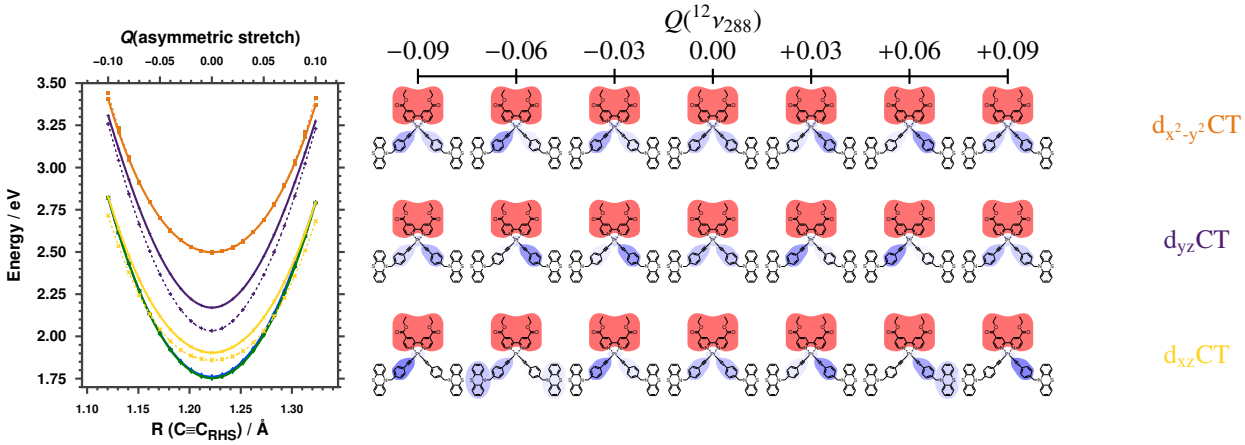

Figure 5.30: Potential energy curves along the asymmetric acetylide stretch mode, $^{12}\nu_{288}$, of [Pt(bipyCOOEt)(C≡C-Ph-CH_2-PTZ)$_2$], alongside representative electron density distributions for the three MLCT states, calculated using ground state and simplified Time-Dependent B3LYP(ZORA-PT)/TZ2P/COSMO(CH_2Cl_2). Scalar relativistic effects were included using the Zero-Order Regular Approximation (ZORA) Hamiltonian and spin-orbit coupling was included in the sTD procedure perturbatively. Displacement vectors for the vibrations are illustrated in Figure 5.5. In the calculations none of the core electrons were frozen. 100 spin-pure excitations were found, resulting in a total of 400 spin-free excitations at each increment. Spin-free states of majority singlet character are connected by thick lines, whereas spin-free states of majority triplet character are connected by thin, dashed lines. The states are colour coded as follows: ^{13}CSS (green), ^{12}CSS (blue), d_{xz}CT (yellow), d_{yz}CT (purple) and $d_{x^2-y^2}$CT (orange). The electron density distributions shown are for the lowest energy spin-free states of majority triplet character. Blue regions denote an area of relative loss of electron density and red relative gain of electron density, with respect to the ground state at that geometry.

majority triplet character. The **13-12** acetylide vibrational modes are asymmetrical and so the vibrational wavefunction is not symmetrical. By fitting a Morse oscillator to the points calculated along the $^{13}\nu_{288}$, we can use numerical methods to estimate the anharmonicity of the vibrational *eigenstates*. The wavefunctions of the first two vibrational eigenstates of a representative Morse oscillator fitted to one of the states of d_{yz}CT character, v_0 and v_1, have approximately 53% of their probability density on the extended part of $^{13}\nu_{288}$. Furthermore, since the vibrations are asymmetrical, the magnitude of extension of the ^{13}C≡^{13}C bond on the extended part of the surface sampled by the wavefunctions is greater than the magnitude of contraction of the bond on the contracted part of the surface sampled. Since the degree of polarisation is proportional to the degree of perturbation from equilibrium, it is more probable that the states of d_{yz}CT character will be in a geometry with greater coupling to, for example, the ^{12}CSS state than the ^{13}CSS state along the $^{13}\nu_{288}$ coordinate. This is increased at higher vibrational energy levels, since these sample regions of the surface of greater extension. Recalling that Equation 5.1 suggests

coupling is proportional to the difference in energy between two states, it should be noted that the gap between the d_{yz}CT states of majority triplet character and the CSSs is almost constant in the vibrationally accessible region, though it is very slightly larger on the contraction part of the $^{13}\nu_{288}$ coordinate. It should also be noted that the equivalent vibration on the $^{12}C\equiv^{12}C$ side of the molecule, $^{13}\nu_{289}$, will be of almost identical character. Therefore the fact that a wavepacket on the zeroth vibrational level of $^{13}\nu_{289}$ or $^{13}\nu_{288}$ of d_{yz}CT couples more strongly to the CSS on the opposite side of the molecule would be balanced by the complementary effect on the other vibrational mode. Increased coupling to CSSs on one side over another could only be achieved if one of the vibrational modes was excited and the other was not, i.e. one of the two vibrational modes was selectively excited. This is consistent with the observed directionality of vibrational control in the experiments.

The directional increase of coupling with the CSSs caused by polarisation of the excited states of d_{yz}CT character along the acetylide-centred vibrational coordinates does not fully explain the experimental observations. For example, since the effect of polarisation-induced coupling is greater in the vibrationally excited state than the vibrational ground state, it would be expected that the degree of directionality observed would be proportional to the lifetime of vibrational excitation and therefore selective excitation of $^{13}\nu_{288}$ should be less effective than selective excitation of $^{13}\nu_{289}$. This is not the case, in fact, the opposite is observed. One possible explanation for this is that the vibrational modes which are strongly coupled to $^{13}\nu_{288}$ (See Section 5.2) play a prominent role in the excited state dynamics and increase coupling between the states of d_{yz}CT and CSS character in a directional manner. Unfortunately, investigations into these coordinates were not possible due to resource constraints. Future investigations will focus on increasing the number of vibrational coordinates included in the calculations and using the results to construct a model Hamiltonian for use in quantum wavepacket dynamic calculations to gain quantitative insight into the excited state dynamics of the molecule.

5.5 Conclusion

The vibrational and electronic structure of [Pt(bipyCOOEt)(C≡C-Ph-CH_2-PTZ)$_2$] was successfully characterised through a number of theoretical methods. In Section 5.2, the unexpectedly

complex ground state FTIR in the acetylide region of the three isotopomers **12-12**, **13-12** and **13-13** were found to be caused by the presence of strongly-coupled combination bands by means of Generalized Vibrational Perturbation Theory to second order (GVPT2) with the B3LYP functional and a mixed basis set comprised of SDD for Pt and 6-311G(d,p) for all other atoms. The results of ultrafast vibrational control experiments were detailed in section 5.2.1. In Section 5.3.1 it was shown that the ground state UV-visible absorption spectra of [Pt(bipyCOOEt)(C≡C-Ph-CH_2-PTZ)$_2$] was well described by Time-Dependent B3LYP (TD-B3LYP) and simplified TD-B3LYP (sTD-B3LYP) calculations, the latter of which included Scalar Relativistic (SR) effects as well as perturbative Spin-Orbit Coupling (SOC) through the Zero-Order Regular Approximation (ZORA) Hamiltonian. In Section 5.4, the Potential Energy Surface (PES) within these methods along the vibrational coordinates previously identified in Section 5.2 were investigated. An explanation for the observed directional vibrational control could not be found from a purely energetic basis and so further investigations into the coupling between electron states were performed, detailed in Section 5.4.1. A mechanism was proposed to explain some of the observations, in which polarisation of the d_{yz}CT states along the vibrational coordinates targeted in the experiments increases coupling with the CSSs located on the opposite side to vibrational excitation, consistent with observations. The difference in magnitude of effect observed in the experiments could not be explained by this effect alone; however, it was suggested that the combination band may be responsible for this phenomenon.

Future work will extend these investigations by expanding the number of vibrational coordinates included in the calculations, with the intention of producing a model Hamiltonian suitable for quantum wavepacket dynamic simulations, for example, using the vibronic coupling Hamiltonian that has been successfully been applied to similar systems in the past.[238,354–356] Whilst relativistic effects were included in some of these calculations, this could be improved by including SOC self-consistently with a more advanced method, such as with the Two- or Four- Component (2C or 4C) ZORA Hamiltionian. It should be noted that some disagreement was observed between the overall topology of the excited states PESs obtained in the methods used in Section 5.4. This could be resolved by further systematic investigations, including using alternative but computationally feasible methods that take a different approach, such as

DFT/Multi-Reference Configuration Interaction (MRCI) or Algebraic Diagrammatic Construction to Second Order (ADC(2)).[357–360]

Part III

Other work

Chapter 6

Main group azides

Main group azides have recently gained attention for their physical properties, in particular for their use as "high-energy materials," or explosives in common parlance.[361] Group 14 polyazides are well known, but elusive.[56,361] Fortunately, characterisation of these potentially pressure- and friction-sensitive compounds using conventional techniques is possible. One reason for this is that the azido group is strongly polarised and thus yields intense vibrational spectroscopic signals. However, resolving the spectra of these compounds can be challenging. Recently, the Portius group sought to synthesise low-valent, homoleptic polyazides, $[E(N_3)_3]^-$, where E is one of the two group 14 elements Ge or Sn.[56] The regions of the experimental FTIR spectra of the products in tetrahydrofuran (THF) solvent within which azide stretches would be expected to appear are shown in Figure 6.1.

Two peaks can be identified in the results of the Ge experiment, at 2059 cm^{-1} and 2091 cm^{-1}, and two in the Sn experiment, at 2051 cm^{-1} and 2080 cm^{-1}. Two small peaks can also be identified in the spectra, which are assigned to the minor products of the reaction, hydrazoic acid, HN_3, and the azide anion, N_3^-, formed as a result of the addition of excess NaN_3.[361] Crystallisation of the products of the reaction could be induced by introducing a weakly coordinating counter ion, such as PPh_4^+. This enabled the structure of the crystalline products to be determined using X-ray diffraction techniques. The structures derived from this are shown in Figure 6.2.

The geometries of the triazide components of the crystal structures, $[Ge(N_3)_3]^-$ and $[Sn(N_3)_3]^-$, are shown in Figures 6.2(i) and 6.2(ii), respectively. These exhibit non-

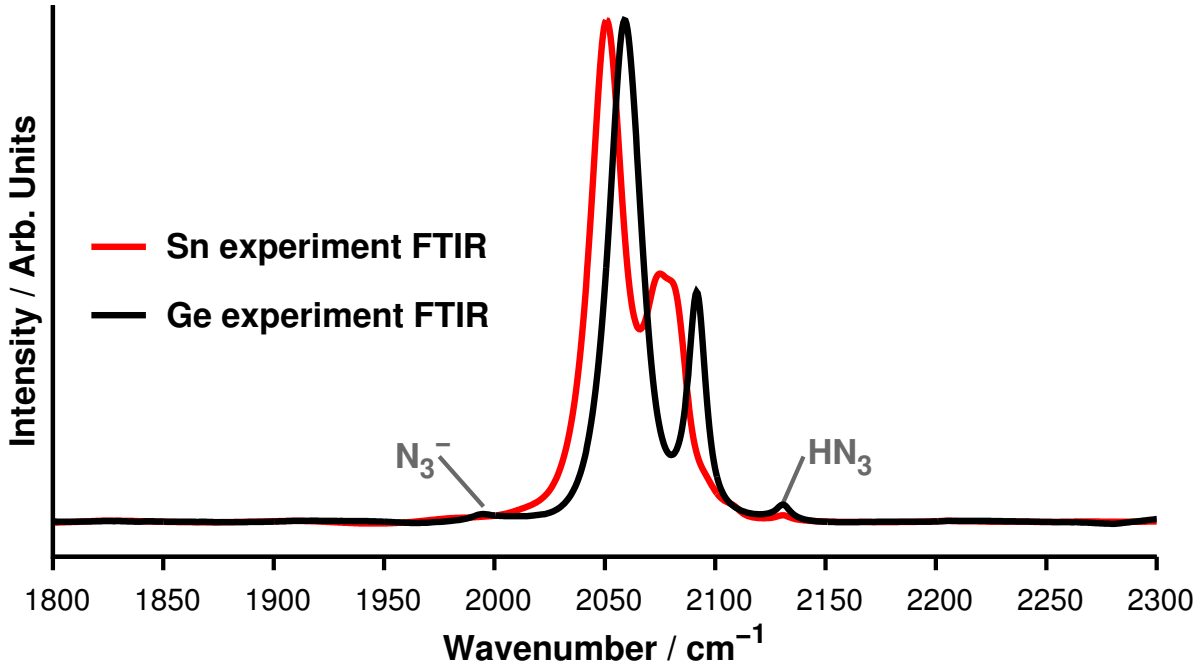

Figure 6.1: Experimental FTIR spectra of unidentified Ge (black line) and Sn (red line) azide compounds in THF solution. The intensity has been normalised such that the lower frequency azide peaks in both spectra are equal in intensity. Peaks corresponding to the azide anion, N_3^-, and hydrazoic acid, HN_3, are indicated.[361]

symmetrical geometries due to differing coordination angles of the azides with respect to the central atom. Two crystalline phases were identified in the products of the Sn reaction. The second phase was found to contain a $[Sn(N_3)_3]^-$ dimer, the geometry of which is shown in Figure 6.2(iii). In this structure, one of the azide groups from each C_3-symmetric $[Sn(N_3)_3]^-$

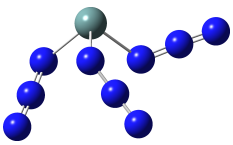

(i) $[Ge(N_3)_3]^-$ within $\{[Ge(N_3)_3]^-[PPh_4]^+\}$ crystal structure.[56]

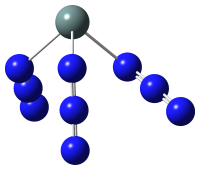

(ii) $[Sn(N_3)_3]^-$ within $\{[Sn(N_3)_3]^-[PPh_4]^+\}$ crystal structure.[362]

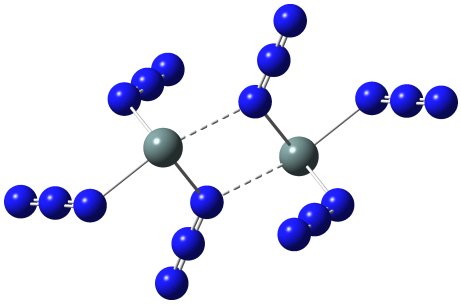

(iii) $[Sn(N_3)_3]^-$ dimer within $\{[Sn(N_3)_3]_2^-[PPh_4]_2^+\}$ crystal structure.[56]

Figure 6.2: Experimental X-ray crystallographic structures of $[E(N_3)_3]^-$, E = Ge, Sn.[56,362]

appears to interact weakly with the Sn(II) centre of the other $[Sn(N_3)_3]^-$. It should be noted that the fact that a crystal structure has been obtained does not mean that these geometries are present in the solution phase: the forces acting upon the system are different in these two situations.

To verify the experimental characterisation of these compounds and their precursors in tetrahydrofuran (THF) solvent, computational investigations were performed. It should be noted that despite the fact that THF is usually considered as a coordinative solvent, since the species studied herein are anions THF is unlikely to coordinate and so explicit solvent was not considered in the calculations. It should also be noted that in azide chemistry, nitrogen atoms are commonly identified based on proximity to the coordinated atom.[361] The labelling scheme is illustrated in Figure 6.3.

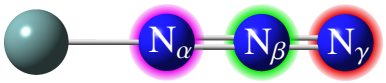

Figure 6.3: Labelling scheme used to indicate position of azide nitrogens, N_κ. The proximal N, highlighted in magenta, is denoted N_α. The central N, highlighted in green, is denoted N_β. The distal N, highlighted in red, is denoted N_γ.[361]

6.1 Conformational flexibility

The geometries of $[GeCl_3]^-$ and $[SnCl_3]^-$, optimised at the B3LYP/cc-pVTZ(-PP)/IEFPCM(THF) level, are depicted in Figures 6.4(i) and 6.5(i), respectively. As expected, the central group 14 atom exhibits tetrahedral geometry. The vacant coordination site is occupied by a lone pair of electrons. Substitution of one of the Cl^- ligands with a N_3^- to form the mono-azide species reveals the potential for conformational flexibility in the compounds. The energetic differences between all of the conformers discussed are presented in Table 6.1. The azide may be arranged such that the distal nitrogen of the azide group, N_γ, lies either "down," below the plane of the coordinating atoms (Conformer (*a*), Figures 6.4(ii) and 6.5(ii)) or "up," above the plane of the coordinating atoms. (Conformer (*b*), Figures 6.4(iii) and 6.5(iii)) A third conformer can also be proposed, in which the azide is coordinated in a "planar" manner, such that N_γ lies

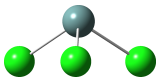

(i) $[GeCl_3]^-$.

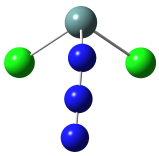

(ii) $[Ge(N_3)Cl_2]^-$ conformer (*a*).

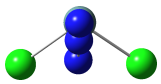

(iii) $[Ge(N_3)Cl_2]^-$ conformer (*b*).

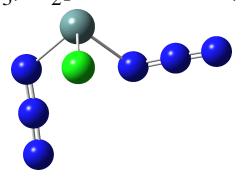

(iv) $[Ge(N_3)_2Cl]^-$ conformer (*a*).

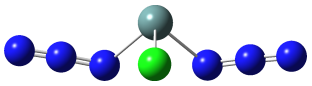

(v) $[Ge(N_3)_2Cl]^-$ conformer (*b*).

Figure 6.4: Low energy conformers of $[Ge(N_3)_{(3-n)}X_n]^-$, $n = 1, 2, 3$, optimised at the B3LYP/cc-pVTZ(-PP)/IEFPCM(THF) level. Relative energies are provided in Table 6.1.

in the plane of the coordinating atoms. However, this conformer could not be optimised for either $[Ge(N_3)Cl_2]^-$ or $[Sn(N_3)Cl_2]^-$. The conformational flexibility found in the mono-azides extends to the di- and tri-azide species and leads to a significant number of inequivalent hypothetical conformers: by combining "up," "down," and "planar" azides, 9 inequivalent diazide conformations and 10 inequivalent triazide conformations can be constructed. This is further complicated by the fact that some conformers are of higher symmetry than others and therefore will have differing degeneracies. Finally, for completeness, it should be noted that since each azide is equivalent, three absolute spatial configurations for each conformer exist,

(i) $[SnCl_3]^-$.

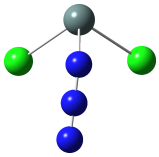

(ii) $[Sn(N_3)Cl_2]^-$ conformer (*a*).

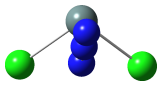

(iii) $[Sn(N_3)Cl_2]^-$ conformer (*b*).

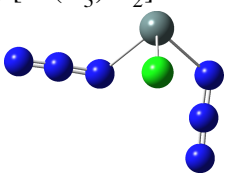

(iv) $[Sn(N_3)_2Cl]^-$ conformer (*a*).

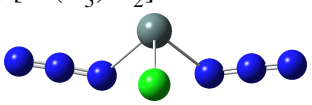

(v) $[Sn(N_3)_2Cl]^-$ conformer (*b*).

Figure 6.5: Low energy conformers of $[Sn(N_3)_{(3-n)}X_n]^-$, $n = 1, 2, 3$, optimised at the B3LYP/cc-pVTZ(-PP)/IEFPCM(THF) level. Relative energies are provided in Table 6.1.

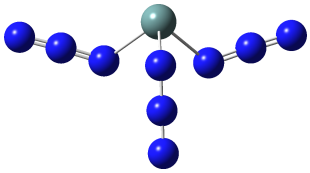

(i) $[Ge(N_3)_3)]^-$ conformer (*a*).

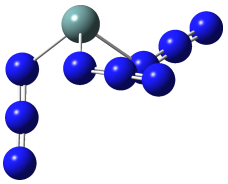

(ii) $[Ge(N_3)_3)]^-$ conformer (*b*).

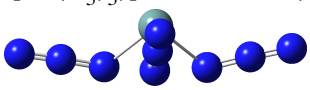

(iii) $[Ge(N_3)_3)]^-$ conformer (*c*).

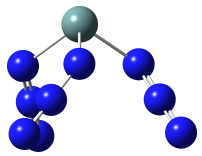

(iv) $[Ge(N_3)_3)]^-$ conformer (*d*).

Figure 6.6: Low energy conformers of $[Ge(N_3)_3)]^-$, optimised at the B3LYP/cc-pVTZ(-PP)/IEFPCM(THF) level. Relative energies are provided in Table 6.1.

which would have an impact on the spectra in some cases if isotopic labelling was employed.

To ensure that as many geometries as possible were found, optimisations were performed in all cases from initial geometries corresponding to each of the hypothetical conformers of that species. Only conformers with a relative electronic energy within 5.7 kJ mol^{-1} of the lowest energy conformer were included in the analysis, since at room temperature this energy difference corresponds to a 10:1 population ratio within a Boltzmann distribution. The low energy conformations of the diazides $[Ge(N_3)_2Cl]^-$ and $[Sn(N_3)_2Cl]^-$ are shown in Figures 6.4 and 6.5, respectively. The low energy diazides have both "up" and "down" azides. Interestingly, despite the fact that the "down" conformer of the mono-azido species is significantly more stable than the "up" conformer, the combination of two "down" azide ligands is unstable. This is due to increased repulsion between azide ligands in the "down, down" conformation compared to other conformations since the azides must be in close proximity in the "down, down" conformation.

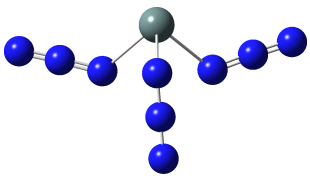

(i) $[Sn(N_3)_3)]^-$ conformer (*a*).

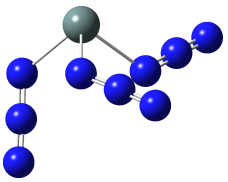

(ii) $[Sn(N_3)_3)]^-$ conformer (*b*).

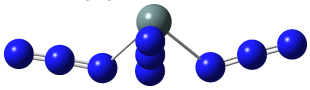

(iii) $[Sn(N_3)_3)]^-$ conformer (*c*).

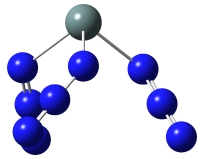

(iv) $[Sn(N_3)_3)]^-$ conformer (*d*).

Figure 6.7: Low energy conformers of $[Sn(N_3)_3)]^-$, optimised at the B3LYP/cc-pVTZ(-PP)/IEFPCM(THF) level. Relative energies are provided in Table 6.1.

The low energy conformations of the triazides $[Ge(N_3)_3]^-$ and $[Sn(N_3)_3]^-$ are illustrated in Figures 6.6 and 6.7, respectively. The lowest energy conformer in both cases is the "up, up, down" conformer (*a*). This is very closely followed by the "up, planar, down" conformer (*b*), which is very similar to the conformation of $[Ge(N_3)_3]^-$ observed in the crystal structure of $\{[Ge(N_3)_3]^-[PPh_4]^+\}$ shown in Figure 6.2(i). Interestingly the addition of thermodynamic corrections to the electronic energy to yield the Gibbs energy causes conformer (*b*) to be more stable than (*a*) for $[Ge(N_3)_3]^-$ but in $[Sn(N_3)_3]^-$, (*b*) is less stable than (*a*) in terms of Gibbs energy. The third conformer in both cases is the "up, up, up" conformer, which is more favourable than (*a*) in terms of Gibbs energy in both cases. The final conformer, (*d*), has a "down, down, down" configuration and is of near-C_3 symmetry. This conformer is similar to the crystal structure of $\{[Sn(N_3)_3]^-[PPh_4]^+\}$ shown in Figure 6.2(ii). This conformer is the least stable of the low energy conformers, both in terms of electronic and Gibbs energies.

As discussed above, a crystal structure of $\{[Sn(N_3)_3]^-[PPh_4]^+\}$ was obtained in which a $[Sn(N_3)_3]^-$ dimer is observed. (See Figure 6.2(iii)) Calculations were performed attempting to optimise the dimer, to investigate the potential of dimerisation in solution for both $[Ge(N_3)_3]^-$

Species	Conformer	E_{rel} / kJ mol^{-1}	G_{rel} / kJ mol^{-1}	Relative pop. at r.t.	No. absolute configurations	Mole fraction
$[Ge(N_3)Cl_2)]^-$	(*a*)	0.00	0.00	1.00	3	0.84
	(*b*)	4.81	4.13	0.19	3	0.16
$[Ge(N_3)_2Cl]^-$	(*a*)	0.00	0.00	1.00	6	0.83
	(*b*)	0.55	2.28	0.40	3	0.17
$[Ge(N_3)_3]^-$	(*a*)	0.00	0.00	0.70	3	0.16
	(*b*)	0.35	−0.89	1.00	6	0.47
	(*c*)	1.27	−0.85	0.98	3	0.23
	(*d*)	4.10	2.02	0.31	6	0.14
$[Sn(N_3)Cl_2)]^-$	(*a*)	0.00	0.00	1.00	3	0.58
	(*b*)	2.57	0.80	0.73	3	0.42
$[Sn(N_3)_2Cl]^-$	(*a*)	0.00	0.00	0.83	6	0.62
	(*b*)	0.31	−0.46	1.00	3	0.38
$[Sn(N_3)_3]^-$	(*a*)	0.00	0.00	0.84	3	0.32
	(*b*)	0.59	2.55	0.30	6	0.22
	(*c*)	0.72	−0.44	1.00	3	0.38
	(*d*)	3.06	5.03	0.11	6	0.08
	dimer	10.80				
	dimer+BSSE*	21.48				

Table 6.1: Summary of energetic differences between conformers of $[E(N_3)_{(3-n)}(X)_n]^-$, E = Ge, Sn; $n = 0, 1, 2, 3$. Calculations were performed using B3LYP/cc-pVTZ(-PP)/IEFPCM(THF). Geometries are illustrated in Figures 6.4, 6.5, 6.6 and 6.7. * Basis Set Superposition Error (BSSE) taken a from gas phase, counterpoise corrected calculation.[294,295]

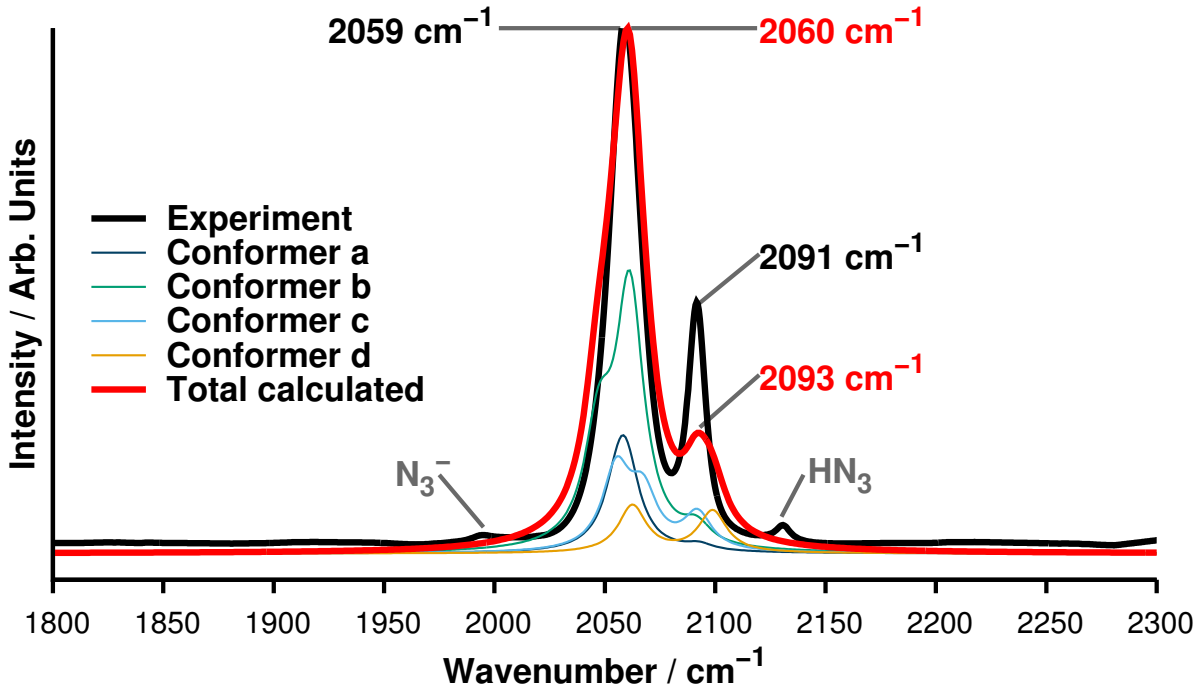

Figure 6.8: Comparison of experimental FTIR spectrum of $[Ge(N_3)_3]^-$ with harmonic B3LYP/cc-pVTZ(-PP)/IEFPCM(THF) calculated spectrum. The contributions from individual conformers are shown and are weighted according to their relative population at room temperature. (See Table 6.1) Harmonic frequencies are empirically scaled by 0.957. Calculated spectra fitted with Lorentzian functions with FWHM = 8 cm^{-1}.

and $[Sn(N_3)_3]^-$. A $[Sn(N_3)_3]^-$ dimer was successfully optimised; however, no $[Ge(N_3)_3]^-$ dimer could be optimised. The optimised geometry of the $[Sn(N_3)_3]^-$ dimer is shown in Figure 6.11(i). The dimer was found to be unstable with respect to the monomer: including counterpose corrections to account for Basis Set Superposition Error (BSSE), the population of the dimer in solution would be $\sim 10^{-4}\%$ of the population of the most stable $[Sn(N_3)_3]^-$ monomer conformation. It should be noted if an alternative, all-electron basis set for Ge was used, a $[Ge(N_3)_3]^-$ dimer could be optimised. This will be discussed in further detail in Section 6.1.1.

The calculated IR spectra of $[Ge(N_3)_3]^-$ and $[Sn(N_3)_3]^-$ are compared with experimental FTIR spectra in Figures 6.8 and 6.9, respectively. The spectra are normalised such that the intensity of the lower energy peak of the total calculated spectrum matches the corresponding peak in the experimental spectrum. Good agreement is achieved between calculated and experimental spectra in both cases. It should be noted that in both cases, the dominant conformer has a spectrum that does not fully match the experimental spectrum. In both cases, the intensity of the higher energy peak is underestimated in the calculations. This may be improved by the in-

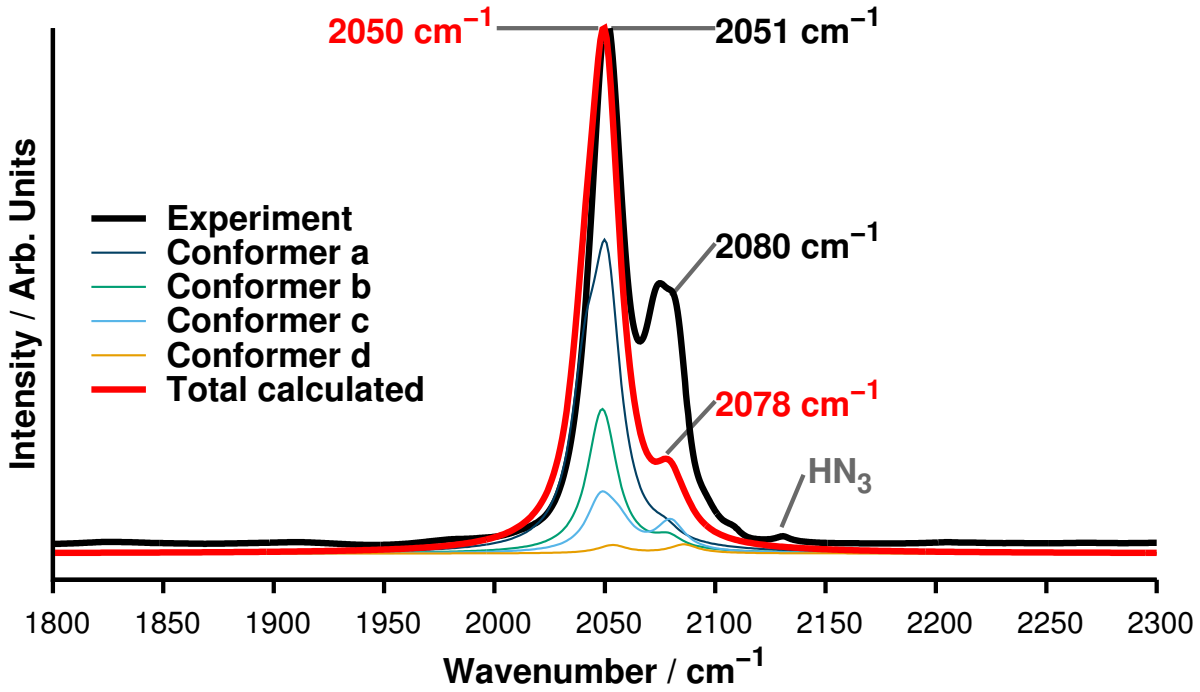

Figure 6.9: Comparison of experimental FTIR spectrum of $[Sn(N_3)_3]^-$ with harmonic B3LYP/cc-pVTZ(-PP)/IEFPCM(THF) calculated spectrum. The contributions from individual conformers are shown and are weighted according to their relative population at room temperature. (See Table 6.1) Harmonic frequencies are empirically scaled by 0.957. Calculated spectra fitted with Lorentzian functions with FWHM = 8 cm^{-1}.

clusion of anharmonic corrections in the calculations. It should be noted that both experimental spectra exhibit small peaks that can be assigned to either hydrazoic acid, HN_3, or the free azide anion, N_3^-.[361]

To further verify the identity of the synthesised compounds, the ^{14}N NMR chemical shifts of the conformers of $[Ge(N_3)_3]^-$ and $[Sn(N_3)_3]^-$ were computed using the Gauge Independent Atomic Orbitals method (GIAO).[289–293] The isotropic magnetic shielding tensor of N_i, σ_i, is related to the experimentally measured chemical shift, δ_i, by the equation

$$\delta_i = \frac{\sigma_i - \sigma_{\text{ref}}}{\sigma_{\text{ref}}}, \tag{6.1}$$

where σ_{ref} is the isotropic magnetic shielding tensor of a reference atom, in this case the N atom of nitromethane.[56] Since the rotation of the azide ligands is much faster than the timescale of the experimental acquisition of an NMR spectrum, the values of δ_i at the three nitrogen positions, N_κ, were averaged. The calculated chemical shifts are in good agreement with experimental val-

Species	Conformer	$\delta(N_\alpha)$ / ppm	$\delta(N_\beta)$ / ppm	$\delta(N_\gamma)$ / ppm
$[Ge(N_3)_3]^-$	(*a*)	−310.0	−152.2	−235.1
	(*b*)	−312.5	−152.8	−235.3
	(*c*)	−309.1	−150.8	−232.2
	(*d*)	−315.5	−155.4	−238.6
	weighted avg.	−311.1	−152.3	−234.6
	exptl.	−263	−136	−207
$[Sn(N_3)_3]^-$	(*a*)	−310.4	−151.7	−243.3
	(*b*)	−313.4	−152.6	−244.5
	(*c*)	−308.4	−150.6	−240.7
	(*d*)	−316.1	−154.5	−247.2
	weighted avg.	−310.2	−151.4	−242.5
	exptl.	−260	−136	−218

Table 6.2: Calculated ^{14}N NMR chemical shifts of $[E(N_3)_3]^-$, E = Ge, Sn. Calculations were performed using B3LYP/cc-pVTZ(-PP)/IEFPCM(THF) and the Gauge Independent Atomic Orbitals (GIAO) method.[289–293] The chemical shifts for the N_κ positions are averaged among the three nitrogens at that position. See Figure 6.3 for illustration of the notation used to indicate position. The chemical shift of nitromethane, calculated using the same method, was used as the reference. The weighted average was computed according to the relative populations of the conformers at room temperature. (See Table 6.1)

ues, although the margin of error increases as proximity to the central atom increases. Since the chemical shift is sensitive to core-electronic structure, this may be due to the fact that relativistic effects are neglected.[204]

6.1.1 Selection of basis set

As previously mentioned, some calculations involving $[Ge(N_3)_3]^-$ were performed using the all-electron basis set, cc-pVTZ-DK, for Ge.[287] This basis set was constructed by fitting to Scalar Relativistic (SR) Dirac-Hartree-Fock calculations, in which SR effects are included with the Douglas-Kroll-Hess (DKH) Hamiltonian.[230,287] However, Ge is a not remarkably heavy nucleus: the Lorentz factor of the 1s electrons of Ge, $\gamma = 1.0284$, very close to unity. This suggests that it might be reasonable to discard SR effects and include all electrons in the calculation. Indeed, if this approach is taken, one can compare the calculated IR spectrum to the experimentally measured FTIR and obtain very good agreement, arguably competitive with the results obtained using the cc-pVTZ(-PP) basis set. (See Figure 6.10)

One might be tempted to conclude, therefore, that SR effects are weak in Ge. However, optimisation of the $[Ge(N_3)_3)]^-$ dimer using the all electron basis set cc-pVTZ-DK yields an unusual geometry, which is compared to the geometry of the $[Sn(N_3)_3)]^-$ dimer in Figure 6.11

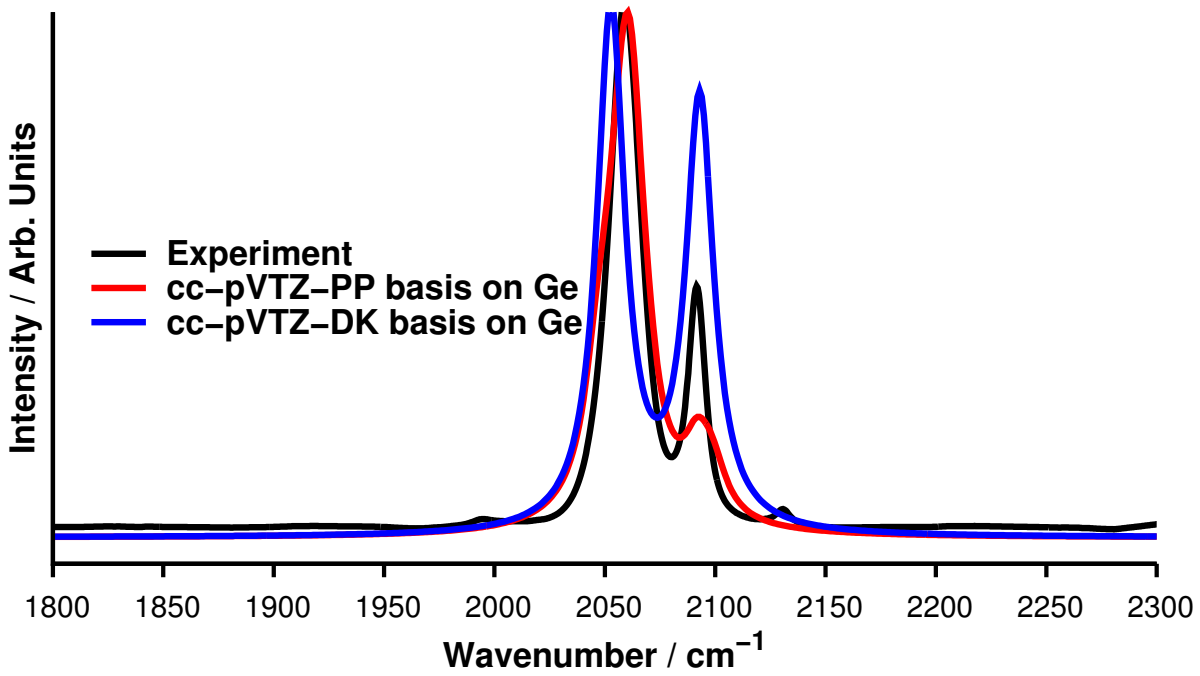

Figure 6.10: Comparison of FTIR spectra of $[Ge(N_3)_3]^-$ calculated using the cc-pVTZ-PP and cc-pVTZ-DK basis sets for Ge with the B3LYP functional, the cc-pVTZ basis set for N and THF solvent implictly with the IEFPCM. Harmonic frequencies were scaled empirically by 0.957 when cc-pVTZ-PP was used and 0.937 when cc-pVTZ-DK was used. Calculated spectra fitted with Lorentzian functions with FWHM = 8 cm^{-1}.

The non-relativistic all-electron calculations predict that one of the azides of each monomer coordinates to the central Ge in a linear fashion. This is exceedingly unlikely. Indeed, searching the Cambridge Structural Database reveals that the most common coordination angle for azides is ∼124°. (See Figure 6.12) It should be noted that no linear non-metal azide coordination angles were found, suggesting that the geometry optimised with the cc-pVTZ-DK basis set

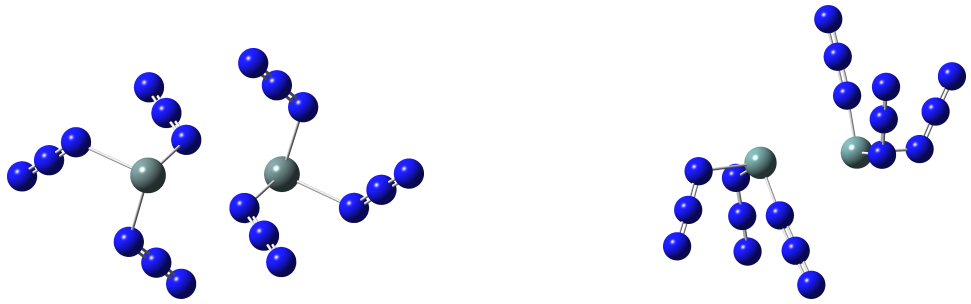

(i) $[Sn(N_3)_3)]^-$ dimer. **(ii)** $[Ge(N_3)_3)]^-$ dimer.

Figure 6.11: Comparison of optimised geometries of the $[Sn(N_3)_3]^-$ and $[Ge(N_3)_3]^-$ dimers. The $[Sn(N_3)_3]^-$ dimer was optimised using B3LYP/cc-pVTZ(-PP)/IEFPCM(THF) and the $[Ge(N_3)_3]^-$ dimmer was optimised using B3LYP/cc-pVTZ(-DK)/IEFPCM(THF). It should be noted that optimisations performed of the $[Ge(N_3)_3]^-$ dimer using B3LYP/cc-pVTZ(-PP)/IEFPCM(THF) dissociated.

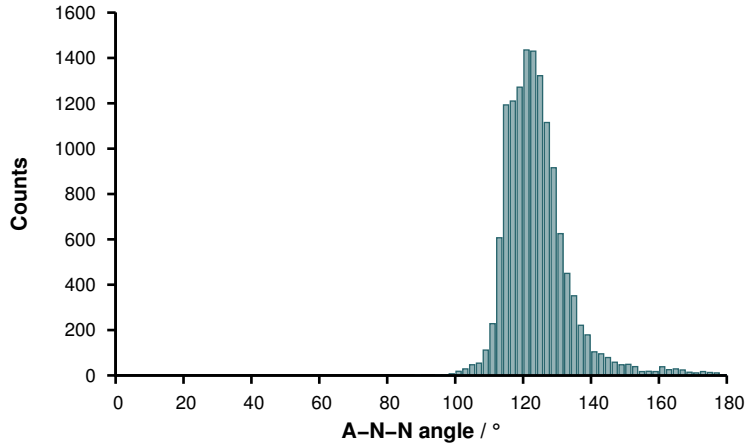

Figure 6.12: Histogram showing frequency of azide coordination angles A–N–N, where A is any atom and N–N forms part of an N–N–N chain that has a bond angle between 170-180°, within the Cambridge Structural Database.[363] It should be noted that no linear non-metal azide bonds were found. *Accessed 14/09/2016.*

is not physical. Unfortunately, technical limitations in the Gaussian 09 software preclude the possibility of optimising the $[Ge(N_3)_3)]^-$ dimer with the DKH Hamiltonian, since optimisations are limited to systems with fewer than 50 degrees of freedom. This resulted in the use of the cc-pVTZ-PP basis set, which includes an effective core potential to describe the core-electrons, for Ge in place of the cc-pVTZ-DK basis in the calculations reported in Section 6.1.

6.2 Conclusion

In summary, the synthesis of two low-valent, homoleptic polyazides, $[E(N_3)_3]^-$; E = Ge, Sn, was confirmed by comparison of calculated and experimental IR and ^{14}N NMR spectra. By thoroughly investigating the possible conformations of $[E(N_3)_3]^-$, good agreement was obtained between calculated and experimental spectra. This highlights the importance of considering conformational flexibility of molecules in computational investigations. In Section 6.1.1, the use of an inadequate basis set was shown to give qualitative agreement in calculations of the vibrational spectrum; however, the optimisation of an un-physical geometry highlights the fact that basis sets must be selected judiciously.

Part IV

Conclusion

Chapter 7

Conclusions and future work

This work largely focused on investigating Pt acetylide complexes in which excited state Electron Transfer (ET) could be manipulated by means of selective vibrational excitation.

In Chapter 4, the ground and excited state properties of the compounds **PTZ-CH_2-Pt-NAP**, **PTZ-Pt-NAP**, **OMePTZ-Pt-NAP** and **PTZ-Pt^H-NAP** were investigated by means of Density Functional Theory (DFT) and Time-Dependent DFT in the form of the B3LYP hybrid functional, using the SDD, 6-31G(d) and cc-pVTZ basis sets in various combinations. Good agreement between the experimentally determined ground state vibrational and electronic spectra, and computed spectra is achieved, as well as reasonable agreement between experimental and computed excited state vibrational spectra for some systems.

Excited state Potential Energy Surface (PES) investigations, also performed using TD-DFT, along a number of different coordinates reveal that the experimentally observed excited state dynamics may be due to a crossover between the Charge Transfer (CT) and Charge Separated State (CSS) PESs, with the "unrelaxed" surfaces, shown in Figure 4.17, showing particularly strong agreement. These investigations show that careful choices must be made when investigating excited state PESs to properly describe vibrational modes. The efficacy of the most simplistic models is questioned, since though they show reasonable agreement with experiment when computing vibrational and electronic spectra, they fail to provide a good framework to describe excited state dynamics.

In Chapter 5, the unexpectedly complex ground state vibrational structure of [Pt(bipyCOOEt)(C≡C-Ph-CH_2-PTZ)$_2$] was resolved by means of calculations including anharmonic correc-

tions. The appearance of an additional band in the acetylide region, reported experimentally,[54] was found to be due to the presence of a near-resonant combination band, though there was no formal Fermi-resonance found between the combination band and near-by acetylide fundamental bands.

The electronic structure of [Pt(bipyCOOEt)(C≡C-Ph-CH_2-PTZ)$_2$] was also investigated using non-relativistic and relativistic TD-DFT. It was found that by using the simplified TD-DFT scheme, including scalar relativistic effects self-consistently and spin-orbit coupling perturbatively, with an extensive basis set (TZ2P), a good description of the UV-vis absorption spectra of the complex could be achieved. This selection of methods was then employed to calculate sections of the ground and excited state PES of [Pt(bipyCOOEt)(C≡C-Ph-CH_2-PTZ)$_2$] along the prominent vibrational coordinates identified. Using this data, it was postulated that the experimentally observed directional vibrational control in this system[55] was due to increased coupling between select excited states as a result of polarisation of the excited state during vibration, shown in Figure 5.29.

In Chapter 6, the ground state FTIR spectra of two novel main group triazide compounds were resolved. This was achieved as a result of an extensive investigation of conformational flexibility was conducted and population averaged vibrational spectra were calculated. The importance of a careful choice of basis set was also highlighted by the example of qualitatively incorrect geometries obtained when an inappropriate basis set was used.

Chapters 4 and 5 demonstrate that time-independent quantum chemical calculations can be used to gain qualitative insight into the time-dependent behaviour of complex systems. In the context of vibrational control, despite the clear similarities in chemical structure between the molecules discussed in these chapters, the proposed mechanisms underlying these phenomena are different. To gain a quantitative understanding of these mechanism, future work should focus on performing time-dependent simulations on these systems with the aim of developing a *predictive* model for controllable electron transfer. This could then be used in the future to design functional materials that display controllable electron transfer.

Part V

Appendices

Appendix A

A.1 Selected excitation energies

Number	Energy (cm^{-1})	f	Major contributions	Assignment
1	20266	0.0000	HOMO→LUMO (100%)	CSS
2	21476	0.4794	H−1 →LUMO (90%)	CT
3	21988	0.0791	H−2 →LUMO (87%)	CT′
4	24172	0.1655	H−3 →LUMO (91%)	dπ^*
5	27755	0.0000	H−5 →LUMO (99%)	dπ^*
6	28351	0.0035	HOMO→L+1 (13%), HOMO→L+2 (62%), HOMO→L+4 (21%)	$\pi\pi^*$

Table A.1: The lowest six calculated electronic excitations of singlet **PTZ-CH_2-Pt-NAP** at the B3LYP/cc-pVTZ level. f stands for oscillator strength. Major contributions are defined as having a >10% contribution to the transition.

Number	Energy (cm^{-1})	f	Major contributions	Assignment
1	3823	0.0000	$HOMO_\beta$ →$LUMO_\beta$ (100%)	CSS
2	5443	0.0039	$H-2_\beta$ →$LUMO_\beta$ (89%)	CT
3	6979	0.1516	$H-1_\beta$ →$LUMO_\beta$ (94%)	CT′
4	10218	0.0484	$H+2_\alpha$ →$L+2_\alpha$ (21%), $H-4_\beta$ →$LUMO_\beta$ (74%)	$\pi\pi^*$
	10899	0.0001	$H-5_\beta$ →$LUMO_\beta$ (99%)	dπ^*
6	11102	0.0028	$H\text{-}6_\beta$ →$LUMO_\beta$ (85%)	dπ^*

Table A.2: The lowest six calculated electronic excitations of the Franck-Condon triplet of **PTZ-CH_2-Pt-NAP** at the B3LYP/cc-pVTZ level. f stands for oscillator strength. Major contributions are defined as having a >10% contribution to the transition.

Number	Energy (cm^{-1})	f	Major contributions	Assignment
1	20328	0.0000	HOMO→LUMO (100%)	CSS
2	21924	0.5730	H−1 →LUMO (90%)	CT
3	22203	0.0856	H−2 →LUMO (88%)	CT′
4	24955	0.0735	H−3 →LUMO (95%)	$d\pi^*$
5	27815	0.0008	HOMO→L+1 (64%), HOMO→L+2 (23%), HOMO→L+3 (10%)	$\pi\pi^*$
6	28042	0.0000	H−5 →LUMO (99%)	$d\pi^*$

Table A.3: The lowest six calculated electronic excitations of singlet **PTZ-Pt-NAP** at the B3LYP/cc-pVTZ level. f stands for oscillator strength. Major contributions are defined as having a >10% contribution to the transition.

Number	Energy (cm^{-1})	f	Major contributions	Assignment
1	3817	0.0000	$HOMO_\beta$ →$LUMO_\beta$ (100%)	CSS
2	5624	0.0009	H−2_β →$LUMO_\beta$ (89%)	CT
3	7860	0.1519	H−1_β →$LUMO_\beta$ (94%)	CT′
4	10234	0.0381	H+2_α →L+2_α (17%), H−4_β →$LUMO_\beta$ (73%)	$\pi\pi^*$
5	11020	0.0028	H-6_β →$LUMO_\beta$ (85%)	$d\pi^*$
6	11122	0.0001	H−5_β →$LUMO_\beta$ (99%)	$d\pi^*$

Table A.4: The lowest six calculated electronic excitations of the Franck-Condon triplet of **PTZ-Pt-NAP** at the B3LYP/cc-pVTZ level. f stands for oscillator strength. Major contributions are defined as having a >10% contribution to the transition.

Number	Energy (cm^{-1})	f	Major contributions	Assignment
1	18041	0.0000	HOMO→LUMO (100%)	CSS
2	21867	0.5435	H−1 →LUMO (88%)	CT
3	22174	0.1064	H−2 →LUMO (86%)	CT′
4	24836	0.0833	H−3 →LUMO (94%)	$d\pi^*$
5	26281	0.0000	HOMO→L+1 (69%), HOMO→L+2 (28%)	$\pi\pi^*$
6	27719	0.0000	H−4 →LUMO (100%)	CSS′

Table A.5: The lowest six calculated electronic excitations of singlet **OMePTZ-Pt-NAP** at the B3LYP/cc-pVTZ level. f stands for oscillator strength. Major contributions are defined as having a >10% contribution to the transition.

Number	Energy (cm^{-1})	f	Major contributions	Assignment
1	1538	0.0	$HOMO_\beta$ →$LUMO_\beta$ (100%)	CSS
2	5589	0.0013	$H-2_\beta$ →$LUMO_\beta$ (88%)	CT
3	7736	0.152	$H-1_\beta$ →$LUMO_\beta$ (92%)	CT′
4	10229	0.0401	$H+2_\alpha$ →$L+2_\alpha$ (19%), $H-5_\beta$ →$LUMO_\beta$ (73%)	$\pi\pi^*$
5	11028	0.0028	$H-7_\beta$ →$LUMO_\beta$ (85%)	$d\pi^*$
6	11110	0.0001	$H-6_\beta$ →$LUMO_\beta$ (99%)	$d\pi^*$

Table A.6: The lowest six calculated electronic excitations of the Franck-Condon triplet of **OMePTZ-Pt-NAP** at the B3LYP/cc-pVTZ level. f stands for oscillator strength. Major contributions are defined as having a >10% contribution to the transition.

Number	Energy (cm^{-1})	f	Major contributions	Assignment
1	20070	0.0002	HOMO→LUMO (100%)	CSS
2	23948	0.6917	H−2 →LUMO (14%), H−1 →LUMO (83%)	CT
3	24289	0.0104	H−4 →LUMO (11%), H−2 →LUMO (71%), H−1 →LUMO (15%)	CT′
4	27316	0.0533	H−4 →LUMO (81%), H−2 →LUMO (13%)	CT″
5	27871	0.0004	HOMO→L+1 (46%), HOMO→L+3 (42%)	$\pi\pi^*$
6	28701	0.0000	H−3 →LUMO (99%)	CSS′

Table A.7: The lowest six calculated electronic excitations of singlet **PTZ-Pt^{H}-NAP** at the B3LYP/SDD+6-31G(d). f stands for oscillator strength. Major contributions are defined as having a >10% contribution to the transition.

Number	Energy (cm^{-1})	f	Major contributions	Assignment
1	2672	0.0006	$HOMO_\beta$ →$LUMO_\beta$ (100%)	CSS
2	6240	0.0024	$H-3_\beta$ →$LUMO_\beta$ (10%), $H-1_\beta$ →$LUMO_\beta$ (84%)	CT
3	9542	0.0940	$H+2_\alpha$ →$L+4_\alpha$ (16%), $H-4_\beta$ →$LUMO_\beta$ (21%), $H-3_\beta$ →$LUMO_\beta$ (53%)	CT′
4	9801	0.0028	$H-5_\beta$ →$LUMO_\beta$ (85%)	$\pi\pi^*$
5	10821	0.0116	$H+2_\alpha$ →$L+4_\alpha$ (13%), $H-4_\beta$ →$LUMO_\beta$ (46%), $H-3_\beta$ →$LUMO_\beta$ (23%), $H-1_\beta$ →$LUMO_\beta$ (10%)	$d\pi^*$
6	11288	0.0003	$H-2_\beta$ →$LUMO_\beta$ (98%)	CT′

Table A.8: The lowest six calculated electronic excitations of the Franck-Condon triplet of **PTZ-Pt^{H}-NAP** at the B3LYP/SDD+6-31G(d). f stands for oscillator strength. Major contributions are defined as having a >10% contribution to the transition.

A.2 B3LYP/cc-pVTZ frontier molecular orbitals of PTZ-Pt^{H}-NAP

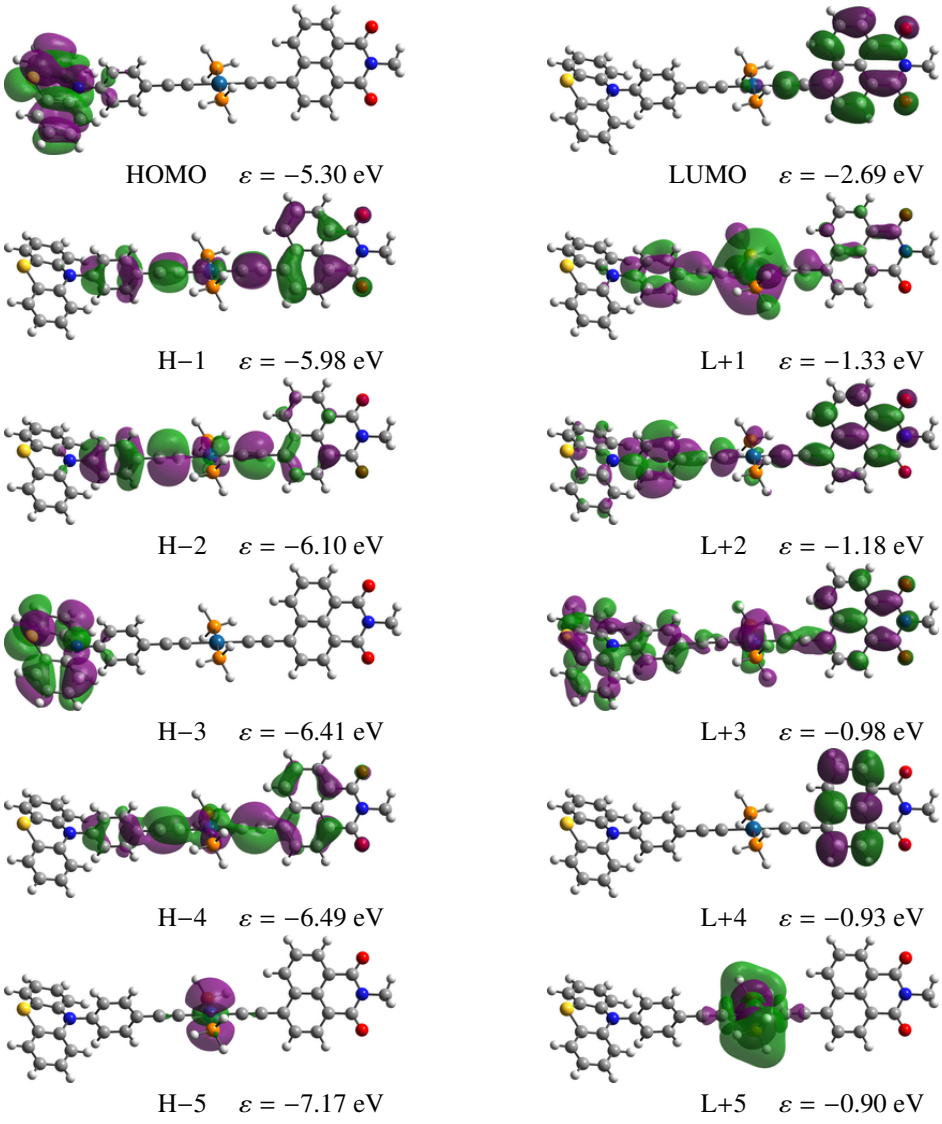

Figure A.1: Singlet frontier molecular orbitals of **PTZ-Pt^{H}-NAP** at the B3LYP/cc-pVTZ) level.

A.3 Calculated Cartesian displacements of the ν_a(C≡C) mode in the ground and excited state of PTZ-Pt^{H}-NAP.

State	Type	Displacement				Ratio of displacement
		C_a	C_b	C_c	C_d	
S_0	GS	0.73	−0.63	−0.13	0.16	0.96:0.04
S_1	CSS	−0.74	0.65	0.00	0.00	1.00:0.00
S_2	CT	0.57	−0.49	−0.41	0.48	0.59:0.41
T_1	^{3}NAP	0.75	−0.63	0.00	0.00	1.00:0.00
T_2	CSS	-	-	-	-	-
T_3	CT	0.62	−0.54	−0.35	0.41	0.70:0.30

Table A.9: Normalised[274] Cartesian displacements for the atoms NAP–C_a≡C_b–Pt–C_c≡C_d–Ph–PTZ along the molecular axis in the ground and excited state ν_a(C≡C) mode of **PTZ-Pt^{H}-NAP** at the B3LYP/SDD+6-31G(d) level.

A.4 Deconvolution of UV/vis absorption spectrum of [Pt(bipyCOOEt)(C≡C-Ph-CH_2-PTZ)$_2$].

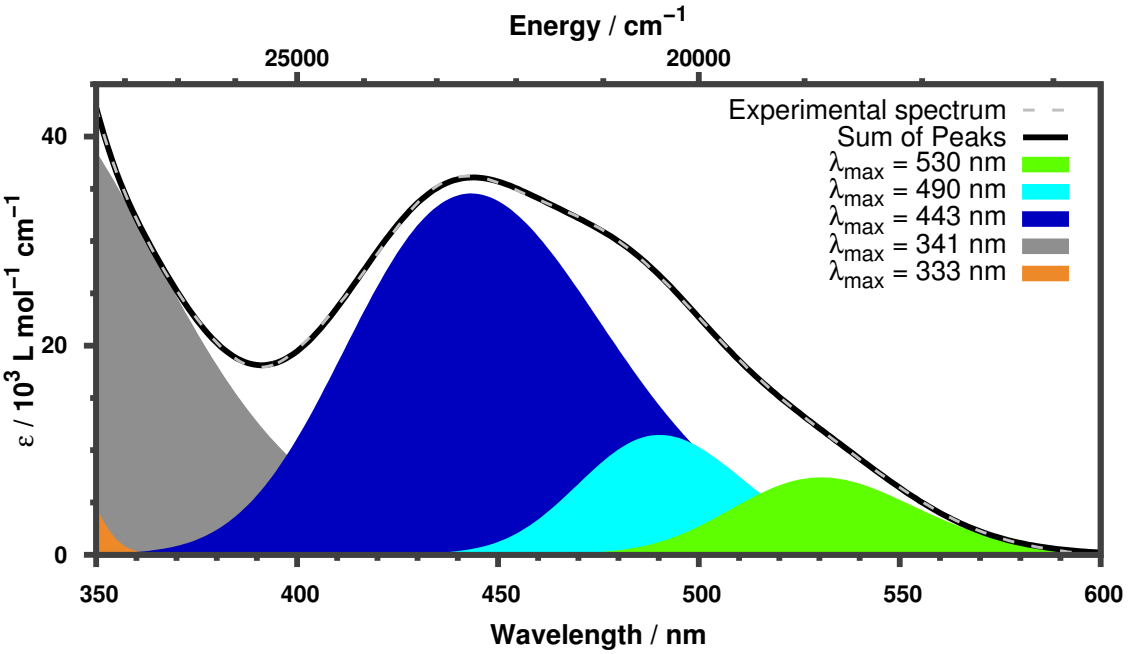

Figure A.2: Deconvolution of experimental UV-vis absorption spectra of [Pt(bipyCOOEt)(C≡C-Ph-CH_2-PTZ)$_2$]. The experimental spectrum is shown as a dashed grey line and the component Gaussian curves are shown as filled curves. The sum of the Gaussian curves is shown as a thick black line. The parameters of the Gaussian curves are provided in Table A.10. The residual sum of squares error, $\chi^2 = 0.0025$. It should be noted that the two peaks λ_{max}=333 and λ_{max}=341 are used to reduce residual error in the 400 nm to 600 nm region and are not intended to be meaningful.

λ_{max} / nm	$\tilde{\nu}_{max}$ / cm^{-1}	FWHM / cm^{-1}	Amplitude / 10^3 L mol^{-1} cm^{-1}
530	18852 (42)	1886 (34)	7.313 (0.301)
490	20397 (25)	2000 (64)	11.377 (0.771)
443	22557 (13)	3800 (68)	34.464 (0.402)
341	29309 (616)	1336 (532)	10.221 (9.895)
333	30024 (570)	6526 (620)	44.033 (4.940)

Table A.10: Parameters of the Gaussian curves used to deconvolute the experimental UV-vis absorption spectra of [Pt(bipyCOOEt)(C≡C-Ph-CH_2-PTZ)$_2$]. Standard deviations for the parameters are provided in brackets. It should be noted that the two peaks λ_{max}= 333 and λ_{max}= 341 are used to reduce residual error in the 400 nm to 600 nm region and are not intended to be meaningful.

A.5 Calculated Cartesian displacements of the acetylide modes of [Pt(bipyCOOEt)(C≡C-Ph-CH_2-PTZ)$_2$].

Species	Vibration	Displacement				Ratio of displacement
		C_a	C_b	C_c	C_d	
12-12	$^{12}\nu_{289}$	0.46	−0.52	0.47	−0.54	0.48:0.52
	$^{12}\nu_{288}$	0.47	−0.54	−0.45	0.52	0.52:0.48
13-12	$^{13}\nu_{289}$	−0.05	0.05	−0.66	0.74	0.01:0.99
	$^{13}\nu_{288}$	0.65	−0.74	−0.05	0.06	0.99:0.01

Table A.11: Normalised[274] Cartesian displacements of the acetylide modes of [Pt(bipyCOOEt)(C≡C-Ph-CH_2-PTZ)$_2$]. Atoms C_a and C_b are on the right-hand or ^{13}C labelled side of **12-12** and **13-12**, respectively, and C_a is connected to the Pt centre. Atoms C_c and C_d are on the left-hand or ^{12}C labelled side of **12-12** and **13-12**, respectively, and C_a is connected to the Pt centre. Calculations performed using B3LYP/SDD[Pt]6-311G(d,p)[H,C,N,O,S]/IEFPCM(CH_2Cl_2). *Eigenvectors* of the vibrational modes are shown in Figure 5.5.

Bibliography

(1) N. S. Kardashev, 'Transmission of Information by Extraterrestrial Civilizations', *Astronomicheskii Zhurnal*, **1964**, *41*, 282–287.
(Cited on page 2)

(2) M. M. Ćirković, 'Kardashev's Classification at 50+: a Fine Vehicle with Room for Improvement', *Serbian Astronomical Journal*, **2015**, *2015*, 1–15.
(Cited on page 2)

(3) *EPSRC online portfolio*, http://www.epsrc.ac.uk/research/ourportfolio (Cited on page 3).

(4) Department of Economic and Social Affairs of the United Nations Secretariat, *The Millennium Development Goals Report 2014*, tech. rep., 2014 (Cited on page 3).

(5) Intergovernmental Panel on Climate Change, *Climate Change 2014: Impacts, Adaptation and Vulnerability - Contributions of the Working Group II to the Fifth Assessment Report: Summary for Policy Makers*, tech. rep., IPCC, 2014 (Cited on page 3).

(6) NASA, *Sun Fact Sheet*, http://nssdc.gsfc.nasa.gov/planetary/factsheet/sunfact.html (Cited on page 3).

(7) N. S. Lewis, 'Research Opportunities to Advance Solar Energy Utilization', *Science*, **2016**, *351*, aad1920.
(Cited on page 3)

(8) M. R. Wasielewski, 'Photoinduced Electron Transfer in Supramolecular Systems for Artificial Photosynthesis', *Chemical Reviews*, **1992**, *92*, 435–461.
(Cited on page 3)

(9) D. Gust, T. A. Moore and A. L. Moore, 'Mimicking Photosynthetic Solar Energy Transduction', *Accounts of Chemical Research*, **2001**, *34*, 40–48.
(Cited on page 3)

(10) V. Balzani, A. Credi and M. Venturi, 'Photochemical Conversion of Solar Energy', *ChemSusChem*, **2008**, *1*, 26–58.
(Cited on page 3)

(11) S. Berardi, S. Drouet, L. Francàs, C. Gimbert-Suriñach, M. Guttentag, C. Richmond, T. Stoll and A. Llobet, 'Molecular Artificial Photosynthesis', *Chemical Society Reviews*, **2014**, *43*, 7501–7519.
(Cited on page 3)

(12) D. M. Schultz and T. P. Yoon, 'Solar Synthesis: Prospects in Visible Light Photocatalysis', *Science*, **2014**, *343*, 1239176.
(Cited on page 3)

(13) S. Fukuzumi, K. Ohkubo and T. Suenobu, 'Long-Lived Charge Separation and Applications in Artificial Photosynthesis', *Accounts of Chemical Research*, **2014**, *47*, 1455–1464.
(Cited on page 3)

(14) D. Kim, K. K. Sakimoto, D. Hong and P. Yang, 'Artificial Photosynthesis for Sustainable Fuel and Chemical Production', *Angewandte Chemie International Edition*, **2015**, *54*, 3259–3266.
(Cited on page 3)

(15) D. Gust, T. A. Moore and A. L. Moore, 'Solar Fuels via Artificial Photosynthesis', *Accounts of Chemical Research*, **2009**, *42*, 1890–1898.
(Cited on page 3)

(16) R. J. Cogdell, T. H. P. Brotosudarmo, A. T. Gardiner, P. M. Sanchez and L. Cronin, 'Artificial Photosynthesis – Solar Fuels: Current Status and Future Prospects', *Biofuels*, **2010**, *1*, 861–876.
(Cited on page 3)

(17) H. Zhou, R. Yan, D. Zhang and T. Fan, 'Challenges and Perspectives in Designing Artificial Photosynthetic Systems', *Chemistry - A European Journal*, **2016**, *22*, 9870–9885.
(Cited on page 3)

(18) L. Hammarström, 'Accumulative Charge Separation for Solar Fuels Production: Coupling Light-Induced Single Electron Transfer to Multielectron Catalysis', *Accounts of Chemical Research*, **2015**, *48*, 840–850.
(Cited on page 3)

(19) M. Natali, S. Campagna and F. Scandola, 'Photoinduced Electron Transfer Across Molecular Bridges: Electron- and Hole-Transfer Superexchange Pathways', *Chemical Society Reviews*, **2014**, *43*, 4005–4018.
(Cited on page 3)

(20) A. H. Zewail, 'Laser Selective Chemistry – Is It Possible?', *Physics Today*, **1980**, *33*, 27.
(Cited on pages 3, 4)

(21) P. F. Barbara, T. J. Meyer and M. A. Ratner, 'Contemporary Issues in Electron Transfer Research', *The Journal of Physical Chemistry*, **1996**, *100*, 13148–13168.
(Cited on page 3)

(22) V. Balzani, P. Ceroni and A. Juris, *Photochemistry and Photophysics: Concepts, Research, Applications*, Wiley-VCH, Weinheim, 1st edn., 2014.
(Cited on pages 3, 4, 11)

(23) I. V. Hertel and W. Radloff, 'Ultrafast Dynamics in Isolated Molecules and Molecular Clusters', *Reports on Progress in Physics*, **2006**, *69*, 1897–2003.
(Cited on pages 4, 57)

(24) M. Chergui, 'Ultrafast Photophysics of Transition Metal Complexes', *Accounts of Chemical Research*, **2015**, *48*, 801–808.
(Cited on pages 4, 16, 49)

(25) D. P. Hoffman and R. A. Mathies, 'Femtosecond Stimulated Raman Exposes the Role of Vibrational Coherence in Condensed-Phase Photoreactivity', *Accounts of Chemical Research*, **2016**, *49*, 616–625.
(Cited on page 4)

(26) J. J. Gerdy, M. Dantus, R. M. Bowman and A. H. Zewail, 'Femtosecond Selective Control of Wave Packet Population', *Chemical Physics Letters*, **1990**, *171*, 1–4.
(Cited on page 4)

(27) M. Gruebele and A. H. Zewail, 'Femtosecond Wave Packet Spectroscopy: Coherences, the Potential, and Structural Determination', *The Journal of Chemical Physics*, **1993**, *98*, 883–902.
(Cited on page 4)

(28) V. I. Prokhorenko, A. M. Nagy and R. J. D. Miller, 'Coherent Control of the Population Transfer in Complex Solvated Molecules at Weak Excitation. An Experimental Study', *The Journal of Chemical Physics*, **2005**, *122*, 184502.
(Cited on page 5)

(29) V. I. Prokhorenko, A. M. Nagy, S. A. Waschuk, L. S. Brown, R. R. Birge and R. J. D. Miller, 'Coherent Control of Retinal Isomerization in Bacteriorhodopsin', *Science*, **2006**, *313*, 1257–1261.
(Cited on page 5)

(30) P. van der Walle, M. T. W. Milder, L. Kuipers and J. L. Herek, 'Quantum Control Experiment Reveals Solvation-Induced Decoherence', *Proceedings of the National Academy of Sciences*, **2009**, *106*, 7714–7717.
(Cited on page 5)

(31) M. Liebel and P. Kukura, 'Lack of Evidence for Phase-Only Control of Retinal Photoisomerization in the Strict One-Photon Limit', *Nature Chemistry*, **2016**, DOI: 10.1038/nchem.2598.
(Cited on page 5)

(32) G. M. Roberts, D. J. Hadden, L. T. Bergendahl, A. M. Wenge, S. J. Harris, T. N. V. Karsili, M. N. R. Ashfold, M. J. Paterson and V. G. Stavros, 'Exploring Quantum Phenomena and Vibrational Control in σ^* Mediated Photochemistry', *Chemical Science*, **2013**, *4*, 993–1001.
(Cited on page 5)

(33) S. S. Skourtis, D. H. Waldeck and D. N. Beratan, 'Inelastic Electron Tunneling Erases Coupling-Pathway Interferences', *The Journal of Physical Chemistry B*, **2004**, *108*, 15511–15518.
(Cited on pages 5, 77)

(34) D. Xiao, S. S. Skourtis, I. V. Rubtsov and D. N. Beratan, 'Turning Charge Transfer On and Off in a Molecular Interferometer with Vibronic Pathways.', *Nano Letters*, **2009**, *9*, 1818–1823.
(Cited on pages 5, 6, 77)

(35) D. N. Beratan, S. S. Skourtis, I. A. Balabin, A. Balaeff, S. Keinan, R. Venkatramani and D. Xiao, 'Steering Electrons on Moving Pathways', *Accounts of Chemical Research*, **2009**, *42*, 1669–1678.
(Cited on page 5)

(36) Z. Lin, C. M. Lawrence, D. Xiao, V. V. Kireev, S. S. Skourtis, J. L. Sessler, D. N. Beratan and I. V. Rubtsov, 'Modulating Unimolecular Charge Transfer by Exciting Bridge Vibrations', *Journal of the American Chemical Society*, **2009**, *131*, 18060–18062.
(Cited on pages 5, 56, 77, 99)

(37) H. Carias, D. N. Beratan and S. S. Skourtis, 'Floquet Analysis for Vibronically Modulated Electron Tunneling', *The Journal of Physical Chemistry B*, **2011**, *115*, 5510–5518.
(Cited on pages 5, 77, 79, 101)

(38) P. Antoniou, Z. Ma, P. Zhang, D. N. Beratan and S. S. Skourtis, 'Vibrational Control of Electron-Transfer Reactions: a Feasibility Study for the Fast Coherent Transfer Regime', *Physical Chemistry Chemical Physics*, **2015**, *17*, 30854–30866.
(Cited on pages 5, 77, 101, 102)

(39) J. Lin, D. Balamurugan, P. Zhang, S. S. Skourtis and D. N. Beratan, 'Two-Electron Transfer Pathways', *The Journal of Physical Chemistry B*, **2015**, *119*, 7589–7597.
(Cited on pages 5, 77)

(40) M. A. Soler, A. E. Roitberg, T. Nelson, S. Tretiak and S. Fernandez-Alberti, 'Analysis of State-Specific Vibrations Coupled to the Unidirectional Energy Transfer in Conjugated Dendrimers', *The Journal of Physical Chemistry A*, **2012**, *116*, 9802–9810.
(Cited on page 5)

(41) M. A. Soler, T. Nelson, A. E. Roitberg, S. Tretiak and S. Fernandez-Alberti, 'Signature of Non-adiabatic Coupling in Excited-State Vibrational Modes', *The Journal of Physical Chemistry A*, **2014**, *118*, 10372–10379.
(Cited on pages 6, 68)

(42) A. E. Nazarov, V. Y. Barykov and A. I. Ivanov, 'Effect of Intramolecular High-Frequency Vibrational Mode Excitation on Ultrafast Photoinduced Charge Transfer and Charge Recombination Kinetics', *The Journal of Physical Chemistry C*, **2015**, *119*, 2989–2995.
(Cited on pages 6, 101, 102)

(43) V. Y. Barykov and A. I. Ivanov, 'Excited States of the High-Frequency Vibrational Modes and Kinetics of Ultrafast Photoinduced Electron Transfer', *Russian Journal of Physical Chemistry A*, **2016**, *90*, 491–497.
(Cited on pages 6, 102)

(44) K. E. Dorfman, Y. Zhang and S. Mukamel, 'Coherent Control of Long-Range Photoinduced Electron Transfer by Stimulated X-ray Raman Processes', *Proceedings of the National Academy of Sciences*, **2016**, *113*, 10001–10006.
(Cited on page 6)

(45) A. A. Bakulin, A. Rao, V. G. Pavelyev, P. H. M. van Loosdrecht, M. S. Pshenichnikov, D. Niedzialek, J. Cornil, D. Beljonne and R. H. Friend, 'The Role of Driving Energy and Delocalized States for Charge Separation in Organic Semiconductors', *Science*, **2012**, *335*, 1340–1344.
(Cited on page 6)

(46) A. A. Bakulin, R. Lovrincic, X. Yu, O. Selig, H. J. Bakker, Y. L. A. Rezus, P. K. Nayak, A. Fonari, V. Coropceanu, J.-L. Brédas and D. Cahen, 'Mode-Selective Vibrational Modulation of Charge Transport in Organic Electronic Devices', *Nature Communications*, **2015**, *6*, 7880.
(Cited on page 6)

(47) A. Pereverzev, E. R. Bittner and I. Burghardt, 'Energy and Charge-Transfer Dynamics Using Projected Modes', *The Journal of Chemical Physics*, **2009**, *131*, 034104.
(Cited on page 6)

(48) X. Yang and E. R. Bittner, 'Intramolecular Charge- and Energy-Transfer Rates with Reduced Modes: Comparison to Marcus Theory for Donor–Bridge–Acceptor Systems', *The Journal of Physical Chemistry A*, **2014**, *118*, 5196–5203.
(Cited on page 6)

(49) X. Yang and E. R. Bittner, 'Computing Intramolecular Charge and Energy Transfer Rates Using Optimal Modes', *The Journal of Chemical Physics*, **2015**, *142*, 244114.
(Cited on page 6)

(50) P. A. Scattergood, M. Delor, I. V. Sazanovich, O. V. Bouganov, S. A. Tikhomirov, A. S. Stasheuski, A. W. Parker, G. M. Greetham, M. Towrie, E. S. Davies, A. J. H. M. Meijer and J. A. Weinstein, 'Electron Transfer Dynamics and Excited State Branching in a Charge-Transfer Platinum(II) Donor-Bridge-Acceptor Assembly', *Dalton Transactions*, **2014**, *43*, 17677–17693.
(Cited on pages 6, 56)

(51) M. Delor, P. A. Scattergood, I. V. Sazanovich, A. W. Parker, G. M. Greetham, A. J. H. M. Meijer, M. Towrie and J. A. Weinstein, 'Toward Control of Electron Transfer in Donor-Acceptor Molecules by Bond-Specific Infrared Excitation', *Science*, **2014**, *346*, 1492–1495.
(Cited on pages 6, 7, 56, 70, 73, 75, 77, 87)

(52) W. M. Kwok, D. L. Phillips, P. K.-y. Yeung and V. W.-w. Yam, 'Resonance Raman Investigation of the MLCT Transition in $[Pt(dppm)_2(PhC{\equiv}C)_2]$ and the MMLCT Transition in $[Pt_2(\mu\text{-}dppm)_2(\mu\text{-}PhC{\equiv}C)(PhC{\equiv}C)_2]^{+}$', *The Journal of Physical Chemistry A*, **1997**, *101*, 9286–9295.
(Cited on page 7)

(53) M. Delor, T. Keane, P. A. Scattergood, I. V. Sazanovich, G. M. Greetham, M. Towrie, A. J. H. M. Meijer and J. A. Weinstein, 'On the Mechanism of Vibrational Control of Light-Induced Charge Transfer in Donor–Bridge–Acceptor Assemblies', *Nature Chemistry*, **2015**, *7*, 689–695.
(Cited on pages 7, 57, 77)

(54) S. A. Archer, T. Keane, M. Delor, A. J. H. M. Meijer and J. A. Weinstein, '^{13}C or Not ^{13}C: Selective Synthesis of Asymmetric Carbon-13-Labeled Platinum(II) cis-Acetylides', *Inorganic Chemistry*, **2016**, *55*, 8251–8253.
(Cited on pages 8, 80–82, 85, 86, 88–92, 155)

(55) M. Delor, S. A. Archer, T. Keane, A. J. H. M. Meijer, I. V. Sazanovich, G. M. Greetham, M. Towrie and J. A. Weinstein, 'Directing Light-Induced Electron Transfer at Molecular Crossroads using Vibrational Excitation', *submitted*.
(Cited on pages 8, 82, 98–101, 155)

(56) B. Peerless, T. Keane, A. J. H. M. Meijer and P. Portius, 'Homoleptic Low-Valent Polyazides of Group 14 Elements', *Chemical Communications*, **2015**, *51*, 7435–7438.
(Cited on pages 8, 142, 143, 149)

(57) E. Schrödinger, 'Quantisierung als Eigenwertproblem - Erste Mitteilung', *Annalen der Physik*, **1926**, *384*, 361–376.
(Cited on pages 9, 40)

(58) E. Schrödinger, 'Quantisierung als Eigenwertproblem - Zweite Mitteilung', *Annalen der Physik*, **1926**, *384*, 489–527.
(Cited on page 9)

(59) E. Schrödinger, 'Der Stetige Übergang von der Mikro- zur Makromechanik', *Die Naturwissenschaften*, **1926**, *14*, 664–666.
(Cited on page 9)

(60) E. Schrödinger, 'Über das Verhältnis der Heisenberg-Born-Jordanschen Quantenmechanik zu der Meinem', *Annalen der Physik*, **1926**, *384*, 734–756.
(Cited on page 9)

(61) E. Schrödinger, 'Quantisierung als Eigenwertproblem - Dritte Mitteilung', *Annalen der Physik*, **1926**, *385*, 437–490.
(Cited on page 9)

(62) E. Schrödinger, 'Quantisierung als Eigenwertproblem - Veirte Mitteilung', *Annalen der Physik*, **1926**, *386*, 109–139.
(Cited on page 9)

(63) E. Schrödinger, 'An Undulatory Theory of the Mechanics of Atoms and Molecules', *Physical Review*, **1926**, *28*, 1049–1070.
(Cited on pages 9, 40)

(64) J. Binney and D. Skinner, *The Physics of Quantum Mechanics*, Oxford University Press, 1st edn., 2014.
(Cited on pages 10, 16, 17, 19)

(65) K. F. Sundman, 'Mémoire sur le Problème des Trois Corps', *Acta Mathematica*, **1913**, *36*, 105–179.
(Cited on page 11)

(66) L. K. Babadzanjanz, 'Existence of the Continuations in the N-Body Problem', *Celestial Mechanics*, **1979**, *20*, 43–57.
(Cited on page 11)

(67) Q.-d. Wang, 'The Existence of Global Solution of the N-Body Problem', *Chinese Astronomy and Astrophysics*, **1986**, *10*, 135–142.
(Cited on page 11)

(68) L. K. Babadzanjanz, 'On the Global Solution of the N-Body Problem', *Celestial Mechanics & Dynamical Astronomy*, **1993**, *56*, 427–449.
(Cited on page 11)

(69) F. Diacu, 'The Solution of the N-Body Problem', *The Mathematical Intelligencer*, **1996**, *18*, 66–70.
(Cited on pages 11, 16)

(70) H. Mustroph, 'Potential-Energy Surfaces, the Born-Oppenheimer Approximations, and the Franck-Condon Principle: Back to the Roots', *ChemPhysChem*, **2016**, *17*, 2616–2629.
(Cited on page 11)

(71) M. Born and J. Franck, 'Quantentheorie und Molekelbildung', *Zeitschrift für Physik*, **1925**, *31*, 411–429.
(Cited on pages 11, 12)

(72) J. Franck, 'Elementary Processes of Photochemical Reactions', *Transactions of the Faraday Society*, **1926**, *21*, 536–542.
(Cited on pages 11, 12)

(73) E. U. Condon, 'A Theory of Intensity Distribution in Band Systems', *Physical Review*, **1926**, *28*, 1182–1201.
(Cited on page 11)

(74) E. U. Condon, 'Coupling of Electronic and Nuclear Motions in Diatomic Molecules', *Proceedings of the National Academy of Sciences*, **1927**, *13*, 462–466.
(Cited on page 11)

(75) M. Born and R. Oppenheimer, 'Zur Quantentheorie der Molekeln', *Annalen der Physik*, **1927**, *20*, 457–484.
(Cited on pages 12, 49)

(76) M. Born and R. Oppenheimer, in *Quantum Chemistry - Classic Scientific Papers*, ed. H. Hettema, World Scientific Publishing Co. Pte. Ltd., Singapore, 1st edn., 2000, ch. 1, pp. 1–24 (Cited on pages 12, 49).

(77) E. U. Condon, 'Nuclear Motions Associated with Electron Transitions in Diatomic Molecules', *Physical Review*, **1928**, *32*, 858–872.
(Cited on page 12)

(78) M. Born and V. Fock, 'Beweis des Adiabatensatzes', *Zeitschrift für Physik*, **1928**, *51*, 165–180.
(Cited on page 12)

(79) M. Born and K. Huang, *Dynamical Theory of Crystal Lattices*, Clarendon Press, Oxford, 1st edn., 1954.
(Cited on page 12)

(80) P. W. Atkins and R. Friedman, *Molecular Quantum Mechanics*, Oxford University Press, Oxford, 4th edn., 2011, vol. 134, p. 588.
(Cited on page 13)

(81) J. R. Reimers, L. K. McKemmish, R. H. McKenzie and N. S. Hush, 'Non-Adiabatic Effects in Thermochemistry, Spectroscopy and Kinetics: the General Importance of all Three Born–Oppenheimer Breakdown Corrections', *Physical Chemistry Chemical Physics*, **2015**, *17*, 24641–24665.
(Cited on page 14)

(82) L. K. McKemmish, R. H. McKenzie, N. S. Hush and J. R. Reimers, 'Electron–Vibration Entanglement in the Born–Oppenheimer Description of Chemical Reactions and Spectroscopy', *Physical Chemistry Chemical Physics*, **2015**, *17*, 24666–24682.
(Cited on page 14)

(83) T. J. Lee, D. J. Fox, H. F. Schaefer III and R. M. Pitzer, 'Analytic Second Derivatives for Renner-Teller Potential Energy Surfaces. Examples of the Five Distinct Cases', *The Journal of Chemical Physics*, **1984**, *81*, 356–361.
(Cited on page 15)

(84) T. Barrow, R. N. Dixon and G. Duxbury, 'The Renner Effect in a Bent Triatomic Molecule Executing a Large Amplitude Bending Vibration', *Molecular Physics*, **1974**, *27*, 1217–1234.
(Cited on page 15)

(85) C. Jungen, K.-E. J. Hallin and A. J. Merer, 'Orbital Angular Momentum in Triatomic Molecules II. Vibrational and K-type Rotational Structure, and Intensity Factors in the $\tilde{A}^2A_1$-X^2B_1 transitions of NH_2 and H_2O^+', *Molecular Physics*, **1980**, *40*, 25–63.
(Cited on page 15)

(86) G. Duxbury and R. N. Dixon, 'The Renner Effect in a Bent Triatomic Molecule Using the Adiabatic Approach', *Molecular Physics*, **1981**, *43*, 255–274.
(Cited on page 15)

(87) G. J. Halász, Á. Vibók, R. Baer and M. Baer, 'Renner-Teller Nonadiabatic Coupling Terms: an ab-initio Study of the HNH Molecule', *The Journal of Chemical Physics*, **2006**, *124*, 081106.
(Cited on page 15)

(88) H. A. Jahn and E. Teller, 'Stability of Polyatomic Molecules in Degenerate Electronic States. I. Orbital Degeneracy', *Proceedings of the Royal Society A: Mathematical, Physical and Engineering Sciences*, **1937**, *161*, 220–235.
(Cited on page 15)

(89) D. R. Yarkony, 'Diabolical Conical Intersections', *Reviews of Modern Physics*, **1996**, *68*, 985–1013.
(Cited on page 15)

(90) D. R. Yarkony, 'Conical Intersections: The New Conventional Wisdom', *The Journal of Physical Chemistry A*, **2001**, *105*, 6277–6293.
(Cited on page 16)

(91) J. Biesner, L. Schnieder, J. Schmeer, G. Ahlers, X. Xie, K. H. Welge, M. N. R. Ashfold and R. N. Dixon, 'State Selective Photodissociation Dynamics of Ã State Ammonia. I', *The Journal of Chemical Physics*, **1988**, *88*, 3607–3616.
(Cited on page 16)

(92) J. Biesner, L. Schnieder, J. Schmeer, G. Ahlers, X. Xie, K. H. Welge, M. N. R. Ashfold and R. N. Dixon, 'State Selective Photodissociation Dynamics of Ã State Ammonia. II', *The Journal of Chemical Physics*, **1989**, *91*, 2901–2911.
(Cited on page 16)

(93) D. P. Hoffman, S. R. Ellis and R. A. Mathies, 'Characterization of a Conical Intersection in a Charge-Transfer Dimer with Two-Dimensional Time-Resolved Stimulated Raman Spectroscopy', *The Journal of Physical Chemistry A*, **2014**, *118*, 4955–4965.
(Cited on page 16)

(94) F. Wang, T. Ziegler, E. van Lenthe, S. J. A. van Gisbergen and E. J. Baerends, 'The Calculation of Excitation Energies Based on the Relativistic Two-Component Zeroth-Order Regular Approximation and Time-Dependent Density-Functional with Full Use of Symmetry', *The Journal of Chemical Physics*, **2005**, *122*, 204103.
(Cited on pages 16, 48)

(95) A. Szabo and N. S. Ostlund, *Modern Quantum Chemistry: Introduction to Advanced Electronic Structure Theory*, Dover Publications Inc., Mineola, Dover Edit, 1996.
(Cited on pages 17, 21, 25, 26, 104)

(96) P. Echenique and J. L. Alonso, 'A Mathematical and Computational Review of Hartree–Fock SCF Methods in Quantum Chemistry', *Molecular Physics*, **2007**, *105*, 3057–3098.
(Cited on pages 17, 19, 21, 22)

(97) P. A. M. Dirac, 'A New Notation for Quantum Mechanics', *Mathematical Proceedings of the Cambridge Philosophical Society*, **1939**, *35*, 416–418.
(Cited on page 20)

(98) J. C. Slater, 'The Theory of Complex Spectra', *Physical Review*, **1929**, *34*, 1293–1322.
(Cited on page 21)

(99) E. U. Condon, 'The Theory of Complex Spectra', *Physical Review*, **1930**, *36*, 1121–1133.
(Cited on page 21)

(100) P.-O. Löwdin, 'Quantum Theory of Many-Particle Systems. I. Physical Interpretations by Means of Density Matrices, Natural Spin-Orbitals, and Convergence Problems in the Method of Configurational Interaction', *Physical Review*, **1955**, *97*, 1474–1489.
(Cited on page 21)

(101) D. R. Hartree, 'The Wave Mechanics of an Atom with a Non-Coulomb Central Field. Part I. Theory and Methods', *Mathematical Proceedings of the Cambridge Philosophical Society*, **1928**, *24*, 89–110.
(Cited on page 22)

(102) D. R. Hartree, 'The Wave Mechanics of an Atom with a Non-Coulomb Central Field. Part II. Some Results and Discussion', *Mathematical Proceedings of the Cambridge Philosophical Society*, **1928**, *24*, 111–132.
(Cited on page 22)

(103) D. R. Hartree, 'The Wave Mechanics of an Atom with a Non-Coulomb Central Field. Part III. Term Values and Intensities in Series in Optical Spectra', *Mathematical Proceedings of the Cambridge Philosophical Society*, **1928**, *24*, 426–437.
(Cited on page 22)

(104) D. R. Hartree, 'The Wave Mechanics of an Atom with a Non-Coulomb Central Field. Part IV. Further Results relating to Terms of the Optical Spectrum', *Mathematical Proceedings of the Cambridge Philosophical Society*, **1929**, *25*, 310–314.
(Cited on page 22)

(105) P.-O. Löwdin, in *Advances in Chemical Physics*, ed. I. Prigogine, John Wiley & Sons, Inc., 1959, vol. 2, pp. 207–322 (Cited on page 23).

(106) J. Cioslowski, 'Density-Driven Self-Consistent-Field Method: Density-Constrained Correlation Energies in the Helium Series', *Physical Review A*, **1991**, *43*, 1223–1228.
(Cited on page 24)

(107) E. R. Davidson, S. A. Hagstrom, S. J. Chakravorty, V. M. Umar and C. F. Fischer, 'Ground-State Correlation Energies for Two- to Ten-Electron Atomic Ions', *Physical Review A*, **1991**, *44*, 7071–7083.
(Cited on page 24)

(108) E. Valderrama, E. V. Ludeña and J. Hinze, 'Analysis of Dynamical and Nondynamical Components of Electron Correlation Energy by Means of Local-Scaling Density-Functional Theory', *The Journal of Chemical Physics*, **1997**, *106*, 9227–9235.
(Cited on page 24)

(109) E. Ramos-Cordoba, P. Salvador and E. Matito, 'Separation of Dynamic and Nondynamic Correlation', *Physical Chemistry Chemical Physics*, **2016**, *18*, 24015–24023.
(Cited on pages 24, 25)

(110) F. Jensen, *Introduction to Computational Chemistry*, John Wiley & Sons Ltd, Second, 2007, p. 599.
(Cited on page 25)

(111) E. G. Lewars, *Computational Chemistry: Introduction to the Theory and Applications of Molecular and Quantum Mechanics*, Springer, 2nd edn., 2011.
(Cited on pages 25, 26)

(112) H. S. Yu, S. L. Li and D. G. Truhlar, 'Perspective: Kohn-Sham Density Functional Theory Descending a Staircase', *The Journal of Chemical Physics*, **2016**, *145*, 130901.
(Cited on page 25)

(113) P. Hohenberg and W. Kohn, 'Inhomogeneous Electron Gas', *Physical Review*, **1964**, *136*, B864–B871.
(Cited on pages 25, 31, 51)

(114) M. Levy, 'Universal Variational Functionals of Electron Densities, First-Order Density Matrices, and Natural Spin-Orbitals and Solution of the v-Representability Problem', *Proceedings of the National Academy of Sciences of the United States of America*, **1979**, *76*, 6062–6065.
(Cited on page 26)

(115) E. H. Lieb, 'Density Functionals for Coulomb Systems', *International Journal of Quantum Chemistry*, **1983**, *24*, 243–277.
(Cited on page 26)

(116) J. E. Harriman, 'Geometry of Density Matrices. I. Definitions, N-Matrices and 1 Matrices', *Physical Review A*, **1978**, *17*, 1249–1256.
(Cited on page 26)

(117) J. E. Harriman, 'Geometry of Density Matrices. II. Reduced Density Matrices and N-Representability', *Physical Review A*, **1978**, *17*, 1257–1268.
(Cited on page 26)

(118) E. J. Baerends, O. V. Gritsenko and R. van Meer, 'The Kohn-Sham Gap, the Fundamental Gap and the Optical Gap: the Physical Meaning of Occupied and Virtual Kohn-Sham Orbital Energies', *Physical Chemistry Chemical Physics*, **2013**, *15*, 16408–16425.
(Cited on pages 26, 29)

(119) A. Borgoo, J. A. Green and D. J. Tozer, 'Molecular Binding in Post-Kohn–Sham Orbital-Free DFT', *Journal of Chemical Theory and Computation*, **2014**, *10*, 5338–5345.
(Cited on page 26)

(120) W. Kohn and L. J. Sham, 'Self-Consistent Equations Including Exchange and Correlation Effects', *Physical Review*, **1965**, *140*, A1133–A1138.
(Cited on pages 26, 27, 51)

(121) R. van Meer, O. V. Gritsenko and E. J. Baerends, 'Physical Meaning of Virtual Kohn–Sham Orbitals and Orbital Energies: An Ideal Basis for the Description of Molecular Excitations', *Journal of Chemical Theory and Computation*, **2014**, *10*, 4432–4441.
(Cited on page 29)

(122) J. A. Pople, P. M. W. Gill and B. G. Johnson, 'Kohn-Sham Density-Functional Theory Within a Finite Basis Set', *Chemical Physics Letters*, **1992**, *199*, 557–560.
(Cited on pages 29, 30)

(123) A. D. Becke, 'Perspective: Fifty Years of Density-Functional Theory in Chemical Physics', *The Journal of Chemical Physics*, **2014**, *140*, 18A301.
(Cited on page 30)

(124) A. D. Becke, 'Density-Functional Thermochemistry. III. The Role of Exact Exchange', *The Journal of Chemical Physics*, **1993**, *98*, 5648–5652.
(Cited on pages 31, 51, 54, 83)

(125) C. Lee, W. Yang and R. G. Parr, 'Development of the Colle-Salvetti Correlation-Energy Formula into a Functional of the Electron Density', *Physical Review B*, **1988**, *37*, 785–789.
(Cited on pages 31, 51, 54, 83)

(126) F. J. Devlin, J. W. Finley, P. J. Stephens and M. J. Frisch, 'Ab Initio Calculation of Vibrational Absorption and Circular Dichroism Spectra Using Density Functional Force Fields: A Comparison of Local, Nonlocal, and Hybrid Density Functionals', *The Journal of Physical Chemistry*, **1995**, *99*, 16883–16902.
(Cited on pages 31, 131)

(127) A. Dreuw and M. Head-Gordon, 'Failure of Time-Dependent Density Functional Theory for Long-Range Charge-Transfer Excited States: the Zincbacteriochlorin-bacteriochlorin and Bacteriochlorophyll-spheroidene Complexes', *Journal of the American Chemical Society*, **2004**, *126*, 4007–4016.
(Cited on pages 31, 35, 105)

(128) F. Furche and J. P. Perdew, 'The Performance of Semilocal and Hybrid Density Functionals in 3d Transition-Metal Chemistry', *The Journal of Chemical Physics*, **2006**, *124*, 044103.
(Cited on page 31)

(129) J. M. Herbert, X. Zhang, A. F. Morrison and J. Liu, 'Beyond Time-Dependent Density Functional Theory Using Only Single Excitations: Methods for Computational Studies of Excited States in Complex Systems', *Accounts of Chemical Research*, **2016**, *49*, 931–941.
(Cited on page 31)

(130) C. Latouche, F. Palazzetti, D. Skouteris and V. Barone, 'High-Accuracy Vibrational Computations for Transition-Metal Complexes Including Anharmonic Corrections: Ferrocene, Ruthenocene, and Osmocene as Test Cases', *Journal of Chemical Theory and Computation*, **2014**, *10*, 4565–4573.
(Cited on pages 31, 82, 87, 104)

(131) M. Steinmetz and S. Grimme, 'Benchmark Study of the Performance of Density Functional Theory for Bond Activations with (Ni,Pd)-Based Transition-Metal Catalysts', *ChemistryOpen*, **2013**, *2*, 115–124.
(Cited on page 31)

(132) T. Weymuth, E. P. A. Couzijn, P. Chen and M. Reiher, 'New Benchmark Set of Transition-Metal Coordination Reactions for the Assessment of Density Functionals', *Journal of Chemical Theory and Computation*, **2014**, *10*, 3092–3103.
(Cited on page 31)

(133) N. Mardirossian and M. Head-Gordon, 'Mapping the Genome of Meta-Generalized Gradient Approximation Density Functionals: the Search for B97M-V', *The Journal of Chemical Physics*, **2015**, *142*, 074111.
(Cited on page 31)

(134) A. Vlček Jr. and S. Záliš, 'Modeling of Charge-Transfer Transitions and Excited States in d^6 Transition Metal Complexes by DFT Techniques', *Coordination Chemistry Reviews*, **2007**, *251*, 258–287.
(Cited on pages 31, 35, 62)

(135) M. R. Silva-Junior, M. Schreiber, S. P. A. Sauer and W. Thiel, 'Benchmarks for Electronically Excited States: Time-Dependent Density Functional Theory and Density Functional Theory Based Multireference Configuration Interaction', *The Journal of Chemical Physics*, **2008**, *129*, 104103.
(Cited on pages 31, 104)

(136) S. Ketkov, N. Isachenkov, E. Rychagova and W.-B. Tzeng, 'Electronic Excited States of Chromium and Vanadium Bisarene Complexes Revisited: Interpretation of the Absorption Spectra on the Basis of TD DFT Calculations', *Dalton Transactions*, **2014**, *43*, 17703–17711.
(Cited on page 31)

(137) E. Runge and E. K. U. Gross, 'Density-Functional Theory for Time-Dependent Systems', *Physical Review Letters*, **1984**, *52*, 997–1000.
(Cited on pages 32, 33, 36, 51)

(138) L. J. Bartolotti, 'Time-Dependent Extension of the Hohenberg-Kohn-Levy Energy-Density Functional', *Physical Review A*, **1981**, *24*, 1661–1667.
(Cited on page 32)

(139) B. M. Deb and S. K. Ghosh, 'Schrödinger Fluid Dynamics of Many-Electron Systems in a Time-Dependent Density-Functional Framework', *The Journal of Chemical Physics*, **1982**, *77*, 342.
(Cited on page 32)

(140) L. J. Bartolotti, 'Time-Dependent Kohn-Sham Density-Functional Theory', *Physical Review A*, **1982**, *26*, 2243–2244.
(Cited on page 32)

(141) V. Peuckert, 'A New Approximation Method for Electron Systems', *Journal of Physics C: Solid State Physics*, **1978**, *11*, 4945–4956.
(Cited on pages 32, 36)

(142) S. Chakravarty, M. B. Fogel and W. Kohn, 'Dynamic Response of Inhomogeneous Fermi Systems', *Physical Review Letters*, **1979**, *43*, 775–778.
(Cited on pages 32, 36)

(143) R. van Leeuwen, 'Causality and Symmetry in Time-Dependent Density-Functional Theory', *Physical Review Letters*, **1998**, *80*, 1280–1283.
(Cited on page 32)

(144) J. Schirmer and A. Dreuw, 'Critique of the Foundations of Time-Dependent Density-Functional Theory', *Physical Review A*, **2007**, *75*, 36–38.
(Cited on page 32)

(145) N. T. Maitra, R. van Leeuwen and K. Burke, 'Comment on "Critique of the Foundations of Time-Dependent Density-Functional Theory"', *Physical Review A*, **2008**, *78*, 056501.
(Cited on page 32)

(146) J. Schirmer and A. Dreuw, 'Reply to "Comment on 'Critique of the Foundations of Time-Dependent Density-Functional Theory"'', *Physical Review A*, **2008**, *78*, 056502.
(Cited on page 32)

(147) A. Holas, M. Cinal and N. H. March, 'Comment on "Critique of the Foundations of Time-Dependent Density-Functional Theory"', *Physical Review A*, **2008**, *78*, 016501.
(Cited on page 32)

(148) J. Schirmer and A. Dreuw, 'Reply to "Comment on 'Critique of the Foundations of Time-Dependent Density Functional Theory"'', *arXiv*, **2008**, 0807.3303.
(Cited on page 32)

(149) G. Vignale, 'Real-Time Resolution of the Causality Paradox of Time-Dependent Density-Functional Theory', *Physical Review A*, **2008**, *77*, 062511.
(Cited on page 32)

(150) J. Schirmer, 'Modifying the Variational Principle in the Action-Integral-Functional Derivation of Time-Dependent Density-Functional Theory', *Physical Review A*, **2010**, *82*, 052510.
(Cited on page 32)

(151) J. Schirmer, 'Reexamination of the Runge-Gross Action-Integral Functional', *Physical Review A*, **2012**, *86*, 012514.
(Cited on page 32)

(152) M. E. Casida and M. Huix-Rotllant, 'Progress in Time-Dependent Density-Functional Theory', *Annual Review of Physical Chemistry*, **2012**, *63*, 287–323.
(Cited on pages 32, 35)

(153) M. Ruggenthaler, S. E. B. Nielsen and R. van Leeuwen, 'Analytic Density Functionals with Initial-State Dependence and Memory', *Physical Review A*, **2013**, *88*, 022512.
(Cited on page 32)

(154) N. T. Maitra, 'Perspective: Fundamental Aspects of Time-Dependent Density Functional Theory', *The Journal of Chemical Physics*, **2016**, *144*, 220901.
(Cited on pages 32, 34, 35)

(155) T. K. Ng and K. S. Singwi, 'Time-Dependent Density-Functional Theory in the Linear-Response Regime', *Physical Review Letters*, **1987**, *59*, 2627–2630.
(Cited on pages 32, 34)

(156) R. van Leeuwen, 'Key Concepts in Time-Dependent Density-Functional Theory', *International Journal of Modern Physics B*, **2001**, *15*, 1969–2023.
(Cited on pages 32, 34)

(157) E. K. U. Gross and W. Kohn, in *Advances in Quantum Chemistry*, Elsevier, 1990, vol. 21, pp. 255–291 (Cited on pages 33, 36).

(158) M. E. Casida, in *Recent Advances in Density Functional Methods*, ed. D. P. Chong, World Scientific Publishing Co. Pte. Ltd., 1995, ch. 5, pp. 155–192 (Cited on pages 33, 34, 36).

(159) M. A. Mosquera, 'Action Formalism of Time-Dependent Density-Functional Theory', *Physical Review A*, **2013**, *88*, 022515.
(Cited on page 33)

(160) Y. Kurzweil and R. Baer, 'Time-Dependent Exchange-Correlation Current Density Functionals With Memory', *The Journal of Chemical Physics*, **2004**, *121*, 8731.
(Cited on page 35)

(161) H. Appel, E. K. U. Gross and K. Burke, 'Excitations in Time-Dependent Density-Functional Theory', *Physical Review Letters*, **2003**, *90*, 043005.
(Cited on page 35)

(162) B. G. Levine, C. Ko, J. Quenneville and T. J. Martínez, 'Conical Intersections and Double Excitations in Time-Dependent Density Functional Theory', *Molecular Physics*, **2006**, *104*, 1039–1051.
(Cited on pages 35, 123)

(163) D. J. Tozer and N. C. Handy, 'On the Determination of Excitation Energies using Density Functional Theory', *Physical Chemistry Chemical Physics*, **2000**, *2*, 2117–2121.
(Cited on page 35)

(164) K. B. Wiberg, A. E. de Oliveira and G. W. Trucks, 'A Comparison of the Electronic Transition Energies for Ethene, Isobutene, Formaldehyde, and Acetone Calculated Using RPA, TDDFT, and EOM-CCSD. Effect of Basis Sets', *The Journal of Physical Chemistry A*, **2002**, *106*, 4192–4199.
(Cited on page 35)

(165) F. Furche and R. Ahlrichs, 'Adiabatic Time-Dependent Density Functional Methods for Excited State Properties', *The Journal of Chemical Physics*, **2002**, *117*, 7433.
(Cited on page 35)

(166) A. Dreuw, J. L. Weisman and M. Head-Gordon, 'Long-Range Charge-Transfer Excited States in Time-Dependent Density Functional Theory Require Non-Local Exchange', *The Journal of Chemical Physics*, **2003**, *119*, 2943–2946.
(Cited on page 35)

(167) A. Dreuw and M. Head-Gordon, 'Single-Reference ab initio Methods for the Calculation of Excited States of Large Molecules', *Chemical Reviews*, **2005**, *105*, 4009–4037.
(Cited on pages 35, 36, 38, 103, 104)

(168) C. J. Cramer and D. G. Truhlar, 'Density Functional Theory for Transition Metals and Transition Metal Chemistry', *Physical Chemistry Chemical Physics*, **2009**, *11*, 10757–816.
(Cited on pages 35, 38)

(169) R. Send, M. Kühn and F. Furche, 'Assessing Excited State Methods by Adiabatic Excitation Energies', *Journal of Chemical Theory and Computation*, **2011**, *7*, 2376–2386.
(Cited on pages 35, 38)

(170) A. D. Laurent and D. Jacquemin, 'TD-DFT Benchmarks: A Review', *International Journal of Quantum Chemistry*, **2013**, *113*, 2019–2039.
(Cited on pages 35, 38, 94, 104, 105)

(171) J. I. Fuks and N. T. Maitra, 'Challenging Adiabatic Time-Dependent Density Functional Theory with a Hubbard Dimer: the Case of Time-Resolved Long-Range Charge Transfer', *Physical Chemistry Chemical Physics*, **2014**, *16*, 14504–14513.
(Cited on page 35)

(172) J. E. Subotnik, E. C. Alguire, Q. Ou, B. R. Landry and S. Fatehi, 'The Requisite Electronic Structure Theory To Describe Photoexcited Nonadiabatic Dynamics: Nonadiabatic Derivative Couplings and Diabatic Electronic Couplings', *Accounts of Chemical Research*, **2015**, *48*, 1340–1350.
(Cited on pages 35, 49)

(173) C. Latouche, D. Skouteris, F. Palazzetti and V. Barone, 'TD-DFT Benchmark on Inorganic Pt(II) and Ir(III) Complexes', *Journal of Chemical Theory and Computation*, **2015**, *11*, 3281–3289.
(Cited on pages 35, 38)

(174) J. Theilhaber, 'Ab initio Simulations of Sodium using Time-Dependent Density-Functional Theory', *Physical Review B*, **1992**, *46*, 12990–13003.
(Cited on page 35)

(175) K. Yabana and G. Bertsch, 'Time-Dependent Local-Density Approximation in Real Time', *Physical Review B*, **1996**, *54*, 4484–4487.
(Cited on page 35)

(176) K. Lopata and N. Govind, 'Modeling Fast Electron Dynamics with Real-Time Time-Dependent Density Functional Theory: Application to Small Molecules and Chromophores', *Journal of Chemical Theory and Computation*, **2011**, *7*, 1344–1355.
(Cited on page 35)

(177) S. Tussupbayev, N. Govind, K. Lopata and C. J. Cramer, 'Comparison of Real-Time and Linear-Response Time-Dependent Density Functional Theories for Molecular Chromophores Ranging from Sparse to High Densities of States', *Journal of Chemical Theory and Computation*, **2015**, *11*, 1102–1109.
(Cited on page 35)

(178) A. Bende and V. Toşa, 'Modeling Laser Induced Molecule Excitation using Real-Time Time-Dependent Density Functional Theory: Application to 5- and 6-benzyluracil', *Physical Chemistry Chemical Physics*, **2015**, *17*, 5861–5871.
(Cited on page 35)

(179) Environmental Molecular Sciences Laboratory, *Resonant Excitation of Zinc Porphyrin*, https://www.youtube.com/watch?v=ZYsktRlhMOg (Cited on page 35).

(180) A. McLachlan and M. Ball, 'Time-Dependent Hartree-Fock Theory for Molecules', *Reviews of Modern Physics*, **1964**, *36*, 844–855.
(Cited on page 36)

(181) C. Jamorski, M. E. Casida and D. R. Salahub, 'Dynamic Polarizabilities and Excitation Spectra from a Molecular Implementation of Time-Dependent Density-Functional Response Theory: N2 as a Case Study', *The Journal of Chemical Physics*, **1996**, *104*, 5134.
(Cited on page 36)

(182) T. Ziegler, M. Krykunov and J. Autschbach, 'Derivation of the RPA (Random Phase Approximation) Equation of ATDDFT (Adiabatic Time Dependent Density Functional Ground State Response Theory) from an Excited State Variational Approach Based on the Ground State Functional', *Journal of Chemical Theory and Computation*, **2014**, *10*, 3980–3986.
(Cited on page 36)

(183) C. Lanczos, 'An Iteration Method for the Solution of the Eigenvalue Problem of Linear Differential and Integral Operators', *Journal of Research of the National Bureau of Standards*, **1950**, *45*, 255–282.
(Cited on page 37)

(184) E. R. Davidson, 'The Iterative Calculation of a Few of the Lowest Eigenvalues and Corresponding Eigenvectors of Large Real-Symmetric Matrices', *Journal of Computational Physics*, **1975**, *17*, 87–94.
(Cited on pages 37, 51, 53, 131)

(185) B. Liu, in *Numerical Algorithms In Chemistry: Algebraic Methods - Report on the Workshop August 9-11, 1978*, ed. C. Moler and I. Shavitt, Lawrence Berkeley Laboratory, University of California, Berkeley, 1978, ch. 1, pp. 49–54 (Cited on page 37).

(186) J. Olsen, H. J. A. Jensen and P. Jørgensen, 'Solution of the Large Matrix Equations Which Occur in Response Theory', *Journal of Computational Physics*, **1988**, *74*, 265–282.
(Cited on pages 37, 51, 132)

(187) E. R. Davidson and W. J. Thompson, 'Monster Matrices: Their Eigenvalues and Eigenvectors', *Computers in Physics*, **1993**, *7*, 519.
(Cited on pages 37, 51, 53, 131)

(188) R. Bauernschmitt, M. Häser, O. Treutler and R. Ahlrichs, 'Calculation of Excitation Energies within Time-Dependent Density Functional Theory using Auxiliary Basis Set Expansions', *Chemical Physics Letters*, **1997**, *264*, 573–578.
(Cited on page 37)

(189) R. E. Stratmann, G. E. Scuseria and M. J. Frisch, 'An Efficient Implementation of Time-Dependent Density-Functional Theory for the Calculation of Excitation Energies of Large Molecules', *The Journal of Chemical Physics*, **1998**, *109*, 8218–8224.
(Cited on pages 37, 51, 107, 132)

(190) S. Hirata and M. Head-Gordon, 'Time-Dependent Density Functional Theory within the Tamm–Dancoff Approximation', *Chemical Physics Letters*, **1999**, *314*, 291–299.
(Cited on pages 37, 38, 104)

(191) S. J. A. van Gisbergen, J. G. Snijders and E. J. Baerends, 'Implementation of Time-Dependent Density Functional Response Equations', *Computer Physics Communications*, **1999**, *118*, 119–138.
(Cited on pages 37, 53, 131)

(192) S. Grimme, 'A Simplified Tamm-Dancoff Density Functional Approach for the Electronic Excitation Spectra of Very Large Molecules', *The Journal of Chemical Physics*, **2013**, *138*, 244104.
(Cited on pages 38, 40, 112)

(193) C. Bannwarth and S. Grimme, 'A Simplified Time-Dependent Density Functional Theory Approach for Electronic Ultraviolet and Circular Dichroism Spectra of Very Large Molecules', *Computational and Theoretical Chemistry*, **2014**, *1040-1041*, 45–53.
(Cited on pages 38, 40, 112)

(194) T. Risthaus, A. Hansen and S. Grimme, 'Excited States using the Simplified Tamm-Dancoff-Approach for Range-Separated Hybrid Density Functionals: Development and Application.', *Physical Chemistry Chemical Physics*, **2014**, *16*, 14408–14419.
(Cited on pages 38, 112)

(195) K. Nishimoto and N. Mataga, 'Electronic Structure and Spectra of Some Nitrogen Heterocycles', *Zeitschrift für Physikalische Chemie*, **1957**, *12*, 335–338.
(Cited on page 39)

(196) K. Ohno, 'Some Remarks on the Pariser-Parr-Pople Method', *Theoretica Chimica Acta*, **1964**, *2*, 219–227.
(Cited on page 39)

(197) G. Klopman, 'A Semiempirical Treatment of Molecular Structures. II. Molecular Terms and Application to Diatomic Molecules', *Journal of the American Chemical Society*, **1964**, *86*, 4550–4557.
(Cited on page 39)

(198) P.-O. Löwdin, 'On the Non-Orthogonality Problem Connected with the Use of Atomic Wave Functions in the Theory of Molecules and Crystals', *The Journal of Chemical Physics*, **1950**, *18*, 365–375.
(Cited on page 39)

(199) D. C. Ghosh and N. Islam, 'Semiempirical Evaluation of the Global Hardness of the Atoms of 103 Elements of the Periodic Table Using the Most Probable Radii as their Size Descriptors', *International Journal of Quantum Chemistry*, **2010**, *110*, 1206–1213.
(Cited on page 39)

(200) V. Chernyak and S. Mukamel, 'Density-Matrix Representation of Nonadiabatic Couplings in Time-Dependent Density Functional (TDDFT) Theories', *The Journal of Chemical Physics*, **2000**, *112*, 3572.
(Cited on page 40)

(201) R. Send and F. Furche, 'First-Order Nonadiabatic Couplings from Time-Dependent Hybrid Density Functional Response Theory: Consistent Formalism, Implementation, and Performance', *The Journal of Chemical Physics*, **2010**, *132*, 044107.
(Cited on page 40)

(202) Q. Ou, G. D. Bellchambers, F. Furche and J. E. Subotnik, 'First-order derivative couplings between excited states from adiabatic TDDFT response theory', *The Journal of Chemical Physics*, **2015**, *142*, 064114.
(Cited on page 40)

(203) *The Collected Papers of Albert Einstein*, http://einsteinpapers.press.princeton.edu/ (Cited on page 40).

(204) M. Reiher and A. Wolf, *Relativistic Quantum Chemistry*, Wiley-VCH Verlag GmbH, D-69451 Weinheim, Germany, 2nd edn., 2014.
(Cited on pages 40, 43, 46–49, 109, 150)

(205) R. Ramírez-Tagle, L. Alvarado-Soto, A. Villavicencio-Wastavino and L. Alvarez-Thon, 'Relativistic Effects on the Aromaticity of the Halogenated Benzenes: C_6X_6, X = H, F, Cl, Br, I, At', *Physical Chemistry Chemical Physics*, **2016**, *18*, 25751–25755.
(Cited on page 40)

(206) P. Pyykkö and J.-P. Desclaux, 'Relativity and the Periodic System of Elements', *Accounts of Chemical Research*, **1979**, *12*, 276–281.
(Cited on page 40)

(207) P. Pyykkö, 'Relativistic Effects in Structural Chemistry', *Chemical Reviews*, **1988**, *88*, 563–594.
(Cited on page 40)

(208) P. A. M. Dirac, 'The Quantum Theory of the Electron', *Proceedings of the Royal Society A: Mathematical, Physical and Engineering Sciences*, **1928**, *117*, 610–624.
(Cited on page 43)

(209) P. A. M. Dirac, 'The Quantum Theory of the Electron. Part II', *Proceedings of the Royal Society A: Mathematical, Physical and Engineering Sciences*, **1928**, *118*, 351–361.
(Cited on page 43)

(210) P. A. M. Dirac, 'Quantum Mechanics of Many-Electron Systems', *Proceedings of the Royal Society A: Mathematical, Physical and Engineering Sciences*, **1929**, *123*, 714–733.
(Cited on page 43)

(211) P. A. M. Dirac, 'A Theory of Electrons and Protons', *Proceedings of the Royal Society A: Mathematical, Physical and Engineering Sciences*, **1930**, *126*, 360–365.
(Cited on page 43)

(212) S. Wilson, 'On the Use of Many-Body Perturbation Theory and Quantum-Electrodynamics in Molecular Electronic Structure Theory', *Journal of Molecular Structure: THEOCHEM*, **2001**, *547*, 279–291.
(Cited on pages 43, 48)

(213) T. Saue, 'Relativistic Hamiltonians for Chemistry: A Primer', *ChemPhysChem*, **2011**, *12*, 3077–3094.
(Cited on pages 47, 48, 109)

(214) J. Sucher, 'Foundations of the Relativistic Theory of Many-Electron Atoms', *Physical Review A*, **1980**, *22*, 348–362.
(Cited on pages 48, 109)

(215) W. Liu, 'Ideas of Relativistic Quantum Chemistry', *Molecular Physics*, **2010**, *108*, 1679–1706.
(Cited on page 48)

(216) L. L. Foldy and S. A. Wouthuysen, 'On the Dirac Theory of Spin $\frac{1}{2}$ Particles and Its Non-Relativistic Limit', *Physical Review*, **1950**, *78*, 29–36.
(Cited on pages 48, 109)

(217) D. Peng and M. Reiher, 'Exact Decoupling of the Relativistic Fock Operator', *Theoretical Chemistry Accounts*, **2012**, *131*, 1081.
(Cited on pages 48, 109)

(218) W. Liu and I. Lindgren, 'Going Beyond "No-Pair Relativistic Quantum Chemistry"', *The Journal of Chemical Physics*, **2013**, *139*, 014108.
(Cited on page 48)

(219) C. Chang, M. Pelissier and P. Durand, 'Regular Two-Component Pauli-Like Effective Hamiltonians in Dirac Theory', *Physica Scripta*, **1986**, *34*, 394–404.
(Cited on page 48)

(220) A. J. Sadlej, J. G. Snijders, E. van Lenthe and E. J. Baerends, 'Four Component Regular Relativistic Hamiltonians and the Perturbational Treatment of Dirac's Equation', *The Journal of Chemical Physics*, **1995**, *102*, 1758–1766.
(Cited on page 48)

(221) E. van Lenthe, E. J. Baerends and J. G. Snijders, 'Relativistic Regular Two-Component Hamiltonians', *The Journal of Chemical Physics*, **1993**, *99*, 4597–4610.
(Cited on pages 48, 53)

(222) E. van Lenthe, E. J. Baerends and J. G. Snijders, 'Relativistic Total Energy using Regular Approximations', *The Journal of Chemical Physics*, **1994**, *101*, 9783–9792.
(Cited on pages 48, 53)

(223) E. van Lenthe, R. van Leeuwen, E. J. Baerends and J. G. Snijders, 'Relativistic Regular Two-Component Hamiltonians', *International Journal of Quantum Chemistry*, **1996**, *57*, 281–293.
(Cited on pages 48, 53)

(224) E. van Lenthe, J. G. Snijders and E. J. Baerends, 'The Zero-Order Regular Approximation for Relativistic Effects: The Effect of Spin–Orbit Coupling in Closed Shell Molecules', *The Journal of Chemical Physics*, **1996**, *105*, 6505–6516.
(Cited on pages 48, 53)

(225) E. van Lenthe, A. Ehlers and E. J. Baerends, 'Geometry Optimizations in the Zero Order Regular Approximation for Relativistic Effects', *The Journal of Chemical Physics*, **1999**, *110*, 8943–8953.
(Cited on pages 48, 53)

(226) M. Filatov and D. Cremer, 'On the Physical Meaning of the ZORA Hamiltonian', *Molecular Physics*, **2003**, *101*, 2295–2302.
(Cited on page 48)

(227) F. Wang and T. Ziegler, 'Theoretical Study of the Electronic Spectra of Square-Planar Platinum (II) Complexes based on the Two-Component Relativistic Time-Dependent Density-Functional Theory', *The Journal of Chemical Physics*, **2005**, *123*, 194102.
(Cited on pages 48, 108, 109)

(228) A. J. Sadlej, 'Improving Upon the ZORA Hamiltonian', *International Journal of Quantum Chemistry*, **2006**, *106*, 2518–2524.
(Cited on page 48)

(229) K. G. Dyall and E. van Lenthe, 'Relativistic Regular Approximations Revisited: an Infinite-Order Relativistic Approximation', *The Journal of Chemical Physics*, **1999**, *111*, 1366.
(Cited on page 48)

(230) M. Barysz and A. J. Sadlej, 'Two-Component Methods of Relativistic Quantum Chemistry: from the Douglas–Kroll Approximation to the Exact Two-Component Formalism', *Journal of Molecular Structure: THEOCHEM*, **2001**, *573*, 181–200.
(Cited on pages 48, 150)

(231) A. Wolf, M. Reiher and B. A. Hess, 'The Generalized Douglas–Kroll Transformation', *The Journal of Chemical Physics*, **2002**, *117*, 9215–9226.
(Cited on page 48)

(232) A. K. Rajagopal and J. Callaway, 'Inhomogeneous Electron Gas', *Physical Review B*, **1973**, *7*, 1912–1919.
(Cited on page 48)

(233) A. K. Rajagopal, 'Inhomogeneous Relativistic Electron Gas', *Journal of Physics C: Solid State Physics*, **1978**, *11*, L943–L948.
(Cited on page 48)

(234) A. H. MacDonald and S. H. Vosko, 'A Relativistic Density Functional Formalism', *Journal of Physics C: Solid State Physics*, **1979**, *12*, 2977–2990.
(Cited on page 48)

(235) G. Hunter, 'Conditional Probability Amplitudes in Wave Mechanics', *International Journal of Quantum Chemistry*, **1975**, *9*, 237–242.
(Cited on page 49)

(236) G. Hunter, 'Nodeless Wave Function Quantum Theory', *International Journal of Quantum Chemistry*, **1980**, *17*, 133–137.
(Cited on page 49)

(237) G. Hunter, 'Nodeless Wave Functions and Spiky Potentials', *International Journal of Quantum Chemistry*, **1981**, *14*, 755.
(Cited on page 49)

(238) H. Köppel, W. Domcke and L. S. Cederbaum, in *Advances in Chemical Physics*, ed. I. Prigogine and S. A. Rice, John Wiley & Sons Ltd, 1984, vol. 57, ch. 2 (Cited on pages 49, 139).

(239) G. A. Worth and L. S. Cederbaum, 'Beyond Born-Oppenheimer: Molecular Dynamics Through a Conical Intersection', *Annual Review of Physical Chemistry*, **2004**, *55*, 127–158.
(Cited on page 49)

(240) L. S. Cederbaum, 'Born-Oppenheimer Approximation and Beyond for Time-Dependent Electronic Processes', *The Journal of Chemical Physics*, **2008**, *128*, 124101.
(Cited on page 49)

(241) A. Abedi, N. T. Maitra and E. K. U. Gross, 'Exact Factorization of the Time-Dependent Electron-Nuclear Wave Function', *Physical Review Letters*, **2010**, *105*, 123002.
(Cited on page 49)

(242) A. Abedi, N. T. Maitra and E. K. U. Gross, 'Correlated Electron-Nuclear Dynamics: Exact Factorization of the Molecular Wavefunction', *The Journal of Chemical Physics*, **2012**, *137*, 22A530.
(Cited on page 49)

(243) Y. C. Chiang, S. Klaiman, F. Otto and L. S. Cederbaum, 'The Exact Wavefunction Factorization of a Vibronic Coupling System', *The Journal of Chemical Physics*, **2014**, *140*, 054104.
(Cited on page 49)

(244) N. I. Gidopoulos and E. K. U. Gross, 'Electronic Non-Adiabatic States: Towards a Density Functional Theory Beyond the Born-Oppenheimer Approximation', *Philosophical Transactions of the Royal Society. Series A, Mathematical, Physical, and Engineering Sciences*, **2014**, *372*, 20130059/1–9.
(Cited on page 49)

(245) R. K. Preston and J. C. Tully, 'Effects of Surface Crossing in Chemical Reactions - the H_3 System', *The Journal of Chemical Physics*, **1971**, *54*, 4297–4304.
(Cited on page 49)

(246) J. C. Tully and R. K. Preston, 'Trajectory Surface Hopping Approach to Nonadiabatic Molecular Collisions: The Reaction of H^+ with D_2', *The Journal of Chemical Physics*, **1971**, *55*, 562–572.
(Cited on page 49)

(247) M. Barbatti, 'Nonadiabatic Dynamics with Trajectory Surface Hopping Method', *Wiley Interdisciplinary Reviews: Computational Molecular Science*, **2011**, *1*, 620–633.
(Cited on page 49)

(248) H.-D. Meyer, U. Manthe and L. S. Cederbaum, 'The Multi-Configurational Time-Dependent Hartree Approach', *Chemical Physics Letters*, **1990**, *165*, 73–78.
(Cited on page 50)

(249) M. H. Beck, A. Jäckle, G. A. Worth and H.-D. Meyer, 'The Multiconfiguration Time-Dependent Hartree (MCTDH) Method: a Highly Efficient Algorithm for Propagating Wavepackets', *Physics Reports*, **2000**, *324*, 1–105.
(Cited on page 50)

(250) H.-D. Meyer and G. A. Worth, 'Quantum Molecular Dynamics: Propagating Wavepackets and Density Operators Using the Multiconfiguration Time-Dependent Hartree Method', *Theoretical Chemistry Accounts*, **2003**, *109*, 251–267.
(Cited on page 50)

(251) J. C. Light, I. P. Hamilton and J. V. Lill, 'Generalized Discrete Variable Approximation in Quantum Mechanics', *The Journal of Chemical Physics*, **1985**, *82*, 1400–1409.
(Cited on page 50)

(252) J. C. Light and T. Carrington, in *Advances in Chemical Physics*, 2000, vol. 114, pp. 263–310 (Cited on page 50).

(253) A. J. H. M. Meijer and E. M. Goldfield, in *Tutorials in Molecular Reaction Dynamics*, ed. M. Brouard and C. Vallance, Royal Society of Chemistry, 1st edn., 2010, ch. 3, pp. 49–87 (Cited on page 50).

(254) J. Z. H. Zhang, *Theory and Application of Quantum Molecular Dynamics*, World Scientific Publishing Co. Pte. Ltd., 1998.
(Cited on page 50)

(255) M. J. Frisch, G. W. Trucks, H. B. Schlegel, G. E. Scuseria, M. A. Robb, J. R. Cheeseman, G. Scalmani, V. Barone, B. Mennucci, G. A. Petersson, H. Nakatsuji, M. Caricato, X. Li, H. P. Hratchian, A. F. Izmaylov, J. Bloino, G. Zheng, J. L. Sonnenberg, M. Hada, M. Ehara, K. Toyota, R. Fukuda, J. Hasegawa, M. Ishida, T. Nakajima, Y. Honda, O. Kitao, H. Nakai, T. Vreven, J. A. Montgomery Jr., J. E. Peralta, F. Ogliaro, M. J. Bearpark, J. J. Heyd, E. Brothers, K. N. Kudin, V. N. Staroverov, R. Kobayashi, J. Normand, K. Raghavachari, A. Rendell, J. C. Burant, S. S. Iyengar, J. Tomasi, M. Cossi, N. Rega, J. M. Millam, M. Klene, J. E. Knox, J. B. Cross, V. Bakken, C. Adamo, J. Jaramillo, R. Gomperts, R. E. Stratmann, O. Yazyev, A. J. Austin, R. Cammi, C. Pomelli, J. W. Ochterski, R. L. Martin, K. Morokuma, V. G. Zakrzewski, G. A. Voth, P. Salvador, J. J. Dannenberg, S. Dapprich, A. D. Daniels, Ö. Farkas, J. B. Foresman, J. V. Ortiz, J. Cioslowski and D. J. Fox, *Gaussian 09, Revision D.01*, 2013 (Cited on pages 51, 53, 84).

(256) B. Mennucci and J. Tomasi, 'Continuum Solvation Models: a New Approach to the Problem of Solute's Charge Distribution and Cavity Boundaries', *The Journal of Chemical Physics*, **1997**, *106*, 5151–5158.
(Cited on pages 51, 54, 83)

(257) M. Cossi, V. Barone, B. Mennucci and J. Tomasi, 'Ab initio Study of Ionic Solutions by a Polarizable Continuum Dielectric Model', *Chemical Physics Letters*, **1998**, *286*, 253–260.
(Cited on pages 51, 54, 83)

(258) D. Andrae, U. Häußermann, M. Dolg, H. Stoll and H. Preuß, 'Energy-Adjusted ab initio Pseudopotentials for the Second and Third Row Transition Elements', *Theoretica Chimica Acta*, **1990**, *77*, 123–141.
(Cited on pages 51, 83, 106)

(259) T. H. Dunning Jr. and P. J. Hay, in *Modern Theoretical Chemistry*, ed. H. F. Schaefer, Plenum: New York, 3rd edn., 1977, pp. 1–28.
(Cited on page 51)

(260) P. C. Hariharan and J. A. Pople, 'The Influence of Polarization Functions on Molecular Orbital Hydrogenation Energies', *Theoretica Chimica Acta*, **1973**, *28*, 213–222.
(Cited on page 51)

(261) M. M. Francl, W. J. Pietro, W. J. Hehre, M. S. Gordon, D. J. DeFrees and J. A. Pople, 'Self-Consistent Molecular Orbital Methods. XXIII. A Polarization-Type Basis Set for Second-Row Elements', *The Journal of Chemical Physics*, **1982**, *77*, 3654.
(Cited on page 51)

(262) T. H. Dunning Jr., 'Gaussian Basis Sets for Use in Correlated Molecular Calculations. I. The Atoms Boron Through Neon and Hydrogen', *The Journal of Chemical Physics*, **1989**, *90*, 1007–1023.
(Cited on pages 51, 54, 106)

(263) T. H. Dunning Jr., K. A. Peterson and A. K. Wilson, 'Gaussian Basis Sets for use in Correlated Molecular Calculations. X. The Atoms Aluminum through Argon Revisited', *The Journal of Chemical Physics*, **2001**, *114*, 9244–9253.
(Cited on pages 51, 106)

(264) D. Figgen, K. A. Peterson, M. Dolg and H. Stoll, 'Energy-Consistent Pseudopotentials and Correlation Consistent Basis Sets for the 5d Elements Hf-Pt', *The Journal of Chemical Physics*, **2009**, *130*, 164108.
(Cited on pages 51, 106)

(265) R. Krishnan, J. S. Binkley, R. Seeger and J. A. Pople, 'Self-Consistent Molecular Orbital Methods. XX. A Basis Set for Correlated Wave Functions', *The Journal of Chemical Physics*, **1980**, *72*, 650–654.
(Cited on pages 51, 83, 106)

(266) A. D. McLean and G. S. Chandler, 'Contracted Gaussian Basis Sets for Molecular Calculations. I. Second Row Atoms, Z = 11–18', *The Journal of Chemical Physics*, **1980**, *72*, 5639.
(Cited on pages 51, 83, 106)

(267) J. Baker, A. A. Jarzecki and P. Pulay, 'Direct Scaling of Primitive Valence Force Constants: An Alternative Approach to Scaled Quantum Mechanical Force Fields', *The Journal of Physical Chemistry A*, **1998**, *102*, 1412–1424.
(Cited on page 52)

(268) M. D. Halls, J. Velkovski and H. B. Schlegel, 'Harmonic Frequency Scaling Factors for Hartree-Fock, S-VWN, B-LYP, B3-LYP, B3-PW91 and MP2 with the Sadlej pVTZ Electric Property Basis Set', *Theoretical Chemistry Accounts*, **2001**, *105*, 413–421.
(Cited on page 52)

(269) K. K. Irikura, R. D. Johnson and R. N. Kacker, 'Uncertainties in Scaling Factors for ab initio Vibrational Frequencies', *The Journal of Physical Chemistry A*, **2005**, *109*, 8430–8437.
(Cited on page 52)

(270) I. M. Alecu, J. Zheng, Y. Zhao and D. G. Truhlar, 'Computational Thermochemistry: Scale Factor Databases and Scale Factors for Vibrational Frequencies Obtained from Electronic Model Chemistries', *Journal of Chemical Theory and Computation*, **2010**, *6*, 2872–2887.
(Cited on page 52)

(271) I. V. Sazanovich, M. A. H. Alamiry, A. J. H. M. Meijer, M. Towrie, E. S. Davies, R. D. Bennett and J. A. Weinstein, 'Photoinduced Charge Separation in a Pt^{II} Acetylide Donor–Acceptor Triad Based on 2-(1-pyrazole)-pyridine Modified with Naphthalene Mono-Imide Electron Acceptor', *Pure and Applied Chemistry*, **2013**, *85*, 1331–1348.
(Cited on pages 52, 81, 82, 87)

(272) I. V. Sazanovich, J. Best, P. A. Scattergood, M. Towrie, S. A. Tikhomirov, O. V. Bouganov, A. J. H. M. Meijer and J. A. Weinstein, 'Ultrafast Photoinduced Charge Transport in Pt(II) Donor–Acceptor Assembly Bearing Naphthalimide Electron Acceptor and Phenothiazine Electron Donor', *Physical Chemistry Chemical Physics*, **2014**, *16*, 25775–25788.
(Cited on pages 52, 81, 82, 87, 97, 98)

(273) E. B. Wilson, J. C. Decius and P. C. Cross, *Molecular Vibrations: The Theory of Infrared and Raman Vibrational Spectra*, Dover Publications Inc., New York, 1980, p. 388.
(Cited on page 53)

(274) J. W. Ochterski, *Vibrational Analysis in Gaussian*, tech. rep., Gaussian Inc., 1999 (Cited on pages 53, 121, 125, 162, 164).

(275) E. J. Baerends, T. Ziegler, A. J. Atkins, J. Autschbach, D. Bashford, A. Bérces, F. M. Bickelhaupt, C. Bo, P. M. Boerritger, L. Cavallo, D. P. Chong, D. V. Chulhai, L. Deng, R. M. Dickson, J. M. Dieterich, D. E. Ellis, M. van Faassen, A. Ghysels, A. Giammona, S. J. A. van Gisbergen, A. W. Götz, S. Gusarov, F. E. Harris, P. van den Hoek, C. R. Jacob, H. Jacobsen, L. Jensen, J. W. Kaminski, G. van Kessel, F. Kootstra, A. Kovalenko, M. Krykunov, E. van Lenthe, D. A. McCormack, A. Michalak, M. Mitoraj, S. M. Morton, J. Neugebauer, V. P. Nicu, L. Noodleman,

V. P. Osinga, S. Patchkovskii, M. Pavanello, C. A. Peeples, P. H. T. Philipsen, D. Post, C. C. Pye, W. Ravenek, J. I. Rodríguez, P. Ros, R. Rüger, P. R. T. Schipper, H. van Schoot, G. Schreckenbach, J. S. Seldenthuis, M. Seth, J. G. Snijders, M. Solà, M. Swart, D. Swerhone, G. te Velde, P. Vernooijs, L. Versluis, L. Visscher, O. Visser, F. Wang, T. A. Wesolowski, E. M. van Wezenbeek, G. Wiesenekker, S. K. Wolff, T. K. Woo and A. L. Yakovlev, *ADF2016, SCM, Theoretical Chemistry, Vrije Universiteit, Amsterdam, The Netherlands, http://www.scm.com.* (Cited on pages 53, 129).

(276) C. Fonseca Guerra, J. G. Snijders, G. te Velde and E. J. Baerends, 'Towards an Order-*N* DFT Method', *Theoretical Chemistry Accounts*, **1998**, *99*, 391–403.
(Cited on page 53)

(277) G. te Velde, F. M. Bickelhaupt, E. J. Baerends, C. Fonseca Guerra, S. J. A. van Gisbergen, J. G. Snijders and T. Ziegler, 'Chemistry with ADF', *Journal of Computational Chemistry*, **2001**, *22*, 931–967.
(Cited on page 53)

(278) E. van Lenthe and E. J. Baerends, 'Optimized Slater-type Basis Sets for the Elements 1–118', *Journal of Computational Chemistry*, **2003**, *24*, 1142–1156.
(Cited on pages 53, 110)

(279) A. Rosa, E. J. Baerends, S. J. A. van Gisbergen, E. van Lenthe, J. A. Groeneveld and J. G. Snijders, 'Electronic Spectra of $M(CO)_6$ (M = Cr, Mo, W) Revisited by a Relativistic TDDFT Approach', *Journal of the American Chemical Society*, **1999**, *121*, 10356–10365.
(Cited on page 53)

(280) F. Wang and T. Ziegler, 'A Simplified Relativistic Time-Dependent Density-Functional Theory Formalism for the Calculations of Excitation Energies including Spin-Orbit Coupling Effect', *The Journal of Chemical Physics*, **2005**, *123*, 154102.
(Cited on pages 53, 109, 132)

(281) A. Klamt and G. Schüürmann, 'COSMO: a New Approach to Dielectric Screening in Solvents with Explicit Expressions for the Screening Energy and its Gradient', *Journal of the Chemical Society, Perkin Transactions 2*, **1993**, 799–805.
(Cited on page 53)

(282) C. C. Pye and T. Ziegler, 'An Implementation of the Conductor-like Screening Model of Solvation within the Amsterdam Density Functional Package', *Theoretical Chemistry Accounts*, **1999**, *101*, 396–408.
(Cited on page 53)

(283) M. Franchini, P. H. T. Philipsen, E. van Lenthe and L. Visscher, 'Accurate Coulomb Potentials for Periodic and Molecular Systems through Density Fitting', *Journal of Chemical Theory and Computation*, **2014**, *10*, 1994–2004.
(Cited on page 53)

(284) A. D. Becke, 'A Multicenter Numerical Integration Scheme for Polyatomic Molecules', *The Journal of Chemical Physics*, **1988**, *88*, 2547.
(Cited on page 53)

(285) M. Franchini, P. H. T. Philipsen and L. Visscher, 'The Becke Fuzzy Cells Integration Scheme in the Amsterdam Density Functional Program Suite', *Journal of Computational Chemistry*, **2013**, *34*, 1819–1827.
(Cited on page 53)

(286) A. K. Wilson, D. E. Woon, K. A. Peterson and T. H. Dunning Jr., 'Gaussian Basis Sets for use in Correlated Molecular Calculations. IX. The Atoms Gallium through Krypton', *The Journal of Chemical Physics*, **1999**, *110*, 7667–7676.
(Cited on page 54)

(287) W. A. de Jong, R. J. Harrison and D. A. Dixon, 'Parallel Douglas–Kroll Energy and Gradients in NWChem: Estimating Scalar Relativistic Effects using Douglas–Kroll Contracted Basis Sets', *The Journal of Chemical Physics*, **2001**, *114*, 48–53.
(Cited on pages 54, 150)

(288) K. A. Peterson, 'Systematically Convergent Basis Sets with Relativistic Pseudopotentials. I. Correlation Consistent Basis Sets for the Post-d Group 13–15 Elements', *The Journal of Chemical Physics*, **2003**, *119*, 11099–11112.
(Cited on page 54)

(289) F. London, 'Théorie Quantique des Courants Interatomiques dans les Combinaisons Aromatiques', *Journal de Physique et le Radium*, **1937**, *8*, 397–409.
(Cited on pages 54, 149, 150)

(290) R. McWeeny, 'Perturbation Theory for the Fock-Dirac Density Matrix', *Physical Review*, **1962**, *126*, 1028–1034.
(Cited on pages 54, 149, 150)

(291) R. Ditchfield, 'Self-Consistent Perturbation Theory of Diamagnetism. I. A Gauge-Invariant LCAO Method for N.M.R. Chemical Shifts', *Molecular Physics*, **1974**, *27*, 789–807.
(Cited on pages 54, 149, 150)

(292) K. Wolinski, J. F. Hinton and P. Pulay, 'Efficient Implementation of the Gauge-Independent Atomic Orbital Method for NMR Chemical Shift Calculations', *Journal of the American Chemical Society*, **1990**, *112*, 8251–8260.
(Cited on pages 54, 149, 150)

(293) J. R. Cheeseman, G. W. Trucks, T. A. Keith and M. J. Frisch, 'A Comparison of Models for Calculating Nuclear Magnetic Resonance Shielding Tensors', *The Journal of Chemical Physics*, **1996**, *104*, 5497–5509.
(Cited on pages 54, 149, 150)

(294) S. F. Boys and F. Bernardi, 'The Calculation of Small Molecular Interactions by the Differences of Separate Total Energies. Some Procedures with Reduced Errors', *Molecular Physics*, **1970**, *19*, 553–566.
(Cited on pages 54, 147)

(295) S. Simon, M. Duran and J. J. Dannenberg, 'How Does Basis Set Superposition Error Change the Potential Surfaces for Hydrogen-Bonded Dimers?', *The Journal of Chemical Physics*, **1996**, *105*, 11024.
(Cited on pages 54, 147)

(296) T. A. A. Oliver, N. H. C. Lewis and G. R. Fleming, 'Correlating the Motion of Electrons and Nuclei with Two-Dimensional Electronic-Vibrational Spectroscopy', *Proceedings of the National Academy of Sciences of the United States of America*, **2014**, *111*, 10061–10066.
(Cited on page 68)

(297) F. Terenziani and A. Painelli, 'Two-Dimensional Electronic-Vibrational Spectra: Modeling Correlated Electronic and Nuclear Motion', *Physical Chemistry Chemical Physics*, **2015**, *17*, 13074–13081.
(Cited on page 68)

(298) T. L. Courtney, Z. W. Fox, L. Estergreen and M. Khalil, 'Measuring Coherently Coupled Intramolecular Vibrational and Charge-Transfer Dynamics with Two-Dimensional Vibrational–Electronic Spectroscopy', *The Journal of Physical Chemistry Letters*, **2015**, *6*, 1286–1292.
(Cited on page 68)

(299) Y. Yue, T. Grusenmeyer, Z. Ma, P. Zhang, R. H. Schmehl, D. N. Beratan and I. V. Rubtsov, 'Electron Transfer Rate Modulation in a Compact Re(I) Donor-Acceptor Complex', *Dalton Transactions*, **2015**, *44*, 8609–8616.
(Cited on pages 77, 99)

(300) J. van Slageren, A. Klein and S. Záliš, 'Ligand-to-Ligand Charge Transfer States and Photochemical Bond Homolysis in Metal-Carbon Bonded Platinum Complexes', *Coordination Chemistry Reviews*, **2002**, *230*, 193–211.
(Cited on page 78)

(301) J. E. McGarrah and R. Eisenberg, 'Dyads for Photoinduced Charge Separation Based on Platinum Diimine Bis(acetylide) Chromophores: Synthesis, Luminescence and Transient Absorption Studies', *Inorganic Chemistry*, **2003**, *42*, 4355–4365.
(Cited on pages 78, 79, 98)

(302) J. E. McGarrah, J. T. Hupp and S. N. Smirnov, 'Electron Transfer in Platinum(II) Diimine-Centered Triads: Mechanistic Insights from Photoinduced Transient Displacement Current Measurements', *The Journal of Physical Chemistry A*, **2009**, *113*, 6430–6436.
(Cited on pages 79, 97, 98)

(303) *Atomic and Molecular Beams: The State of the Art 2000*, ed. R. Campargue, Springer-Verlag Berlin Heidelberg, New York, 2001.
(Cited on page 79)

(304) O. Ghafur, A. Rouzée, A. Gijsbertsen, W. K. Siu, S. Stolte and M. J. J. Vrakking, 'Impulsive Orientation and Alignment of Quantum-State-Selected NO Molecules', *Nature Physics*, **2009**, *5*, 289–293.
(Cited on page 79)

(305) M. Lisaj and O. Kühn, 'Laser-Driven Localization of Collective CO Vibrations in Metal-Carbonyl Complexes', *The Journal of Chemical Physics*, **2014**, *141*, 204303.
(Cited on page 79)

(306) S. A. Archer and J. A. Weinstein, 'Charge-Separated Excited States in Platinum(II) Chromophores: Photophysics, Formation, Stabilization and Utilization in Solar Energy Conversion', *Coordination Chemistry Reviews*, **2012**, *256*, 2530–2561.
(Cited on page 79)

(307) R. J. Cross and M. F. Davidson, 'Formation and Isomerisation of cis-bis(phenylethynyl)bis(tertiary phosphine)platinum Complexes', *Journal of the Chemical Society, Dalton Transactions*, **1986**, 1987–1992.
(Cited on page 79)

(308) F. Hua, S. Kinayyigit, J. R. Cable and F. N. Castellano, 'Green Photoluminescence from Platinum(II) Complexes Bearing Silylacetylide Ligands', *Inorganic Chemistry*, **2005**, *44*, 471–473.
(Cited on pages 81, 82)

(309) F. Hua, S. Kinayyigit, J. R. Cable and F. N. Castellano, 'Platinum(II) Diimine Diacetylides: Metallacyclization Enhances Photophysical Properties', *Inorganic Chemistry*, **2006**, *45*, 4304–4306.
(Cited on pages 81, 82)

(310) J. M. Bowman, 'The Self-Consistent-Field Approach to Polyatomic Vibrations', *Accounts of Chemical Research*, **1986**, *19*, 202–208.
(Cited on page 82)

(311) W. H. Miller, R. Hernandez, N. C. Handy, D. Jayatilaka and A. Willetts, 'Ab initio Calculation of Anharmonic Constants for a Transition State, with Application to Semiclassical Transition State Tunneling Probabilities', *Chemical Physics Letters*, **1990**, *172*, 62–68.
(Cited on pages 82, 84)

(312) J. M. L. Martin, T. J. Lee, P. R. Taylor and J.-P. François, 'The Anharmonic Force Field of Ethylene, C_2H_4, by Means of Accurate ab initio Calculations', *The Journal of Chemical Physics*, **1995**, *103*, 2589.
(Cited on pages 82, 84)

(313) V. Barone, 'Anharmonic Vibrational Properties by a Fully Automated Second-Order Perturbative Approach', *The Journal of Chemical Physics*, **2005**, *122*, 014108.
(Cited on pages 82, 84, 91)

(314) J. Bloino and V. Barone, 'A Second-Order Perturbation Theory Route to Vibrational Averages and Transition Properties of Molecules: General Formulation and Application to Infrared and Vibrational Circular Dichroism Spectroscopies', *The Journal of Chemical Physics*, **2012**, *136*, 124108.
(Cited on pages 82–84)

(315) A. P. Charmet, P. Stoppa, N. Tasinato, S. Giorgianni, V. Barone, M. Biczysko, J. Bloino, C. Cappelli, I. Carnimeo and C. Puzzarini, 'An Integrated Experimental and Quantum-Chemical Investigation on the Vibrational Spectra of Chlorofluoromethane', *The Journal of Chemical Physics*, **2013**, *139*, 164302.
(Cited on pages 82, 84)

(316) V. Barone, M. Biczysko and J. Bloino, 'Fully Anharmonic IR and Raman Spectra of Medium-Size Molecular Systems: Accuracy and Interpretation', *Physical Chemistry Chemical Physics*, **2014**, *16*, 1759–1787.
(Cited on pages 82, 84)

(317) F. Vazart, C. Latouche, J. Bloino and V. Barone, 'Vibronic Coupling Investigation to Compute Phosphorescence Spectra of Pt(II) Complexes', *Inorganic Chemistry*, **2015**, *54*, 5588–5595.
(Cited on page 82)

(318) F. Vazart and C. Latouche, 'Validation of a Computational Protocol to Simulate Near IR Phosphorescence Spectra for Ru(II) and Ir(III) Metal Complexes', *Theoretical Chemistry Accounts*, **2015**, *134*, 144.
(Cited on page 82)

(319) J. Bloino, M. Biczysko and V. Barone, 'General Perturbative Approach for Spectroscopy, Thermodynamics, and Kinetics: Methodological Background and Benchmark Studies', *Journal of Chemical Theory and Computation*, **2012**, *8*, 1015–1036.
(Cited on page 83)

(320) A. M. Rosnik and W. F. Polik, 'VPT2+K Spectroscopic Constants and Matrix Elements of the Transformed Vibrational Hamiltonian of a Polyatomic Molecule with Resonances using Van Vleck Perturbation Theory', *Molecular Physics*, **2014**, *112*, 261–300.
(Cited on page 83)

(321) E. Fermi, 'Über den Ramaneffekt des Kohlendioxyds', *Zeitschrift für Physik*, **1931**, *71*, 250–259.
(Cited on page 83)

(322) B. T. Darling and D. M. Dennison, 'The Water Vapor Molecule', *Physical Review*, **1940**, *57*, 128–139.
(Cited on page 83)

(323) S. V. Krasnoshchekov, E. V. Isayeva and N. F. Stepanov, 'Criteria for First- and Second-Order Vibrational Resonances and Correct Evaluation of the Darling-Dennison Resonance Coefficients using the Canonical Van Vleck Perturbation Theory', *The Journal of Chemical Physics*, **2014**, *141*, 234114.
(Cited on page 83)

(324) J. S. Lipkin, R. Song, E. E. Fenlon and S. H. Brewer, 'Modulating Accidental Fermi Resonance: What a Difference a Neutron Makes', *Journal of Physical Chemistry Letters*, **2011**, *2*, 1672–1676.
(Cited on page 83)

(325) R. Costard, C. Greve, H. Fidder and E. T. J. Nibbering, 'Hydrogen Bonding Induced Enhancement of Fermi Resonances: Ultrafast Vibrational Energy Flow Dynamics in Aniline-d5', *The Journal of Physical Chemistry B*, **2015**, *119*, 2711–2725.
(Cited on page 83)

(326) W. Schneider and W. Thiel, 'Anharmonic Force Fields from Analytic Second Derivatives: Method and Application to Methyl Bromide', *Chemical Physics Letters*, **1989**, *157*, 367–373.
(Cited on page 85)

(327) C. Latouche, *Personal communication* (Cited on page 87).

(328) A. D. Boese, W. Klopper and J. M. L. Martin, 'Anharmonic Force Fields and Thermodynamic Functions using Density Functional Theory', *Molecular Physics*, **2004**, *103*, 863–876.
(Cited on page 87)

(329) A. D. Boese, W. Klopper and J. M. L. Martin, 'Assessment of Various Density Functionals and Basis Sets for the Calculation of Molecular Anharmonic Force Fields', *International Journal of Quantum Chemistry*, **2005**, *104*, 830–845.
(Cited on page 87)

(330) C. Puzzarini, M. Biczysko and V. Barone, 'Accurate Harmonic/Anharmonic Vibrational Frequencies for Open-Shell Systems: Performances of the B3LYP/N07D Model for Semirigid Free Radicals Benchmarked by CCSD(T) Computations', *Journal of Chemical Theory and Computation*, **2010**, *6*, 828–838.
(Cited on page 87)

(331) V. Barone, M. Biczysko, J. Bloino and C. Puzzarini, 'Accurate Molecular Structures and Infrared Spectra of trans-2,3-Dideuterooxirane, Methyloxirane, and trans-2,3-Dimethyloxirane', *The Journal of Chemical Physics*, **2014**, *141*, 034107.
(Cited on page 87)

(332) T. A. Niehaus, T. Hofbeck and H. Yersin, 'Charge-Transfer Excited States in Phosphorescent Organo-Transition Metal Compounds: a Difficult Case for Time Dependent Density Functional Theory?', *RSC Advances*, **2015**, *5*, 63318–63329.
(Cited on page 94)

(333) F. Plasser, M. Barbatti, A. J. A. Aquino and H. Lischka, 'Electronically Excited States and Photodynamics: a Continuing Challenge', *Theoretical Chemistry Accounts*, **2012**, *131*, 1073.
(Cited on page 103)

(334) E. A. Amin and D. G. Truhlar, 'Zn Coordination Chemistry: Development of Benchmark Suites for Geometries, Dipole Moments, and Bond Dissociation Energies and Their Use To Test and Validate Density Functionals and Molecular Orbital Theory', *Journal of Chemical Theory and Computation*, **2008**, *4*, 75–85.
(Cited on page 104)

(335) M. Schreiber, M. R. Silva-Junior, S. P. A. Sauer and W. Thiel, 'Benchmarks for Electronically Excited States: CASPT2, CC2, CCSD, and CC3', *The Journal of Chemical Physics*, **2008**, *128*, 134110.
(Cited on page 104)

(336) D. Bousquet, R. Fukuda, P. Maitarad, D. Jacquemin, I. Ciofini, C. Adamo and M. Ehara, 'Excited-State Geometries of Heteroaromatic Compounds: A Comparative TD-DFT and SAC-CI Study', *Journal of Chemical Theory and Computation*, **2013**, *9*, 2368–2379.
(Cited on page 104)

(337) D. Bousquet, R. Fukuda, D. Jacquemin, I. Ciofini, C. Adamo and M. Ehara, 'Benchmark Study on the Triplet Excited-State Geometries and Phosphorescence Energies of Heterocyclic Compounds: Comparison Between TD-PBE0 and SAC-CI', *Journal of Chemical Theory and Computation*, **2014**, *10*, 3969–3979.
(Cited on page 104)

(338) J. B. Foresman, M. Head-Gordon, J. A. Pople and M. J. Frisch, 'Toward a Systematic Molecular Orbital Theory for Excited States', *The Journal of Physical Chemistry*, **1992**, *96*, 135–149.
(Cited on page 104)

(339) Gaussian Inc., *Plotting UV/vis Spectra from Oscillator & Dipole Strengths*, http://www.gaussian.com/g_whitepap/tn_uvvisplot.htm (Cited on page 104).

(340) H. Mori, R. Kojima, Y. Mochizuki, W. Uenohara, I. Umezawa and N. Matsushita, 'Importance of Spin-Orbit Coupling Effect and Solvent Effect in Electronic Transition Assignments of Pt^{II} Complexes: In the Case of cis/trans-[$Pt^{II}Cl_2(NH_3)_2$]', *Journal of Molecular Structure*, **2013**, *1035*, 218–223.
(Cited on pages 108, 109)

(341) S. Záliš, Y. C. Lam, H. B. Gray and A. Vlček Jr., 'Spin-Orbit TDDFT Electronic Structure of Diplatinum(II,II) Complexes', *Inorganic Chemistry*, **2015**, *54*, 3491–3500.
(Cited on pages 108, 109)

(342) J. Moon, T. K. Kim and J. Kim, 'Ground and Low-Lying Excited States of PtCN and PdCN: Theoretical Investigation Including Spin–Orbit Coupling', *Theoretical Chemistry Accounts*, **2016**, *135*, 127.
(Cited on page 108)

(343) N. Moreno, F. Ferraro, E. Flórez, C. Z. Hadad and A. Restrepo, 'Spin–Orbit Coupling Effects in Au_mPt_n Clusters ($m + n = 4$)', *The Journal of Physical Chemistry A*, **2016**, *120*, 1698–1705.
(Cited on page 108)

(344) W. Zou and B. Suo, 'Theoretical Study of Low-Lying Electronic States of PtX (X = F, Cl, Br, and I) Including Spin–Orbit Coupling', *The Journal of Physical Chemistry A*, **2016**, *120*, 6357–6370.
(Cited on page 108)

(345) D. D. Koelling and B. N. Harmon, 'A Technique for Relativistic Spin-Polarised Calculations', *Journal of Physics C: Solid State Physics*, **1977**, *10*, 3107–3114.
(Cited on page 109)

(346) H. Gollisch and L. Fritsche, 'Relativistic One-Particle Equation for Electron States of Heavy Metals', *Physica Status Solidi (b)*, **1978**, *86*, 145–150.
(Cited on page 109)

(347) T. Takeda, 'The Scalar Relativistic Approximation', *Zeitschrift für Physik B Condensed Matter and Quanta*, **1978**, *32*, 43–48.
(Cited on page 109)

(348) *ADF Bugfix Change-log*, https://www.scm.com/support/downloads/changelog/ (Cited on page 114).

(349) S. J. A. van Gisbergen, F. Kootstra, P. R. T. Schipper, O. V. Gritsenko, J. G. Snijders and E. J. Baerends, 'Density-Functional-Theory Response-Property Calculations with Accurate Exchange-Correlation Potentials', *Physical Review A*, **1998**, *57*, 2556–2571.
(Cited on page 116)

(350) S. H. Vosko, L. Wilk and M. Nusair, 'Accurate Spin-Dependent Electron Liquid Correlation Energies for Local Spin Density Calculations: a Critical Analysis', *Canadian Journal of Physics*, **1980**, *58*, 1200–1211.
(Cited on page 131)

(351) C. Creutz, M. D. Newton and N. Sutin, 'Metal–Ligand and Metal–Metal Coupling Elements', *Journal of Photochemistry and Photobiology A: Chemistry*, **1994**, *82*, 47–59.
(Cited on page 134)

(352) R. J. Cave and M. D. Newton, 'Generalization of the Mulliken-Hush Treatment for the Calculation of Electron Transfer Matrix Elements', *Chemical Physics Letters*, **1996**, *249*, 15–19.
(Cited on page 134)

(353) R. J. Cave and M. D. Newton, 'Calculation of Electronic Coupling Matrix Elements for Ground and Excited State Electron Transfer Reactions: Comparison of the Generalized Mulliken–Hush and Block Diagonalization Methods', *The Journal of Chemical Physics*, **1997**, *106*, 9213–9226.
(Cited on page 134)

(354) G. A. Worth, G. Welch and M. J. Paterson, 'Wavepacket Dynamics Study of $Cr(CO)_5$ after Formation by Photodissociation: Relaxation Through an $(E \oplus A) \otimes e$ Jahn–Teller Conical Intersection', *Molecular Physics*, **2006**, *104*, 1095–1105.
(Cited on page 139)

(355) J. Eng, C. Gourlaouen, E. Gindensperger and C. Daniel, 'Spin-Vibronic Quantum Dynamics for Ultrafast Excited-State Processes', *Accounts of Chemical Research*, **2015**, *48*, 809–817.
(Cited on page 139)

(356) M. Pápai, G. Vankó, T. Rozgonyi and T. J. Penfold, 'High-Efficiency Iron Photosensitizer Explained with Quantum Wavepacket Dynamics', *The Journal of Physical Chemistry Letters*, **2016**, *7*, 2009–2014.
(Cited on page 139)

(357) D. Escudero and W. Thiel, 'Assessing the Density Functional Theory-Based Multireference Configuration Interaction (DFT/MRCI) Method for Transition Metal Complexes', *The Journal of Chemical Physics*, **2014**, *140*, 194105.
(Cited on page 140)

(358) D. Escudero, W. Thiel and B. Champagne, 'Spectroscopic and Second-Order Nonlinear Optical Properties of Ruthenium(II) Complexes: a DFT/MRCI and ADC(2) Study', *Physical Chemistry Chemical Physics*, **2015**, *17*, 18908–18912.
(Cited on page 140)

(359) M. Fumanal and C. Daniel, 'Description of Excited States in [Re(Imidazole)$(CO)_3$(Phen)]$^+$ Including Solvent and Spin-Orbit Coupling Effects: Density Functional Theory versus Multiconfigurational Wavefunction Approach', *Journal of Computational Chemistry*, **2016**, *37*, 2454–2466.
(Cited on page 140)

(360) D. Lefrancois, D. R. Rehn and A. Dreuw, 'Accurate Adiabatic Singlet-Triplet Gaps in Atoms and Molecules Employing the Third-Order Spin-Flip Algebraic Diagrammatic Construction Scheme for the Polarization Propagator', *The Journal of Chemical Physics*, **2016**, *145*, 084102.
(Cited on page 140)

(361) P. Portius and M. Davis, 'Recent Developments in the Chemistry of Homoleptic Azido Complexes of the Main Group Elements', *Coordination Chemistry Reviews*, **2013**, *257*, 1011–1025.
(Cited on pages 142–144, 149)

(362) P. Portius, *Personal communication* (Cited on page 143).

(363) *Cambridge Structural Database*, http://webcsd.ccdc.cam.ac.uk/ (Cited on page 152).